The use of ultra-high temperature thermal energy storage for industrial decarbonisation

Sebastian Joseph Samuel Hudson



Doctor of Philosophy

The University of Edinburgh

2024

Abstract

Sustainable energy solutions are crucial to mitigating global warming. The integration of Ultra-High Temperature Thermal Energy Storage (UHTS) into industrial processes and power generation stands out as a compelling strategy to decarbonise pre-existing infrastructure. This thesis introduces a novel approach to enhancing energy efficiency and reducing carbon emissions within the framework of existing thermal power cycles and industrial operations. Through an extensive review of current energy storage technologies, this study identifies UHTS as a critical technology capable of facilitating the transition to a low-carbon economy.

Employing computational methods, quantitative modelling techniques are used to explore the feasibility of UHTS deployment. The research examines the feasibility of retrofitting Rankine and Brayton cycles, specifically a gas turbine (GT) and a heat recovery steam generator (HRSG), with UHTS, assessing enhancements in operational efficiency and environmental performance.

This research also includes the development of a comprehensive mathematical model to simulate the optimal operational behaviour of a UHTS system integrated into GTs, HRSGs and Industrial Boilers (IBs) under two design conditions - arbitrage profitability and fuel displacement. This model allows for an evaluation of the impact on the cost-effectiveness of a UHTS system, and the resulting carbon footprint reduction across different industrial applications.

This study's findings emphasise the potential of UHTS to improve the flexibility and sustainability of thermal power generation and industrial heat processes. Integration into the combustion chamber of a GT for hybrid burning is shown to offer a fuel displacement of up to 88.9 %, facilitating a reduction in NOx of 93.8 %, CO of 98.6 %, and CO_2 of 86.6 %. Flow augmentation of the inlet of a HRSG is shown to be viable with minimal design alterations, providing additional heat in the manner of supplemental firing, without the use of additional fuel. The feasibility of fully replacing the inlet flow with a UHTS system has also been explored, outlining the requirement for flow stratification measured to make the retrofit route viable. The research also demonstrates that UHTS integration can provide an average monthly arbitrage profitability of up to £2,225,000, and carbon emission reductions of 33,900 tonnes.

The implementation of UHTS can significantly boost the viability of an increasingly renewable grid, by providing the ability to reliably dispatch stored renewable energy, thereby decreasing reliance on fossil fuels and curtailing industrial carbon emissions.

The results and conclusions presented in this thesis outlined a detailed investigation of UHTS technologies, encapsulating their operational, economic, and environmental benefits. The research offers valuable insights for design engineers, policymakers, and industrial investors. It outlines the benefits of further development and implementation of UHTS, based on its ability to drive an increase in the profitability of pre-existing systems, whilst aligning with decarbonisation goals.

Lay Summary

Fossil fuels are widely used in power plants and industries such as manufacturing to heat a fluid to produce work. In gas turbines (GTs), natural gas is combusted to heat air, which is used to generate electricity. Once the gas turbine has extracted all the heat it can, the cooler (but still hot) air exits the system. From here, the air from the GT exhaust can enter a heat recovery steam generator (HRSG), extracting even more of the heat. Similarly, gas is combusted in industrial boilers (IBs) to produce steam which can be used to provide heat to various processes.

However, the burning of fossil fuels is directly linked to climate change, as it releases significant amounts of greenhouse gases, like carbon dioxide, into the atmosphere. To mitigate these effects and prevent further global warming, it's crucial to reduce our reliance on fossil fuels. This can be achieved by producing a greater proportion of our electricity from renewable sources, such as wind and solar. However, output from these sources is not guaranteed and is affected by factors such as the weather, which impact the security of supply.

A promising solution to this challenge is Ultra-High Temperature Thermal Energy Storage (UHTS), a new technology that allows for the storage and use of electricity from renewable sources. By storing excess electricity in the form of heat, UHTS can provide energy for power generation and industrial processes when needed, reducing the dependence on fossil fuels.

UHTS works by using excess electricity from the grid to heat a contained mass, which can then discharge this heat on demand by transferring the energy to a fluid that passes through the heated mass. This thesis examines the use of UHTS to supply heated air to GTs, HRSGs, and IBs, potentially fully or partially replacing the need for fuel.

A computational fluid dynamics (CFD) program is used to investigate the technical effects of incorporating this heated air into the combustion chamber of a GT and the inlet of a HRSG. This approach evaluates operational efficiency improvements and environmental performance enhancements.

Additionally, a mathematical model is developed to simulate the optimal operation of a UHTS system when connected to GTs, HRSGs and IBs under two modes. The first assesses the profitability of storing energy when there is a surplus and prices are low, then discharging later when there is an electricity deficit and prices are higher, generating profit via arbitrage. The second model maximises how much fuel the UHTS can displace, reducing the environmental impact of the systems.

The findings show the potential of UHTS to significantly improve the sustainability of processes currently reliant on heat from fossil fuels. Notably, integrating UHTS into GT combustion chambers can displace a significant percentage of the fuel required, leading to substantial reductions in emissions. Moreover, introducing heat flow to a HRSG can boost the flow temperature, enhancing the system output in a renewable manner without requiring major modifications. Additionally, the economic viability of UHTS, including potential arbitrage profits and reduced carbon emissions, underscores its potential to enhance the profitability of existing systems while contributing to decarbonisation goals.

This thesis demonstrates that the integration of UHTS into pre-existing systems presents a significant opportunity to combat climate change by providing a renewable alternative to fossil fuels.

Declaration

I hereby declare that the research presented in this thesis, unless explicitly stated otherwise or referenced, is my own work and was composed in the Institute for Energy Systems, School of Engineering at The University of Edinburgh. This work has not been submitted for any other degree of professional qualification except as specified.

Signed:



Sebastian Joseph Samuel Hudson, October 14, 2024

Acknowledgements

In the journey towards completing my PhD, a number of individuals have played critical and supportive roles, for which I am profoundly grateful.

First, my thanks are extended to my principal supervisor, Dr. Adam Robinson, whose guidance and mentorship have been indispensable throughout my project. Adam's insights, alongside the freedom he granted me in my research, have not only inspired me but also significantly contributed to my development as a researcher. In addition to this, Adam provided a range of opportunities to further my development over the course of this PhD, providing teaching, supervision and industrial experience. The trust and support that Adam provided, especially through challenging periods, have been fundamental in maintaining my focus and commitment to my work.

I would also like to express my gratitude to my second supervisor, Professor. Mathieu Lucquiaud, now at the University of Sheffield, for his valuable insights and detailed feedback on my research. His contributions in reviewing my work have been invaluable.

My fellow doctoral students working on the Ultra-High Temperature Energy Systems project— Aldo, Stuart, Thibaut, Tarek, and Haris. Thank you for your camaraderie and for making the work environment enjoyable and supportive. The friendships formed and the shared experiences have been a source of joy and encouragement throughout this journey. I would like to extend a particular thanks to 'The Cloistered Nuns', for always being there for support and their willingness to act as a sounding board in my more stressed moments.

In addition to the research group, I want to thank Mennat for her support and willingness to listen to me talk about nothing of great importance in our office. I also extend thanks to the University of Edinburgh, including the broader community in the School of Engineering, the Institute for Energy Systems and the Graduate School. I also want to thank all those I have crossed paths with during my PhD, including the lovely friends who supported me through the pandemic, your kindness and support have made my experience in Edinburgh unforgettable.

I would like to express my sincere gratitude to Luke for providing me with a crash course in Python coding. Your patience, expertise, and willingness to help have been invaluable to my development.

I extend my gratitude to the University of Edinburgh Jiu Jitsu Club, and The Jiu Jitsu Foundation as a whole, for playing a pivotal role in maintaining my physical and mental well-being and expanding my social circle beyond the confines of my PhD studies. These friendships have provided a much-needed balance and have taught me so much about myself, both on and off the mats. The club has not only kept me active but also introduced me to a community of friends who have managed to put up with me over the years. I can't think of any other group of people who I'd be so happy with breaking me on such a regular basis!

To put it simply, I would not have been able to finish this work without you, Anna. You have been the bedrock of support throughout the challenging journey of my PhD. Your unwavering belief in me, even during moments when I doubted myself and thought continuing was impossible, has been my source of strength and motivation. Your ability to see beyond the hurdles and encourage me to push forward has been nothing short of remarkable. You have consistently gone above and beyond, offering not just emotional support but also practical help in countless ways, including all the coffees you made me! Your presence, understanding, and

love have made all the difference, making the challenges I've faced surmountable. Thank you for being there, for every word of encouragement, every gesture of support, and for believing in me even when I couldn't. Your role in this journey has been invaluable, and I am endlessly grateful for everything you do. Additionally, I want to express my gratitude to Anna's parents, Alison and Dave, for their warmth and support. You welcomed me into your family and provided constant encouragement, which has been an invaluable source of comfort. My heartfelt thanks go to Halloumi and Cheddar, my cats, for their unconditional love and support. Their cuddles have provided much-needed moments of comfort amidst the rigours of PhD life.

My appreciation goes to my family for their unwavering support, even during those times didn't want it! Your love, encouragement, and motivation have been the foundation upon which I've built my resilience and determination. Without you, I undoubtedly wouldn't be where I am today. Although I may not vocalise my gratitude as often as I should, please know that I truly value and cherish everything you have done for me over the years. Your sacrifices have not gone unnoticed, and your belief in me has been unwavering. This extends to James and Eden, without whom, I may never have survived my first year as an undergraduate!

Finally, I extend my gratitude to everyone who has been part of my life's journey, contributing in various ways to my personal and professional growth. I would not be who I am today without you. This PhD has been a journey of growth, challenges, and personal discovery, made possible by the collective support and encouragement of everyone mentioned and many unmentioned. To each of you, I owe a debt of gratitude. Thank you.

Contents

1 Introduction **1**
1.1 Context . . . 1
1.1.1 Emissions Regulation . . . 2
1.1.2 Evolving Electricity Network . . . 4
1.1.3 Storage Timescales . . . 6

2 Literature review **12**
2.1 Energy Storage Technologies . . . 12
2.1.1 Mechanical . . . 13
2.1.2 Electrical . . . 19
2.1.3 Chemical . . . 21
2.1.4 Thermal . . . 27
2.1.5 Comparative Analysis . . . 33
2.2 Ultra High-Temperature Thermal Energy Storage . . . 34
2.2.1 Benefits . . . 35
2.2.2 Current UHTS Systems . . . 36
2.2.3 Future of UHTS Systems . . . 37
2.3 Heat Utilisation . . . 37
2.3.1 Rankine Cycle . . . 37
2.3.2 Brayton Cycle . . . 40
2.3.3 Industrial Boilers . . . 43
2.3.4 Integration Challenges . . . 44
2.4 Integration Economics . . . 45
2.5 Aims and Objectives . . . 47

3 Rankine Cycle Integration **49**
3.1 Rankine Integration Overview . . . 49
3.2 Introduction . . . 49
3.2.1 Stored Heat Integration . . . 53
3.3 Integrating UHTS into Rankine Cycles . . . 54
3.3.1 Heat Recovery Steam Generators . . . 55
3.3.2 HRSG Integration . . . 56
3.3.3 Flow Characteristics . . . 59
3.3.4 Flow Analysis . . . 66

3.4 Computational Flow Modelling . . . 68
3.4.1 Governing Equations . . . 68
3.4.2 Numerical Discretisation . . . 70
3.4.3 Pressure-Linkage . . . 73
3.4.4 Solvers . . . 74
3.4.5 Turbulence Modelling . . . 76
3.5 HRSG Model . . . 79
3.5.1 Model Setup . . . 80
3.5.2 HRSG Geometry . . . 80
3.5.3 Boundary Conditions . . . 82
3.5.4 HRSG Mesh Independence . . . 85
3.6 HRSG Integration Feasbility . . . 89
3.6.1 No Retrofit Case . . . 90
3.6.2 Select Retrofit Cases . . . 91
3.6.3 Notable Effects . . . 97
3.6.4 Comparison of Supplementary and Full Conversion Retrofit Systems . . . 105
3.7 Summary of HRSG Integration Feasibility . . . 107

4 Brayton Cycle Integration 110
4.1 Brayton Integration Overview . . . 110
4.2 Introduction . . . 110
4.3 Computational Combustion Modelling . . . 114
4.3.1 Premixed Combustion . . . 115
4.3.2 Non-Premixed Combustion . . . 116
4.3.3 Partially Premixed Combustion . . . 118
4.3.4 Thermophysical Interaction . . . 119
4.4 Combustion Chamber Model . . . 120
4.4.1 Combustion Chamber Geometry . . . 121
4.4.2 Boundary Conditions . . . 122
4.4.3 Mesh Transition . . . 123
4.4.4 Combustion Chamber Mesh Independence . . . 124
4.5 Model Validation . . . 125
4.6 GT Hybrid Combustion . . . 128
4.6.1 Fuel . . . 129
4.6.2 Carbon Dioxide . . . 131
4.6.3 NOx . . . 132
4.6.4 Carbon Monoxide . . . 134
4.7 Summary of GT Integration . . . 135

5 Economic Analysis 137
5.1 Integration Economics Overview . . . 137
5.2 UK Energy System . . . 137
5.2.1 Opportunities within the Electricity Network . . . 138
5.2.2 Current Economic Models . . . 140

5.2.3 Energy Market Factors . . . 141
5.2.4 Future Network Prediction . . . 146
5.3 Data Acquisition . . . 150
5.3.1 Electricity Prices . . . 150
5.3.2 Natural Gas Prices . . . 152
5.3.3 Carbon Tax Prices . . . 154
5.3.4 Carbon Output . . . 155
5.3.5 Future Data . . . 156
5.4 UHTS Utilisation Model Development . . . 159
5.4.1 Language Selection . . . 159
5.4.2 Technical Requirements . . . 160
5.4.3 Optimised Storage Use Model Description . . . 165
5.5 Application of Economic Models . . . 172
5.5.1 Model Verification . . . 172
5.5.2 Model Validation . . . 173
5.5.3 Base Model Results . . . 173
5.5.4 Discharge System Efficiency Variation . . . 183
5.5.5 Temporal Optimisation Period Adaptation . . . 189
5.5.6 Time Step Adaptation . . . 191
5.5.7 Recommendations for Model Development . . . 197
5.6 Summary of Economic Feasibility . . . 198

6 Conclusion **200**
6.1 Key Findings . . . 200
6.2 Future Work . . . 201

List of Figures

1.1 Historic atmospheric CO_2 concentration over the past 800,000 years. 1
1.2 Advancement of international climate agreements since the Kyoto Protocol. . . 3
1.3 Global surface temperature rise in comparison to pre-industrial levels. 4
1.4 Split of electricity generation by source in 2022. 5
1.5 Annual UK wind curtailment from 2017-2022 6
1.6 UK grid frequency over a 1-hour period. 7
1.7 UK Transmission System Demand over a 24-hour period on the first day of each month in 2023 8
1.8 UK Transmission System Demand over 2023, averaged over each day. 9
1.9 Layout of the UHTS system proposed. 10

2.1 Key properties of grid-scale energy storage technologies. 13
2.2 Diagram of a Flywheel Energy Storage system. 14
2.3 Diagram of a Pumped Hydro Energy Storage system. 16
2.4 Diagram of a Compressed Air Energy Storage system. 18
2.5 Diagram of a Capacitor Energy Storage system. 19
2.6 Diagram of a Superconducting Magnetic Energy Storage system. 21
2.7 Diagram of a Li-ion Energy Storage cell. 22
2.8 Diagram of a Flow Battery Energy Storage system. 24
2.9 Diagram of a hydrogen generation, storage and utilisation system. 25
2.10 Process diagram of Andasol II solar power plant. 29
2.11 Diagram of 1414 Degrees SiBox Latent Thermal Storage System. 31
2.12 Diagram of a UHTS, with both charge and discharge systems. 35
2.13 Schematic of Rankine Cycle. 38
2.14 Schematic of Brayton Cycle. 40
2.15 Gas turbine combustor designs: (A) can, (B) annular, and (C) can-annular. . . 41

3.1 T-s diagram of ideal Rankine Cycle. 50
3.2 Rankine Cycle with basic reheat integration. 51
3.3 Efficiency of steam-powered generators against maximum electrical output. . . 52
3.4 Simplified HRSG diagram. 56
3.5 Supplementary firing in a HRSG. 57
3.6 Schematic to show relative location of the primary superheater. 60
3.7 Work produced from steam cycles with increasing Turbine Outlet Temperatures (TOT). 61

3.8 Effect of gas-side velocity on the heat transfer coefficient of a tube bundle. . . 63
3.9 Visual representation of Finite Difference Method. 70
3.10 Visual representation of Finite Element Method. 72
3.11 Visual representation of Finite Volume Method. 72
3.12 Overview of the pressure-based segregated and coupled algorithms. 74
3.13 Overview of the density-based algorithms. 75
3.14 Labelled geometry of HRSG. 81
3.15 Outline of HRSG geometry with the surface of interest highlighted. 82
3.16 Outlet velocity profile of GT into HRSG. 83
3.17 Example of the inlet geometry angles employed. 85
3.18 Volume of mesh density variation. 87
3.19 Meshing sphere density variable comparison at the primary superheater. 88
3.20 Contours of temperature, velocity, Reynolds Number and Turbulent Kinetic Energy at the primary superheater for Case 0. 90
3.21 Comparison between Case 0 and Case 1-b-100 of flow properties at SP1 when supplementing the GT outlet flow. 93
3.22 Comparison between Case 0 and Case 3-d-300 of flow properties at SP1 when fully converting to heat from the UHTS. 96
3.23 A comparison of temperature homogeneity at SP1 for multi-pipe inlet against annular inlet geometries. 98
3.24 Comparison of the duct outlet velocity profile created by a multi-pipe inlet and an annular inlet, with a 90° inlet angle and a 300 m/s inlet velocity. 99
3.25 Visualisation of flow area for each inlet angle. 101
3.26 Velocity pathlines showing flow reversal from a counter-current inlet when redirected by a bulk flow. 102
3.27 Comparison of contours of velocity, Reynolds Number and Turbulent Kinetic Energy at the primary superheater. 103

4.1 Process flow diagram of a thermal storage system integrated with a GT for complete conversion or hybrid operation. 112
4.2 Combustion model transition throughout flame from the Tay validation model (When c=0: non-premixed, 1: premixed). 118
4.3 A) Tay Combustion System Arrangement. B) Individual Tay Can-Annular Combustor. 121
4.4 Geometry of Tay combustion chamber (Green: Wall, Blue: Porous Wall, Clear: Gas Inlet/Outlet). 122
4.5 Geometry of GE DLN 2 Series Industrial combustion chamber. 124
4.6 Locations of horizontal cross-sections used to measure data throughout scaled Tay combustion chamber. 125
4.7 Comparison of experimental and simulated temperature data at horizontal cross-sections throughout the Tay combustion chamber. 126
4.8 Comparison of experimental and simulated concentrations of O_2, CO_2 and CO at horizontal cross-sections 0.8 m from the fuel inlet of the Tay combustion chamber. 127

4.9 Locations of horizontal cross-sections (dashes) and interior faces used to measure data throughout the combustion chamber. 129
4.10 Combustion progress variable along the length of the combustion chamber for different systems a) 760 K, b) 1000 K, c) 1250 K, d) 1500 K, e) 1750 K. . . . 130
4.11 Mole fraction of CO_2 at the system outlet for various inlet temperatures. . . . 131
4.12 Temperature contours for four models along a vertical cross-section at the fuel inlet axis for different air inlet temperatures: a) 760 K, b) 1000 K, c) 1250 K, d) 1500 K, e) 1750 K. 132
4.13 Volume of the region in which NOx is produced in the combustion chamber at various air inlet temperatures, based on Fluent Rate of NOx production a) 760 K, b) 1000 K, c) 1250 K, d) 1500 K, e) 1750 K. 133
4.14 NOx mole fraction at nine cross-sections down the length of the combustion chamber with various inlet air temperatures. 134
4.15 Mole fraction of CO at the system outlet for various inlet temperatures. 135

5.1 Integration of distributed assets into the network via a Virtual Power Plant. . . 138
5.2 Technology Readiness Level and maturity of various energy storage technologies. 139
5.3 Published example of the auction clearing price calculation. 146
5.4 FES Net-Zero scenarios. 147
5.5 GB total NG price projection. 148
5.6 Carbon price projection for EU ETS 148
5.7 Comparison of PyPSA-GB generation with actual generation - 2018. 149
5.8 Comparison of Day-Ahead Auction Price against System Sell and Buy Imbalance Prices. 151
5.9 Example of imbalance price variation over each SP in the 2021 year. 152
5.10 Comparison of UK Natural Gas prices based on market. 153
5.11 Comparison of the different carbon emissions taxes seen in the UK. 155
5.12 Comparison of conversion factors for NG, coal, and fuel oil. 156
5.13 Modelled generation mix over a 3-day period in 2050. 157
5.14 Historical variation in spark spread and dark spread. 158
5.15 Flowchart of the logic process for arbitrage optimisation. 167
5.16 Simplified visualisation of the grid search process in which the CT/DT combination with the greatest output is marked. 169
5.17 Flowchart of the logic process for savings optimisation. 171
5.18 Gross profit differential from the standard operation of a GT, HRSG, and IB against that produced during boosted operation, under the arbitrage model. . . 174
5.19 Cumulative annual profit differential from the standard operation of a GT, HRSG, and IB, under the arbitrage model. 175
5.20 Inlet energy displacement percentage and operational savings for a GT, HRSG, and IB under the fuel displacement model. 177
5.21 Carbon tax savings and CO_2 displaced for a GT, HRSG, and IB under the fuel displacement model. 178
5.22 Projected future profit differentials from 2025 - 2050 for a GT, HRSG, and IB under the arbitrage model. 180

5.23 Projected future carbon tax savings from 2025 - 2050 for GTs, HRSGs, and IBs under the fuel displacement model. 182
5.24 Profit differentials per month in 2021 for GTs, HRSGs and IBs operating at differing efficiencies, under the arbitrage model. 184
5.25 Boost percentage per month in 2021 for GTs, HRSGs and IBs operating at differing efficiencies, under the arbitrage model. 185
5.26 Fuel displacement percentage and associated Charge Trigger per month in 2021 for GTs, HRSGs, and IBs operating at differing efficiencies, under the fuel displacement model. 187
5.27 Mass of CO_2 displaced per month in 2021 for GTs, HRSGs and IBs operating at differing efficiencies, under the arbitrage model. 188
5.28 Comparison of the mass of CO_2 displaced per optimisation step over the course of 2021, when discharging via a GT. 191
5.29 Profitability per month in 2021 for GTs, HRSGs, and IBs optimised over 30 minute and 60 minute SPs, under the arbitrage model. 192
5.30 Operational boundaries per month in 2021 for GTs, HRSGs, and IBs optimised over 30 minute and 60 minute SPs, under the arbitrage model. 194
5.31 Charging cost differential per month in 2021 for GTs, HRSGs, and IBs optimised over 30 minute and 60 minute SPs, under the fuel displacement model. 195
5.32 Operational cost differential per month in 2021 for GTs, HRSGs, and IBs optimised over 30 minute and 60 minute SPs, under the fuel displacement model. 196
5.33 Charge Trigger variation per month in 2021 for GTs, HRSGs, and IBs optimised over 30 minute and 60 minute SPs, under the fuel displacement model. 197

List of Tables

2.1 Comparative Analysis of Energy Storage Technologies. 33

3.1 Gas turbine exhaust gas composition. 83
3.2 Case names for each HRSG model. 84
3.3 Mesh independence comparison at the primary superheater in a HRSG for MI1, MI2, and MI3. 86
3.4 Mesh independence comparison at the primary superheater in a HRSG for MIJ1, MIJ2, MIJ3, MIJ4, and MIJ5. 87
3.5 Overview of HRSG Model Settings 88
3.6 Case 0 HRSG results at the primary superheater. 90
3.7 Flow conditions at SP1 of optimal retrofit cases for a supplementation retrofit and a replacement retrofit. 92
3.8 Primary superheater surface flow properties with flow supplementation. 92
3.9 Primary superheater surface flow properties with complete flow replacement. . 95
3.10 Comparison of average absolute velocity variation from Case 0 between supplementary retrofit, and full conversion retrofit systems. 106
3.11 Comparison of average absolute Re variation from Case 0 between supplementary retrofit, and full conversion retrofit systems. 106

4.1 Mesh independence comparison between average velocity and temperature at various z locations for MI1 and MI2. 124
4.2 Comparison of experimental and modelled temperature. 126
4.3 Comparison of experimental and modelled component concentrations. 127
4.4 Overview of GT Model Settings 128
4.5 Boundary conditions producing 1873 K outlet in the heavy-duty combustion chamber. 130
4.6 Mole fraction of NOx at outlet face of the combustion chamber. 134

5.1 Carbon Price Support rates over time. 154
5.2 Operational parameters for UHTS system implementation across various discharge technologies. 171
5.3 System profitability comparison for a GT, HRSG, and IB under the arbitrage model. 176
5.4 Fuel displacement percentages each month from 2025 - 2050 for a GT, HRSG, and IB under the fuel displacement model. 181

5.5 Comparison of mean profit differential for a GT, HRSG, and IB under the arbitrage model. 184
5.6 Variation in key performance indicators of the arbitrage model with varying temporal granularity of datasets. 189
5.7 Variation in key performance indicators of the fuel displacement model with varying temporal granularity of datasets. 190

Nomenclature

Abbreviations

AFR Air-Fuel Ratio

BMRS Balancing Mechanism Reporting Service

CAES Compressed Air Energy Storage

CAPEX Capital Expenditure

CCGT Combined Cycle Gas Turbine

CCPP Combined Cycle Power Plant

CCS Carbon Capture and Storage

CFD Computational Fluid Dynamics

CO Carbon Monoxide

CO_2 Carbon Dioxide

COP Conference of the Parties

CPF Carbon Price Floor

CPS Carbon Price Support

CSP Concentrated Solar Power

CT Charge Trigger

DLN Dry Low-NOx

DNS Direct Numerical Simulation

DT Discharge Trigger

EES Electrical Energy Storage

EES Energy Storage System

EGR Exhaust Gas Recirculation

ES Energy Storage

EU ETS European Union Emissions Trading System

FES Future Energy Scenarios

GHG Greenhouse Gas

GT Gas Turbine

HP High Pressure

HRSG Heat Recovery Steam Generator

HTF Heat Transfer Fluid

IB Industrial Boiler

IP Intermediate Pressure

IPCC Intergovernmental Panel on Climate Change

LES Large Eddy Simulation

LCOE Levelised Cost of Electricity

LOPF Linear Optimal Power Flow

LP Low Pressure

LTES Latent Thermal Energy Storage

MES Mechanical Energy Storage

NG Natural Gas

NOx Nitrogen Oxides

PDF Probability Density Function

PHS Pumped Hydro Energy Storage

PCM Phase Change Material

PM Particulate Matter

RANS Reynolds-Averaged Navier-Stokes

RES Renewable Energy Sources

RSM Reynolds Stress Model

SBP System Buy Price

SIMPLE Semi-Implicit Method for Pressure-Linked Equations

SMES Superconducting Magnetic Energy Storage

SO_2 Sulphur Dioxide

SP Settlement Period

SP1 Primary Superheater 1

SSP System Sell Price

STES Sensible Thermal Energy Storage

TES Thermal Energy Storage

TIT Turbine Inlet Temperature

TKE Turbulent Kinetic Energy

TRL Technology Readiness Level

TSD Transmission System Demand

UHTS Ultra-High Temperature Thermal Energy Storage

UK ETS United Kingdom Emissions Trading Scheme

Symbols

α Thermal Diffusivity (m^2/s)

χ Scalar Dissipation Rate ($1/s$)

δ_{ij} Kronecker Delta (-)

$\dot{\omega}_\alpha$ Reaction Rate ($mol/(m^3.s)$)

$\dot{Q}$ Heat Accumulation (W)

μ Dynamic Viscosity ($Pa \cdot s$)

ν_T Viscosity Coefficient (Pa.s)

ρ Density (kg/m^3)

$_t$ Turbulent Schmidt Number (-)

σ_k Prandtl Number (-)

τ Viscous Stress Tensor (Pa)

τ_c	Chemical Time Scale (s)
τ_t	Turbulence Time Scale (s)
c	Progress Variable (-)
C_p	Specific Heat Capacity (J/(kg · K))
CV	Calorific Value (J/kg)
D_a	Fick's Diffusion Constant (m^2/s)
E	Energy (J)
H	Enthalpy (J)
h	Fluid Kinetic Energy (J)
J	Diffusion Flux (kg/(m^2 · s))
k	Kinetic Energy (J)
k	Thermal Conductivity (W/(m.K))
k	Turbulent Kinetic Energy (m^2/s^2)
Ka	Karlovitz Number (-)
m	Mass (kg)
P	Power (W)
p	Static Pressure (Pa)
Q	Heat (J)
q_j	Molecular Transport of Energy (W/m^2)
R	Specific Gas Constant (J/(kg · K))
Re	Reynolds Number (-)
S_c	Reaction Progress Source Term (-)
SAP	Store Air Percentage (-)
Sc	Schmidt Number (-)
T	Temperature (K)
t	Time (s)
u	Velocity (m/s)

U_t Turbulent Flame Speed (m/s)

V Volume (m^3)

v Velocity (m/s)

Z Mixture Fraction (-)

Subscripts

b Burnt Mixture

core Storage Core

f Fuel

HTF Heat Transfer Fluid

initial Initial Conditions

inlet Inlet Conditions

max Maximum Conditions

min Minimum Conditions

outlet Outlet Conditions

ox Oxidiser

peak Peak Conditions

stored Stored Energy

u Unburnt Mixture

usable Usable Energy

Superscripts

$'$ Fluctuating Component

$-$ Average Value

Chapter 1

Introduction

1.1 Context

There is a scientific consensus that the global climate system is undergoing rapid change. Not only is the average global temperature rising, but the rate of change is also increasing. This is occurring due to the mass of pollutant gases that modern industrial processes emit into the atmosphere, intensifying the greenhouse effect. Much of this can be attributed to the reliance on fossil fuels to meet growing energy requirements.

Global carbon dioxide (CO_2) concentrations have increased from approximately 280 ppm in the mid-19th century to a current value greater than 417 ppm. This is the greatest concentration in at least 800,000 years, resulting in an average temperature increase of 1.26 (1.0 to 1.6) °C in 2022 (Forster et al., 2023; Lüthi et al., 2008; The Royal Society, 2010). This is visualised in Figure 1.1.

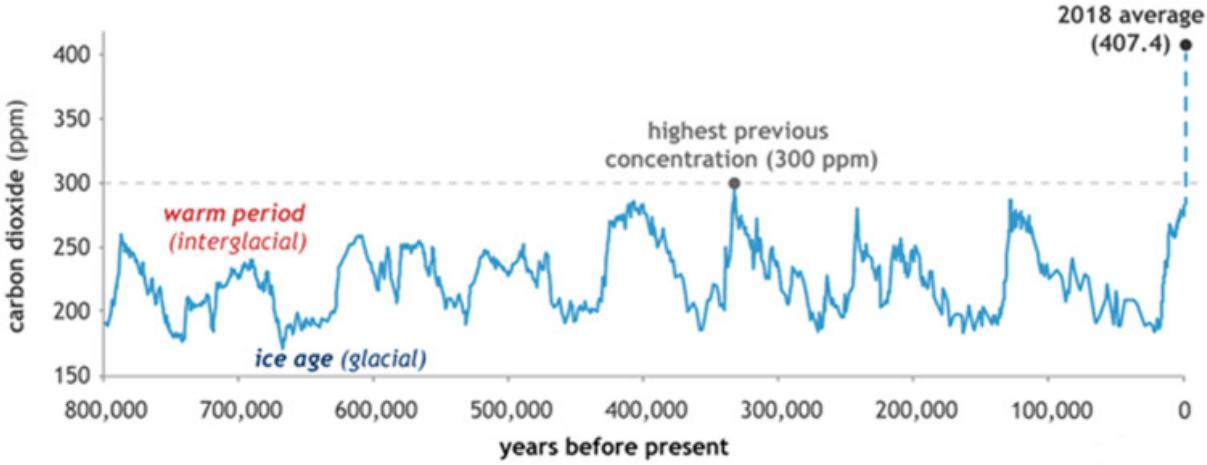


Figure 1.1: Historic atmospheric CO_2 concentration over the past 800,000 years (Liu et al., 2024).

As a result, rising sea levels threaten land, decreasing agricultural yield disrupts the security of food supplies, and more frequent occurrences of extreme weather events pose a secondary threat to the populace (Cobourn, 2023; Durand et al., 2022; Semba et al., 2022).

Furthermore, the environmental impact of these emissions can have an indirect, yet severe, impact on the health of the global population (DEFRA, 2017). In the UK alone, long-term exposure to air pollution is estimated to cause up to 36,000 premature mortalities yearly (Office for Health Improvement & Disparities, 2022; Kelly, 2018).

The negative impacts of fossil fuel combustion on the economy, health, and environment are well documented. As such, there is a consensus that their continued use is unsustainable. From an economic perspective, as fuel is the most significant contributing factor to the operating costs of many systems, their economic feasibility is highly sensitive to price fluctuations (Foster et al., 2017). Due to the dwindling availability, sourcing fossil fuels will grow more challenging, likely driving up prices. This will make renewable energy sources (RES) more economically viable, prompting a shift away from fossil fuels (EIA, 2018). However, this change in generation will result in additional challenges, such as economically balancing supply and demand, and a reduction in grid inertia to manage grid frequency.

1.1.1 Emissions Regulation

Since 1999, there has been an increase in the implementation of climate-focused policies, such as the carbon price floor (CPF), to drive a reduction in fossil fuel use (Seely, 2009). These policies are implemented as the combustion of fossil fuels provides a significant contribution to the total sum of pollutants emitted to the atmosphere, particularly CO_2, SO_2, NOx and particulate matter (PM). Each of these pollutants has been shown to cause adverse environmental changes in all components of the climate system. As emissions laws become more stringent, such policies will further increase the cost associated with fossil-driven generation, making them even less commercially viable.

To counter the aforementioned risks, a range of international policies have been implemented to minimise the emissions from power generation. In 1997, the United Nations Framework Convention on Climate Change (UNFCCC) introduced the Kyoto Protocol, setting emissions targets for between 2008-2012, though this was limited to developed nations. In 2012, the Doha Amendment was adopted, setting targets between 2013-2020 (United Nations, 1998, 2012).

Since the Kyoto Protocol and its Doha Amendment, global climate policy progressed. Effective from November 2016, the 2015 Paris Agreement aimed to limit global warming well below 2 °C, aiming for 1.5 °C. This increases the responsibility beyond developed nations, requiring all signatories to submit plans for reducing emissions. This was to be achieved by focussing on the enhancement of renewable energy, and improving energy efficiency (UNFCCC, 2015). The 2021 Glasgow Climate Pact further pressures nations to hasten the reduction of coal use. This transition in climate policy highlights an escalating commitment to addressing climate change through global cooperation and the continuous updating of national strategies to mitigate its effects (UNFCCC, 2021). In 2023, the UAE Consensus focused on the reinforcement of international commitments towards greenhouse gas (GHG) reduction goals by transitioning away from fossil fuels (COP, 2024).

These international agreements commit countries to reducing their emissions of GHGs by setting internationally binding emissions reduction targets, with greater reduction targets placed on developed countries based on their ability their economic and technical capacity to

reduce emissions and their historic contribution to current levels of GHGs in the atmosphere (Oberthur and Ott, 1999; Bortscheller, 2010). The progression of these agreements is shown in Figure 1.2.

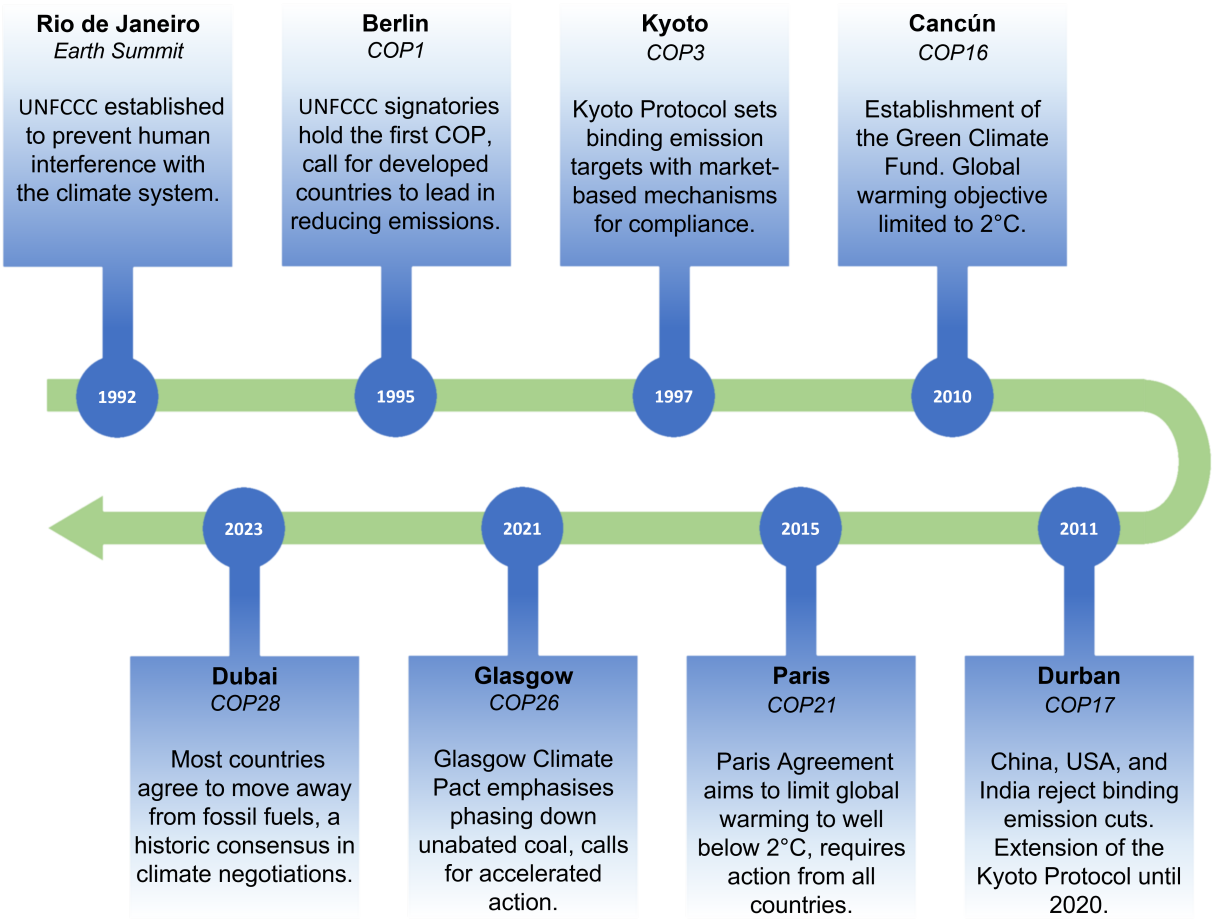


Figure 1.2: Advancement of international climate agreements since the Kyoto Protocol.

The initial reduction target for the UK was to decrease emissions from 1990 levels by 8 % by 2012. The amendment increased this reduction to 20 % by 2020, which had been met by 2009 without allowance for emission trading (Department of Energy & Climate Change, 2012).

Domestically, the UK also implemented legislative frameworks to combat emissions. This included the 2008 Climate Change Act, which originally aimed to cut emissions by 80 % of that of the 1990 levels by 2050. This target was amended in 2019, to commit to a 100 % reduction by 2050. Currently, an interim target is to reduce emissions by 78 % by 2035. As of 2023, UK emissions are down 53 % from those of 1990. However, in order to fully align with the provisions of the Paris Agreement and limit the global temperature rise to 1.5 °C above pre-industrial levels, it is noted that further action is required (UK Parliament, 2008; Bell et al., 2016; Department for Business, 2018).

Despite these efforts to reduce GHG emissions, projections indicate that global warming remains a critical concern. The Intergovernmental Panel on Climate Change (IPCC) warns that current commitments are insufficient to limit warming to 1.5 °C. Under the most optimistic

scenario, which assumes rapid decarbonisation, global warming could be limited to 1.5 °C by the end of the century. However, under high-emission scenarios, the global temperature increase could exceed 4 °C by 2100. This is shown in Figure 1.3.

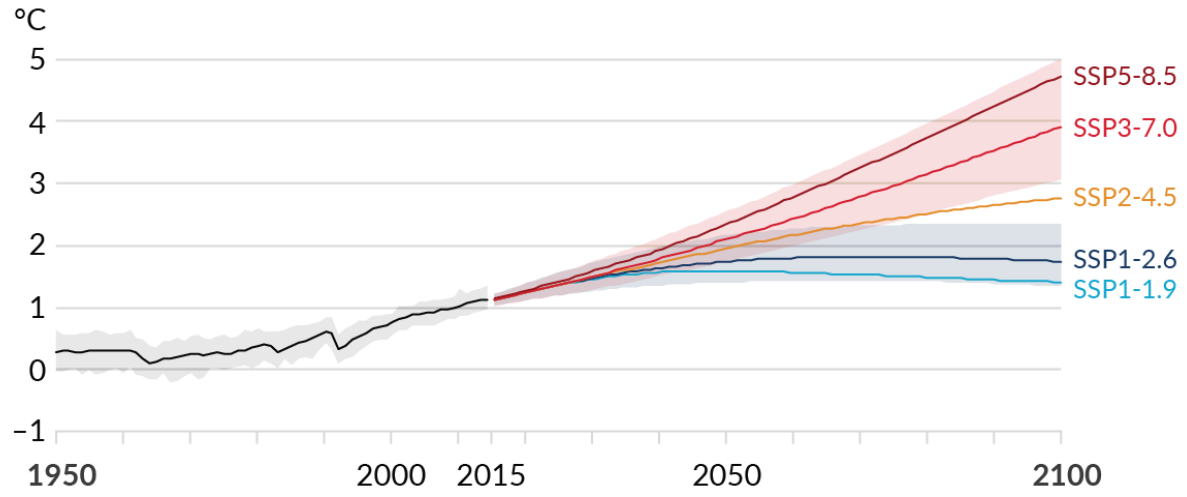


Figure 1.3: Global surface temperature rise in comparison to pre-industrial levels [adapted from Masson-Delmotte et al. (2023)].

1.1.2 Evolving Electricity Network

Given the global reliance on power generation and high energy industries, in order to limit warming to 1.5°C, the deployment of renewable generators is critical to meet emissions targets. As a result, renewables are projected to supply 70-85 % of electricity by 2050 (Masson-Delmotte et al., 2018).

Electricity is the fastest-growing energy supply due to an increased reliance on RES. This trend is predicted to continue in the coming years as policy drives all sectors to decarbonise by moving towards electrification. The overall energy demand from gas and electricity is forecast to remain relatively constant up to 2050 due to an increase in system efficiencies, with the highest prediction estimating a 1,083 TWh requirement, down from the 1,272 TWh in 2022 (National Grid, 2023). Although the overall energy demand will remain fairly consistent, electricity demand is expected to be significant in 2050 due to these factors, up to a maximum of 770 TWh in 2050 from 321 TWh in 2022 (BEIS, 2022). With 85 % of this being generated by renewables in 2050, 617 TWh would need to be produced using renewable sources, up from 135 TWh in 2022 (Department for Energy Security and Net Zero, 2023; National Grid, 2023).

One of the sectors that will see a large change is transportation, with the annual electricity demand for this alone reaching around 130 TWh (National Grid, 2023). Some studies predict that this may result in over 35 million active electric vehicles (EVs) by 2050, replacing the vast majority of petrol and diesel vehicles (National Grid, 2019; Butcher et al., 2018). Additionally, green hydrogen production processes will likely require a significant supply of electricity. This is due to production via electrolysis, using over 177 TWh in some models (National Grid, 2023).

Since 2010, the UK's total renewable energy capacity has more than quintupled (Department for Business, 2022) in response to these targets. Renewable generation is projected to rise to 770 TWh by 2050, representing an 86.9 % share of total generation (Department for Business, 2022; National Grid, 2023).

With the increased penetration of RESs into the grid, harmful emissions will be minimised, and low-carbon power generation will begin to take over from the ageing fossil fuel based generation systems (National Grid, 2023). In 2022, the proportion of electricity generation from renewables in the UK reached 41.5 %, with over half of this coming from wind generation (Department for Energy Security and Net Zero, 2023). This generation split is shown in Figure 1.4, with 'Other Renewables' accounting for systems such as hydroelectric generation.

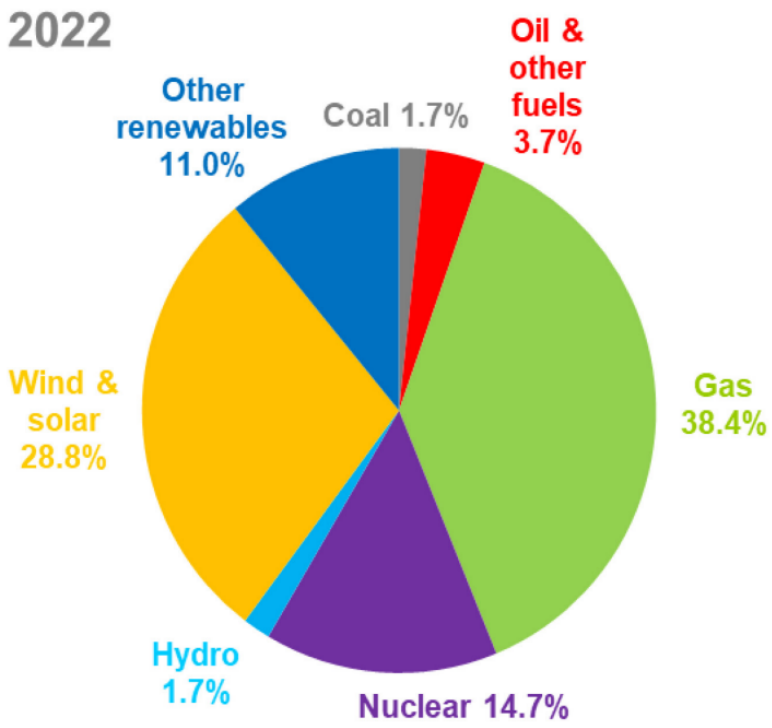


Figure 1.4: Split of electricity generation by source in 2022 (Department for Energy Security and Net Zero, 2023).

The above projections necessitate a strategic re-evaluation of energy infrastructure to accommodate an increasing share of RESs. Increased reliance on these sources raises concerns over their inherent intermittency, as this may pose a threat to the stability of supply due to periods of little or no generation. Additionally, a known issue which may occur during periods of low demand is increased grid congestion, which results in the curtailment of intermittent renewable generation, reducing the overall efficiency of the entire network.

The majority of renewable curtailment comes from wind, representing around 90 % across 2020-21. In 2021, 2.3 TWh of output was curtailed, costing £141,000,000 (Matson and Knighton, 2022). This is expected to improve over the coming years due to improved transmission from Scotland to England, where 80 % of the curtailment occurred. This is outlined in Figure 1.5 However, there will still be considerable financial and energy wastage in a network

supplied primarily by renewables.

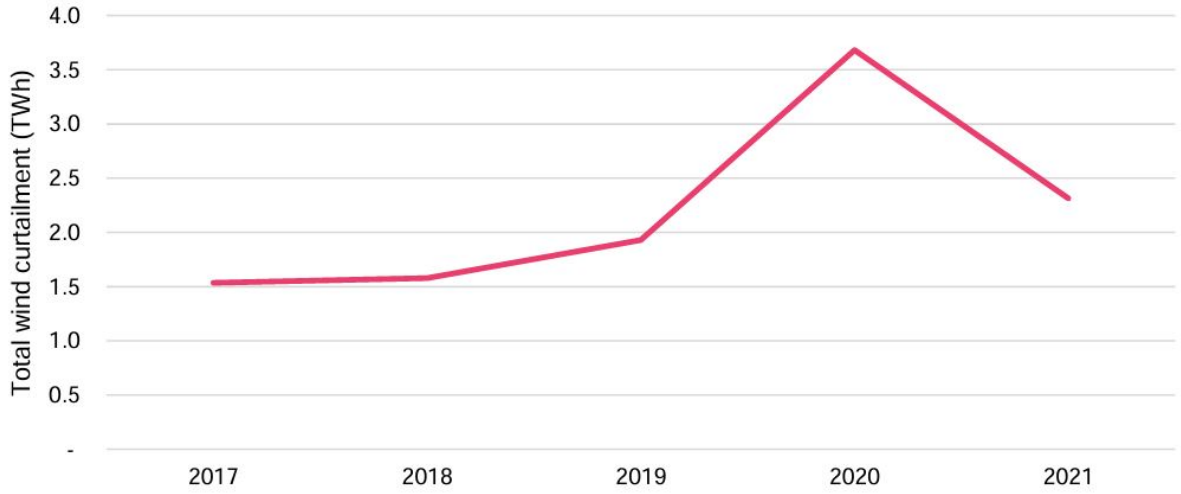


Figure 1.5: Annual UK wind curtailment from 2017-2022 (Matson and Knighton, 2022).

These renewables would also diminish the ability to maintain grid frequency (Barelli et al., 2015; Wang et al., 2018; Argyrou et al., 2018). This is because the significant synchronous reserve provided by rotating turbo-machinery, which grants the grid inertia is removed when conventional generation sites are retired for renewable energy systems. Grid inertia allows short-term fluctuations in demand (up to a few seconds) to be passively controlled, maintaining the grid frequency at an almost constant level (Rouse et al., 2018). However, advancements in power electronics aim to address this by generating synthetic inertia. These methods replicate the inertia provided by conventional generation units, allowing the grid to respond to frequency variations (Fritzsch and Jacquod, 2023).

The issues associated with increased renewable penetration may be counteracted with the use of energy storage (ES) systems, which can be implemented to capture the energy that would otherwise be curtailed for deployment at a later time, as required (Wang et al., 2018; Yang and Nehorai, 2014). This may be utilised using load manipulation techniques such as peak shaving (Uddin et al., 2018), load levelling (DinAli and Dincer, 2018), and time shifting (Hida et al., 2010).

1.1.3 Storage Timescales

An important factor to consider when looking at ES technologies is their timescale of storage. These range from seconds to minutes, hours, days or seasons. At the shortest timescales, energy storage systems can be used to maintain power quality by controlling frequency. The variation in grid frequency over the course of an hour is shown in Figure 1.6. In a renewable system, this would be affected by unpredictable variations, such as clouds passing over solar PVs or a sudden drop in wind speed, although the diverse location of renewable generators minimises the effect of this. Even so, short-term storage with a fast response time may be utilised to assist in these situations. As the infrastructure for the aforementioned synchronous

reserve already exists in the mature technology of gas and steam turbines, along with some mechanical storage systems such as pumped hydro storage, these generation sites may be integrated into the discharge cycle of an ES system, and grid inertia may be maintained to account for frequency fluctuations.

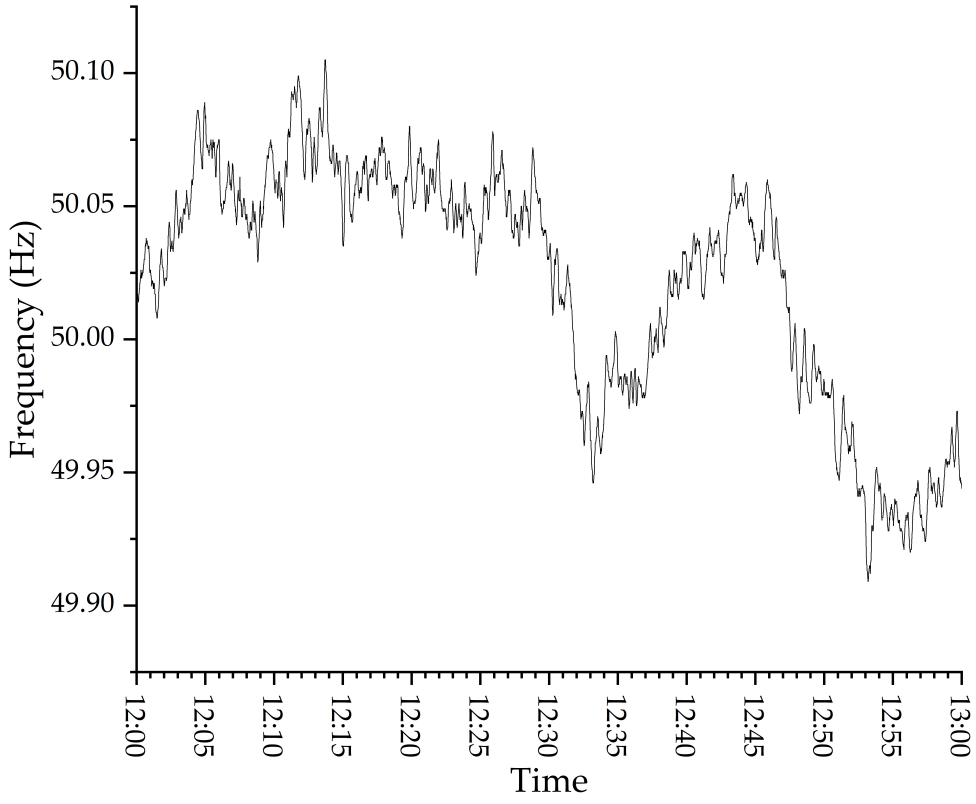


Figure 1.6: UK grid frequency over a 1-hour period (National Grid ESO, 2024).

For storage of hours to days, the grid may be backed up against the inherent intermittency of renewables. These systems are able to provide peak shaving, storing at off-peak times of day to discharge at peak periods. This is suitable for integration into a renewable heavy grid as it can use the excess energy, which would have otherwise resulted in curtailment to account for a short-term lack of wind or prolonged, widespread cloud coverage. Additionally, this can account for the overnight drop in renewable generation due to the lack of solar production, or potentially extended periods in which there may be no wind. Medium-duration storage systems have the financial advantage of time shifting, providing the ability to store cheaper energy on a weekday to sell at higher weekend prices (Luo et al., 2015). The UK Transmission System Demand (TSD) is shown in Figure 1.7. TSD is the Transmission System generation requirement and is equal to the national demand plus the additional generation required to meet station load, pump storage pumping, and interconnector exports.

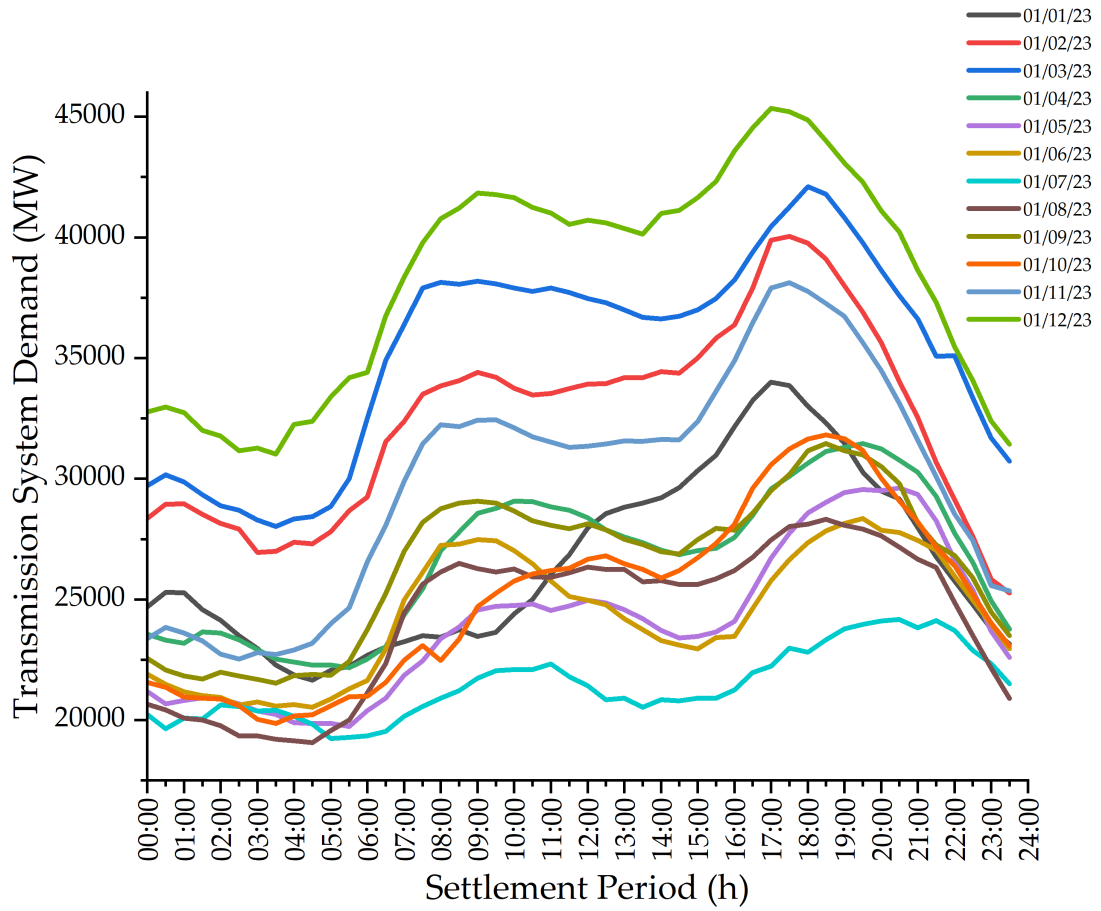


Figure 1.7: UK Transmission System Demand over a 24-hour period on the first day of each month in 2023 (National Grid ESO, 2024).

Finally, seasonal storage on the time scale of months may account for variations in renewable generation throughout the year due to cyclical weather conditions. The TSD variation over the year is shown in Figure 1.8. With this, a continuous renewably sourced supply is possible throughout the year, accounting for reduced photovoltaic and wind generation periods (Gao et al., 2015). These systems are likely to be vital in the future when the majority of electricity is provided by renewables and must prioritise storage capacity and minimal energy loss over time (Blanco and Faaij, 2018). The need for longer-term storage development is also being recognised (Rosenzweig et al., 2001; Masson-Delmotte et al., 2018) and provided for within domestic UK policies (Oberthur and Ott, 1999).

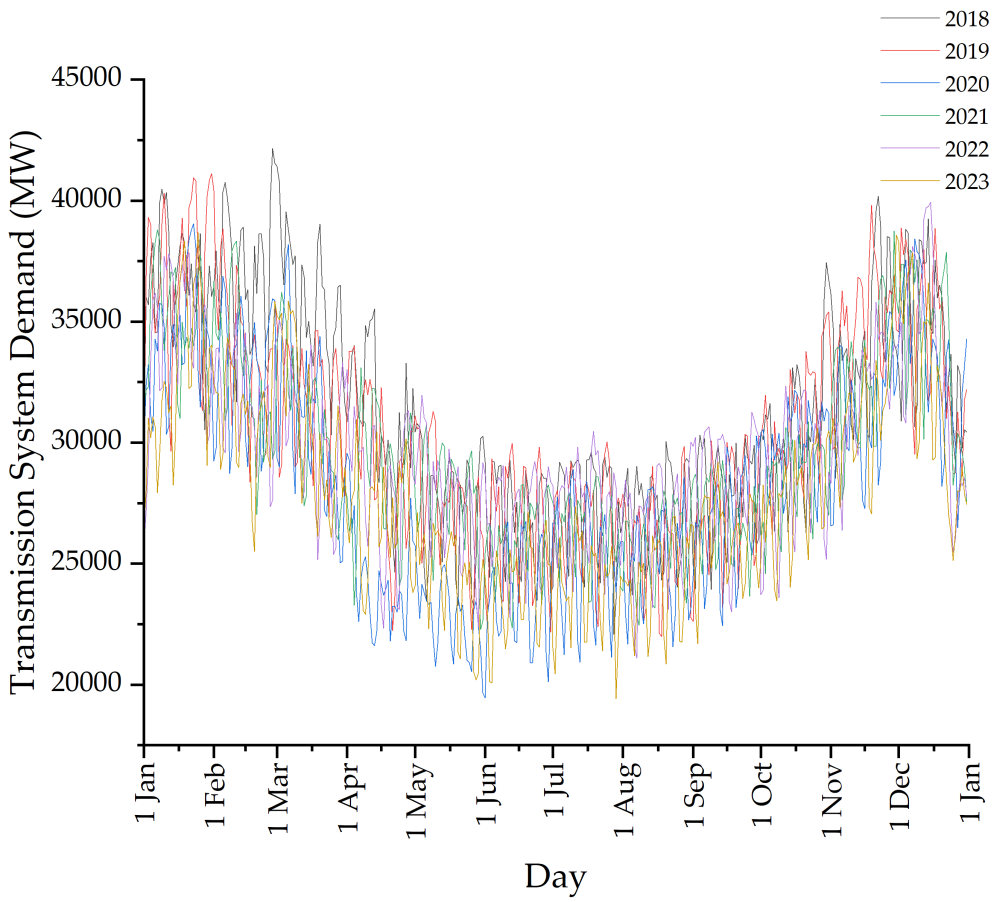


Figure 1.8: UK Transmission System Demand over 2023, averaged over each day (National Grid ESO, 2024).

Several methods of energy storage are available to achieve long-duration storage. Considerable progress is being made in the deployment of chemical or electrochemical storage in the form of batteries, hydrogen, or other gas storage. As of 2024, lithium-ion is predicted to account for 93 % of the total installed energy storage capacity. The most mature storage technology used in the UK is mechanical storage, particularly pumped hydro, which provides 25.8 GWh of storage as of December 2022 (Loukatou, 2022), though the scope of this also includes technologies such as flywheels and compressed air storage. Further technologies include electromagnetic storage, thermal storage, and thermochemical.

The primary design criteria for energy storage technologies are their lifetime, cost, energy density (and therefore storage capacity), efficiency (in storage, but also during charge and discharge), power (both during charge and discharge), storage period, and charge and discharge times. As these characteristics vary significantly between storage technologies, no single type best suits all grid requirements. A challenge for each type of energy storage system is its integration into commercial projects. Though many energy storage technologies have been developed, not all are appropriate for grid-scale deployment. As thermal energy storage (TES) systems have the ability to attain energy densities greater than most current storage methods,

they are becoming viable for use with a range of technologies to utilise stored energy produced by renewables at times of lower demand (BEIS, 2016).

The Ultra-High Temperature Thermal Energy Storage (UHTS) system proposed by Robinson (2017, 2018) builds on this concept. The system proposes the use of an aluminium storage medium due to the material abundance, low cost and favourable physical properties. As this is a latent heat storage system, when fully charged, the storage medium will be in a liquid state and contained within an alumina vessel. The UHTS system is charged electrically using resistance heaters to raise the temperature of the aluminium core to 1,800 K. To discharge the store, a heat transfer fluid is passed through a network of pipes within the system to extract heat. Secondary thermal masses surround the insulated storage medium to capture heat lost via radiation, the primary source of losses in this system. This energy can then be recovered to the core using a heat pump system. The proposed system is estimated to produce an electric-to-electric efficiency of 57 %. This is an advanced system, currently at a low TRL. A layout of this system is presented in Figure 1.9.

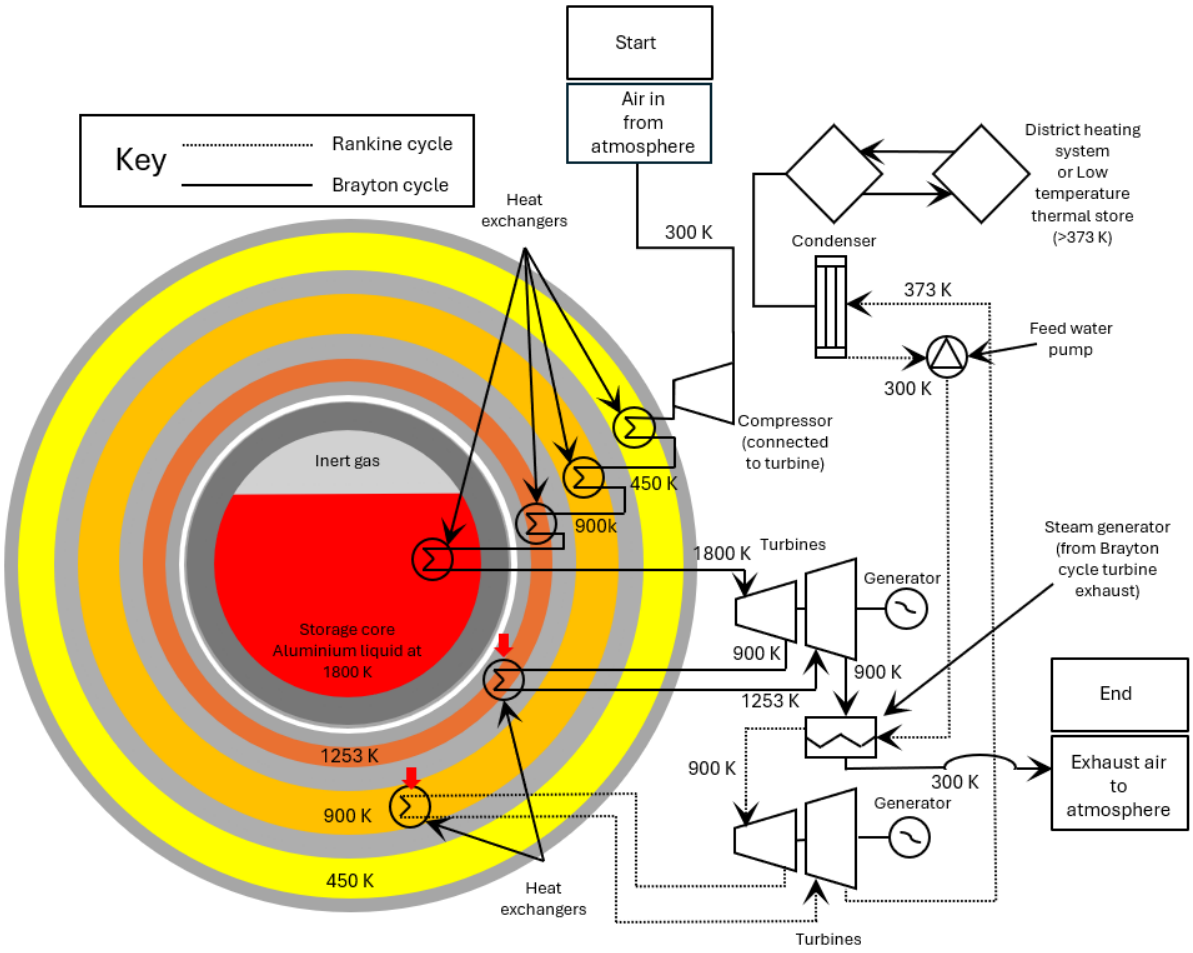


Figure 1.9: Layout of the UHTS system proposed by Robinson (2017).

The high-temperature heat provided presents significant advantages, both technologically and commercially. High storage temperatures enable greater energy densities and round-trip efficiencies, which lead to lower costs per unit of recovered power (Wang et al., 2018;

Dlugokencky and Tans, 2018). With the system designed to minimise radiative thermal losses, it is able to provide heat to meet demand at an hourly to a seasonal scale.

A major factor in the decarbonisation of the energy system is the replacement of combustion for the supply of heat. High-grade thermal energy is required in various processes, from heating to power generation. The development of UHTS provides the ability to dispatch renewably sourced heat on demand. Additionally, with increased discharge temperatures, there is a wider range of discharge applications, such as use in heat engines and high-temperature processes, including cement production and pharmaceutical processes. Based on this, several high-temperature thermal energy storage technologies have been studied and developed.

These systems have an opportunity to replace the use of fossil fuels in a range of environments, introducing renewably sourced heat. UHTS would be suitable for both new build cases and utilisation with existing infrastructure, though the design and integration of the system would likely differ significantly. For instance, pipework integration may be incorporated into sections of a new build which may be too expensive or complex to access for a retrofit.

As the technology continues to advance, integrating UHTS from the design phase of new projects could become a standard practice. This would allow for more efficient and effective energy storage, tailored to the specific needs of the new build system. Designing infrastructure that complements UHTS technology would enhance performance, making it ideal for future energy projects. As the demand for sustainable energy solutions grows, the role of UHTS in new builds is likely to expand, offering benefits in both operational efficiency and environmental impact. This approach would allow for optimal performance and easier maintenance, achieving the full potential of UHTS technology from the outset.

However, whilst there is significant potential for UHTS to be considered in conjunction with new builds, this work was driven by the need to extend the feasible lifetime of existing assets, allowing them to meet emissions regulations and remain economically viable. To decarbonise pre-existing systems, the focus on retrofitting UHTS provides a cost-effective solution to enhance performance and reduce emissions without the need for entirely new infrastructure. This approach maximises the value of sunk assets and aligns with sustainability goals by reducing the environmental impact of older systems.

Chapter 2

Literature review

This chapter provides a comprehensive examination of contemporary energy storage systems, highlighting ongoing research in the sector. It further investigates the current advancements in UHTS systems, exploring their capabilities and the suitable discharge technologies that can be employed. Additionally, an analysis of the economic aspects of energy storage systems is presented, offering insights into the cost-effectiveness, efficiency gains, and financial viability associated with the integration of these systems into existing power generation and industrial processes. This review aims to outline the technological progress, integration challenges, and economic implications of energy storage integration, shedding light on the potential to update and improve the current energy system.

2.1 Energy Storage Technologies

There are several solutions to counter the inherent intermittency of renewable technologies. The IPCC special report states that energy storage (ES) technologies would enable the balancing of variable renewables without the use of NG-based back-ups (Masson-Delmotte et al., 2018). There is a range of possible technologies to enable the deployment of ES, some of which are well-understood and industrially mature, with others in earlier stages of development. For commercial applications, the ES system should be able to charge using renewably sourced energy and discharge to provide power to the grid on demand. The bulk of these technologies come in the form of mechanical, thermal, electro-mechanical, electro-chemical and chemical (Argyrou et al., 2018). Although there are many proposed systems for ES, not all are economically feasible for integration into a fully renewable system in their current state. A review of a range of ES technologies and an overview of grid-applicable storage technologies are given in Figure 2.1.

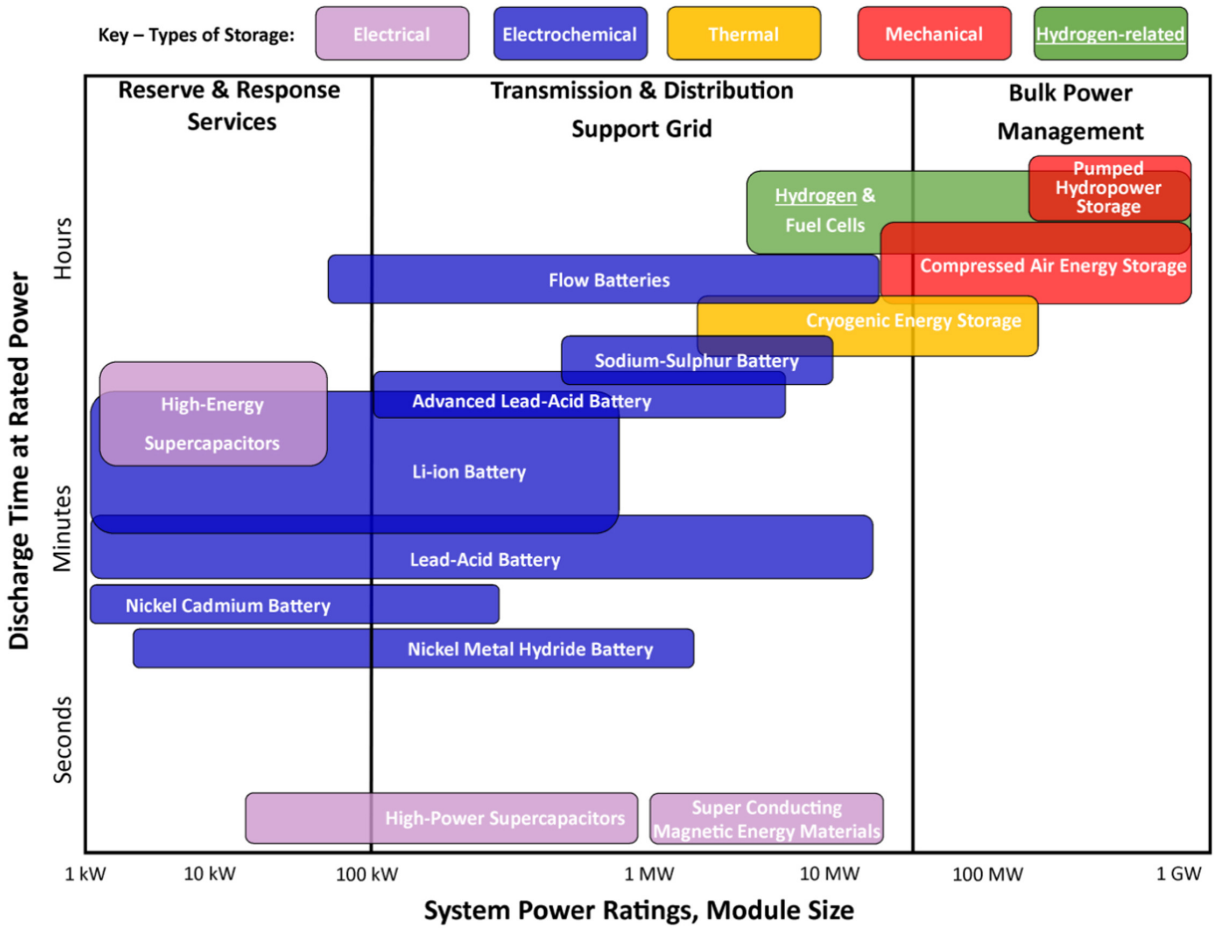


Figure 2.1: Key properties of grid-scale energy storage technologies (Møller et al., 2017).

2.1.1 Mechanical

As the name suggests, mechanical energy storage (MES) is a technology that enables the storage of mechanical energy. MES systems can be categorised into two broad classes, namely kinetic energy storage (KES) and potential energy storage (PES). Both of these can offer several advantages over other energy storage technologies. For example, they can provide high power output and fast response times, making them well-suited for applications such as grid stabilisation and frequency regulation. They also have the potential for long lifetimes and low maintenance costs, as they often use simple mechanical components.

However, MES systems are not without limitations. Notably, they have relatively low energy density, making them less suitable for applications in which large amounts of energy need to be stored for grid-scale time-shifting. MES systems can also have relatively high upfront capital costs, which can be a barrier to deployment.

Despite these limitations, MES systems are increasingly used for grid-scale energy storage, alongside various other applications. Ongoing research and development is focused on improving the energy density and cost-effectiveness of these systems, making them more competitive with other storage technologies in the future (Frate et al., 2021).

Flywheel

Flywheel Energy Storage (FES) is a kinetic energy storage technology that stores energy in a spinning rotor. FES systems store kinetic energy based on a mass being set into rotational motion. To discharge, the rotor is decelerated, and the stored energy can be used to generate electricity or mechanical power. Flywheel material, geometry and length influence the volume of energy stored and the specific energy of the flywheel. Stored energy is proportional to the rotor mass moment of inertia and the square of the wheel speed. The key components of a flywheel system are the rotor and the bearings. A diagram of FES is shown in Figure 2.2.

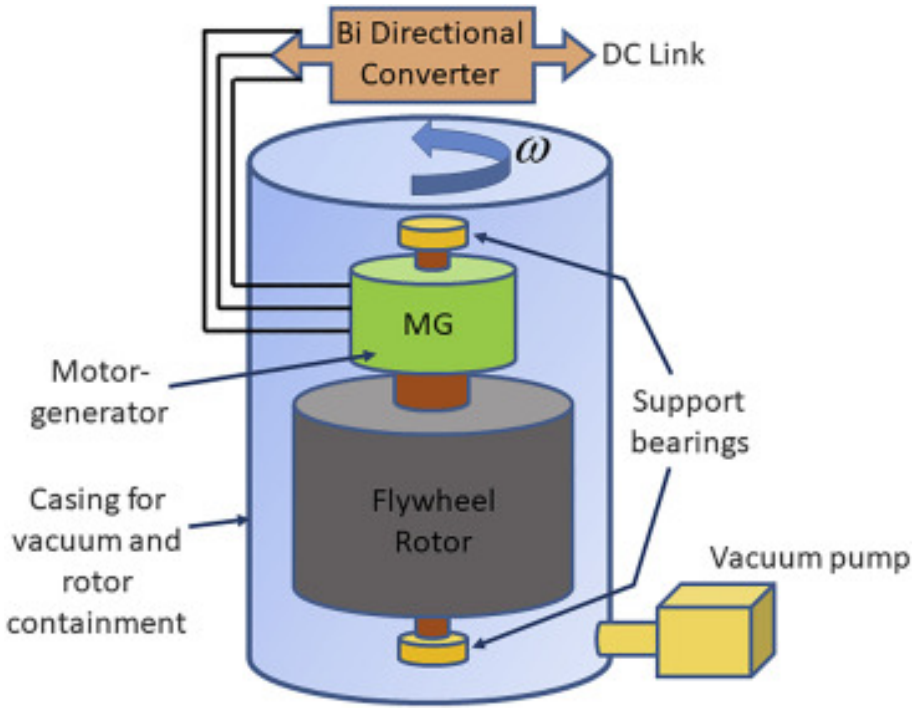


Figure 2.2: Diagram of a Flywheel Energy Storage system (Pullen, 2019).

The rotor is the rotating mass component of the system. Whilst historically this has been made from steel or aluminium due to their strength and low cost, there is increasing use of composite materials. Glass fibre reinforced plastic (GFRP) or carbon fibre reinforced plastic (CFRP) is now used due to their high strength-to-weight ratio and fatigue resistance. These materials can also provide improved damping characteristics, reducing vibrations and improving the overall performance of the flywheel system. Carbon fibre is a particularly attractive material for flywheels due to its high strength, stiffness, and low weight. However, carbon fibre is also relatively expensive, which limits its implementation (Olabi et al., 2021).

Bearings are critical in supporting high-speed rotation and are designed to provide low friction and high durability under the high-speed conditions present within a flywheel. As such, innovations in bearing technologies are key to maximising efficiency by minimising frictional losses. Ceramic bearings offer low friction and high wear resistance, whilst operating at higher temperatures than typical steel bearings. Polymeric bearings, such as those made from PTFE or PEEK, are also used in flywheel systems due to their self-lubricating properties. These

materials are advantageous in high-speed flywheel applications as they can help to reduce wear, prolonging the lifespan of the system. The latest flywheels use magnetic bearing systems to reduce frictional losses further (Buchroithner, 2023).

Flywheel systems have several advantages over other forms of energy storage systems. Primarily, they have high energy efficiencies, with round-trip efficiencies ranging from 70 % to 90 %, depending on the design and size of the system. Key factors which affect the efficiency are bearing losses and windage losses, caused by air resistance, though this is minimised through the use of magnetic levitation and a vacuum, respectively (Rao et al., 2015). This efficiency is higher than that of other mechanical storage systems, such as pumped hydro storage or compressed air energy storage.

FES systems are particularly advantageous for applications requiring high power output over short durations, frequent charge-discharge cycles, or rapid response times, such as in grid stabilisation and frequency regulation. A key area in which they are currently utilised is regenerative braking systems in electric vehicles (Erhan and Özdemir, 2021).

Notably, there are significant limitations associated with FES systems. The primary concern when considering grid-scale storage is the lower energy densities of 22-98 kWh/m^3 produced when compared to non-mechanical energy storage technologies. This makes them less suitable for long-term energy storage applications. These systems also experience high self-discharge losses between 5 % and 20 % per hour due to bearing friction and air resistance (Hasan et al., 2013; Mahela and Shaik, 2016). Over time, this friction can result in bearing wear that can lead to a further decrease in efficiency, necessitating regular maintenance to ensure optimal performance.

Safety is another critical concern with FES systems due to the high rotational speeds involved. Suitable containment is essential to mitigate risks in the event of a rotor failure. Modern FES systems incorporate robust containment strategies and advanced materials to enhance safety and reliability.

Furthermore, flywheel systems rely on high-speed rotation to store and release energy. This can be a safety concern if the flywheel is not properly contained, or if there is a mechanical failure in the system. As such, even though flywheels are designed to have an extended lifetime, they require regular maintenance to ensure that the bearings and other components are functioning properly, increasing complexity and cost.

FES technology has seen practical applications in various fields, from grid-scale energy storage providing frequency regulation services to integration within electric vehicles for regenerative braking. One notable example is Beacon Power's 20 MW facility in Stephentown, New York, which underscores the potential of flywheel systems in enhancing grid reliability and efficiency (Rounds and Peek, 2009).

FES technology has been implemented in various applications, including grid-scale energy storage for frequency regulation and integration within electric vehicles for regenerative braking. A notable example in Ireland is the 2 MW flywheel energy storage system installed by Schwungrad Energie in Rhode, County Offaly. This facility demonstrates the potential of flywheel systems to enhance grid stability and efficiency by providing rapid response services and supporting renewable energy integration1.

Ongoing research and development is aimed at overcoming current limitations by exploring new materials, designs, and integration strategies. This aims to improve energy density, reduce

costs, and expand the scope of FES system applications. As these technologies mature, flywheel energy storage stands to play a valuable role in the transition towards more sustainable and resilient energy systems.

Pumped Hydro

Pumped Hydro Storage (PHS) stands as the predominant energy storage mechanism globally, accounting for around 95 % of global active storage capacity (Argyrou et al., 2018). The technology is mature, going back as far as the 1890s, and can provide both high energy capacity and high power output, with a short response time.

The principle of PHS involves the storage of electrical energy as gravitational potential energy by pumping water from a lower-elevation reservoir to a higher one during periods of low energy demand and low electricity prices. This stored energy is then converted back into electrical energy by allowing the water to flow back to the lower reservoir through turbines, normally during peak demand periods. This is shown in Figure 2.3.

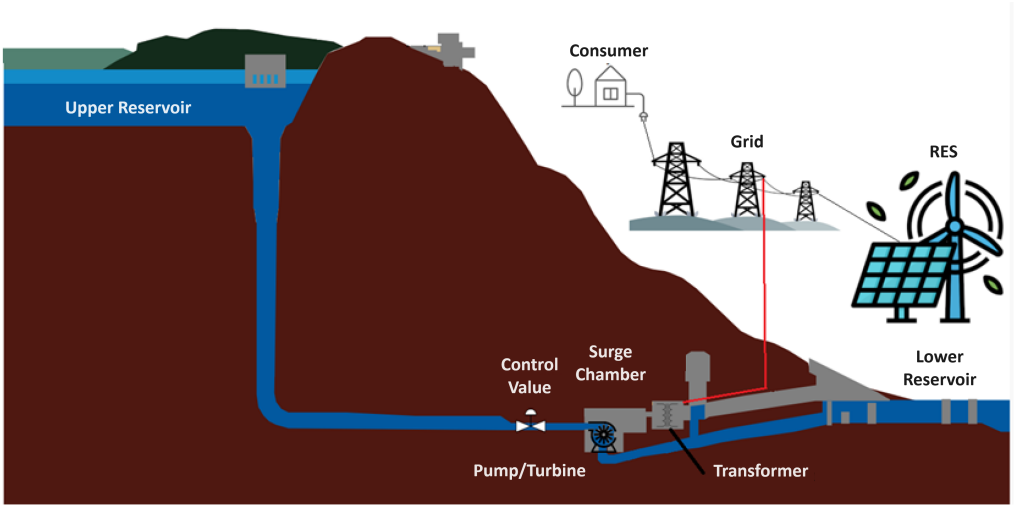


Figure 2.3: Diagram of a Pumped Hydro Energy Storage system [adapted from (Nikolaos et al., 2023)].

This cyclical operation allows PHS to offer round-trip efficiencies between 70 % to 85 %, making it an effective solution for grid regulation (Nikolaos et al., 2023). The ability of PHS to rapidly respond to grid demands, coupled with its high capacity for energy storage, makes it particularly valuable in balancing the intermittency of renewable energy sources such as wind and solar power.

Additionally, this technology sees minimal degradation over cycles meaning that the capacity of PHS which has already been implemented may continue to be used for the foreseeable future. Recent advancements in PHS technology have focused on enhancing efficiency and flexibility. The introduction of variable-speed reversible turbines and generators has allowed for more precise control over the storage and discharge process, improving overall efficiency and responsiveness (Sivakumar et al., 2014). Moreover, the integration of smaller, modular lower

reservoirs has expanded the potential applications of PHS, enabling its deployment in a wider range of geographical settings.

The Dinorwig Power Station is an example of PHS in the UK, as one of the largest PHS systems in the world. With a 1,800 MW output, and the capability of reaching full load in just 16 seconds, Dinorwig is an integral part of the grid, providing stability and peak load management. The station achieves an average efficiency of 74 %, showcasing the effectiveness of PHS in large-scale energy storage and generation (Fuchs et al., 2015).

Despite its widespread use and benefits, the expansion of PHS is constrained by geographical and environmental factors. The technology necessitates specific topographical conditions, including a suitable elevation difference between the upper and lower reservoirs, typically exceeding 300 meters, to achieve optimal energy generation efficiency (Lu et al., 2018). Additionally, the availability of sufficient water resources and the presence of suitable geological formations are crucial for the construction and operation of PHS plants. These requirements limit the feasibility of new PHS projects, as suitable sites are often located in environmentally sensitive or protected areas, raising concerns about ecological impact and land use.

To overcome these limitations approaches such as the use of fabricated structures or existing water bodies, such as abandoned mines and artificial lakes, are being explored. These solutions aim to leverage existing infrastructure to create PHS systems without significantly altering the environment.

The future development of PHS is reliant on overcoming the challenges posed by its geographical constraints and environmental impact. Efforts are focused on identifying new sites, optimising the use of existing reservoirs, and minimising the ecological footprint of PHS projects. The integration of PHS with renewable energy sources and the modernisation of ageing infrastructure present opportunities for enhancing the efficiency and sustainability of the energy grid.

Compressed Air

Compressed Air Energy Storage (CAES) has also been utilised for large-scale energy storage. It is attractive for grid deployment due to its high energy density and cycle efficiency, along with its low capital cost. Energy is stored by using a compressor to produce high-pressure air (typically up to 70 bar) during off-peak periods, storing this compressed air in underground formations like salt caverns or abandoned mines (Olabi et al., 2021). At times of demand, this air is expanded through a turbine in order to generate electricity. A diagram of this is shown in Figure 2.4.

The operational cycle of CAES involves two key phases: charging, where electrical energy is converted into high-pressure air; and discharging, where this potential energy is converted back into electrical energy. The efficiency of this process is influenced by the method used to manage the heat generated during air compression.

Traditional CAES systems, such as those in Huntorf, Germany, and McIntosh, Alabama, USA, have storage capacities of 1,160 MWh and 2,860 MWh and achieve efficiencies of 42 % and 54 % respectively (Khan et al., 2019). This is done by combusting natural gas to reheat the air during expansion, which prevents them from being fully renewable systems. These installations demonstrate the capability for long-term operation, with both exceeding three

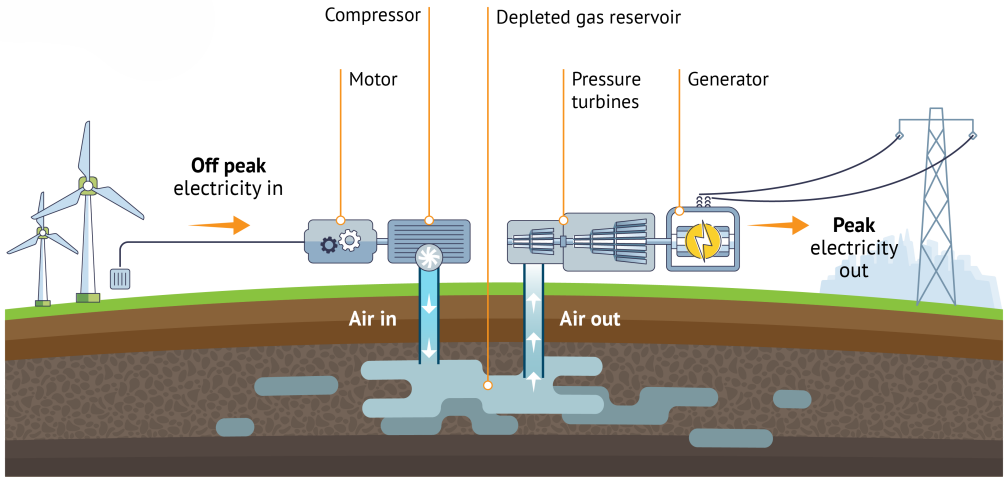


Figure 2.4: Diagram of a Compressed Air Energy Storage system (Energy Encylopedia, 2024).

decades in service, being operational since 1978 and 1991 respectively.

Storing the heat emitted during the compression stages and transferring it back to the air during expansion brings the process closer to being isothermal. This minimises the thermal losses within the process and removes the need for the addition of energy from combustion. This can be implemented in an Advanced Adiabatic Compressed Air Energy Storage (AA-CAES) system, which uses multiple compressor stages in order to increase compression efficiency and can maximise the thermal storage potential using a storage medium tailored to the temperature increase from each compression stage (Rabi et al., 2023). StorElectric, a UK start-up is projected to build a 500 MWh CAES system capable of efficiencies of up to 60 %, with this boosted to 70 % with the integration of thermal storage (Howitt, 2018).

While CAES offers a high-energy storage solution, the conventional reliance on fossil fuels for air reheating has raised concerns about its sustainability. The shift towards AA-CAES addresses this by moving closer to a fully renewable process, minimising environmental impact and aligning with global energy transition goals.

Similarly to PHS, though not to the same extent, CAES is geographically constrained, which limits its deployment potential. A geological formation must lie at a sufficient depth below the ground with a suitable cap rock to prevent leakage whilst also maintaining structural integrity under operational stresses (Guo et al., 2021). Additionally, the rock must be sufficiently porous to provide adequate storage volume whilst being strong enough to maintain its structural integrity. The store may not contain any minerals which undergo a rapid oxidation reaction when the pressured air is injected.

As the energy sector evolves towards more sustainable practices, CAES stands as a key technology for enabling the integration of renewable energy sources into the grid. The ongoing advancements in AA-CAES and the exploration of new geological sites for CAES deployment are critical for overcoming the limitations of this technology. The development of CAES, particularly in its advanced adiabatic form, promises to enhance grid reliability, support renewable energy integration, and contribute to the decarbonisation of the energy sector. However, even with further development, this technology will not be suitable for on-site deployment at most sites

at a large scale due to the geological requirements.

2.1.2 Electrical

Electrical Energy Storage (EES) systems are pivotal in modern power networks for enhancing grid stability, improving energy efficiency, and facilitating the integration of renewable energy sources. EES technologies offer unique advantages in terms of power density, efficiency, and response times.

Capacitor

Capacitive energy storage systems, also known as electrostatic energy storage devices, primarily comprise electrostatic capacitors and electrochemical supercapacitors which store energy in the electric field between two electrodes. A diagram of this is shown in Figure 2.5.

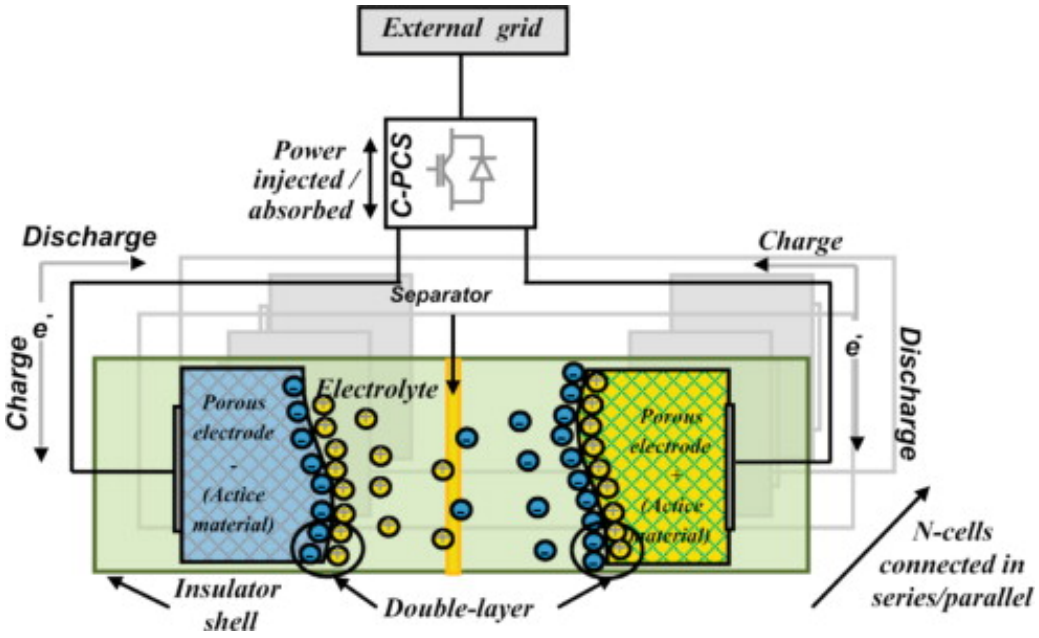


Figure 2.5: Diagram of a Capacitor Energy Storage system (Kalaiselvam and Parameshwaran, 2014).

Electrostatic capacitors are characterised by their high power density and long lifespan, albeit with relatively low energy density. In contrast, supercapacitors bridge the gap between conventional capacitors and batteries, offering higher energy density while maintaining significant power density and rapid charge-discharge capabilities (Conway, 1999).

One of the primary advantages of capacitors is their high power density, depending on the specific technology and design. This makes them particularly useful for applications that require short impulses of high-power energy, such as frequency regulation and grid stabilisation. Capacitors also have a long cycle life, typically between 100,000-1,000,000 cycles (Simon and Gogotsi, 2008), and can operate in a wide range of temperatures and environments.

Electric Double-Layer Capacitors (EDLCs), also known as supercapacitors, use two layers of carbon electrodes separated by an electrolyte to store large volumes of energy. They are commonly used in hybrid electric vehicles, renewable energy systems, and grid-scale energy storage applications.

The primary limitation of capacitors is their relatively low energy density compared to other energy storage technologies, which can range from 0.1-5 Wh/kg (Schneuwly and Gallay, 2000; Simon and Gogotsi, 2008). This means that capacitors are an expensive solution for applications that require long-term energy storage, such as seasonal energy storage.

Despite their limitations, capacitors have several potential applications for grid-scale energy storage. They can provide rapid response times and high-power output for grid stabilisation and support and can be used in combination with other energy storage technologies for optimal performance.

Supercapacitor-based energy storage systems for commercial use are in development by companies such as Skeleton Technologies and Maxwell Technologies (Kaenket et al., 2023). However, these systems are currently more commonly used for applications such as electric vehicles and renewable energy integration, rather than grid-scale energy storage. These technologies are still relatively untested for grid-scale energy storage. However, ongoing research and pilot projects are exploring their deployment. A project in the Canary Islands utilised a supercapacitor with a capacity of 4 MW and a 5-second capacity for frequency reserve that overall increases grid reliability (Skoglund, 2017).

While capacitors have the potential to play an important role in the future of grid-scale energy storage, further development is required to improve energy density and reduce costs, in order to make them more competitive with other energy storage technologies.

Superconducting Magnetic

Superconducting Magnetic Energy Storage (SMES) is a technology for storing energy in a magnetic field created by the flow of direct current in a superconducting coil. The energy is stored in the magnetic field and can be discharged by allowing the magnetic field to collapse, inducing an electrical current in a nearby conductor.

SMES systems typically consist of a superconducting coil that is kept at cryogenic temperatures using liquid helium. The coil is made from superconducting materials such as niobium-titanium or niobium-tin alloy, due to their extremely low electrical resistance when cooled to cryogenic temperatures. When a direct current is applied to the coil, a magnetic field is created that stores energy. A diagram is shown in Figure 2.6.

Modern SMES systems can charge and discharge with a round-trip efficiency of up to 95 %. They are also able to achieve more than 100,000 discharge cycles without significant degradation in performance and have a high power density between 0.5 and 2 kW/kg, making them suitable for grid-scale energy storage applications (Amiryar and Pullen, 2017; Kebede et al., 2022). These properties, along with their fast response time, make SMES suitable for applications that require high power output in short bursts, such as grid stabilisation and frequency regulation.

However, SMES systems have several limitations that have prevented their widespread deployment. The primary limitation is the high cost of cryogenically cooling the system to

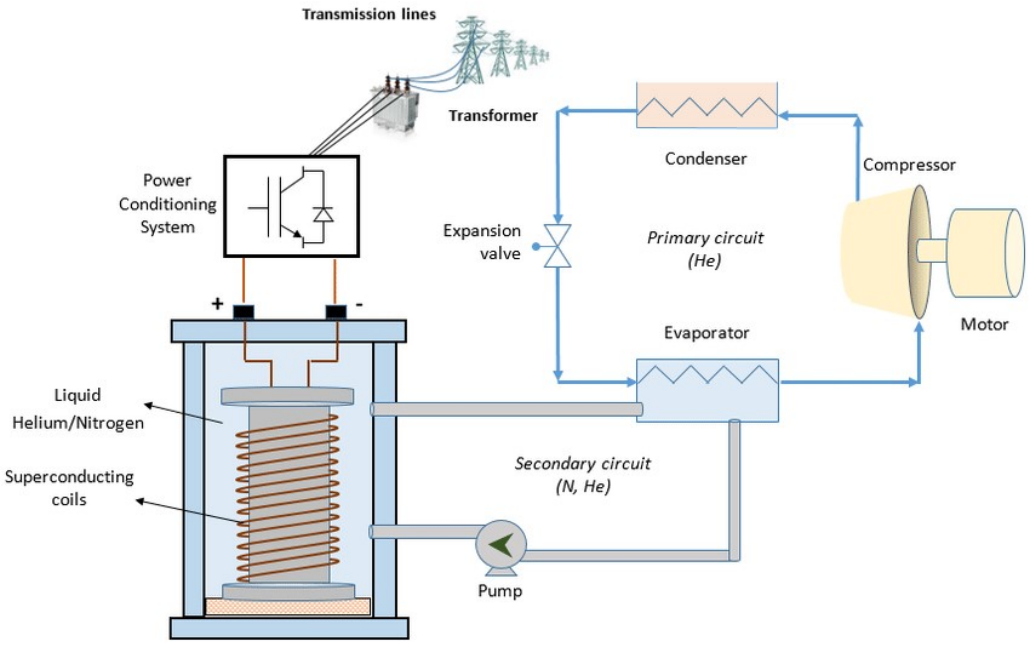


Figure 2.6: Diagram of a Superconducting Magnetic Energy Storage system (Nikolaidis and Poullikkas, 2017).

maintain the superconducting properties of the coil. A further drawback is their relatively low energy densities, which make them impractical for applications where space is limited, such as a retrofit to a pre-existing site. The superconducting coil also needs to be carefully designed and fabricated to avoid damage from the large forces generated by the magnetic field (Evans et al., 2024).

There is ongoing work to improve the efficiency, energy density, and cost-effectiveness of SMES systems. A primary focus is the development of high-temperature superconducting materials, which could reduce the need for cryogenic cooling. As such, research is focused on improving superconducting coils to increase SMES energy storage, improving the overall system efficiency and reducing operational costs (Iwasa, 2009).

2.1.3 Chemical

Chemical energy storage refers to the process of storing energy in the chemical bonds of molecules. This energy can be released later by breaking these bonds through a chemical reaction, thereby generating heat, electricity, or other forms of energy. Chemical energy storage is used in a variety of applications, including batteries, fuel cells, and hydrogen storage systems.

Chemical energy storage is attractive because it can provide high energy densities. However, chemical energy storage systems can also be expensive and complex to manufacture, and can sometimes pose safety risks due to the potential for chemical reactions or leaks.

The potential benefits of chemical energy storage have spurred research into improving these technologies for grid-scale deployment. For instance, lithium-ion batteries have gained widespread acceptance in recent years as an effective means of storing energy for grid-scale applications due to their high energy density and long cycle life. Similarly, hydrogen storage

systems are being developed as a potential means of storing excess renewable energy. However, challenges remain in optimising the cost, performance and safety of chemical energy storage systems for practical deployment in grid-scale applications.

Liquid Electrolyte Batteries

With their continued development over the past 200 years, there are a range of available battery technologies. These technologies are based on a collection of electrochemical cells, comprised of an anode and a cathode within an electrolyte, first invented by Alessandro Volta. They store energy in the form of chemical potential through charge transfer reactions and release this as electrical energy. This occurs when electrons are released in a redox reaction and then flow externally between electrodes.

Lithium-ion (Li-ion) batteries, the current standard, first became commercially available when they were introduced by Sony in the early 1990s (Hossain and Hoque, 2018). Over the past 30 years, these cells have been continuously improved, resulting in their energy density doubling in that time. As Li-ion cells outperform similar types of batteries such as Lead-acid, nickel-metal hydride (Ni-MH) and Nickel-Cadmium (NiCad), they are now prevalent throughout modern society, being used in an array of technologies such as mobile phones, power tools and electric vehicles.

The chemistry of a Li-ion cell involves lithium ions migrating between the electrodes via an electrolyte during the charge and discharge reactions. Within a Li-ion cell, ionic lithium is embedded within the structure of other materials to form the cathode. Common cathode materials are Lithium Cobalt Oxide (Lithium Cobaltate), Lithium Manganese Oxide (Lithium Manganate), Lithium Iron Phosphate, Lithium Nickel Manganese Cobalt (NMC) and Lithium Nickel Cobalt Aluminium Oxide (NCA) whilst graphite is commonly used to construct the anode (Nitta et al., 2015). A diagram is shown in Figure 2.7.

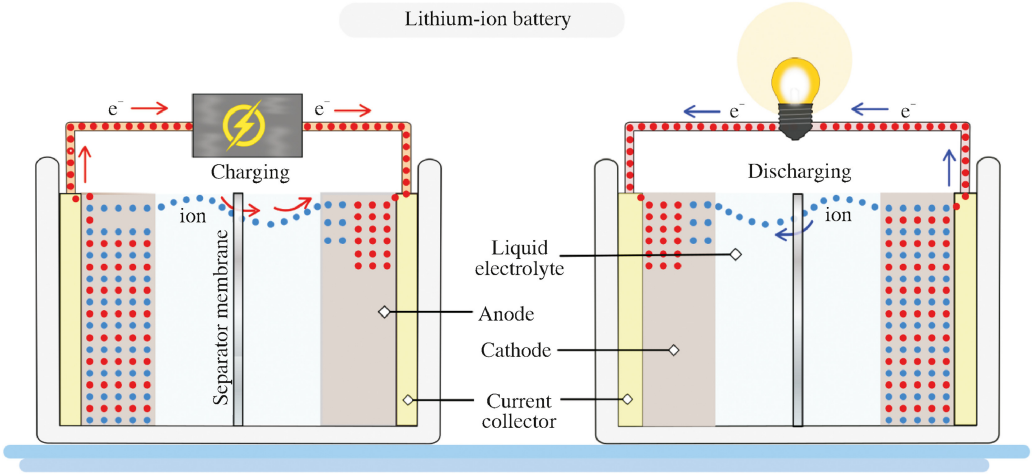


Figure 2.7: Diagram of a Li-ion Energy Storage cell (Mitali et al., 2022).

Li-ion battery systems are comprised of multi-cell modules arranged in series or parallel to meet specific requirements. Critical to their operation is a Battery Management System (BMS), which monitors cell parameters to ensure safety, as Li-ion batteries lack inherent

overcharge dissipation capabilities. The BMS alongside appropriate mechanical and thermal management safeguards against potential safety risks such as thermal runaway. This approach to battery system design underscores the importance of integrating electrochemical innovation with advanced control mechanisms to harness the full potential of the technology (Rosen and Farsi, 2023).

Currently, mass-produced cells containing lithiated metal oxide cathodes and carbon anodes cost around 150 $/kWh, providing cell voltages of around 3.70 V and a specific energy of around 190 Wh/kg. However, there is an estimated upper limit of 400 Wh/kg (Park et al., 2019) for Li-ion technologies. The performance characteristics vary depending on the electrode materials selected, but with this comes a change in life, safety and power capabilities.

Future technologies look to improve on this, with Solid State Batteries (SSBs), which use low-density solid-state electrolytes such as polymer or sulphides that may reach 480 Wh/kg. However, these technologies are still theoretical (Ulvestad, 2019).

Additionally, significant research is being undertaken into Lithium-Air (Li-Air) batteries. These theoretically have a high energy density of up to 3500 Wh/kg along with a low cost (Jaradat et al., 2021). However, practical challenges hindering Li-Air batteries include low specific capacities, issues with positive electrode reversibility, low specific capacity, and stabilisation of the negative metal electrode (Liang et al., 2022).

Redox Flow Batteries

Flow batteries, also known as redox batteries, are unique in terms of electrochemical energy storage devices. They are distinguished by their ability to decouple energy and power capacities, facilitated by the external storage of electrolytes which are circulated through an electrochemical cell during operation. Flow batteries offer promising solutions for large-scale energy storage applications, particularly in grid stabilisation, peak shaving, and integration of renewable energy sources.

The principle of this technology is similar to that of conventional batteries in that they store energy as chemical potential. The difference, however, is that the two electrolytes are stored separately in external tanks and pumped through a cell stack where a redox reaction of the two solutions occurs, the pathway being dependent on whether the system is charging or discharging. This stack comprises electrodes separated by an ion-exchange membrane which allows ionic transfer while preventing electrolyte mixing (Revankar, 2019). This is shown in Figure 2.8.

Current systems include Zinc-Bromine Flow Batteries (ZnBr), Vanadium Redox Flow Batteries (VRB) and Iron-Chromium Flow Batteries (ICB). In the example of a ZnBr flow battery, during charging, electrons pass through the membrane from the NaBr side to ZnBr. When the ZnBr solution is reduced, a metallic zinc layer is formed on the carbon composite anode, whilst the bromine is evolved at the cathode when the NaBr is oxidised. During discharge, the system is run in reverse and electrons are released at the anode to do work in an external circuit when returning to the cathode. In this process, the zinc metal is oxidised, and the bromine, which had previously formed a viscous oil during its charging period and must be agitated into the catholyte solution, is reduced. The round-trip efficiency of flow battery systems can be up to 85 % (Ashok and Kumar, 2024).

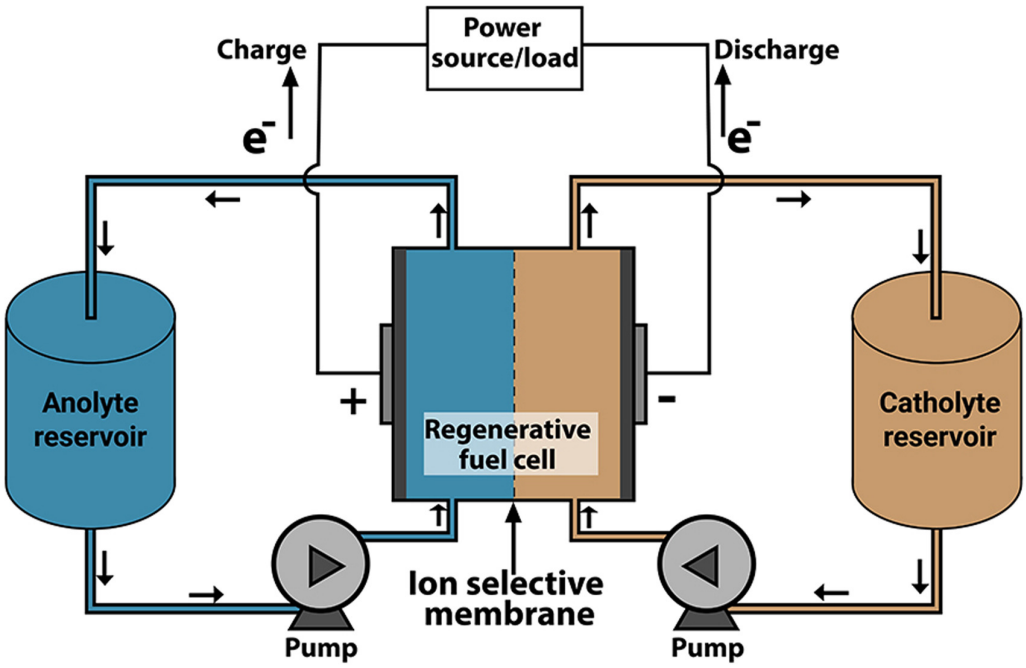


Figure 2.8: Diagram of a Flow Battery Energy Storage system (Argyrou et al., 2018).

The scalability of energy capacity is determined by the volume of stored electrolytes, which highlights the versatility of flow batteries (Sun et al., 2017). Independently, the power can be scaled by altering the size and number of cell stacks. This decoupling enables the tailoring of flow battery systems to specific requirements of various applications, ranging from frequency regulation to load levelling and long-duration energy storage. As the two electrolytes are stored separately, this results in a very small self-discharge which is an inherent advantage of the system.

Moreover, flow batteries are characterised by their extended cycle life and operational durability, undergoing over 10,000 cycles with minimal degradation, which can translate to operational lifespans exceeding 20 years (Kear et al., 2012). Additionally, the electrolytes commonly used in flow batteries offer inherent safety benefits, including lower flammability and reduced risk of thermal runaway, further enhancing their applicability in diverse settings (Li et al., 2011).

Despite the notable advantages of flow batteries, several challenges hinder their widespread adoption, particularly in grid-scale applications. One of the primary hurdles is the relatively lower energy density compared to conventional solid-state batteries. These are 20-40 Wh/kg, which is significantly lower than that of Li-ion batteries outlined above (Allam et al., 2023).

Furthermore, the cost of electrolytes and ion-exchange membranes is high and contributes significantly to the overall capital cost. These membranes are also prone to degradation, impacting the long-term performance and increasing maintenance requirements (Li et al., 2011). Further failure due to chemical stresses occurs in components which come into contact with the electrolytes. Due to the high costs of these materials, the maintenance costs of these systems are high.

Hydrogen

Interest in H_2 storage is quickly growing as the technology has a higher storage capacity than most other storage techniques. The current standard for hydrogen production is through hydrocarbon reforming, accounting for 95 % of production. However, this process is far from environmentally sustainable due to its high GHG output, with a global warming potential (GWP) of $\tilde{1}2$ kg CO_2e (Nnabuife et al., 2023). However, it is possible for hydrogen to be produced on a large scale without emissions using renewably sourced electricity to split water into its constituents using alkaline electrolysis. There is also significant research into high-temperature electrolysis (HTE) which may allow for higher electric-to-hydrogen, much greater than that of conventional electrolysers (Fallah Vostakola et al., 2023). Once H_2 has been produced, it can then be stored for extended periods without a significant self-discharge, making it suitable to provide mid to long-term storage. Hydrogen is currently stored as either a pressurised gas, liquefied gas or as a solid metal hydride. To convert the energy stored chemically back into electricity, fuel cells may be implemented, although combustion in a CCPP can provide greater efficiencies. This cycle is shown in Figure 2.9.

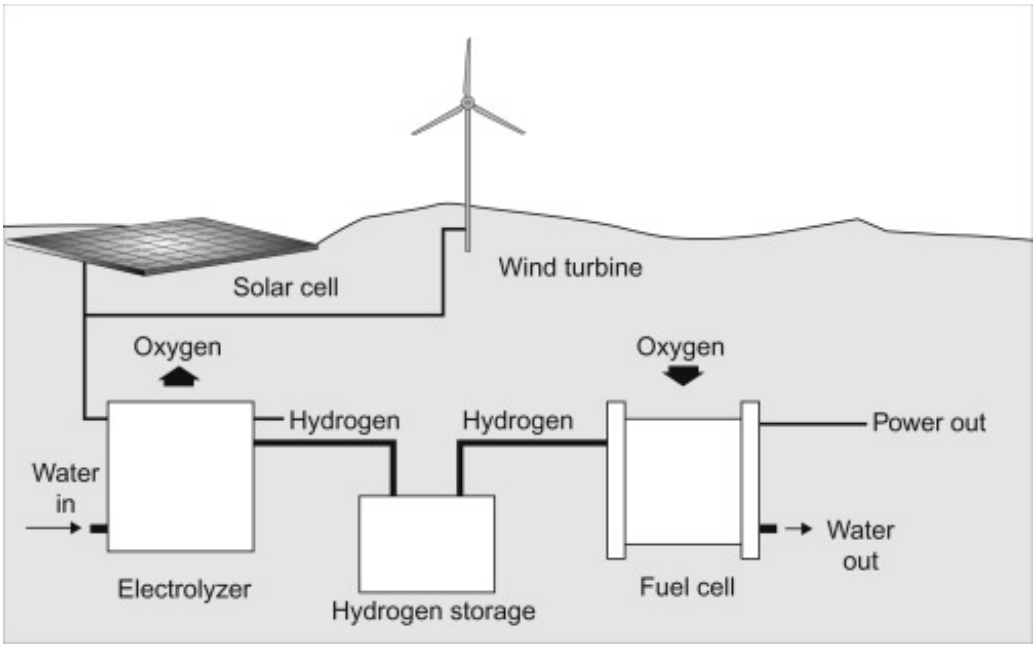


Figure 2.9: Diagram of a hydrogen generation, storage and utilisation system (Breeze, 2018).

Currently, one of the most promising methods for stationary power applications being explored is solid oxide electrolyser cells (SOEC), well known as highly efficient energy converters, which aim to produce H_2 via HTE using only renewable energies. In this process, H_2 is produced through the decomposition of steam using a combination of high-temperature heat and electrical energy. The efficiency is higher than that of standard alkaline electrolysis as there is a smaller specific electricity requirement allowing the voltage at the electrodes to be lower. This process has the potential to be a renewable, cost-effective method to produce hydrogen with overall efficiency in excess of 80 % LHV and convert it back to electricity by running the cell in reverse with efficiencies of 60 % LHV (Posdziech et al., 2018; Schwarze et al., 2017).

However, there are issues which need to be resolved with SOEC for this technology to be industrially viable, such as long-term performance degradation at the electrodes. Some major degradation mechanisms which have been identified are the contact between cell components, air electrode delamination, chromium poisoning, microstructure degradation and seal leakage.

Current compressed hydrogen storage technologies compress the gas to up to 200 bar for storage within a Type I tank for industrial use. Constructed solely from metal, Type I tanks are the cheapest and most widespread technology for industrial storage. New type IV (composite tanks with polymer linings) cylinders are being developed, which may support storage at up to 800 bar, increasing the volumetric density of the storage gas and, therefore, increasing the energy density. For storage at a larger scale, underground caverns such as salt domes, aquifers and depleted gas fields are also potentially an option if the site is able to satisfy the required parameters. However, this storage method is currently only at the stage of feasibility studies (Amid et al., 2016). Although the compression technology is simple, at a commercial level, it incurs high capital and operational costs to operate (15 % of the stored LHV) and maintain the system.

Hydrogen liquefaction can be achieved with the use of cryogenics, lowering the temperature to 20 K. This storage method is able to provide a high energy density, more than twice that of compressed storage, making it volumetrically and gravimetrically efficient. As with compressed hydrogen, the liquefaction infrastructure is a limiting factor due to its availability and cost. Furthermore, producing cryogenic hydrogen (LH_2) requires a large energy input (more than 30 % of the stored LHV) and further input to maintain its state (Al Ghafri et al., 2022). Due to this, boil-off losses (evaporation due to heat leakage) of up to 1-5 % per day may be incurred as gaseous hydrogen must be vented to prevent over-pressurisation (Zhang et al., 2023). Not only does this reduce the overall efficiency of the storage system, but it also raises safety concerns due to the release of hydrogen and the possibility of a failure in the pressure relief system. For this to be a viable system, further research must be undertaken to develop tank materials which are stronger, lighter and cheaper, along with techniques to minimise boil-off and capture released boil-off for re-liquefaction efficiently.

Material-based storage technologies may be used to achieve high volumetric hydrogen storage densities. Hydrogen is stored through adsorption, bulk absorption or chemical interaction with a solid matrix which may be later manipulated to release the hydrogen on demand. The most mature of these technologies are reversible metal hydrides (MH). In this process, hydrogen absorbs at low pressure (up to 10 bar) and is released upon the addition of heat. This process is favourable as it has a low energy cost and is intrinsically safe due to the endothermic nature of the desorption process. Magnesium Hydrides (MgH_2) are currently one of the most promising hydrogen storage technologies due to their high energy density, low cost and lack of toxicity. Recent studies reported MgH_2 achieving energy density values as high as 2600 Wh/kg based on the LHV with a capacity of 7.6 wt % (Shao, 2017). However, there are drawbacks associated with desorption due to the high stability of the MH, requiring substantial thermal input and management ($>$300 °C) to release the hydrogen. Efforts are being made to overcome these issues with the use of alloying, additive addition, nanoscaling and nanoconfinement to alter the desorption kinetics, and thermal requirements (Wang and Wang, 2017). However, despite these efforts, there is not currently a method which makes MgH_2 a commercially viable stand-alone hydrogen store.

To recover the energy stored, the hydrogen can be passed through a fuel cell (FC). There is a range of fuel cell technologies available, including polymer electrolyte membrane (PEM), alkaline fuel cells (AFC), phosphoric acid fuel cells (PAFC), molten carbonate fuel cells (MCFC), and the aforementioned solid oxide fuel cells (SOFC) (Office of Energy Efficiency & Renewable Energy, 2018). The most suitable of these for generation is the SOFC owing to its high-power stack size and its 60 % conversion efficiency. Due to the high operating temperature of this system, it is also suitable for CHP, which may increase its overall combined efficiency in cogeneration (Soleymani et al., 2021). However, these efficiencies have only been demonstrated on a micro-scale and may not be viable once scaled to grid-scale levels and, as previously mentioned, SOFC technology still faces some issues which prevent this.

A further option is the direct combustion of hydrogen in GTs. Many studies have been performed to identify the modifications required to allow an existing GT to be fuelled by hydrogen (Alhuyi Nazari et al., 2022; González Álvarez et al., 2024). Simulations show that overall, hydrogen combustion in place of natural gas can increase both the power output and the combined cycle efficiency in a CCGT by up to 10 % and 0.7 %, respectively, depending on the dilution fluid used (Chiesa et al., 2005). However, this does require the GT to be re-engineered, increasing the turbine blade height, turbine geometry and blade cooling flow to accommodate for the increased gas flow through the system, which is required to maintain the turbine inlet temperature (TIT) and compressor pressure ratio (β). If these modifications are not made, variable guide vane (VGV) operations and β increases may be implemented to allow for a pre-existing turbine to operate using hydrogen as a fuel to minimise NOx emissions (Prakash, 2011). These modifications reduce the improvements to the system made by the fuel switch, with VGV operations slightly reducing the power output and efficiency, whereas the effect of β is dependent on the dilution fluid used.

2.1.4 Thermal

An ES system which appears promising for future use is thermal energy storage (TES). TES allows for the storage of heat at either high or low temperatures by changing the temperature of a storage medium from ambient. Depending on the system used, this energy can be stored from hours to months later. Current technologies such as heat storage tanks, can store heat for a few hours to days, while long-term storage solutions, like borehole thermal energy storage, can retain energy for several months (Sadeghi et al., 2024).

It is attractive for grid deployment due to its high energy densities of up to 0.38 kWh/kg and cycle efficiencies of up to around 60 %. TES provides a range of possibilities due to the scope of potential applications. These include using resistance heaters (using low-cost electricity) or a hot gas stream (waste heat from a high-temperature process) to charge the store by heating the thermal mass. To meet specific demand requirements, this energy may then be discharged as either heat or electricity, depending on the extraction method.

Sensible Heat

Sensible thermal energy storage (STES) is the most common, mature and utilised form of TES, due to its simplicity and low cost. This involves raising or lowering the temperature of a material

without inducing a phase change. The most common materials used are water, rocks, and concrete. To make the system viable for energy storage, the material is insulated to minimise thermal losses to maximise the period of time for which energy storage is retained Zhao et al. (2022). This can be done with materials in any state; however, due to the relationship between temperature and pressure and the required volumes, this is usually focused on solid and liquid materials.

The efficiency of STES systems depends on several factors, including the type of storage material, the size and design of the storage tank, and the operating conditions. Additionally, the use of suitable insulation around the storage tank can minimise heat loss and increase the efficiency of the system.

These systems have several advantages over other thermal energy storage systems. They produce a greater lifespan as the storage material is not subjected to phase change cycles that can cause wear on the containment vessel or heat exchanger surfaces due to volumetric differences when the material is in different states. They can also be more cost-effective, requiring less maintenance and can use more readily available materials, such as water and concrete (Seyitini et al., 2023).

STES technologies are classified as either active or passive storage systems. Within an active system, the storage medium acts as a heat transfer fluid (HTF) as it circulates through the system to reach heat exchangers whilst charging or discharging via forced convection. In contrast to this, passive systems utilise a stationary storage medium and exchange energy via an external HTF (Umate and Sawarkar, 2024).

The more common method of liquid sensible heat storage is through the use of a two-tank system, an active storage system. In a direct two-tank system, a single fluid is stored in two separate tanks, one containing high-temperature fluid and the other, low temperature (Riahi et al., 2020). During charging, fluid flows from the low-temperature storage tank to be heated and stored in the high-temperature tank. When the energy is to be extracted, the hot fluid flows back to the cold tank, releasing its energy which is then able to run a heat engine. The use of a single material for HTF and ES greatly simplifies the operating strategy of the system giving it a major advantage over a system using a solid storage medium.

For liquid sensible storage, the temperature range is limited to between its freezing and boiling point. Water is often used for sensible heat storage due to its abundance, low cost and favourable properties such as a relatively large specific heat capacity of 4.18 kJ/kg·K, high density and non-toxicity. This allows it to achieve a high energy density.

Other materials such as molten salts and mineral oils (such as Caloria) are also commonly used when the operating temperature is outside that suited to water. Molten salts, such as a mixture of potassium nitrate (KNO_3), sodium nitrite ($NaNO_2$), and sodium nitrate ($NaNO_3$), are known for their high specific heat and thermal stability up to 600 °C and as such, offer higher energy storage densities (Vijjapu and Tiwari, 2022).

However, materials such as these do have associated drawbacks. Mineral oils have a high cost associated with a volume large enough to be used for storage and due to their high vapour pressure, pressurised tanks would be required for operation at the higher temperatures associated with some thermal sources, adding a significant capita cost to the system. As for molten salts, precautions must be taken against the solidification of the liquid within the system.

A variation of this to remedy the aforementioned issues is the indirect two-tank system. In these, an extra heat exchanger is used, allowing for two different fluids to be used for the storage fluid and the HTF. Due to this, a HTF can be used at high temperatures to receive the energy from the thermal source and transfer it to the storage fluid. The storage fluid may then flow back and forth to heat the HTF, which can then transfer energy to a heat engine when required for discharging (Guney, 2016). This allows for each to be specifically tailored to behave optimally for their given temperature ranges (HTF with low vapour pressure and storage medium with low freezing point). However, this system incurs additional capital and operational costs due to the addition of an extra heat exchanger and the lower temperature difference between the two storage tanks.

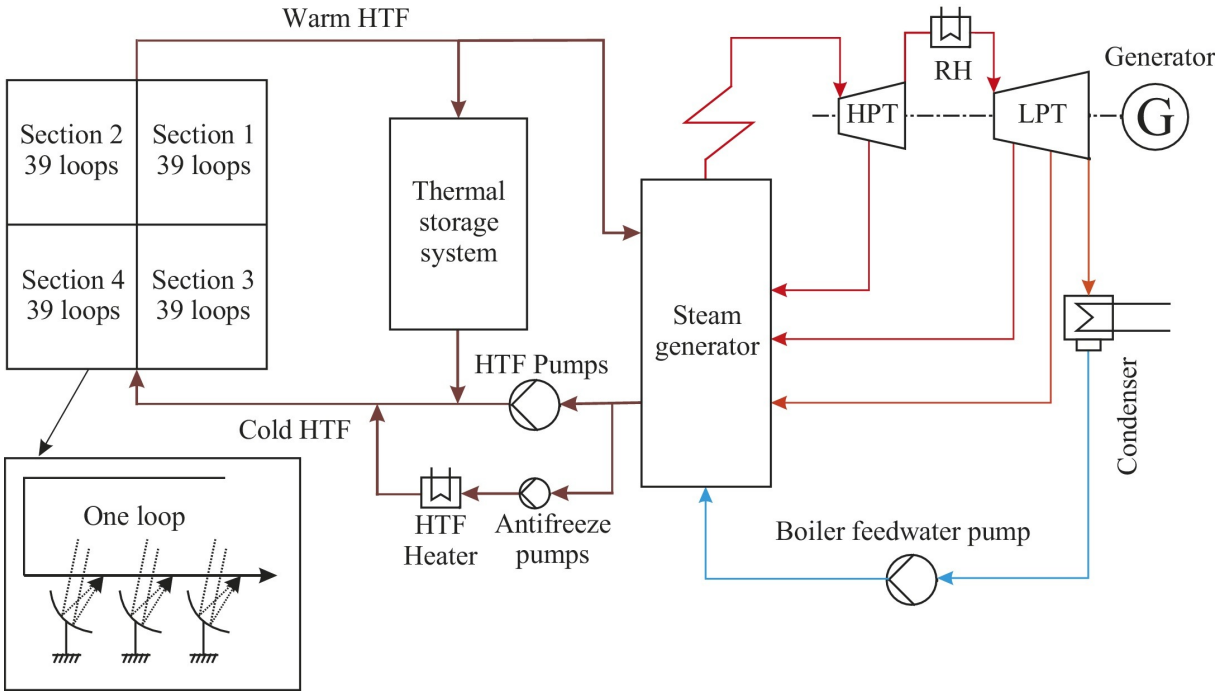


Figure 2.10: Process diagram of Andasol II solar power plant (Al-Maliki et al., 2016).

A notable example of STES in practice is the Andasol Solar Power Station in Spain, which utilises molten salt for heat storage in its CSP plant. The PFD of this system is shown in Figure 2.10. The facility achieves a storage capacity of 1,010 MWh, allowing for electricity generation up to 7.5 hours after sunset, thereby enhancing grid reliability and renewable energy integration (Bauer et al., 2021).

As opposed to these systems, STES may also be designed to store sensible heat within a solid medium. These have a much wider range of operation as they are already frozen, so have no lower temperature limit, and materials will be selected that have a high melting point. Unlike the liquid-based system, the solid cannot be used as a HTF, and thus, solid storage systems may only be passive, using a separate HTF to add or remove energy to the store. Commonly, the storage mediums used are rock, sand, concrete and ceramic thermal bricks.

A common method used for solid sensible storage is the direct single-tank thermocline. In these systems, a packed bed is often utilised, and a high-temperature HTF is passed down

through the bed, transferring heat to the solid bed from the top down and exiting from the base at a low temperature. This creates a temperature gradient or 'thermocline' throughout the bed as heat is transferred to the packing, cooling as it progresses down the bed. Once the uppermost region of the bed has reached thermal equilibrium with the HTF inlet temperature, the thermocline will then begin to move down the packed bed until, eventually, if charged for long enough, the entire bed is at the same temperature at the HTF. During discharge, the cool HTF reverses the flow direction, passing up the bed and extracting heat from the store. Utilising the low-cost materials previously mentioned for packing and the requirement of only one tank reduces the cost of these storage mechanisms compared with many two-tank systems. An advantage of these systems is that they produce a constant outlet temperature (Cascetta et al., 2021).

Indirect solid stores are also used where a HTF is passed through an array of pipes within a solid mass. They operate through a similar principle to that of thermoclines, though, as the heat is transferred through the pipe set within the system, there is no voidage within the solid, increasing the mass of the solid per unit volume. Though this allows the store to attain a greater maximum storage capacity, there is a significant cost associated with the design and manufacture of the pipe network to ensure that the storage medium is optimally utilised.

However, an aspect which must be mentioned regarding storage using sensible heat is that, as the store is discharged, the outlet temperature will decrease. This is because the stored energy and store temperature are intrinsically linked, and so, the power output from the store will decrease over time with a constant flow rate of HTF.

Latent Heat

Latent thermal energy storage (LTES) systems operate by adding or removing energy from a material whilst it undergoes a phase change. Due to this, materials which utilise latent heat storage are often referred to as phase-change materials (PCMs). The most common materials used are paraffin wax and salt hydrates. Compared to sensible thermal storage, systems which exploit the latent heat of a material can store much more energy per unit volume. This is because these systems exploit the large specific heat of fusion associated with a change in the phase of the storage in addition to any sensible heat. A further advantage of PCMs is that they are able to achieve a large storage capacity with only a small change in temperature. As the temperature of the storage medium remains constant during a phase change, these systems are able to provide heat at a constant temperature. This storage technique is most often utilised in a solid-liquid phase change though liquid-gas, solid-gas and solid-solid transitions may also be utilised.

An example is the 1414 Degrees SiBox system, storing thermal energy by heating silicon to its melting point of 1414 °C (Parham et al., 2021). This allows the system to utilise the high latent heat capacity of silicon to achieve energy densities of over 1 kWh/kg of silicon. Figure 2.11 shows a diagram of this system.

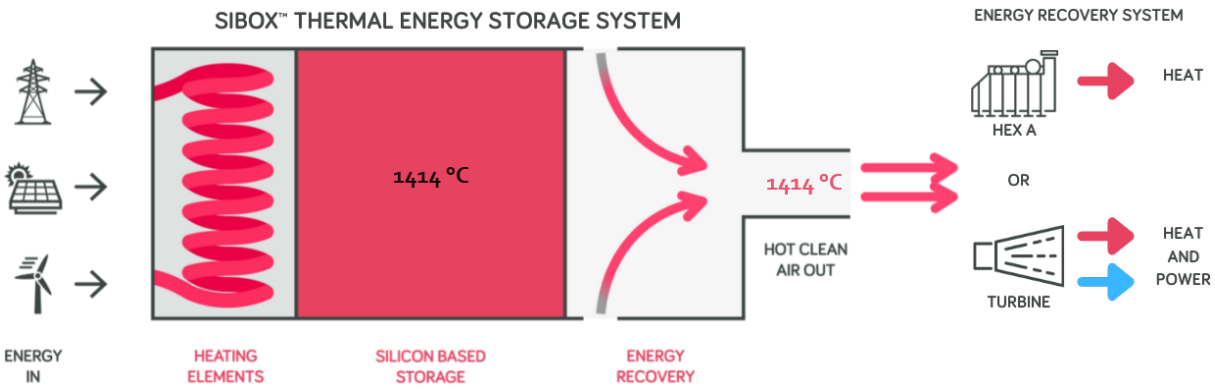


Figure 2.11: Diagram of 1414 Degrees SiBox Latent Thermal Storage System (Parham et al., 2021).

1414 Degrees is using the SiBox system in the Aurora Energy Project, an initiative aimed at establishing a hybrid renewable energy power plant. The project focuses on integrating a 140 MW LTES system into the transmission network, with plans to incorporate concentrated solar power to bolster a shift to a low-carbon electricity system.

This system demonstrates the feasibility of LTES in industrial applications, showcasing the potential for high-density energy storage solutions and the broad range of applications for STES technologies in enhancing renewable energy integration and grid stability.

Like solid sensible storage materials, solid-liquid PCMs can only be used to form passive storage systems. In the majority of cases, energy is transferred from the PCMs to the HTF indirectly to limit contamination, though direct transfer may be used in some cases. To achieve this, a packed bed may be utilised though this incurs large design and construction costs.

Direct transfer is most likely to occur when using water as the PCM. This is the most common material utilised as it is accessible, well-known and has a low cost (Prieto et al., 2024). It is often implemented in cooling systems transitioning it into ice. Other, more specialised types of materials that are utilised as PCMs include organic compounds, inorganic compounds and eutectics.

Organic PCMs are defined as paraffin and non-paraffin products. A large portion of the organic PCMs currently available are paraffin-based, a petrochemical product, predominantly comprised of straight-chain alkanes. Non-paraffin alternatives include materials such as fatty acid esters and alcohols. These materials are limited to operating at low temperatures (often below 900 °C) as they may decompose when heated too far (Jayathunga et al., 2024).

Due to the composition of paraffin PCMs, they are able to offer a wide range of melting temperatures and latent heat of fusion depending on the alkane mixture. As they follow simple chemical trends based on chain length, these materials have predictable physical properties. Furthermore, they are comprised of molecules which are stable over a wide range of operating temperatures, remain chemically inert, are non-corrosive with widely used construction materials and experience very little volume change upon phase transition, making them reliable PCMs. However, they do have low phase change enthalpy in comparison to inorganic PCMs and exhibit poor thermal conductivity, causing them to require a larger surface for heat transfer (Kahwaji et al., 2018).

Of the non-paraffin organic PCMs, fatty acids display the greatest potential due to their relatively high heat of fusion compared to other available materials. Compared to paraffin, fatty acid PCMs exhibit similar properties but lower latent heat capacities than paraffin PCMs. However, they are more economical and sustainable due to their ease of production and that they are sourced from vegetable and animal oils which have a greater continued assurance of supply than petroleum (Magendran et al., 2019).

Inorganic compounds include materials such as molten salts, salt hydrates and metallics. These materials can have up to twice the volumetric latent heat of organic PCMs and exhibit improved thermal conductivity. Salt-based materials are the most mature inorganic PCMs and have a range of advantages. In addition to the two previously mentioned qualities, they are low cost and undergo a very small volume when undergoing a phase transition (Li et al., 2022). However, despite these advantages, these materials are not widely utilised due to their drawbacks. These include issues such as decomposition due to their water content. When the materials undergo a phase change, they lose a fraction of their water each cycle which results in phase separation, limiting their continued use for extended periods of time (Adesusi et al., 2023). Furthermore, though salt base PCMs are compatible with plastics which is an advantage over paraffin, they will corrode many metals.

Metal and alloy PCMs are utilised far less frequently than others. Despite this, they display a very high heat of fusion per unit volume, good chemical stability, present much higher thermal conductivities than organics and have relatively low vapour pressures, making them very good options for PCMs. Examples of materials used in these systems include nickel, tin and aluminium. However, these are majorly limited by their high densities resulting in large weight penalties and are, thus, only considered when there is a volume constraint on the system. Though this issue limits their suitability for use as PCMs, it makes them a good candidate for large-scale TES (Costa and Kenisarin, 2022).

Eutectics are comprised of two or more components with similar phase change points that crystallise when frozen. These can be comprised of solely organic compounds, solely inorganic compounds or a mixture of the two. Combining materials at certain quantities allows interactions which modify the phase change process, enabling the material to achieve desired melting points lower than that of the individual components. This allows for materials to be produced that can meet required temperature ranges whilst maintaining desirable attributes (Sun et al., 2023). One of the currently used eutectic compounds is known as 'Solar Salt' and is commonly used in CSP systems, operating at temperatures up to approximately 600 °C before it experiences thermal decomposition (Peng et al., 2017). However, these materials are more expensive than other PCMs and there are currently only a limited number of eutectic materials which have been produced and research is continuing in this area to broaden the range of available PCMs.

As for liquid-vapour PCMs, though they have a greater storage potential due to the greater enthalpy change from liquid-vapour than from solid-liquid, they are required to account for the large volume of gas which is produced during vaporisation. This system is more likely to operate inversely, using cryogens and liquefying gases such as air, nitrogen, or hydrogen (Tafone et al., 2021). Cryogens used as energy stores exhibit high exergy densities and as they are being converted to a liquid, they can be stored without the issue of volume.

Though PCMs are able to achieve a much greater energy density than sensible systems,

there is a considerable restraint associated with sourcing a suitable material that undergoes a phase change at the required temperature. As the temperature change may be very small, the material used must be carefully selected based on the intended application so that the phase change aligns with the temperatures used in the system. Additionally, if the system is to use stored energy as sensible heat as well, consideration must be made regarding factors such as thermal degradation at increased temperatures. To find appropriate materials which meet these specifications, often complex production techniques are required which incurs a large capital cost.

2.1.5 Comparative Analysis

For grid-scale ESS, factors such as capital cost (CAPEX), storage capacity, power rating, energy density, round-trip efficiency, operational lifetime, and storage duration each impact the viability of the technology for deployment. High CAPEX can be a barrier to adoption, while energy capacity and power rating must align with grid demands. Energy density impacts the footprint of the system, efficiency affects operational costs and energy loss, and the lifetime determines long-term viability. Additionally, the storage duration must align with the intended use. These factors must be optimised to create a viable solution for grid stability, supply security, and integration with renewable energy sources.

Table 2.1: Comparative Analysis of Energy Storage Technologies
(IRENA, 2017; Asri et al., 2021; Rogalev et al., 2022; Saha et al., 2022; Mitali et al., 2022; Söderström, 2016; Datas et al., 2016; Chiu, 2020; IRENA, 2020; Luo et al., 2015).

Technology	CAPEX ($/Wh)	Capacity (MWh)	Power (MW)	Energy Density (Wh/L)	Efficiency (%)	Lifetime (years)	Duration (-)
FES	0.1 - 6	0.01 - 5	0.002 - 20	20 - 80	70 - 95	15 - 25	Days
PHS	0.05 - 0.1	180 - 8,000	100 - 3000	0.2 - 6	70 - 85	40 - 95	Seasonal
CAES	0.02 - 0.7	3 - 2,860	60 - 1,000	2 - 6	40 - 70	20 - 54	Weeks
SMES	0.5 - 10	0.01 - 0.01	0.15 - 10	0.2 - 6	90 - 95	15 - 30	Minutes
Liquid Electrolyte	0.05 - 2.5	0.001 - 250	1 - 100	50 - 735	80 - 96	5 - 20	Days
Flow Batteries	0.32 - 1.68	0.2 - 120	0.05 - 40	15 - 70	60 - 85	5 - 30	Weeks
Hydrogen	0.8 - 16	100 - 10,000	10 - 100	300 - 600	25 - 45	40 - 69	Seasonal
STES	0.001 - 0.1	100 - 12,100	0.1 - 300	50 - 100	50 - 98	15 - 50	Seasonal
LTES	0.4 - 1	50 - 1,000	0.1 - 150	70 - 210	80 - 90	20 - 30	Weeks

Where FES is Flywheel Energy Storage, PHS is Pumped Hydro Energy Storage, CAES is Compressed Air Energy Storage, SMES is Superconducting Magnetic Energy Storage, STES is Sensible Thermal Energy Storage and LTES is Latent Thermal Energy Storage.

Where FES is Flywheel Energy Storage, PHS is Pumped Hydro Energy Storage, CAES is Compressed Air Energy Storage, SMES is Superconducting Magnetic Energy Storage, STES is Sensible Thermal Energy Storage and LTES is Latent Thermal Energy Storage.

The comparative analysis of various energy storage technologies presented in Table 2.1 indicates that each technology has its own set of limitations that prevent widespread adoption. Some of these primary limitations are high capital costs, geographical constraints, efficiency losses, and material scarcity, each of which limits viability (Sánchez et al., 2022). Note that these values are for a single storage system, and they can be increased with the addition of further systems.

TES emerges as a compelling option for grid-scale deployment due to its alignment with key factors. These factors include its low CAPEX and large storage capacity, which is further improved by the high energy density it can achieve. Although their power rating is lower than some options, these are limited by geographical requirements which do not apply to TES. Furthermore, the systems can store energy for extended periods, which is favourable to help limit curtailment.

However, a significant reduction in the cost of ES is required for economically viable integration. Ziegler et al. (2019) predicts that for an energy network that produces only 5 % of its energy from non-renewable sources, the energy capacity cost must reach 0.15 $/Wh. However, for the same technologies to be cost-competitive when RES meet baseload demand 100 % of the time, this cost falls below 0.02 $/Wh.

A potential to further improve economic viability involves retrofitting existing thermal generators with TES. This presents a cost-effective solution in comparison to new stand-alone storage facilities. Schumacher and Maximilian (2019) predict that a TES retrofit would have a CAPEX of 50 % of that of a stand-alone TES system. Additionally, the capital investment in new Combined Cycle Gas Turbine plants ranges from around $1,000 to more than $2,700 per kW of capacity, depending on complexity and the level of environmental control technologies employed (US Energy Information Administration, 2022). A TES retrofit utilising existing infrastructure can significantly reduce the required investment when compared to either a stand-alone ES system or a new power plant.

While this retrofit route offers significant savings, a challenge lies in the operational temperature mismatch between current TES systems and more efficient thermal generators. Thermal plants typically operate at high temperatures, which exceed the output of many existing TES systems. This necessitates advancements in TES systems to store heat at higher temperatures.

Despite the potential of integrating high-temperature TES with existing thermal generators, there remains a notable gap in research concerning this. The broader range of integration methods available due to the higher discharge temperatures requires further investigation. Addressing this knowledge gap will progress the creation of a more sustainable, efficient, and economically viable energy system. As such, this research has the potential to drive significant change in the electricity grid, developing a more flexible system, whilst utilising existing infrastructure and limiting integration costs.

2.2 Ultra High-Temperature Thermal Energy Storage

The second law of thermodynamics states that energy of low quality cannot be fully converted into high-quality energy. The quality of thermal energy is dependent on its temperature, with higher temperatures indicating higher energy quality. As such, lower-temperature thermal storage systems are unable to provide high-quality heat. This affects the value of the heat stored as lower-quality heat is more limited in its applications. Based on this, increasing the temperature of a thermal system is key to improving its efficiency, value and range of applications. This has led to the development of Ultra-High Temperature Thermal Energy Storage (UHTS) systems, which aim to enhance their value by operating at higher temperatures.

Figure 2.12 shows a diagram of a UHTS system, produced by Rondo Energy (2024), demonstrating how renewable energy is utilised to charge the store electrically by heating a storage medium to a high temperature. From here, the energy is extracted using a working fluid, which passes through the storage core and increases in temperature. This heated fluid is then utilised within an industrial process.

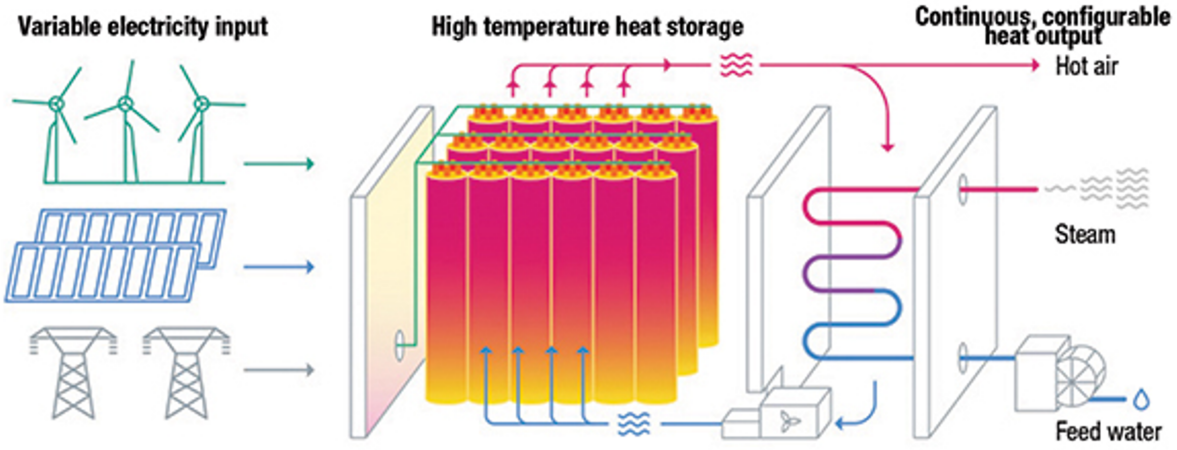


Figure 2.12: Diagram of a UHTS, with both charge and discharge systems (Rondo Energy, 2024).

2.2.1 Benefits

UHTS systems have garnered significant attention in recent years for their potential to revolutionise energy storage and retrieval processes, especially in the context of long-duration storage and both industrial and power generation integration. Designed to operate at temperatures exceeding 1,000 °C, they facilitate improved thermodynamic efficiency and energy density compared to conventional thermal storage technologies. Current systems are able to store energy on a weekly timescale.

Recent advancements have been led by the development of new materials and technologies. These advanced materials are capable of withstanding the temperatures found in UHTS systems, maintaining structural integrity and thermal efficiency. As such, these advanced materials are crucial in enhancing energy storage viability.

Advanced ceramics and graphite composites are also being explored due to their thermal stability and heat transfer characteristics at ultra-high temperatures. Some such materials demonstrate effective heat storage capacities upwards of 150 kWh/m^3 (Dincer and Rosen, 2010).

The efficiency of these systems is governed by the thermophysical properties of the storage media, including specific heat capacity, thermal conductivity, and latent heat of fusion.

The design of UHTS systems poses significant engineering challenges, particularly in terms of thermal insulation, material compatibility, and heat exchanger efficiency. Effective insulation is crucial to minimise thermal losses and maintain system efficiency. This necessitates the development of advanced insulation materials capable of withstanding extreme temperatures.

Additionally, given the corrosive nature of materials at high temperatures, the compatibility of storage materials with containment and heat exchange components is a critical consideration to mitigate the potential for thermal stress-induced material degradation (Zhang et al., 2016).

A key example of these limitations is seen during the extraction of heated air from a UHTS system. This presents practical challenges, primarily due to material limitations. The high temperatures within UHTS systems would cause failure in most conventional materials, such as metals and polymers, due to melting, oxidation, or structural degradation. Whilst specialised materials like ultra-high temperature ceramics (such as HfCN and HfC) have high melting points ($>$3000 °C), they are difficult to process and have a high cost (Wyatt et al., 2023). As such, ultra-high temperature ceramics are not widely used outside of specialised systems. Additionally, the system must be designed to manage thermal expansion and prevent heat loss, which could involve advanced insulation techniques and cooling systems. Another critical issue is the durability and reliability of seals and joints, as there are currently no materials which have suitable properties for these uses at such high temperatures Run and Huang (2023).

2.2.2 Current UHTS Systems

There are currently a few methods of storing high-quality heat. The Californa-based company Rondo Energy produces Heat Batteries, with a focus on the decarbonisation of industrial heat production (Rondo Energy, 2024). Their approach involves converting excess renewable electricity into high-grade heat for later use in industrial processes. This method is particularly beneficial for industries reliant on high temperatures, such as cement and glass manufacturing, which traditionally depend heavily on fossil fuels. The technology developed involves the heating of refractory bricks to temperatures up to 1,500 °C for energy storage, providing storage capacities of up to 300 MWh. The storage temperature of the system aligns it with the operational requirements of various industrial applications, making it a viable alternative to traditional energy sources and other storage methods like hydrogen, which may have lower efficiency rates. In 2023, Rondo Energy deployed a unit to lower carbon emissions in biofuel production.

Also based in California, Antora Energy's high-temperature storage technology involves heating blocks of solid carbon to temperatures above 1,800 °C, making it suitable for industries that demand high-temperature heat (Antora Energy, 2024). The modular nature of Antora's thermal batteries allows for scalability depending on the needs of the application, offering a significant advancement towards decarbonising heavy industries.

Similarly, Edinburgh-based Exergy3 has developed a novel form of ultra-high temperature thermal energy storage to decarbonise high-temperature industrial processes. Their technology, which also stores renewable electricity as 8 MWh of thermal energy at 1,200 °C, offers a scalable, cost-effective solution to harness excess renewable electricity during low-demand periods (Exergy3, 2024).

Each of these technologies integrates with renewable energy sources such as solar and wind power. Integration not only addresses the challenge of renewable intermittency but also opens new avenues for decarbonising industrial heat applications.

This thesis bases the UHTS system on that proposed by Robinson (2017), as outlined in Section 1. This technology is used because aluminium is an abundant and cost-effective storage

material, making it practical for large-scale applications. Its favourable physical properties enhance the efficiency of latent heat storage systems and enable a high operating temperature of 1,800 K, making it suitable for industrial processes and power generation. Additionally, as the technology is currently at a low TRL, there is greater availability of data as it is not restricted due to it being commercially sensitive. Focusing on this technology aligns with the global push towards grid-scale energy storage and promoting renewable energy sources.

2.2.3 Future of UHTS Systems

Looking forward, the advancement of UHTS technologies hinges on the development of novel materials with enhanced thermophysical properties; the optimisation of system designs for improved efficiency and durability; and the integration of UHTS with diverse energy generation and industrial processes. Research efforts are also focused on addressing the challenges associated with UHTS, including reducing material and operational costs and mitigating the environmental impact of high-temperature material extraction and processing.

A possibility for the future development of UHTS systems is the implementation of Regenerative Thermophotovoltaic (TPV) systems, which convert thermal energy into electrical power through photovoltaic cells, allowing the storage systems to directly output electricity efficiently. This combination could lead to improvements in energy conversion efficiency, leveraging the high energy density of UHTS and the direct electrical conversion capabilities of TPV systems. Future research in regenerative integration could lead to the development of more compact and efficient storage and conversion systems, allowing UHTS to generate power on demand, with significantly shorter response times and minimal conversion losses. As such, the intersection of TPV and UHTS technologies holds the potential to significantly advance the capabilities of renewable energy systems (Kelsall, 2023).

2.3 Heat Utilisation

The extraction of power from high-temperature thermal energy stores necessitates efficient and reliable systems capable of converting stored thermal energy into electricity. Among the most prominent and widely utilised systems which utilise high-grade heat are steam turbines, GTs and industrial boilers, each offering unique advantages and operational principles suited to different applications and energy sources.

2.3.1 Rankine Cycle

The Rankine cycle is a thermodynamic cycle used in power generation that commonly utilises steam to generate electricity. It has been extensively studied and optimised over the years. This cycle is widely used for power, with most combustion-based and nuclear power plants employing it. The process involves the conversion of thermal energy into mechanical energy, and then into electrical energy.

The combustion of solid fuels has been a mainstay of power generation for an extended period. Traditionally, coal is used as fuel though more recently, biomass and municipal waste are becoming more common. The boiler is an integral component of a thermal power plant

as it converts the chemical potential energy of fuel into thermal energy through combustion. This is then transferred to the working fluid, usually liquid water or steam, and used to drive a Rankine cycle. This is shown in Figure 2.13 below.

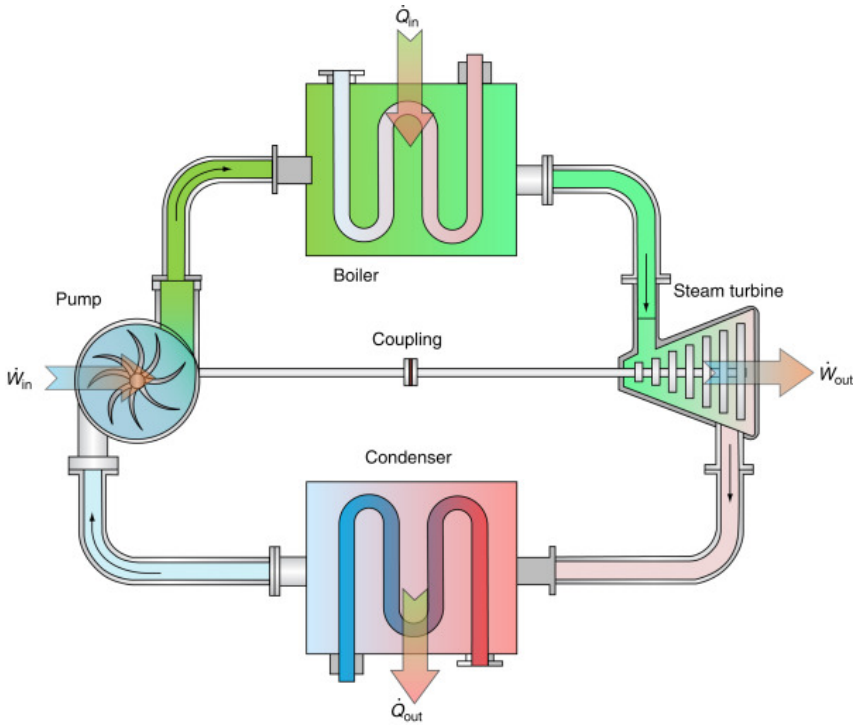


Figure 2.13: Schematic of Rankine Cycle (Dincer, 2018).

A typical boiler layout consists of a combustion region, a water-cooled furnace, a superheater, an economiser, and air preheaters. The combustion region is where the fuel is combusted, producing high-temperature gases. These gases exchange heat with the water-cooled furnace walls. Here heat is transferred to the boiler water through convection and radiation, which is heated to its boiling point, generating steam. The steam passes through the superheater, where it is further heated to higher temperatures and pressures.

From the boiler, a steam turbine is implemented to convert the thermal energy of the superheated steam into work. This is achieved through the expansion of the steam through a series of blades, converting thermal energy into rotational energy. The blades are arranged in stages, each consisting of a set of stationary blades called nozzles and a set of rotating blades. The nozzles convert the pressure energy of the steam into kinetic energy by accelerating the steam to a high velocity. The blades then convert this kinetic energy back into pressure energy by decelerating the steam as it passes through them, rotating and producing mechanical work in the process. The steam turbine is typically a multi-stage device, meaning that the steam passes through several stages of nozzles and blades, each optimised for the steam conditions it will encounter. The number of stages depends on the size of the turbine, and the pressure and temperature of the steam.

The efficiency of steam turbines is contingent upon various factors including inlet steam conditions, turbine design, and the number of stages employed. Advancements in materials science and aerodynamic design have significantly enhanced the efficiency of steam turbines,

enabling them to achieve thermal efficiencies upwards of 40 % in modern power plants (Horlock, 2003).

Once the steam has expanded through the turbine to produce work, it passes through the condenser. The condensation of steam releases energy based on its latent heat of vaporisation. This heat is transferred to the cooling water that flows through the condenser tubes. The condensed water is then sent back to the boiler, where the cycle is repeated. The heated cooling water is then discharged, often through cooling towers.

Further superheating of the steam is a critical advancement to the traditional Rankine cycle, entailing the further heating of steam to temperatures above its saturation point at a given pressure. This process elevates the cycle efficiency by extending the thermodynamic limit of the cycle, allowing for greater work output per unit mass of steam (Rogers and Mayhew, 1992). This also has the benefit of ensuring no moisture is able to condense within the turbines, mitigating the potential for turbine blade damage.

A further development since the inception of the Rankine cycles is the implementation of reheating. This involves the intermediate heating of expanded steam, typically in two or more stages, which allows for a closer approximation to isentropic expansion, thus minimising entropy generation and enhancing cycle efficiency (Kehlhofer, 1999).

Regeneration, leveraging feedwater heaters to preheat the boiler feedwater using extracted steam from various turbine stages, significantly optimises the Rankine cycle. By elevating the feedwater temperature before entering the boiler, the efficiency is improved through the reduction of irreversible losses associated with the heat addition process (Moran et al., 2018). This approach effectively increases the mean temperature at which heat is added to the cycle, improving the overall thermal efficiency.

The selection of working fluids also markedly influences the cycle's performance. Beyond traditional water/steam cycles, Organic Rankine Cycles (ORC) utilise organic fluids with lower boiling points and higher molecular weights, enabling the extraction of useful work from lower-temperature heat sources. ORCs have found applications in capturing waste heat from industrial processes, geothermal power generation, and solar thermal energy, showcasing the versatility of Rankine cycle adaptations in harnessing a wide array of heat sources (Quoilin et al., 2013).

Despite continuous advancements, challenges such as irreversibility and mechanical losses persist, which include friction in turbines and pumps, heat losses to the surroundings, and non-ideal fluid expansion and compression. These inefficiencies result in a discrepancy between theoretical and actual cycle efficiencies, underscoring the necessity for continued research into advanced materials and innovative system designs.

In addressing environmental concerns, particularly those associated with fossil fuel combustion, the exploration of renewable heat sources and the integration of carbon capture and storage technologies within Rankine cycle power plants are of paramount importance. This aligns with global initiatives aimed at reducing GHG emissions and transitioning towards more sustainable energy systems.

The Rankine cycles have been demonstrated as a suitable discharge method for TES systems. In 2019, Siemens Gamesa produced the ETES system which was capable of discharging 130 MWh_e via a steam turbine to generate 1.5 MW (Siemens Gamesa, 2019).

2.3.2 Brayton Cycle

The Brayton cycle is fundamental to modern gas turbine and jet propulsion technologies. It was named after George Brayton, who patented the first continuous-combustion internal combustion engine using this cycle in 1872. Since then, this technology has undergone continuous development, making it a crucial technology in the 21st century. The ideal cycle, often referred to as the Joule cycle, assumes perfect gas behaviour and adiabatic processes in both compression and expansion stages. In practice, however, the Brayton cycle deviates from this due to non-ideal gas behaviour, frictional losses, and irreversibilities in the combustion process. These factors necessitate optimisation strategies to enhance performance. A schematic of the Brayton Cycle is shown in Figure 2.14 below.

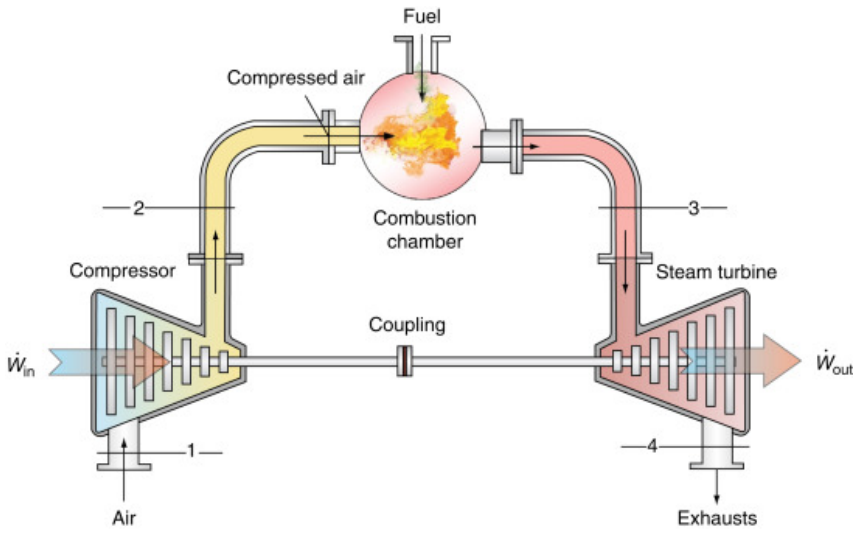


Figure 2.14: Schematic of Brayton Cycle (Dincer, 2018).

In power generation, Brayton cycle-based GTs provide the advantages of rapid start-up times and operational flexibility. This makes them ideal for peak load and emergency power supply applications. Combined cycle power plants, which integrate Brayton cycle GTs with Rankine cycle steam turbines, optimise overall system efficiency, with modern installations achieving thermal efficiencies exceeding 60 % (Inumaru et al., 2021).

In its simplest form, the Brayton cycle consists of four key processes. Isentropic compression is the initial step, responsible for raising the pressure of the working fluid (usually air). The compressor determines the pressure ratio of the cycle and thus affects the overall efficiency of the system. It can be either a centrifugal compressor or an axial compressor, depending on the design of the GT.

In large-scale GTs, axial compressors are often utilised as they're able to achieve large pressure ratios. These use a series of rotating and stationary blades to compress the air. The rotating blades are mounted on a rotor and are shaped like airfoils to accelerate the air, increasing its pressure. The stationary blades, also known as stators, are positioned between the rotating blades and are designed to redirect the airflow and provide additional compression.

The design of the compressor is critical to achieving high efficiency in the Brayton cycle. Advances in manufacturing techniques have led to the development of blade materials which

minimise the gap between the blade tip and the compressor wall, which minimises leaks. This creates a more efficient compressor, with higher pressure ratios and lower losses due to aerodynamic effects.

From the compressor, the pressurised working fluid flows to the combustion system. The primary function of these is to burn fuel, heat the working fluid and produce high-temperature and high-pressure gases that drive the turbine blades. Combustors must operate over a wide range of conditions. These include variability in fuel types, fuel-air ratios, inlet pressures, and temperatures. As a result, they must be designed to provide stable combustion across a range of operating conditions, while minimising emissions of pollutants such as NOx and CO.

The design of combustors is influenced by performance requirements, fuel properties, and environmental regulations. The most common types of combustors used in GTs are can-annular and annular. Can-annular combustors consist of a series of individual combustion chambers, arranged around the perimeter of the turbine. An example of these can be seen in Figure 2.15. The can-annular design is favoured in industrial GTs as it provides greater control, allowing systems to adapt based on fuel variations and the requirement for part-load operation.

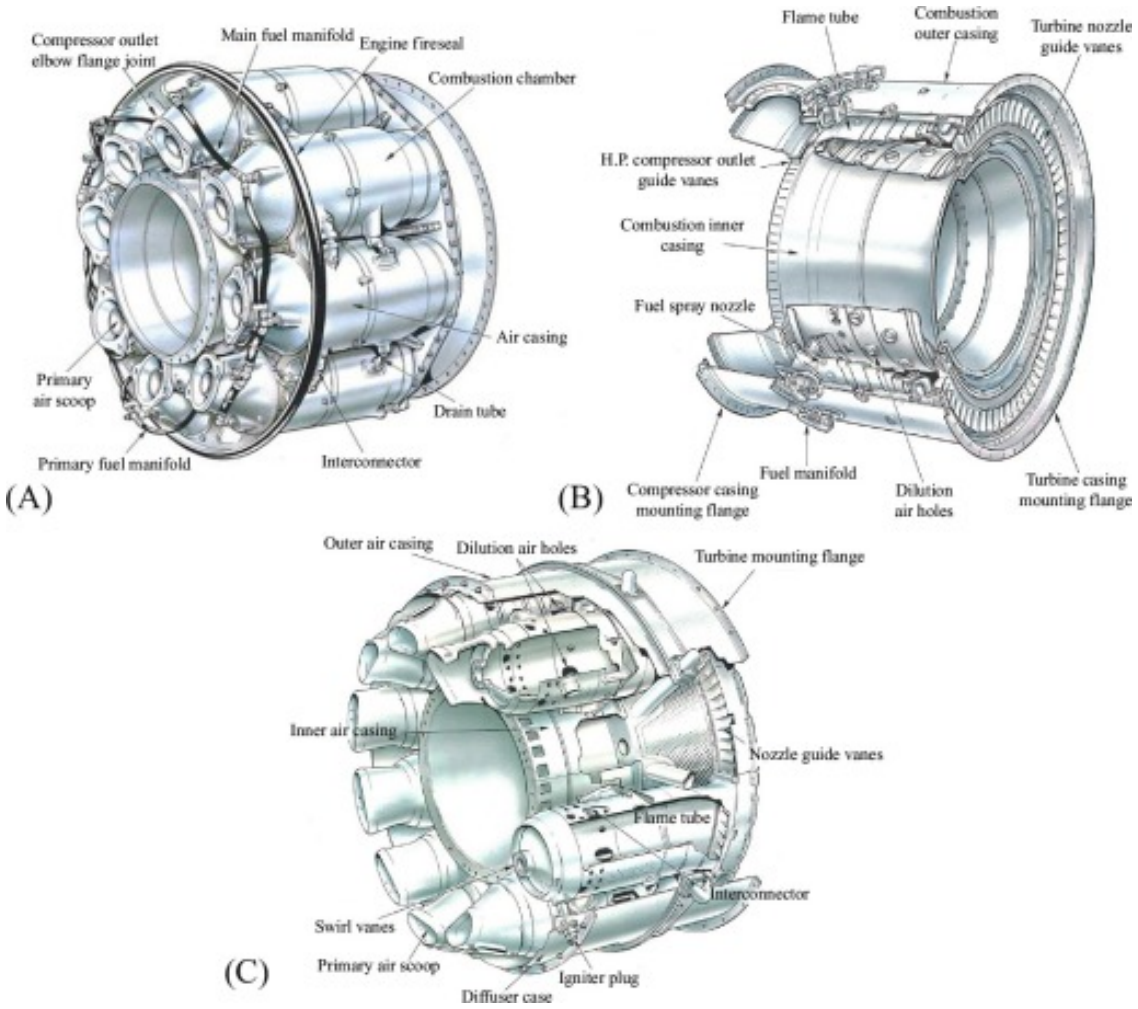


Figure 2.15: Gas turbine combustor designs: (A) can, (B) annular, and (C) can-annular (Noroozian and Asgharian, 2017).

The combustion process involves the mixing of fuel and air in the combustor, followed by ignition and combustion of the mixture. The fuel and air are typically mixed in a fuel injector, which then delivers the mixture to the combustion chamber. To improve the mixing process, air is introduced through a swirler or a perforated plate to increase flow turbulence. Once in the chamber, combustion is initiated by a spark or a pilot flame, which ignites the fuel-air mixture.

The performance of GT combustors is evaluated based on parameters including combustion efficiency, emissions, pressure drop, and temperature distribution. Combustion efficiency is a measure of the extent to which the fuel is burned in the combustor. The temperature distribution is critical for preventing hot spots to ensure the turbine blades are not damaged by excessive heat. Research in GT combustors is focused on improving their performance and reducing emissions of pollutants. This includes the development of new materials and coatings, improved fuel injectors, and advanced combustion technologies such as lean premixed combustion and staged combustion.

To extract the energy, a turbine is used, similar to that in a Rankine Cycle. However, there are variations due to the advanced properties of the flow. The turbine blades are typically made from high-strength alloys. They are designed to withstand the high temperatures and pressures encountered in the combustion process, as well as the effects of some combustion by-products, such as sulphur dioxide (SO_2) which can cause issues like hot corrosion due to the deposition of metal sulphates on blade or vane surfaces (Kosieniak et al., 2012). Additionally, to improve the efficiency of the turbine, several advanced turbine designs have been implemented, such as cooled blades, film cooling, and active clearance control. Cooled blades use advanced cooling technologies to prevent the blades from melting under the high temperatures encountered in the combustion process. In contrast, film cooling injects a cool, high-momentum gas into the boundary layer of the blades to protect them from the hot working fluid. Active clearance control uses sensors and actuators to maintain a small gap between the rotor and stator blades, which reduces fluid leakage and increases the efficiency of the turbine.

One consideration in Brayton cycle applications is the enhancement of thermal efficiency. Techniques such as intercooling, regeneration, and reheating have been employed to achieve this. Intercooling, implemented between compression stages, reduces the work input by cooling the working fluid, bringing the process closer to isothermal compression, and thereby improving overall efficiency. Regeneration capitalises on the waste heat from the turbine exhaust, preheating the compressed air before entering the combustion chamber, reducing fuel requirements and enhancing efficiency. Reheating involves multiple stages of expansion interspersed with reheating of the working fluid, allowing for higher turbine inlet temperatures and more isentropic expansion, further improving the cycle's efficiency (Boyce, 2011).

Despite their widespread adoption and inherent advantages, GTs face environmental challenges, primarily associated with GHG emissions from fossil fuel combustion. Similarly to the Rankine cycle, research focuses on integrating renewable energy sources, such as solar thermal and biomass, and exploring carbon capture and storage (CCS) technologies to mitigate environmental impacts. Additionally, the use of novel working fluids, such as supercritical carbon dioxide (sCO_2), offers potential for efficiency improvements and emissions reduction (Dostal et al., 2004).

Closed-cycle GTs represent an advancement in GT technology, offering enhanced performance compared to their open-cycle counterparts. In these, the working fluid is circulated

within a closed loop, eliminating direct contact between the combustion gases and the working fluid. As a result of this separation, more expensive materials with enhanced thermodynamic properties can be used, which can enhance cycle efficiency compared to an open-cycle system. This separation also allows for the use of optimal working fluids for the given conditions. Energy is added to the cycle by heating the recirculating working fluid using a heat exchanger and external heat generation. As such, the required thermal input can be provided by various high-temperature heat sources, including TES (Adefarati and Bansal, 2019). However, as the working fluid is recycled, these systems cannot be used in conjunction with a Rankine Cycle to produce a combined cycle system.

2.3.3 Industrial Boilers

In some industrial situations, a user may want an output in a form other than electricity. In such cases, steam is often generated as a working fluid through the use of NG. These systems must also be decarbonised to reach net-zero emissions goals. Industrial boilers (IB) are pivotal in generating steam or hot water for applications across multiple sectors, including manufacturing, power generation, and heating. These systems function by converting energy from fuels into heat, which is then transferred to water, thereby producing steam or hot water. The design, efficiency and fuel type of IBs have evolved based on technological advancements and fuel availability.

IBs can be classified into several types based on their design and operating principles. These include fire-tube, water-tube, electric, and condensing boilers.

Fire-tube boilers, where hot gas flows through tubes surrounded by water, are generally compact and are therefore used in smaller operations. In contrast, water-tube boilers circulate water inside tubes that are heated externally by hot gases, a configuration that enables efficient heat transfer and rapid steam generation (Deshmukh et al., 2022). These are suitable for high-pressure and temperature applications and large-scale industrial operations due to their high efficiency and steam production capacity. Current innovations aim to mitigate the challenges posed by corrosive flue gases and further optimise performance for critical industrial processes.

Electric boilers utilise electrical energy to generate steam, removing the need for emissions control and increasing overall energy efficiency. However, high capital costs and grid capacity constraints currently limit effective implementation (Zuberi et al., 2022).

Condensing boilers recover latent heat from exhaust gases. This provides an improvement in efficiency and reduces operational costs. Recovery schemes such as heat pumps have been investigated for their potential to boost power generation and efficiency (Saari et al., 2021). Stirling engines also represent a promising approach to improving the efficiency of biomass-based boilers, enabling the use of low-grade heat sources for power generation (Rahman et al., 2022).

The choice of fuel in IBs significantly impacts their efficiency, operational cost, and environmental footprint. Recent advancements allow for more flexible fuel options, including NG, biomass, and various fuel blends, alongside traditional fuels like oil and coal. The introduction of multi-fuel boilers has increased operational flexibility, allowing for the selection of fuels based on availability and cost. For instance, the utilisation of Biomass Coal Fuel-Sludge (BCFS) briquettes demonstrates a potential reduction in coal use by 16 % (Nor Arifin et al., 2023). Modifications to conventional biomass burners for multi-fuel input have resulted in

substantial improvements in thermal efficiency for various biomass fuels, underscoring the potential for technological advancements to enhance performance (Piawanich et al., 2018).

The choice of combustion technology also plays a crucial role in optimising fuel efficiency. Technologies such as Fluidised Bed Combustion (FBC) have been developed to enhance combustion efficiency, whilst reducing emissions. FBC allows for the efficient use of low-grade fuels in a granular bed, typically sand or limestone, which is fluidised by the flow of combustion air through the bed. This reduces emissions of pollutants such as NOx and SO_2 due to lower combustion temperatures, in addition to the presence of limestone in the bed, which can absorb sulphur pollutants (Pan et al., 2022).

As a large proportion of IBs still rely on standard combustion, they are significant sources of air pollutants, including SO_2, NOx, PM, and CO. Stricter environmental regulations have necessitated the adoption of emissions control technologies (Moreda-Piñeiro et al., 2021). These include Selective Catalytic Reduction (SCR) for NOx reduction, Flue Gas Desulphurisation (FGD) for SO_2 control, and Electrostatic Precipitators (ESPs) and Fabric Filters for PM removal.

One significant issue faced by IBs is the formation of scale on boiler surfaces due to impurities in water, which can significantly reduce heat transfer efficiency. This can in turn lead to overheating, decreased boiler capacity, and premature failure. Additionally, component corrosion can be caused by a reaction with water and its contaminants, further compromising the integrity of the boiler system. Addressing these issues requires a comprehensive approach such as the use of water treatment technologies, the adoption of corrosion-resistant materials, and regular maintenance to ensure optimal performance and longevity. Despite these issues, IBs remain an integral part of the energy infrastructure.

2.3.4 Integration Challenges

As previously discussed, the primary advantage of integrating UHTS into existing thermal systems is the significant reduction in CAPEX costs when compared to new, stand-alone systems. However, integration with technologies such as those outlined in the previous sections presents a promising pathway to enhancing energy systems, this integration is not without its challenges.

One of the primary integration challenges is the compatibility of UHTS systems with existing power generation infrastructures. The necessity for system modifications to accommodate high-temperature storage units often entails significant changes to the plant layout, heat exchangers, and control systems, which can be both costly and technically demanding. Datas (2022); Huili et al. (2021) present the technical complexities involved in this integration process.

The operation of UHTS systems at high temperatures raises significant concerns regarding material durability and thermal stresses. Challenges such as erosion, corrosion, and thermal fatigue of boiler and storage components are exacerbated at the elevated temperatures associated with UHTS systems. Crespi et al. (2023); Dobson et al. (2023) discuss the material selection and design considerations crucial for withstanding the operating conditions.

Current research is being conducted into the integration of CSP into GTs, in order to displace fuel. This research outlines several challenges, as highlighted in the paper by Alzaili and Sayma (2016). One of the primary technical hurdles is the variability of solar input, which necessitates

that these turbines operate effectively over a wide range of conditions. Additionally, there are technical issues related to turbomachinery design, rotor dynamics, control systems, and the need for efficient thermal storage solutions to ensure consistent power output. The hybridisation of GTs with other fuels or thermal storage mechanisms is suggested as a potential solution to achieve a dispatchable system. However, this approach introduces further complexities in combustor design and system controllability.

Whilst the integration of a UHTS system into a thermal generator is cheaper than new, stand-alone systems, the economic feasibility still presents a significant challenge due to the capital costs and uncertain return on investment. Shamsi et al. (2023); Villada et al. (2022) explore the techno-economic aspects of UHTS integration, including financial barriers and the need for innovative economic models to improve cost-effectiveness.

Work by Cabeza et al. (2022); Kunwer et al. (2022) outlines the importance of control systems for these technologies to be successfully integrated and optimised. Advanced control strategies are required to effectively manage the charging and discharging cycles of UHTS systems. The operational complexities involved in maintaining system efficiency and reliability while ensuring operational flexibility are considerable challenges.

The integration of UHTS systems is significantly impacted by existing policy and regulatory frameworks. Mudi et al. (2021); Al Naimi et al. (2020) outline the need for more supportive policies and regulatory frameworks that recognise the benefits of UHTS systems in supporting the transition to renewable energy sources.

The integration of UHTS systems into existing infrastructure offers significant potential benefits but is accompanied by numerous technical, economic and regulator challenges, and requires efforts from a range of sectors.

2.4 Integration Economics

The integration of UHTS systems into GTs, HRSGs, and IBs presents a promising method for enhancing the efficiency and environmental sustainability of pre-existing systems. As such, the economic viability should also be considered.

The cost of implementing UHTS systems is influenced by factors such as storage material costs, system size, and integration complexity. For instance, molten salt UHTS systems, which can operate at temperatures exceeding 550 °C, have low costs ranging from \$0.05 - \$0.1/kWh of capacity, with the potential for significant reductions as materials and technologies mature (Kuravi et al., 2013).

A notable case of the successful integration of UHTS in power generation is the Solar Tres Power Tower in Spain. This system also utilises a molten salt storage system to provide continuous power generation from CSP. The integration has demonstrated a reduction in Levelised Cost of Electricity (LCOE) of up to 15 % compared to stand-alone CSP plants. This highlights the economic benefits of UHTS in enhancing the dispatchability of the plant and reducing reliance on fossil fuels (Gil et al., 2010).

However, despite the promising potential of UHTS integration, economic challenges persist. The high upfront capital costs associated with UHTS systems, alongside the complexity of retrofitting existing facilities, pose barriers to widespread adoption. Additionally, economic

viability is closely linked to factors such as energy market dynamics, fuel prices, and regulatory incentives for renewable energy and system efficiency improvements.

While theoretical models have demonstrated the potential efficiency gains from UHTS integration, empirical data is scarce on system performance under real-world operating conditions, due to the commercial sensitivity of such studies. Access to extended durational studies that monitor UHTS-integrated systems over time, including the reporting of system efficiency, reliability, and degradation rates, are needed to validate theoretical models and refine cost-benefit analyses (Gil et al., 2010).

An example of this is the study by Ameri et al. (2005). This investigates the enhancement of GT performance through Thermal Energy Storage for Turbine Inlet Air-Cooling (TESTIAC). The research evaluates the economic and performance impacts of employing chilled water and ice storage systems at the Kish power plant to mitigate the efficiency losses of GTs operating at high ambient temperatures. The analysis shows a capacity enhancement of 13.6 % and an internal rate of return (IRR) of 27.3 %. Model outputs demonstrate the feasibility of TESTIAC systems in improving GT output during peak demand periods. However, the study is limited to theoretical evaluations, highlighting the need for real-world data to validate these findings. Furthermore, this economic analysis focuses on enhancing GT efficiency through TESTIAC using cooling from low-temperature storage. This research focuses on a targeted application of TES to improve GT performance and its IRR, rather than the broader effects of the energy storage in power networks.

The study by Arteaga and Zareipour (2019) introduces an optimisation model for battery storage systems operating in electricity markets, considering them as price-takers in the energy market and price-makers in ancillary services markets. This model aims to maximise profit while accounting for market uncertainties. The use of both price-taker and price-maker approaches for different market segments offers a realistic revenue estimation. However, this model specifically addresses the unique capabilities and market interactions of battery storage. This makes its use cases relevant for electrical energy storage, rather than thermal as it does not account for the same storage complexities.

Legrand et al. (2022) studied the economic viability of integrating Liquid Air Energy Storage (LAES) with photovoltaic (PV) systems in Spain, with a focus on arbitrage optimisation. It models a 100 MW PV plant combined with two LAES configurations (adiabatic and diabatic) to take advantage of electricity price fluctuations. The analysis reveals potential benefits, particularly with diabatic LAES enhanced by NG, however this results in an increase in CO_2 emissions. While the paper provides a techno-economic assessment which highlights the potential for LAES to enhance renewable energy usage and grid stability, it underscores the need for further research on cost reduction and emission mitigation strategies for broader adoption.

The paper by Hamilton and Neises (2023) presents a mixed-integer linear program (MILP) alongside the System Advisor Model (SAM) to maximise electricity sales revenue against varying electricity prices. This techno-economic model optimises Electric Thermal Energy Storage (ETES) dispatch, achieving a 20 % revenue improvement. It underscores the significance of strategic dispatch in maximising ETES system contributions to grid storage. However, the complexity of the MILP approach poses challenges for users without a strong background in optimisation techniques. This limits the accessibility of the model to a broader audience.

Additionally, the paper primarily focuses on simulated scenarios. This again highlights the need for case studies to validate the model's assumptions and its adaptability to real market conditions. It should be noted that the paper fails to present a sensitivity analysis to outline the effects of a changing data source, which could demonstrate the wider usability of the model.

The study by Soto et al. (2022) also investigates ETES optimisation by examining the integration of molten salt TES with a nuclear reactor for flexible energy dispatch. The research finds that such integration can improve power purchase agreement prices by up to 10 % under California energy market conditions. However, once more, a focus on theoretical market conditions rather than real-world applications limits their direct applicability. Further work would also be required to study the potential environmental impacts of using molten salt systems with nuclear reactors.

An overarching theme from these studies is the lack of research undertaken that focuses specifically on UHTS integration. UHTS systems are able to provide heat at a much higher grade than anything explored in these studies, enhancing the range of deployment options and allowing for alternative uses such as direct boosts in output, rather than an efficiency increase.

Furthermore, there is a gap in research on the policy implications of deploying UHTS systems, especially in regions with stringent environmental regulations and energy market structures. Studies that analyse the policy incentives, regulatory barriers, and market mechanisms that could support the adoption of UHTS are needed to provide a clear pathway for its integration into energy systems.

The economics of integration are significantly influenced by energy market dynamics, including electricity prices, demand response incentives, and carbon pricing mechanisms. Research is needed to understand how these market factors, combined with the aforementioned policies and incentives impact the financial viability of UHTS systems. Dynamic financial models that can adapt to changing market conditions and policy landscapes are crucial for this analysis (Budny et al., 2013). Addressing these research gaps requires a multidisciplinary approach, accounting for knowledge of thermal engineering, economic modelling, environmental science, and policy development.

The ongoing research and development in advanced materials suitable for UHTS, system designs, and integration strategies are vital to realise the economic potential of UHTS integration in GTs, HRSGs, and IBs.

2.5 Aims and Objectives

The main research objectives of this thesis in this context are to:

- Examine the operational requirements for flexible operation of power stations in the future under hybrid operation using stored energy;
- Investigate the modifications required to discharge a UHTS system through thermal generators to produce electricity;
- Understand the consequences this has in terms of emissions from these generation sites and how this may allow them to operate in the future;

- Communicate the potential of the UHTS system to enable increased penetration of renewable generation;
- Identify relevant bottlenecks to a hybrid operation based upon physical and chemical constraints;
- Inform the discussion about the strategic development of infrastructure to utilise existing infrastructure and outline potential future operating problems as a consequence of the changing requirements and operating regimes of power stations and;
- Investigate the economic and environmental impacts of UHTS on various systems.

Chapter 3

Rankine Cycle Integration

3.1 Rankine Integration Overview

This chapter aims to explore the integration of UHTS into the Rankine Cycle, with a focus on enhancing industrial decarbonisation. By replacing conventional heat sources with renewable energy, the chapter seeks to demonstrate how UHTS can be effectively incorporated into existing power generation systems. It introduces an examination of the technical and operational implications of UHTS integration.

To achieve these goals, CFD is employed to model and optimise the flow conditions within a HRSG. The CFD analysis allows for the understanding of the impact of different retrofit strategies, including supplementary and full conversion systems, on the efficiency and sustainability of power generation. By examining the effects of inlet geometry, angle, and velocity on flow characteristics, the chapter identifies optimal retrofit designs that enhance thermal efficiency while maintaining system integrity. The detailed simulations provide insights into the thermal and fluid dynamic behaviour of HRSGs under various operational scenarios, enabling the evaluation of the feasibility of UHTS integration.

Furthermore, the chapter underscores the importance of bespoke retrofit strategies tailored to specific system objectives, whether for incremental efficiency gains or comprehensive system transformation. The findings highlight the potential for significant improvements in thermal efficiency and decarbonisation through the strategic integration of UHTS.

3.2 Introduction

The combustion of fuels to raise steam is a fundamental concept of power generation. This is based on the development of steam engines during the Industrial Revolution, designed to remove water from flooded mines. Whilst historically, steam was produced through the use of fossil fuels such as coal, oil, and natural gas, more recently fuels such as biomass and municipal waste are becoming increasingly commonplace. However, a thermal store may also displace the fuel required to drive a Rankine Cycle. A simple approach to incorporating renewably sourced heat into Rankine Cycles involves the substitution of the conventional heat generation unit with a renewable energy source, allowing for the system to decarbonise.

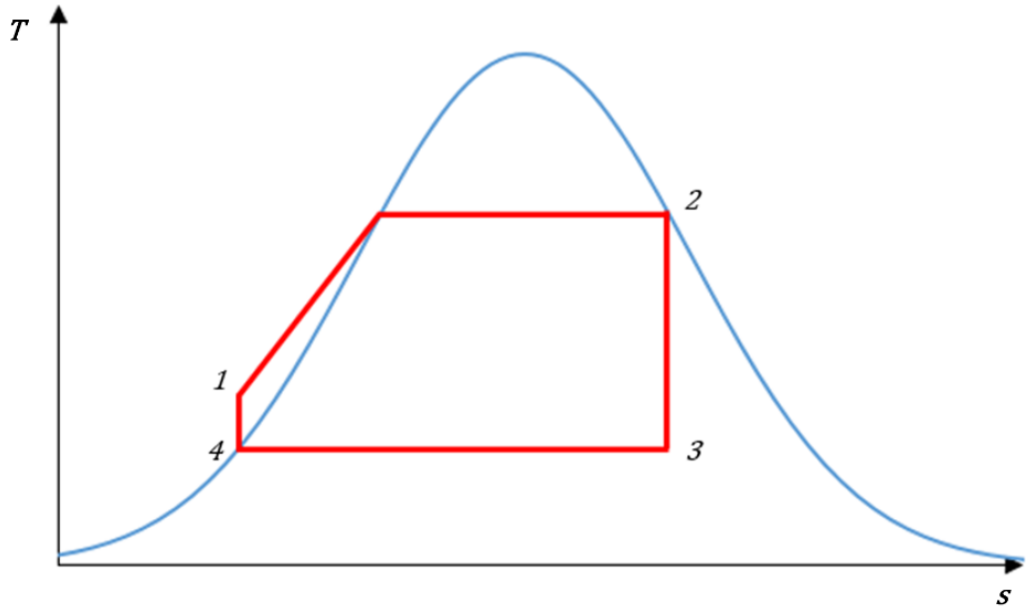


Figure 3.1: T-s diagram of ideal Rankine Cycle.

Figure 3.1 visually represents the changes in temperature and enthalpy throughout the Rankine Cycle through the use of a Temperature-Enthalpy (T-s) diagram. Enthalpy is a key concept in thermodynamics and represents the total heat content of a system. A basic Rankine Cycle transfers thermal energy to water to produce steam at the required energy state (1-2). This steam is then expanded through a turbine to produce mechanical work which drives an electricity generator (2-3). The low-energy steam is then condensed to return to its liquid state (3-4). The water may then be passed through a pump, ready to begin the cycle again (4-1).

While steam remains the predominant working fluid in such systems, the exploration of alternative mixtures, such as ammonia-water in the Kalina Cycle, offers potential efficiency enhancements. These fluids are used as the two have similar molecular weights, therefore, an ammonia-water cycle may function within an existing steam turbine with only slight modifications (Jonsson, 2003). Comparatively, the Kalina Cycle, utilising an ammonia-water mixture, shows a 5-10 % increase in thermal efficiency over the traditional Rankine Cycle, due to its ability to minimise temperature differences during heat exchange (Kalina et al., 1987; Nasruddin et al., 2018).

While the Kalina Cycle offers improved efficiency, the selection of ammonia-water mixtures necessitates careful consideration of environmental and operational factors, such as toxicity and system complexity, to ensure holistic sustainability and feasibility of the cycle. Additionally, there are concerns regarding the corrosive behaviour of these systems due to the nitridation effect, though they may be stabilised through the use of suitable additives.

Steam turbines are an extremely well-developed technology. Over a century of engineering work has rendered them reliable and efficient through continuous optimisation (Dellasala et al., 2018). Due to the maturity of the technology, they have been tailored to a range of applications, providing maximum electrical outputs from 15 kW to 1600 MW (Paulides et al., 2015; Siemens, 2018; Tanuma, 2017). Contemporary advancements in steam turbine

technology, particularly in design and material science, have significantly elevated thermal efficiencies. For example, innovations such as the development of ultra-supercritical turbines, which operate at conditions exceeding the critical point of water (22.12 MPa and 647.14 K), have further driven an increase in operational efficiency. Rankine cycles which utilise this have been seen to produce steam plant thermal efficiencies approaching 50 % (Kumar and Kumar, 2018), making them competitive for grid-scale generation. These systems use steam conditions up to 35 MPa and 700 °C (Pringle et al., 2023; Gianfrancesco, 2017). Specific superalloys, such as Inconel and Haynes alloys, have been instrumental in these advancements, offering enhanced resistance to creep, thermal fatigue and corrosion. These are pivotal properties for the operation of ultra-supercritical turbines.

However, the steam must be generated to a quality that a given turbine can best utilise to achieve these efficiencies. Steam quality refers to the proportion of vapour in a steam and water mixture, indicating the amount of vapour present relative to the total mass of the mixture. A higher quality signifies less moisture and a greater proportion of vapour, essential for maximising turbine efficiency and the plant's energy conversion effectiveness.

In existing large-scale plants, there are multiple reheat and turbine processes within the cycle to maximise the efficiency of the process. A basic process flow diagram is given below in Figure 3.2 to demonstrate how a multi-stage system may be used to maximise the energy that a steam turbine can extract and convert to electricity.

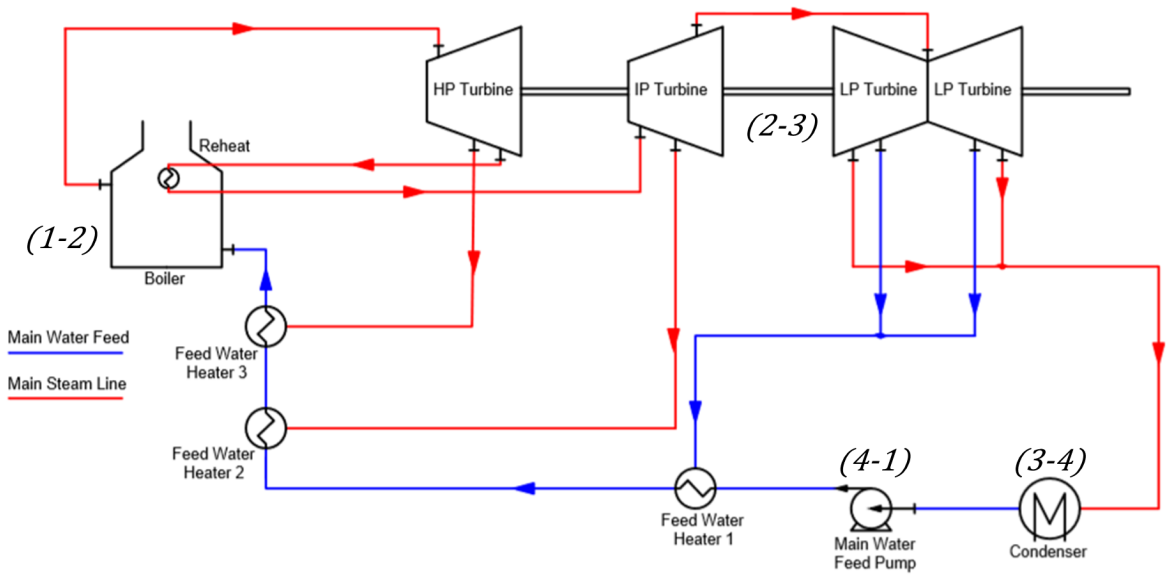


Figure 3.2: Rankine Cycle with basic reheat integration.

Without this optimisation, the system cannot extract as much energy from the steam. Consequently, smaller-scale systems with fewer turbines are inherently less efficient, extracting as little as 15 % of the energy input (Paulides et al., 2015). The relationship between power output and efficiency is presented in Figure 3.3.

Systems with lower efficiencies are often used for cogeneration, also known as combined heat and power (CHP). This is an efficient and reliable approach to generating both electricity and

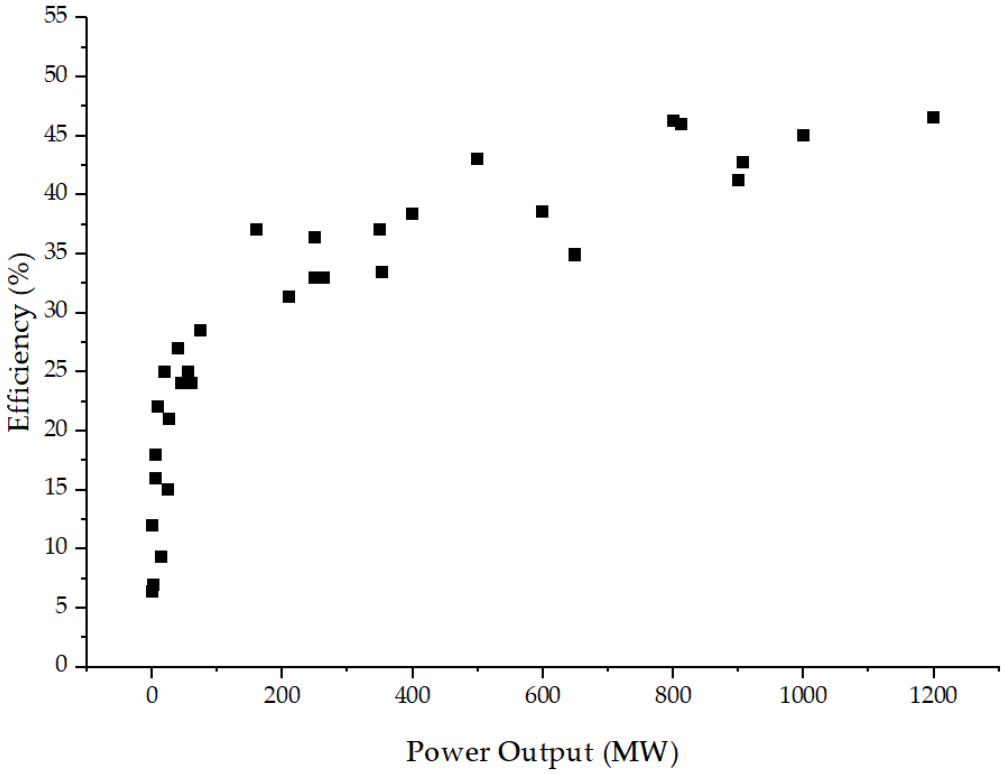


Figure 3.3: Efficiency of steam-powered generators against maximum electrical output (Datas et al., 2016).

thermal energy from a single fuel source. By simultaneously producing power and useful thermal energy, cogeneration systems can achieve significantly higher efficiencies than conventional power generation, where excess heat is often wasted. This process not only optimises the energy utilisation from the fuel but also reduces energy costs. Cogeneration is versatile and can be implemented in a wide range of settings, such as industrial systems, commercial buildings, and localised district heating systems. The use of cogeneration in energy systems supports the transition towards more sustainable energy infrastructures, aligning with efforts to reduce carbon emissions and enhance energy security.

As technologies based on the Rankine cycle continue to develop to allow for increased temperatures, there is an increased opportunity for the implementation of UHTS into steam cycles and combined cycles. Currently, the key factor limiting an increase in steam temperatures, pivotal for efficiency gains, is the thermal resilience of construction materials. For safe operation, clearance must be maintained between the rotating and static components within the turbine to ensure that the two bodies do not contact each other at any operating condition (Nakamura et al., 2010). With the materials currently available, this is not possible whilst utilising peak steam conditions due to thermal expansion at sub-optimal environments such as those during start-up. Furthermore, to meet current rules of thumb for steam generation equipment, materials must be developed to provide a rupture life of 100,000 hours for superheaters operating at base load conditions with advanced steam conditions (Starr, 2014). If these material issues are overcome, it would allow for increased steam temperatures and pressures,

providing increased system outputs and efficiencies. Current innovation looks to push towards steam temperatures greater than 700 °C and pressures above 300 bar (Ohji and Haraguchi, 2017). As such, methods for adapting high-quality heat for integration into Rankine cycles are required. With the continuous evolution of Rankine Cycle technologies and the pressing need for renewable energy integration, the exploration of stored heat integration presents a promising avenue.

3.2.1 Stored Heat Integration

The integration of renewably sourced heat into Rankine Cycles entails the replacement of conventional heat generation with a renewable energy source. This approach aligns with the broader transition towards sustainable energy systems, using renewable resources to reduce dependence on fossil fuels and mitigate environmental impacts. In this context, the conventional boiler or combustion system is replaced, or supplemented with, a renewable heat source that provides the necessary thermal energy to generate steam. This steam, in turn, drives the turbine to produce electricity, following the standard Rankine Cycle process. The integration of renewable heat sources into Rankine Cycles not only enhances the sustainability of power generation but also introduces opportunities to enhance thermal efficiency and operational flexibility. However, this integration necessitates innovative solutions to accommodate input from a UHTS, without being detrimental to the efficiency and reliability of the power generation process. As such, a primary challenge is the method through which the output of a UHTS system is integrated into the Rankine cycle.

Solid-Liquid Heat Exchange

Among the methods aligning closely with existing systems is the direct integration of heat from solid bodies into the Rankine Cycle. Here, the heat may be transferred directly to a water stream to raise steam. This method of generating steam directly provides a higher efficiency as there are fewer transfer-related losses due to the requirement of only a single transfer step.

In this configuration, the renewable heat effectively replaces the waterwall in a standard steam-powered generation site.

In a standard boiler, waterwalls line the surface of the boiler with liquid water entering. Within the waterwall, liquid water transitions to saturated steam due to the transfer of heat from the combustion region. Appropriate design is essential for optimising this phase change, ensuring efficient heat transfer, and enhancing overall power plant performance.

The waterwall tubes are designed for radiant and convective heat transfer, allowing a complete system to maximise overall heat transfer efficiency. Design elements such as spiral or finned tubes further increase efficiency. The effectiveness of waterwalls is a key component to ensure peak operation in boilers.

Waterwalls consist of banks of tubes which line the inside of the boiler. They are made of materials which are resistant to high temperatures, such as high-quality steels or high-temperature alloys.

However, if this design were replicated within a UHTS system, this would require high-pressure steam pipes to be passed through the thermal store. Nickel-based alloys such as Inconel

are used due to their ability to withstand the thermal stresses and corrosive environments that may be present in such systems, though these can typically only withstand temperatures up to around 750 °C (Kościelniak et al., 2021). Whilst there are systems in development to utilise this concept (Johnson and Fiss, 2023), there are major limitations with this technology such as low thermal conductivity of the materials that offer high strength at elevated temperatures, limiting the efficiency of heat transfer. Additionally, the expansion of steam within the pipes causes mechanical stresses, necessitating the incorporation of mechanisms such as expansion joints to prevent damage to the system. Due to this, such a system would not be feasible with currently available materials.

Liquid-Liquid Heat Exchange

Employing a liquid-liquid heat exchanger enables the introduction of high-quality heat into the Rankine Cycle, leveraging fluids like molten salts or metals for efficient heat transfer.

Molten salt steam generators are used in Concentrated Solar Power (CSP) sites and nuclear reactors to raise steam from a high-temperature heat source (Cui et al., 2021). CSP systems commonly use 'Solar Salt', which can operate at temperatures up to approximately 600 °C before it experiences thermal decomposition (Peng et al., 2017). Nuclear systems tend to use FLiBe or FLiNaK, which are, respectively, a binary salt composed of lithium fluoride (LiF) and beryllium fluoride (BeF_2) and a ternary salt mixture composed of three fluoride salts: lithium fluoride (LiF), sodium fluoride (NaF), and potassium fluoride (KF). These molten salts have a maximum operating temperature of approximately 1,287 °C and 1,570 °C, respectively (An et al., 2017; Romatoski and Hu, 2019), though experimental data indicates that a greater fluid bulk temperature results in an increased corrosion rate (Manohar S. Sohal et al., 2010).

Molten metals such as sodium or tin may be utilised similarly. Systems that implement metal as the primary coolant have advantages over those using molten salts as they can extract heat more rapidly and will not degrade at higher temperatures.

Both molten salts and metals are beneficial as they have good thermal stabilities and boast large heat storage capacities as well as high thermal conductivities, enhancing the system heat transfer coefficient. This is particularly so with molten metals.

However, it is vital to not overlook the drawbacks of these systems. Due to the nature of the heat transfer fluids being used, systems require constant energy input to continuously heat them. Without this, they may freeze within the pipes, which could result in a system outage (Bonanos et al., 2019).

3.3 Integrating UHTS into Rankine Cycles

The integration of UHTS systems with Rankine cycles, particularly in heating the working fluid, introduces specific challenges and necessitates innovative solutions. For instance, the development of the Reflux Heat Transfer Storage (RHTS) concept presented by Adinberg et al. (2010) raises high-temperature superheated steam, demonstrating how TES can effectively be used to raise steam to drive a turbine. The RHTS concept uses an intermediate HTF to store heat through a reflux process. The system includes a PCM (often a zinc-tin alloy) storage unit with external discharge and charge heat exchangers. During charging, the HTF vaporises

and transfers heat to the PCM, while during discharging, the hot PCM causes the HTF to evaporate and transfer energy to the working fluid (Liu et al., 2012). This results in increased flexibility and efficiency. The system is designed to produce high-temperature superheated steam, making it suitable for applications in solar thermal power plants. However, the storage method in this system poses challenges regarding efficient heat transfer when integrating into more efficient steam generation technologies.

As for the UHTS system, an intermediary step is required to discharge the UHTS via the Rankine Cycle as the system discharges using air. As such, the thermal energy must be transferred from the UHTS outlet air to a heat transfer fluid suitable for use in a steam turbine.

The primary method for integrating high-quality stored heat into a Rankine cycle is to raise steam by implementing a heat recovery steam generator (HRSG). HRSGs play a central role in thermal power plants, extracting heat from high-temperature gas streams to generate high-quality superheated steam, which is used to generate electricity. Due to the high temperatures associated with UHTS, these systems are able to utilise a HRSG (Chen et al., 2023).

HRSGs play a crucial role in CCPPs, raising steam to supplement the GTs Brayton Cycle with a Rankine Cycle. This improves the overall efficiency by utilising waste heat from the GT exhaust gas to raise steam to drive a series of steam turbines. As such, the efficient integration of an HRSG is essential for optimising the output of the plant.

3.3.1 Heat Recovery Steam Generators

HRSGs are integral components in modern power generation, particularly within combined cycle power plants. These systems capture waste heat from a gas flow and convert it into steam, which can then be used to drive a steam turbine for additional electricity generation or for various industrial processes. HRSGs typically consist of three main sections: the economiser, evaporator, and superheater, each playing a crucial role in maximising thermal efficiency.

HRSGs, functioning as gas-liquid heat exchangers, play a pivotal role in facilitating the phase change necessary for steam generation, adhering to a design that optimises thermal energy recovery. Hot gases drive up the temperature and pressure of a working fluid, usually water. This is used to produce superheated steam at the required energy level. A conventional HRSG comprises three major sections: the economiser; the evaporator; and the superheater (Stultz and Kitto, 2005). The incoming flow characteristics determine the sizing and configuration of these components, and the configuration is often unique for a given power plant.

Firstly, an economiser pre-heats and raises the temperature of the working fluid to near its saturation temperature (Ahmed et al., 2018). Subsequently, the fluid passes into an evaporator to induce a phase change, though the energy input here is limited to that required to boil the liquid. As such, there is no increase in temperature. Finally, the now vaporised working fluid enters the superheater to further increase the temperature of the vapour beyond its saturation temperature to meet the required conditions (Hennessey, 2017). A steam drum is used to ensure the quality of the steam that is passed into the superheater section. This is done to prevent condensation within the turbine, as the formation of liquid droplets reduces efficiency and can damage the blades. A simplified diagram of this process is presented in Figure 3.4. The process is achieved through the use of tube banks, which carry the working fluid, in conjunction with an array of heating surface components and steam drums to maximise the recovery of

thermal energy from an external flow of hot gases.

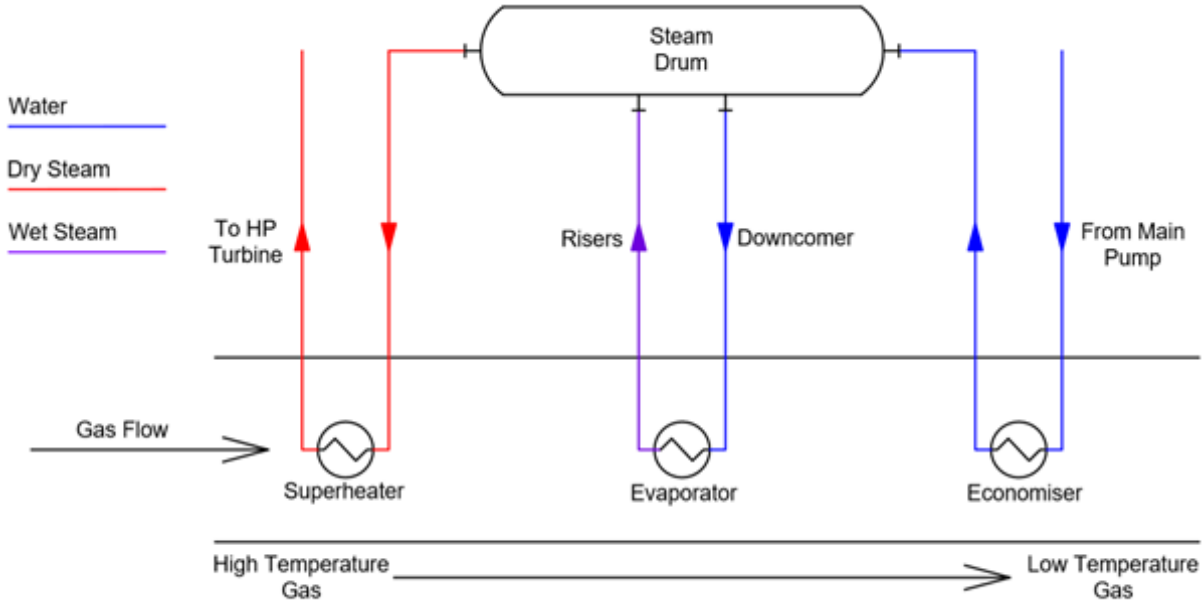


Figure 3.4: Simplified HRSG diagram.

In the most common HRSG, a horizontal drum design, the high-temperature gas flows horizontally through the system. Water is passed through vertical evaporator tubes to raise steam, utilising natural circulation. Vertical drum designs are also utilised as they have a smaller geographical footprint. However, as they operate with the hot gases moving vertically and the working fluid horizontally, they lose the advantage of natural circulation (Polonsky et al., 2019). To improve the economic feasibility of the system, a triple-pressure HRSG has been designed to minimise heat wastage. These produce high-pressure (HP) steam at temperatures around 650 °C and pressures of up to 20 MPa, whilst also using a reheating cycle which produces intermediate-pressure (IP) and low-pressure (LP) steam. This allows for efficient integration into a generation-scale steam turbine (Rackley, 2017).

3.3.2 HRSG Integration

To integrate the UHTS with the HRSG, the heated air may be introduced to supplement, displace or replace the inlet flow. In the case of a combined cycle system, this would involve introducing the heated air between the GTs outlet and the HRSG's inlet. Thermal storage systems with lower storage temperatures would be unable to provide air with heat of a high enough quality, leading to a reduction in the exhaust gas temperature. Without this limitation, a UHTS could be used to increase internal temperatures and flow rates. This can then increase the volume of steam produced, boosting the potential for energy generation from the steam side. Integration of a UHTS system in this manner would additionally increase the flexibility and efficiency of the CCPP.

The process is similar to that seen in supplementary firing, where additional fuel is combusted at the inlet duct to the HRSG in supplementary burners, as shown in Figure 3.5. When

supplementary firing is used, the temperature and mass flow of the exhaust gas are increased. This leads to greater production of steam at higher pressures and temperatures, which, when fed into a steam turbine, results in increased generation but lower overall efficiency due to the increase in fuel used. This process is found to offer increased flexibility in variable heat loads (González Díaz et al., 2016).

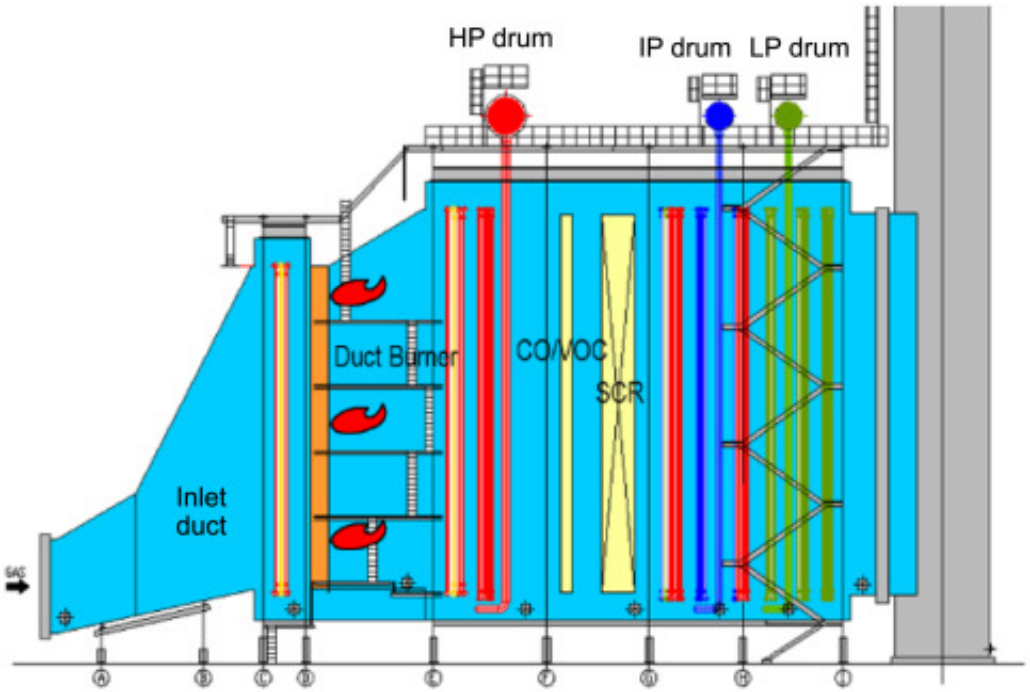


Figure 3.5: Supplementary firing in a HRSG (Shiozaki et al., 2021).

Supplementary firing may be implemented alongside CO_2 capture systems as supplementary firing can increase the concentration of CO_2 in the exhaust gas by combusting fuel with the remaining oxygen from an oxygen-rich initial combustion stage (González Díaz et al., 2016). This allows for an increase in CO_2 capture efficiency when utilising a carbon capture and storage (CCS) system. However, this concept is still theoretical and, to the author's knowledge, has not yet been implemented in an industrial system.

A further role of supplementary firing is to increase the efficiency of a CCPP when operating at part loads (Díaz et al., 2017). This is achieved by heating the cooler exhaust gases, preventing a significant decrease in steam production, and maintaining steam-driven generation at the required level. The same method is also used to account for changing ambient conditions causing reduced flow temperatures due to increased losses (Cáceres et al., 2018).

However, there are limitations on flue gas supplementation, primarily based on the addition of energy. Notable advancements in material science have led to the development of superalloys engineered to endure elevated temperatures and pressures in steam turbines, as evidenced by Morales-Hernández et al. (2014), in their exploration of turbine blade materials. Despite these advances, metallurgical constraints persist - most notably, with steam turbine blades limited to approximately 850 K and the temperature boundaries for tube materials confined to around 1,093 K (González Díaz et al., 2016). Gas flow distribution within heat exchangers

also emerges as a critical design consideration, with uniform distribution essential for ensuring stable operational performance.

Further side effects including increased vibrations in the tube banks due to mechanisms like turbulent buffeting, will arise since the tubes are not designed to withstand vibrations induced by the supplemented flow. As such, the intensity of the flow turbulence and velocity are also essential characteristics to monitor if additional flow is introduced between the turbine outlet and the HRSG inlet.

As the heated air must be introduced within the pre-existing inlet duct to avoid significant redesigns, there will be a resultant increase in flow complexity. This is because the flow will be disturbed and then has a reduced distance within which to reach equilibrium. As a consequence, the increased flow complexity can lead to less efficient heat transfer within the HRSG. The uneven flow distribution can result in certain areas within the heat recovery unit experiencing lower heat transfer rates, which may decrease the overall efficiency of steam generation. Moreover, the shorter distance for the flow to stabilise before interacting with the tube banks can exacerbate this issue, leading to hot spots and uneven heating. This uneven thermal distribution not only affects the efficiency of the HRSG but can also lead to increased thermal stresses on the structural components, potentially reducing the lifespan of the HRSG and increasing maintenance requirements. As such, a detailed analysis of flow characteristics becomes imperative to manage the flow complexities and maintain system integrity and performance.

As an alternative to flow supplementation, the high storage temperature of the UHTS makes it possible to replace the primary heat source of the GT flue gas in its entirety. Here, the thermal store would provide all the necessary energy to the HRSG. Together, they would act as a boiler for a conventional steam-based generation system. In this mode, the store would discharge significantly faster than in augmentation mode, because the thermal store would be required to supply 100 % of the energy input demand.As such, this would be more suited to a smaller-scale system, as the lower energy requirement from the store would reduce the rate of discharge, minimising instances in which the UHTS system would be fully discharged.

Integrating UHTS systems with a HRSG involves navigating technical challenges such as thermal stress management, material compatibility, and flow dynamics, necessitating innovative solutions to harmonise the high-temperature output of UHTS systems with the operational parameters of HRSG units, along with advanced control systems. As UHTS systems can provide heat significantly hotter than the material limits for HRSGs, the outlet temperature of a store must be controlled to provide the required flow temperature and distribution. This is achieved whilst maintaining a constant mass flow by mixing the heated air with an ambient bypass after exiting the thermal store to produce an outlet with the required properties.

There are deployed examples of TES systems used in conjunction with HRSGs to replace boilers and drive a steam turbine without additional energy input. One of these products is the Siemens Gamesa Electric Thermal Energy Storage system (Siemens Gamesa, 2020). This provides a 130 MWh storage capacity by raising the temperature of roughly 1000 tons of rock to 600 °C, the temperature of steam required to drive super-critical steam turbines (Stack et al., 2019). Plans were in place to build a larger version of the system, known as the SWITCH variant. This would have operated by heating the storage medium electrically and then by passing a fluid through the heated area to increase its temperature, which can

thereafter be used to raise steam through transfer to a water stream, essentially replacing the furnace at a conventional steam-driven power station (Siemens Gamesa, 2019). However, this was abandoned due to storage medium material failure in the smaller system.

Once the steam has been produced at the required quality, using water from within the pre-existing cycle to ensure no impurities are introduced, it may be introduced to the Rankine Cycle. The method through which it is introduced will depend on the system in question. For turbines used in power generation, the steam may be introduced in multiple locations (Datas et al., 2016).

Depending on its quality, the additional steam may be sent directly to one of the HP, IP or LP steam turbines to augment the inlet into the turbine directly, increasing the flow through the system and boosting the output whilst maintaining a constant fuel supply (Huda et al., 2014). The process would require the steam turbines to be oversized for the current volume of steam, allowing them to handle an increased flow.

If the Rankine cycle was required to instantaneously boost the power output on the second timescale, the UHTS system may be adapted to raise and store steam to be released on demand. However, the quality of this steam must be maintained, requiring heat loss to be minimised through the use of suitable insulation to ensure the steam remains dry and at a suitable energy level to be used within a turbine. Although storing high-energy steam may pose risks of component failure, overcoming these challenges could enable the development of a system capable of rapidly adjusting to meet demand fluctuations. Similarly to previously discussed steam integration methods, this is achieved by injecting the stored steam directly into a turbine when required, immediately boosting the power output. This method is seen at the Khi Solar One plant, which has a 100 MWh storage capacity, provided through the accumulation of saturated steam to be discharged to drive a steam turbine upon requirement (Collado and Guallar, 2013). The environmental impact of these integrated systems, particularly in terms of reduced emissions and enhanced energy efficiency, aligns with global sustainability goals.

3.3.3 Flow Characteristics

When considering the optimisation of energy utilisation and advancing the performance of HRSGs, the feasibility of retrofitting existing HRSG configurations with alternative inlet systems must be considered. As such, retrofit feasibility is based on downstream temperature, velocity and turbulence at the tube banks and the inlet pressure when compared with design values. The first primary superheater (SP1) will see the greatest impact in these variations as the flow will not have been cooled or stratified by previous tube banks. The schematic in Figure 3.6 shows how the superheater is the first tube bank with which the flow will interact within the HRSG.

The temperature at SP1 must maintain uniformity across the tube banks, with allowable increases up to a specified threshold determined by the material properties of the tubes. To ensure optimal efficiency and avoid damage, the velocity and turbulence within the system should replicate the design conditions, maintaining the intended distribution and magnitude.

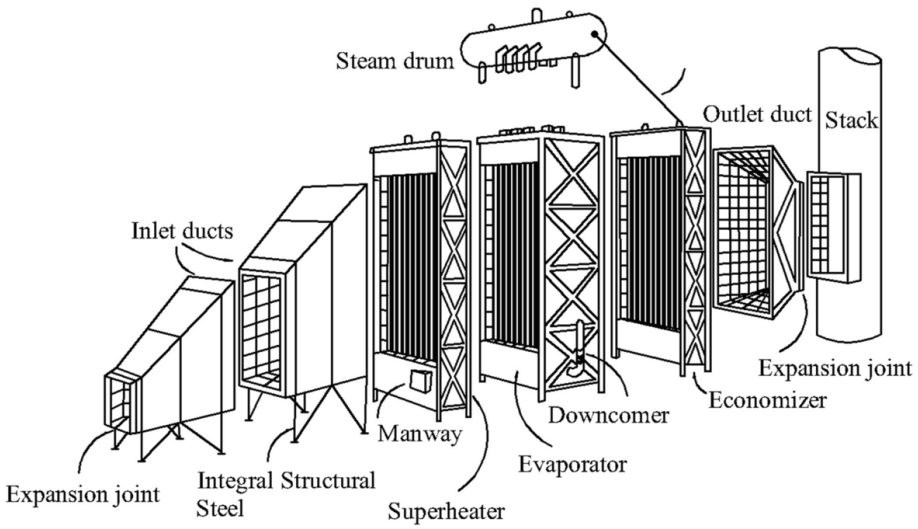


Figure 3.6: Schematic to show relative location of the primary superheater (Arpit and Das, 2023).

Temperature Feasibility

When the gas flow is supplemented, there will be a resultant increase in downstream gas temperature due to the additional heat entering the system. Temperature is a fundamental physical quantity that measures the kinetic energy of the particles in a substance, playing a crucial role in determining the properties of matter. An increase in temperature is advantageous when aiming to increase HRSG generation, up to the maximum allowable tube temperature of 1,093 K (González Díaz et al., 2016). To increase the allowable temperature, a retrofit would be required to replace the tubes with new ones constructed from materials capable of withstanding such high peak temperatures whilst maintaining their structural and functional integrity over prolonged operational periods. This would increase the overall cost and complexity of a HRSG retrofit.

The effects of temperature variation at SP1 must be considered when the exhaust flow is supplemented with heat exceeding the design temperature during base load operation. This is because the exhaust flow temperature will rise beyond the design range for an extended period, necessitating appropriate adjustments. Conversely, if the exhaust flow is supplemented with additional heat at the same temperature as the exhaust flow, and the control system adapts to the variation in flow rate, no heat-related issues will arise.

Even when remaining below the allowable peak temperature, supplemental heat leads to an increased disparity between the bulk and peak temperatures at SP1, resulting in several downsides that will affect the operational lifespan of a HRSG. This pronounced temperature differential can generate significant thermal stresses within the tube material owing to the non-uniform heating across the tube surface. Such stresses are particularly acute at points of peak temperature, where the material undergoes rapid expansion in contrast to the cooler sections, leading to increased susceptibility to creep, thermal fatigue, and other failure mechanisms. This fatigue is characterised by repeated expansion and contraction cycles, which cause the formation of micro-cracks, which negatively impact the structural integrity and longevity of the

tubes (Shin et al., 2012). These fatigue mechanisms compromise the integrity of the tube, increasing the likelihood of failure due to high internal pressures, resulting in ruptures or leaks.

Furthermore, this uneven temperature distribution exacerbates localised corrosion, which can severely compromise the structural integrity and lifespan of the tubes. Areas experiencing peak temperatures are likely to see accelerated corrosion rates, especially prevalent in the presence of corrosive compounds found in the exhaust gases of a GT. A temperature differential can also complicate the thermal management within the HRSG, as it necessitates a design that accommodates a wide range of temperature conditions, thereby increasing complexity and potential costs. Moreover, the operational flexibility of the system is challenged under these conditions, as the HRSG must be capable of efficiently managing the thermal dynamics associated with the variable loads and the intermittent nature of the use of supplemental heat.

To effectively integrate additional heat into the HRSG, the retrofit design should maintain a bulk/peak deviation of less than 5 % without exceeding the 1,093 K temperature limit. This low peak-to-bulk differential minimises potential negative effects and allows for the HRSG to be more easily controlled and optimised during operation to achieve the desired performance.

The effect of this increased temperature on the operation of the system must be considered. Understanding the temperature-induced stress variations is essential for predicting component lifespan and scheduling maintenance, ensuring the long-term reliability of the HRSG system. As such, any alteration that may affect the temperature necessitates a comprehensive life-cycle analysis to evaluate the long-term impacts of retrofit designs on HRSG components, balancing performance enhancements with maintenance and replacement costs (Sanaye and Rezazadeh, 2007).

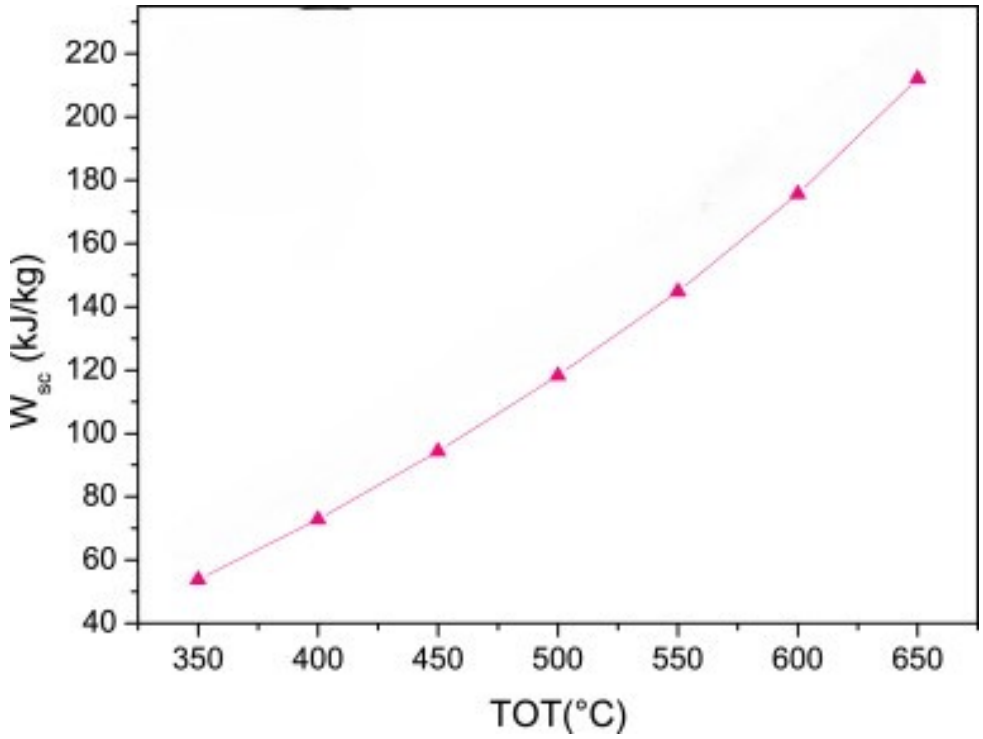


Figure 3.7: Work produced from steam cycles with increasing Turbine Outlet Temperatures (TOT) [adapted from (Nadir and Ghenaiet, 2015)].

As a rise in temperature increases the available thermal energy for steam generation, a greater water flow rate is required to extract this energy while maintaining the steam conditions. This will result in an increased steam output, creating the potential for a greater work output, resulting in an increase in generation if the turbine is sufficiently sized, allowing the HRSG to utilise the energy from the UHTS. This can be seen in Figure 3.7, which shows how an increase in Turbine Outlet Temperature (TOT) results in an increase in work produced by a HRSG.

The control of the water flow rate also plays a pivotal role in preventing the overheating of tubes, which could lead to material degradation and operational inefficiency. This also prevents tube dry-out scenarios, particularly in the superheating sections of the HRSG. Furthermore, the integration with broader system dynamics, including the potential effects on steam drum levels, feedwater flow regulation, and the overall thermodynamic efficiency of the steam cycle must be considered. Such integrative analysis will ensure the optimisation of the HRSG within the context of the entire power generation system.

From a safety perspective, the control of the water flow in response to temperature variations is vital. Such adjustments are not merely for optimising operational performance when supplemental heat is introduced but are also critical for maintaining safety margins, as the increased temperatures and resultant pressures must be managed within the prescribed safety and performance parameters of the HRSG. Moreover, the altered water chemistry at elevated temperatures imposes stricter requirements on water treatment processes to prevent scaling and corrosion within the steam circuit. Finally, the maintenance and inspection protocols must be adapted to account for the heightened thermal environment, potentially leading to increased operational costs and necessitating periodic downtime for thorough inspections.

Retrofits can be employed at tube banks to mitigate temperature-induced tube failure. Thermal barrier coatings can be applied to the external surfaces of the tube banks and act as insulating layers, minimising temperature fluctuations and mitigating peak material temperatures. However, this can also result in a significant reduction in heat transfer. Similarly, the installation of thermal blankets around the tube bundles insulates them from high-temperature gases, thus preventing abrupt temperature spikes, which maintains a more stable thermal environment.

Furthermore, flow distribution plates can be retrofitted within the tube banks to ensure an even distribution of hot gases across the tubes, minimising localised peak temperature hot spots and temperature variations. This would also enhance the overall heat transfer efficiency whilst protecting the tubes. Similarly, the incorporation of turbulators into the tubes themselves can improve heat transfer efficiency and further reduce temperature variations within the tube banks. However, this is a more substantial retrofit due to the need to affix the turbulators to each tube.

These retrofits can contribute to the mitigation of temperature-induced tube failures, which may result from the peak temperatures observed in cases where the HRSG is supplemented with ultra-high temperature air from the UHTS. This mitigation positively affects the reliability and durability of the HRSG.

Velocity Feasibility

Velocity is a vector quantity of speed in a specific direction and represents the rate of change of an object's position with respect to time. When the inlet gas flow is altered or supplemented, it

can vary the gas velocity at the surface of SP1. As for a case with an increased mass flow rate, an increase in average gas velocity is guaranteed as the velocity must increase to accommodate the additional mass of gases passing through the same cross-sectional area at SP1 to maintain the constant mass flow rate.

Both reduced and increased velocities present challenges that can be detrimental to the HRSG's performance and longevity. Whilst a reduction in velocity would mitigate kinetically induced damage to the tube banks, a significant reduction in bulk velocity should be avoided as this has the potential to cause a range of issues. A lower fluid velocity is associated with a diminished heat transfer rate, as shown in Figure 3.8.

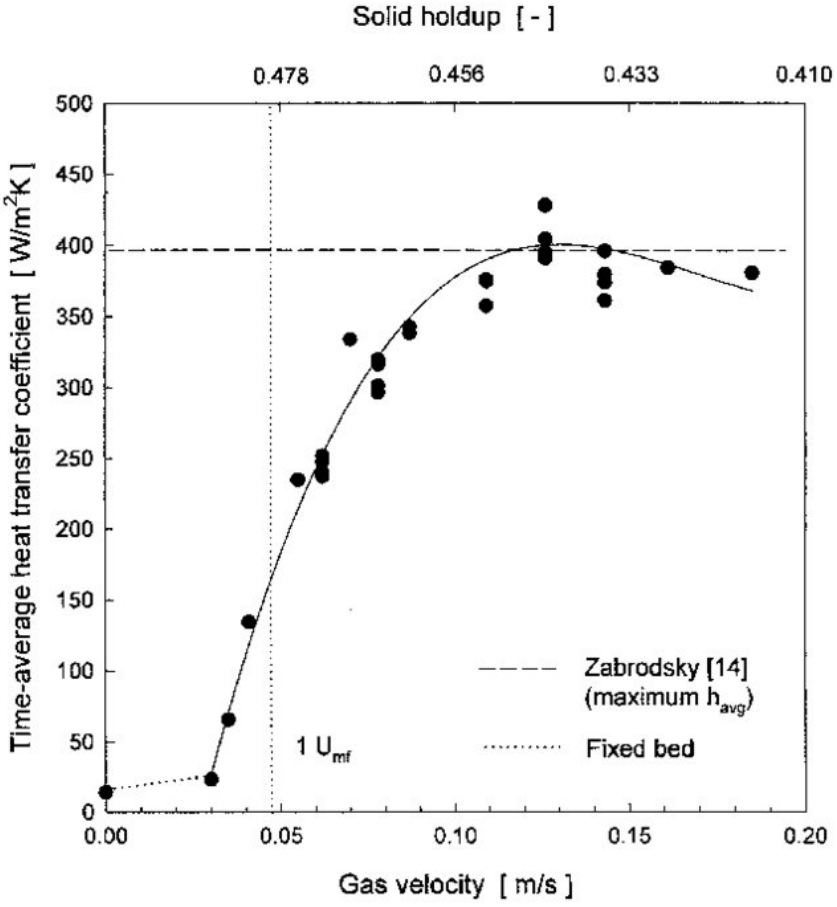


Figure 3.8: Effect of gas-side velocity on the heat transfer coefficient of a tube bundle (Kim et al., 2003).

This reduction is principally due to a decrease in the convective heat transfer coefficient, as higher fluid velocities are instrumental in disrupting the boundary layer on tube surfaces, thereby facilitating more effective heat exchange. Concurrently, there is an increased likelihood of fouling and corrosion at reduced velocities, attributed to the weaker shear forces, which are insufficient in preventing deposit accumulation, coupled with prolonged exposure of tube surfaces to corrosive substances present in the exhaust gases (Tang et al., 2018). Consequently, these factors impair the overall thermal efficiency of the HRSG, as the system's capability to recuperate heat from the exhaust gases is compromised, leading to a diminution in the

efficiency of the power generation cycle. Operational challenges are also evident, with reduced velocity affecting the HRSG's adaptability to load variations, thus engendering operational inefficiencies. Furthermore, a design alteration might be necessary to counterbalance the lower heat transfer rates, requiring a greater heat transfer surface area and a significantly larger retrofit process. While reduced velocities pose a lower risk of tube vibrations compared to scenarios with increased velocities, specific conditions can still induce significant vibrations. Vortex shedding, a phenomenon where vortices are shed alternately from opposite sides of a tube, can occur at certain reduced velocities, matching the natural frequency of the tubes and leading to increased vibration amplitude, known as vortex-induced vibrations. Uneven flow distribution at lower velocities can also contribute to flow-induced vibrations due to differential pressure and flow patterns around the tubes. Additionally, these vibrations at reduced velocities can escalate the risk of wear, potentially culminating in tube failure.

In contrast, while higher velocities can improve heat transfer rates, they can also introduce significant mechanical and operational challenges, diverging from those encountered at reduced velocities. Foremost among these are the increases in erosion and mechanical wear. Elevated fluid velocities, particularly with particulate-laden exhaust gases, can significantly accelerate the erosion of tube surfaces, leading to premature material degradation and potential failure, underscoring the necessity for a careful balance in fluid velocity (Pleshanov et al., 2020). Moreover, higher velocities can induce increased pressure drops across the tube bank, necessitating more powerful and, consequently, more energy-intensive pumping systems. This scenario can result in higher overall energy consumption, thereby offsetting the gains in thermal efficiency. As with reduced velocities, excessive velocities may provoke tube vibrations due to higher dynamic forces, vortex shedding, turbulence, and flow instabilities. These can lead to fatigue failures in tube mounts and supports, posing a substantial risk to the structural integrity of the HRSG (Fabricius et al., 2022). Furthermore, higher fluid velocities are often associated with increased noise levels, which may necessitate additional sound attenuation measures, incurring extra costs and design complexities.

For a feasible retrofit that supplements the flow, the velocity over the superheater should match the design value as closely as possible to minimise the above-mentioned effects. A reduction in velocity is preferable to an increase, as reduced velocities primarily affect heat transfer efficiency, while increased velocities predominantly raise concerns related to mechanical integrity, such as erosion, wear, and tube vibrations.

Strategies to mitigate the velocity through an HRSG can be retrofitted, including several practical approaches. Flow restrictors, such as orifice plates and flow control valves, can be introduced within the inlet duct to create controlled constrictions in the flow path. These constrictions effectively reduce flow velocity while maintaining operational flow rates. Additionally, retrofitting flow deflectors or turning vanes within the ducts can redirect and more evenly distribute the flow, reducing localised high-velocity zones.

Larger retrofits include the installation of diffusers at strategic locations within the system, which can facilitate a gradual expansion of the cross-sectional area, leading to the deceleration of flow and the mitigation of excessive velocity. Similarly, adding expansion chambers within the ductwork can provide space for the flow to expand, resulting in reduced velocity and a smoother flow transition. The incorporation of adjustable dampers or louvers in the ductwork can also offer the flexibility to regulate flow velocity by adjusting airflow restrictions, allowing

velocity can be controlled more precisely.

These retrofit strategies can collectively offer practical solutions to address and control flow velocity in existing duct and HRSG systems, especially those seen in a full conversion system where there is no velocity damping from a bulk flow.

Turbulence Feasibility

Turbulence refers to the chaotic flow of fluids characterised by irregular variations in pressure and flow velocity. A feature of a turbulent flow is eddy generation, which significantly impacts mass, momentum, and energy transfer. When the gas flow is supplemented, the turbulence at SP1 can vary significantly as a result of the increase in mass flow and mixing-induced turbulence.

A consequence of increased turbulence is the enhancement of heat transfer efficiency, as is the case for an increased fluid velocity. However, this enhancement is facilitated through the intensified mixing of fluid particles, which effectively disrupts the thermal boundary layer on heat transfer surfaces, thereby augmenting convective heat transfer processes. While turbulence enhances heat transfer, it can also lead to temperature gradients within the fluid flow, resulting in non-uniform heating of the tube surfaces. This phenomenon, largely absent in uniform velocity increase scenarios, can create localised overheating or thermal stress areas, exacerbating wear and potentially leading to premature failure. Additionally, excessive turbulence can induce thermal fatigue in the tube material. This arises from the highly irregular and fluctuating thermal stresses imposed by the turbulent flow, distinct from the uniform thermal stress profile typically associated with increased velocity. Such thermal fatigue may manifest in the form of micro-cracks and material degradation over time, reducing the structural integrity and lifespan of the tubes. On top of the sole turbulence-related issues, increased turbulence can result in mechanical implications similar to those seen with increased velocity. These include increased erosive wear on superheater tubes and intensified flow-induced vibrations.

Conversely, diminished turbulence at SP1 can lead to gas flow stratification, introducing variations in gas temperature and composition profiles within the HRSG. If any supplementary firing system is installed in the HRSG, lower turbulence levels can impede the combustion process, influencing emission levels. Similar to a reduction in velocity, a reduction in turbulence can also create a decline in heat transfer rates and increase the risk of fouling on heat exchange surfaces.

For a feasible retrofit, the Reynolds Number (Re) over the superheater should match that of the design conditions as closely as possible. Re is a dimensionless quantity which quantifies turbulence based on the ratio of inertial forces to viscous forces. Re should have a maximum variation of 5 % from design conditions to limit the negative effects associated with the retrofit.

When a retrofit is implemented to fully replace the inlet flow into the HRSG, the turbulence at SP1 will vary due to the non-perpendicular nature of the flow inlet. Without sufficient length for the flow to fully develop, the turbulence at SP1 will likely vary significantly from the design case when the inlet flow is fully replaced.

In some cases, a compromise must be made based on which will result in a more manageable effect. A deviation in bulk turbulence can affect overall heat transfer efficiency and flow uniformity within the HRSG, whereas a divergence in peak turbulence primarily produces

localised effects such as overheating of specific tubes, fouling in localised regions, or elevated pressure losses in particular areas. The management of localised complications poses distinct challenges, primarily due to limited visibility and accessibility. Issues at specific regions may only end up being detected upon a failure, as said regions may be less accessible or visible during routine inspections. Once the regions are identified, they require specialised techniques and equipment tailored to the affected area in order to monitor them and identify the root causes of these complications. The severity of these effects is contingent on the magnitude and location of the turbulence divergence. While localised complications may not always significantly affect overall HRSG performance, they may still reduce efficiency, increase maintenance demands and raise safety concerns within the affected regions, while bulk turbulence divergence predominantly affects overall HRSG performance. Due to these factors, a preference is given for a divergence in bulk turbulence over peak turbulence.

A few strategies exist to mitigate increases in turbulence with an additional retrofit. The use of flow straighteners introduces specially designed vanes within the inlet duct. These vanes serve to enhance flow uniformity and counteract uneven velocity profiles and swirl patterns. Similarly to the velocity control retrofits, internal baffles and vanes promote better mixing, disrupt vortices, and create a more consistent flow distribution, reducing turbulence. Devices such as turning vanes and diffusers offer flexible solutions to the flow, further improving stability.

Techniques such as those outlined above play a crucial role in reducing turbulence and minimising the damaging effects of high turbulence on the internals of an HRSG.

3.3.4 Flow Analysis

Literature establishes that computational fluid dynamics (CFD) is commonly used to investigate flow conditions and heat transfer properties in HRSGs (Galindo-García et al., 2014; Boonloi and Jedsadaratanachai, 2022). Yoo et al. (2011) utilises CFD to predict flow parameters such as velocity and temperature throughout a HRSG system. They used the k-ϵ Renormalised Group (RNG) method to obtain the results, which produced results which were validated.

Regarding the addition of flow, Tenbusch (2008) used CFD to model the introduction of supplementary burners to ensure that they produce appropriate flow and temperature distributions at the HRSG inlet. This is achieved by predicting exhaust flow characteristics entering a HRSG and using the information to design flow-correcting structures within the duct.

Li et al. (2019) conducted a simulation of a CCGT with TES to afford flexibility during plant operation, similar to the method in which supplementary firing might be used. This study confirms that stored heat can be used to maintain HRSG temperatures when the GT is not at full load. Whilst this proposes a similar method of implementing thermal storage into a HRSG, this paper does not investigate the physical process of introducing a secondary heated flow to the HRSG inlet.

When modelling a HRSG using CFD, it is computationally expensive to represent individual tubes. Instead, a porous media is commonly used to represent the tube banks. Vytla (2005); Torresi et al. (2009); Tenbusch (2008) use this method to analyse the gas-side flow. In this method, tube banks in the HRSG are modelled as porous media zones with properties, such as the inertial loss coefficient and porosity, estimated based on pressure drop correlations.

It is shown that inlet duct geometry significantly impacts flow conditions entering a HRSG (Hanafizadeh et al., 2015). Adding additional flow to this region will similarly impact flow conditions. Impinging jets are a practical method for UHTS integration in this system due to their inherent characteristics of high heat transfer rates and the high level of mixing that they generate (Katti et al., 2011). However, due to their disruption of the developed flow, they incur a significant pressure drop which must be accounted for, incurring additional operational expense. To investigate this, the inlet ducting where additional flow is introduced via impinging flows into the bulk exhaust gas must be investigated. This builds on significant research conducted using CFD in fluid mixing properties.

Gopalakrishnan and Disimile (2018); Singh et al. (2021) concluded that the SST k-ω model is suitable for predicting velocity characteristics of impinging jets as it produced results that best matched experimental data. It is suggested that a mesh independence study on the impingement region is vital due to the prevalence of false diffusion caused by the flow direction vectors entering at an angle to the mesh elements. It should be noted that while ω models are suited to investigate regions with low Re values near the walls, such as those resulting from impinging jets, they are less appropriate for investigating the bulk flow found within the large diameter inlet duct of a HRSG and are also more difficult to converge than the k-ϵ model.

As multi-jet impingement is extensively used in industrial cooling, it may also be used for heating a bulk flow to its heat transfer properties. Multiple studies demonstrate that the overall heat transfer depends strongly on the injection Re (Lytle and Webb, 1994; Ahmimache et al., 2022). Regarding heat transfer from impingent jets, a study by Singh et al. (2021) on the effect of heat transfer in a system with multiple jets demonstrated that the heat transfer coefficient was improved with a reduced separation between the jets. Lindner et al. (2016) showed that counter-current flow at the inlet junction produced shorter mixing lengths than the conforming or perpendicular inlet flows when multiple inlet jets enter a pipe at various impingement angles. This study, however, is limited to two impinging inlets.

As the literature outlines that CFD is a suitable method to investigate both the characteristics within a HRSG and impinging jets, a CFD model is employed to model an industrial HRSG. Temperature, velocity, and turbulence profiles for the first tube bank reached by the gas flow are obtained and analysed. The UHTS integration scenarios are compared to a 'Case 0', which is the HRSG operating at standard operating conditions. Simulations are performed using the CFD software Ansys Fluent 19.1.

In summary, the integration of renewably sourced heat into Rankine cycles, facilitated by UHTS systems, represents a significant advancement towards more efficient and sustainable power generation. This chapter will explore UHTS integration methodologies and their impact on system resilience, utilising CFD models to accurately predict flow characteristics. The primary objective is to determine the impact of various retrofit modification designs on the downstream flow of an HRSG, particularly at the primary superheater. This analysis will assess the impact of altering inlet geometry, angle, and velocity on the feasibility of retrofitting UHTS to either enhance the design output or replace the flow at the outlet of a GT. This will be determined by examining the downstream impact on flow characteristics such as temperature, velocity, turbulence, and pressure loss. By addressing these aspects, this research aims to fill a critical gap in the literature regarding the practical implementation and optimisation of stored heat to drive a steam turbine.

3.4 Computational Flow Modelling

Computational Fluid Dynamics offers a time and resource-efficient approach to analysing fluid flow behaviours by numerically solving fluid dynamics equations. This method involves discretising the geometry under investigation into a finite number of discrete control volumes or elements, converting the continuous fluid domain into a series of algebraic equations. The process incorporates detailed boundary conditions and employs various solver and turbulence models to simulate realistic flow scenarios accurately. Mesh generation and the definition of initial conditions are pivotal, directly influencing the simulation's accuracy and computational demand. CFD is applicable across multiple sectors, providing valuable insights into flow patterns and physical phenomena with significantly reduced time and resources compared to traditional experimental techniques. This approach, grounded in robust mathematical principles, enables the detailed investigation of fluid flows across a wide range of applications.

3.4.1 Governing Equations

Three-dimensional flow is described using the Navier-Stokes (NS) equations to account for the conservation of continuity, momentum and energy. The conservation of species is an additional consideration for reacting flows, though this will be discussed in Chapter 4, as there are no reacting flows in the present work.

The Navier-Stokes partial differential equations are used to describe property conservation within a fluid. Equation (3.1) gives a general transport equation when density is constant. In this investigation, the Ansys Fluent CFD software is used to solve the NS equations.

$$\rho \frac{D\mathbf{u}}{Dt} = -\nabla p + \mu \nabla^2 \mathbf{u} \tag{3.1}$$

In these equations, ρ denotes the fluid density, $\mathbf{u}$ the velocity vector, p is the pressure, and μ is the dynamic viscosity of the fluid. The term $\frac{D\mathbf{u}}{Dt}$ signifies the material derivative, capturing both the local and convective accelerations of the fluid particles.

Continuity

Continuity embodies the principle of mass conservation, asserting that mass within a closed system remains constant over time, thereby ensuring mass invariance across the fluid domain. This equation underpins the pressure-velocity coupling in CFD simulations, ensuring mass conservation across computational cells. It is solved by calculating the change in density and velocity over a range of nodes. Equation (3.2) expresses the invariance of mass for the x-axis. The continuity equation is given as:

$$\frac{\delta \rho}{\delta t} + \frac{\delta}{\delta x_j}(\rho u_j) = 0 \tag{3.2}$$

Here, ρ is the fluid density, u is the velocity in direction x_j, and t is time.

Momentum

As for the conservation of momentum, the NS equations for each of the three axes are used. The conservation of momentum is crucial for determining the motion and forces within fluid flows, reflecting Newton's second law. For the x-axis, Equation (3.3) equates the rate of change of momentum to the sum of the force due to velocity gradients and pressure plus the body forces plus additional source terms, given as $\vec{F}$.

$$\frac{\delta}{\delta t}(\rho u_i) + \frac{\delta}{\delta x_j}(\rho u_i u_j) = -\frac{\delta p}{\delta x_j} + \frac{\delta \tau_{ij}}{\delta x_i} + \vec{F} \tag{3.3}$$

Here, p is the static pressure, and τ is the viscous stress tensor, defined by the fluid strain rates in Equation (3.4) assuming that the fluid exhibits Newtonian properties.

$$\tau_{ij} = \mu[(\frac{\delta u_i}{\delta x_j} + \frac{\delta u_j}{\delta x_i}) - \frac{2}{3}\delta_{ij}\frac{\delta u_k}{\delta x_k}] \tag{3.4}$$

Where μ is the dynamic viscosity and δ_{ij} is the Kronecker delta, which equals zero unless $i = j$, in which case, it equals 1.

The interplay with turbulence models further modifies this equation, adapting it to account for flow irregularities and eddy formations.

Energy

Similarly to the previous equation, energy is solved for each axis to capture the linkage between internal energy changes, heat transfer, and work interactions within fluid systems. Fluent uses the energy conservation equation to model energy transfer throughout the system. This is for the internal energy of a Fourier conducting medium. In Equation (3.5), α is the thermal diffusivity, and $\dot{Q}$ is the heat accumulation in the x-axis. The equation relates the rate of change of internal energy to the contributions from expansion, diffusion, viscous dissipation, and heat additions.

$$\frac{\delta}{\delta t}(\rho H) + \frac{\delta}{\delta x_j}(\rho u_j H) = \frac{\delta p}{\delta t} - \frac{\delta q_j}{\delta x_j} + \frac{\delta}{\delta x_j}(u_j \tau_{ij}) + \frac{\delta}{\delta x_i}(k\frac{\delta T}{\delta x_i} - \sum_{\alpha=1}^{N} h_\alpha J_{\alpha,i}) \tag{3.5}$$

Where H is the total enthalpy, defined as the sum of static enthalpy, h is the kinetic energy of the fluid, and q_j is the molecular transport of energy. k is the thermal conductivity, T is the temperature and J_α the diffusion flux for species α found using Fick's Law.

Fick's law describes molecular diffusion through the expression of the species concentration flux as a linear function of its concentration gradient. This is shown in Equation (3.6)

$$J_{\alpha,i} = \rho D_\alpha \frac{\delta Y_\alpha}{\delta x_i} \tag{3.6}$$

where D_α is Fick's diffusion constant for a given species.

The energy conservation equation is carried out assuming ideal gas behaviour to allow for reduced computational load and faster convergence times. As such, the equation of state is given as Equation (3.7)

$$p = \rho RT \tag{3.7}$$

where R is the specific gas constant based on the universal gas constant.

This equation's integration into thermal and multiphysics simulations outlines its importance in producing detailed evaluations of energy dynamics within fluid environments. It allows for the prediction of energy transformation, ensuring accurate modelling of complex systems in which thermal effects and physical phenomena intersect.

3.4.2 Numerical Discretisation

The Navier–Stokes equation is a non-linear partial differential equation involving three space dimensions and time. Despite it being possible to solve the equation analytically in some simple cases, it is not possible for the majority. As such, a numerical solution to a discretised form of the equation must be found computationally. Discretisation involves representing the fluid flow at a finite number of points, known as grid points, to store an approximate solution.

There is a range of discretisation methods, with the three most frequently used being: the finite difference method; the finite element method; and the finite volume method. Each has inherent advantages and applications for which it is best suited. The application of each of these methods is based on the specific CFD problem at hand, balancing computational efficiency against the desired accuracy and resolution.

Finite Difference Method

The oldest method applied for numerical solutions of partial differential equations is the finite difference method (FDM). FDM stores the values of variables at specific points and approximates the derivatives of the variables using finite difference approximations (FDAs). These FDAs are derived using Taylor series expansion, as modelled in Figure 3.9, which considers a function of one variable, $y(x)$, discretised at equal intervals of size h.

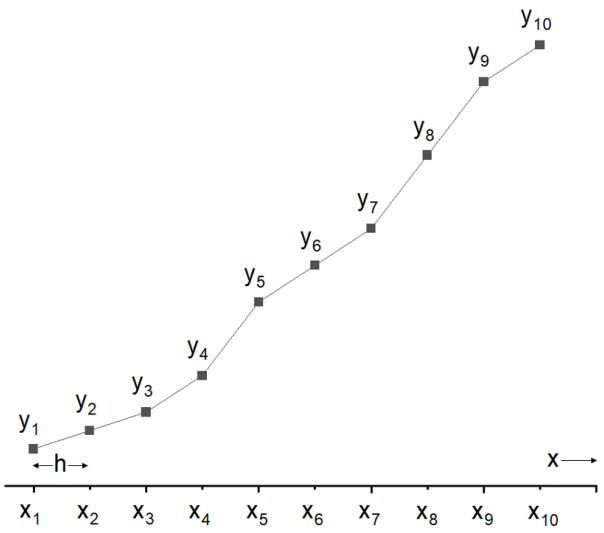


Figure 3.9: Visual representation of Finite Difference Method.

Using the FDA, the second-order, centred approximation $\frac{\delta u_n}{\delta x}$ can be found at the nth grid point. Similarly, the second-order derivative of this can be found. These are given in Equation (3.8) and Equation (3.9). It should be noted that any computational solution is an approximation, and an estimate of the size of errors should be made.

$$\frac{\delta u_n}{\delta x} \approx \frac{u_{n+1} - u_{n-1}}{2h} \tag{3.8}$$

$$\frac{\delta^2 u_n}{\delta x^2} \approx \frac{u_{n+1} - 2u_n + u_{n-1}}{h^2} + O(h^2) \tag{3.9}$$

Here, the $O(h^2)$ value indicates that the errors are proportional to h^2 and have been ignored in this approximation.

To solve a differential equation, consider u velocity exemplified by $u^{''} + u' + u = 0$. Establishing boundary conditions for u at both the inlet and outlet is necessary. Additionally, the number of intervals (N) and the size of each interval (h) must be determined. Using Equation (3.8), the discretised ordinary differential equation is given as Equation (3.10).

$$\frac{u_{n+1} - 2u_n + u_{n-1}}{h^2} + \frac{u_{n+1} - u_{n-1}}{2h} + u_n = 0 \tag{3.10}$$

As the boundary conditions are known, this equation holds for internal points.

The finite difference method is the simplest discretisation method and is easily implemented with equally spaced points. However, it becomes less accurate if the points are not evenly spaced, so it is not often used in CFD codes.

Finite Element Method

The finite element method (FEM) has its roots in structural mechanics. The domain is divided into elements which form the numerical mesh. Each element is defined locally by its nodes and shape functions, which in turn define how values are interpolated within the element. These can be either structured or unstructured, allowing for increased flexibility in the geometry meshing when compared with FDM. The elements store flow field variables at nodes, connecting the elements. This is depicted in Figure 3.10, where the node n_5 impacts each of the elements.

Though FEM can produce highly accurate results for domains with coarse grids and systems with viscous flows, it is primarily suited to the structural analysis of solids. It is not suitable for use when investigating turbulent flow.

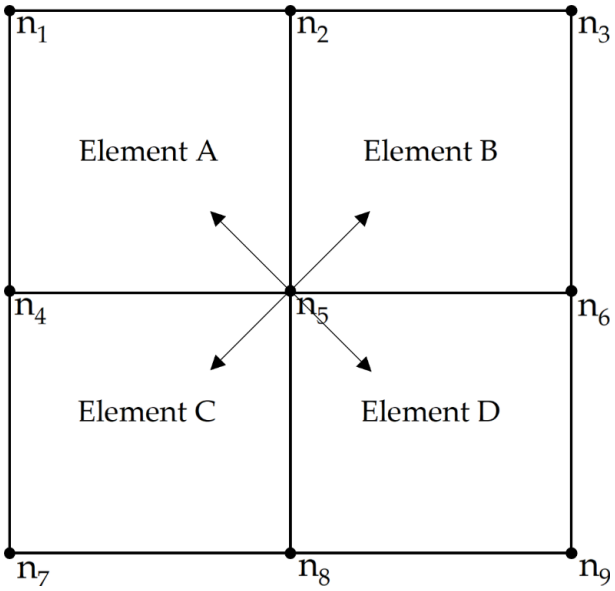


Figure 3.10: Visual representation of Finite Element Method.

Finite Volume Method

The finite volume method (FVM) is the most common approach to solving the Navier-Stokes equations in CFD. Similarly to FEM, the geometry is subdivided into distinct control volumes to which conservation equations are applied. The shape of the volumes is arbitrary, though triangular and rectangular volumes are the most commonly used. These volumes store flow field variables at nodes in their centre and are interpreted as an average value over volume. As averaged values are stored at the central node, it should be noted that this method requires some interpolation to find fluxes at the edge of the cell. This is depicted in Figure 3.11, where forces F_1, F_2 and F_3 represent the fluxes of a conserved quantity across the faces of a control volume.

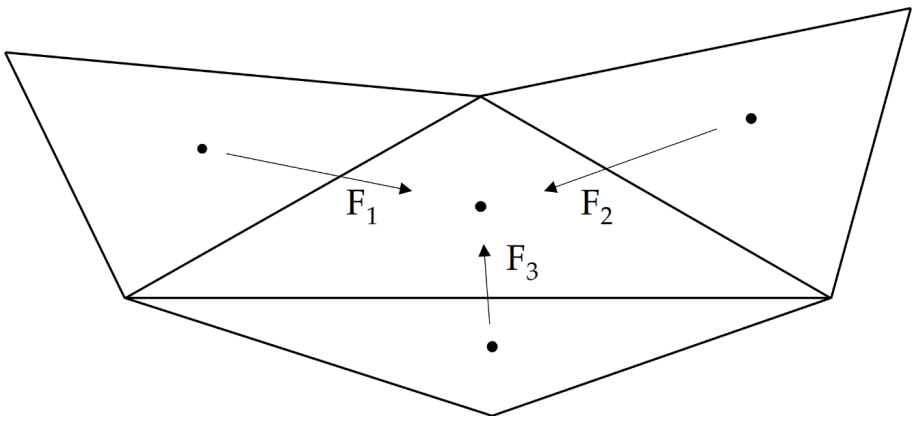


Figure 3.11: Visual representation of Finite Volume Method.

FVM is based on the governing equations for fluid mechanics being written in the form of a conservation law, which may be written in integral or differential form. For the conservation

of mass, the rate of change of the total mass within a volume (V) is equal to the rate at which mass flows in through the surface (S), which forms the boundary of V. This produces Equation (3.11)

$$\frac{\delta}{\delta t}\int\int\int \rho dV = -\int\int \rho u \cdot n dS \tag{3.11}$$

where n is the vector normal to the boundary surface.

By selecting a small volume and employing the divergence theorem to convert the surface integral to a volume integral, Equation (3.12) can be derived for the conservation of mass of a compressible fluid. This holds for the entire domain and each individual control volume.

$$\frac{\delta p}{\delta t} = -\nabla \cdot (\rho u) \tag{3.12}$$

This varies from the FDM as, rather than discretising the differential form of the equation, the FVM instead uses the integral form.

3.4.3 Pressure-Linkage

The Navier-Stokes equations are inherently complex to solve. The momentum equations contain non-linear convection terms which are intricately coupled. Also, pressure is not found using a separate transport equation but is represented as a gradient in all the momentum equations. As such, it is assumed that initial velocity and pressure fields are known based on the boundary conditions. This allows for the calculation of velocity flux to relax the non-linear convection terms within the momentum equations based on the initial velocity field. An updated pressure field is then calculated on this basis. These calculations allow for an updated velocity field to be found based on the terms left within the gradients and the divergence operators. Non-linearity and velocity-pressure linkage issues can be resolved using an appropriate iterative algorithm that adequately calculates the initial fluxes and pressure fields.

Algorithms such as SIMPLE and PISO are designed to calculate the pressures and fluxes from estimated velocities. The pressure values are then corrected by a variant of the continuity equation for pressure correction. This updated pressure is used to correct the velocities. Instabilities can arise within the process because the update between two consecutive solutions is too large for the inner iteration to be easily satisfied. As such, implementing under-relaxation factors (URF) limits the growth of the correction.

An inner iteration process is implemented to solve the linearised momentum equations. For efficiency, this is also an iterative process conducted at each outer iteration until the reduction factor in the Navier-Stokes equation is below a set percentage of the initial residual. In complex turbulent problems, a large number of iterations may be required on the turbulent terms and the mass term. The smaller the URF in the outer iteration, the easier it is to conduct the inner iteration, as the velocities in the new fluxes are closer to the previously calculated velocities, although this increases the time requirement. However, a larger URF will result in a more significant change in velocities, which may lead to instability in the overall outer solution. This two-stage iterative process is conducted until either convergence is achieved or the residuals are low enough.

3.4.4 Solvers

Central to the CFD framework are solvers. These computational tools facilitate the numerical simulation and comprehension of fluid flow phenomena. Solvers in CFD can be broadly classified into two categories: pressure-based and density-based solvers. These solver categories embody distinct mathematical formulations and numerical techniques. The choice between these solvers is a pivotal decision that significantly influences the accuracy and efficiency of CFD simulations. The selection of a suitable solver is influenced by the flow regime, computational constraints, and the specific objectives of the analysis.

Pressure Based

The pressure-based solver was developed for low-speed incompressible flows and later improved to solve compressible flows. The solver uses a projection method to ensure mass is conserved, which derives an equation that satisfies continuity with the velocity field corrected by a pressure based on the continuity and momentum equations. As the governing equations are non-linear and coupled, the solution process iteratively solves the governing equations until the solution converges.

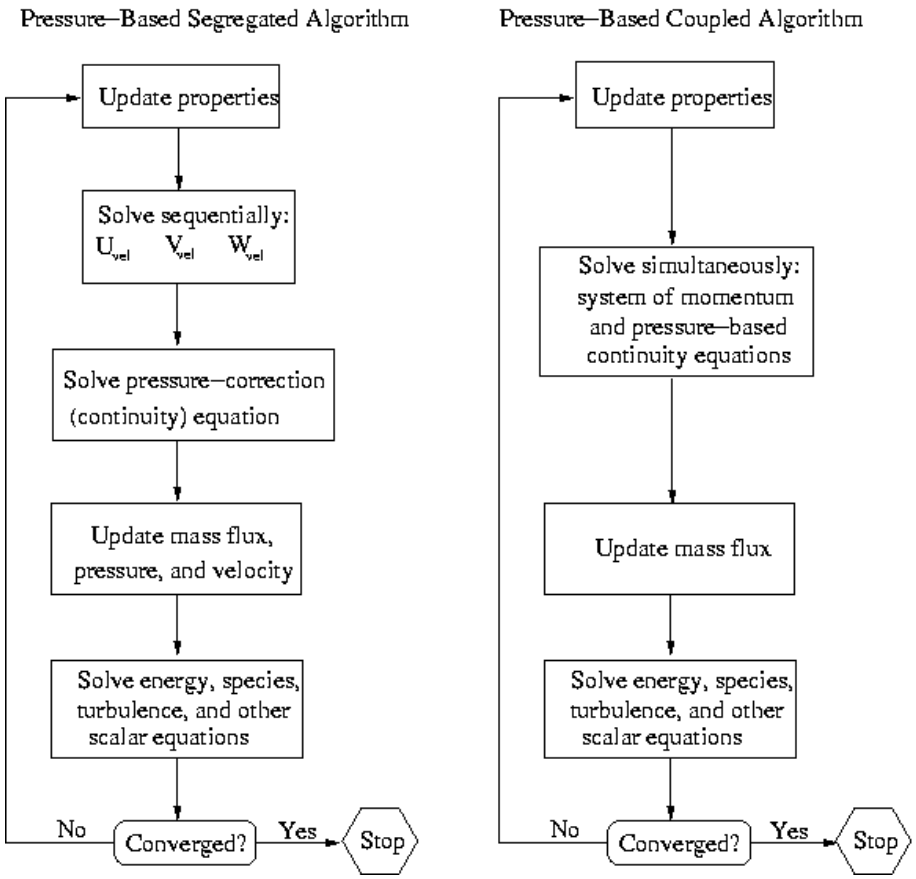


Figure 3.12: Overview of the pressure-based segregated and coupled algorithms (Ansys Inc, 2009).

Two algorithms are available to solve the pressure-based equations in Fluent: segregated

and coupled. The solution procedure for both algorithms is shown in Figure 3.12.

In the pressure-based segregated algorithm, the individual equations that govern the solution variables, such as u, p, T, k and ϵ, are solved sequentially as the governing equations are segregated. As such, each governing equation is decoupled during computation, and only a single discretised equation is stored at a given time. This causes the segregated algorithm to be memory efficient but results in a slow solution convergence.

Conversely, the pressure-based coupled algorithm solves the momentum equations alongside the pressure-based continuity equations. As momentum and continuity are linked in this method, the coupled system of equations is solved within a single step. The remaining equations, such as the energy equation, are solved in a decoupled fashion, similar to the process in the segregated algorithm. As such, the coupled algorithm requires significantly more computational power than the separated algorithm but offers increased convergence speed.

A greater number of physical models are available for use with pressure-based solvers. These include models which are tailored to be used with swirling flows.

Density Based

The density-based solver was developed for high-speed compressible flows and simultaneously solves the governing equations of continuity, momentum, energy and species transport. The density field is obtained from the continuity equations, and the pressure field is solved using equations of state. Governing equations for additional scalars, such as turbulence and radiation, are solved afterwards and sequentially, as shown in Figure 3.13.

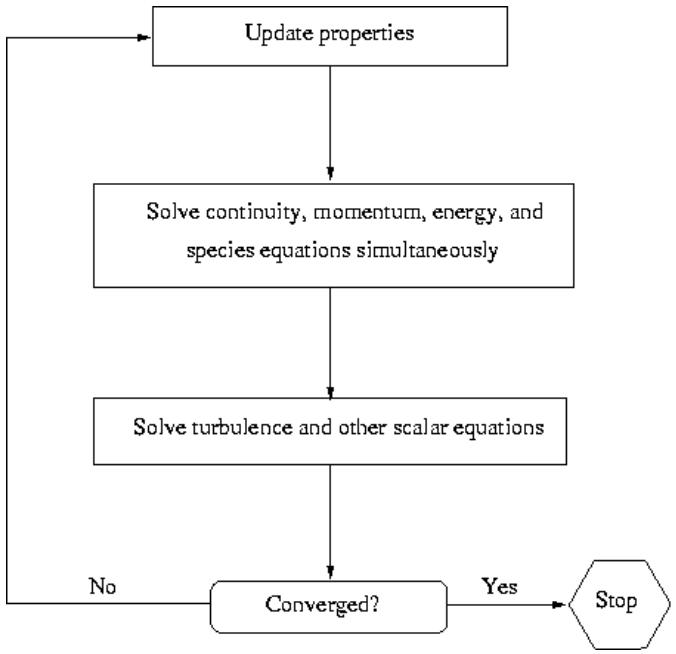


Figure 3.13: Overview of the density-based algorithms (Ansys Inc, 2009).

Similarly to the pressure-based solver, the density-based solver is subdivided into explicit and implicit methods based on the linearisation process. In the explicit method, current values are computed from previous values. For spatial discretisation, this is presented as iterations;

for temporal discretisation, it is presented as time steps. In contrast, with an implicit method, values are computed by solving an equation with both the previous and the present values.

Implicit methods require extra computations and can be more difficult to implement. They are used for problems in which the use of an explicit method requires time steps that would be too small to maintain stability. Using the explicit or implicit method depends on what the model aims to solve.

3.4.5 Turbulence Modelling

At low speeds, fluid flow can be thought of as flowing in sheets or lamina. However, at higher speeds, this structure breaks down with eddies forming. These eddies are three-dimensional, time-dependent vortices that result in a chaotic and random motion known as turbulence. Most flows of practical interest are turbulent. Turbulence is irregular, dissipative and mixing intensive, so the transport of scalar properties is significantly faster than that of molecular transport. Turbulence mixes the flow, making its modelling essential for a detailed understanding of thermal effects, combustion and pollutant transport.

A wide range of time and length scales characterise a turbulent flow. The length scales of eddies have an upper bound given by the geometrical dimensions, whereas the fluid viscosity dictates the lower bound. The smallest vortices are dissipated as heat by fluid viscosity, preventing the continuation of infinitely small eddies. The smallest eddies to occur in a flow field are known as Kolmogorov eddies.

Turbulence modelling is an essential aspect of CFD for capturing the chaotic and random nature of fluid flow. In turbulent simulations, a range of turbulence models can be used to model eddies within the flow. This section briefly introduces the concepts and common models used to approximate turbulent flows. There are three primary methods that are currently in use: Reynolds Averages Navier Stokes (RANS); Large Eddie Simulation (LES); and Direct Numerical Simulation (DNS). Selecting an appropriate turbulence model is crucial to producing valid results. Selection should be based on the Re and complexity of the flow alongside the available computational resources.

RANS

The RANS method models all the turbulent structures, allowing for a relatively coarse grid to be utilised. In many applications, the turbulent fluctuations are of less interest than the mean values of the flow field. As such, when incorporating turbulence into CFD, Reynolds decomposition is implemented to consider the instantaneous velocity as consisting of both an average ($\bar{u}$) and a fluctuating component (u'). Using the equations outlined in Section 3.4.1, Reynolds decomposed values may be substituted in. For example, $\bar{u} + u'$ can be substituted for u to find time-mean quantities.

Implementing these averaged quantities results in the addition of the terms turbulent viscosity (μ_t) and turbulent kinetic energy (k), which results in the closure problem as there are too many unknowns. These new terms require closure in order to solve the new equations.

k-ϵ For systems with recirculating flows, a model is required that accounts for changes in length and velocity scales within the flow. To achieve this, the $k-\epsilon$ model was proposed. This two-equation model has been used and validated extensively, making it the default option in most CFD codes. This model overcomes the closure problem by relating the turbulent kinetic energy (k) and dissipation (ϵ) to turbulent viscosity, μ_t, using Equation 3.13.

$$\mu_t = \rho C_\mu \frac{k^2}{\epsilon} \tag{3.13}$$

where C_μ is a dimensionless constant of 0.09, which is set based on extensive experimental testing.

For each of k (turbulent kinetic energy) and ϵ (rate of dissipation), the transport equations are given as Equation (3.14) and Equation (3.15) respectively:

$$\frac{\delta \rho k}{\delta t} + \frac{\delta \rho k u_i}{\delta x_i} = \delta \frac{(\mu + \frac{\mu_t}{\sigma_k})\frac{\delta k}{\delta x_j}}{\delta x_j} + G_k + G_b - \rho\epsilon - Y_M + S_k \tag{3.14}$$

and

$$\frac{\delta \rho \epsilon}{\delta t} + \frac{\delta \rho \epsilon u_i}{\delta x_i} = \delta \frac{(\mu + \frac{\mu_t}{\sigma_\epsilon})\frac{\delta \epsilon}{\delta x_j}}{\delta x_j} + C_1\epsilon \frac{\delta \epsilon}{\delta k}(G_k + C_3\epsilon G_b) - C_2\epsilon\rho\frac{\epsilon^2}{k}\epsilon + S_\epsilon \tag{3.15}$$

In Equation (3.14), the turbulent Prandtl number, σ_k, is based on k, and G_k gives the generation of turbulence kinetic energy due to the mean velocity gradients. G_b is the generation of turbulence kinetic energy due to buoyancy. In Equation (3.15), the Prandtl number, σ_ϵ, is based on ϵ, and $C_1\epsilon$, $C_2\epsilon$, and $C_3\epsilon$ are model constants.

This model is the simplest turbulence model, requiring only initial conditions or boundary conditions to be supplied. Based on this and its proven performance for various relevant industrial applications, it has become very well-established, being the most widely available turbulence model.

However, the primary drawback is that it does not calculate the individual Reynolds stresses and assumes that the turbulence is isotropic, which can lead to significant errors. Additionally, many of the k-ϵ model simplifications are in the production and destruction terms. This leads to poor performance in some critical cases. Although k-ϵ is widely used, it is not universally applicable.

RSM To overcome one of the primary flaws of the k-ϵ model, the Reynolds Stress Model (RSM) solves an equation for each of the six Reynolds stresses. As such, seven additional equations are solved in a 3D flow simulation, making it the most complex RANS model. Solving for each Reynolds stress is inherently anisotropic, as it predicts independent values for each of the three principal stresses. The term 'anisotropic' refers to the capability of the model to accurately represent turbulence characteristics that vary in different directions. However, it is also necessary to derive an equation for each of the six stresses involving several modelling assumptions. In addition to having equations for each Reynolds stress, the model is able to account for two further physical processes: the pressure-strain correlation term, which has a

net-zero effect on turbulent kinetic energy (meaning it is unaccounted for in k-based models); and a transport term for the Reynolds stresses based on the effect of rotation.

Although RSM is the most generally applicable RANS model and offers improved accuracy over other models, its use incurs an added computational cost based on the requirement to solve an additional seven partial differential equations when compared to k-ϵ. Additionally, while RSM replaces the k equation with the six equations for the Reynolds stresses, the equation for the dissipation rate is retained, limiting the accuracy. It is also reported that this equation can be slow to converge in relation to the other equations in the model, limiting its overall speed.

LES

With access to greater computing power, the limitations of RANS may be overcome by dispensing with time averaging. This is achieved using the LES method. LES directly resolves the large eddies in turbulent flows and models the smaller-scale eddies. This assumes that the most important turbulent transport processes arise from the large to medium-scale eddies, while smaller eddies are principally responsible for the dissipation of the turbulent energy. Direct calculation is used to resolve the eddies that are larger than the size of the finite volume cell, while a more simple model is used to model the universal nature of the eddies that are smaller than the mesh size.

Instead of time-averaging, LES uses a spatial average. The velocity is split into a resolved component, $\bar{u}$ and an unresolved component, u'. If this is carried out for the terms in the Navier-Stokes equations, an extra term is produced compared to the output of a RANS model. This extra term is called the sub-grid scale model, as it represents effects smaller than the grid size. The original sub-grid scale model was that of Smagorinsky (1963), where the following term is added to the momentum equations:

$$(C_s\Delta)^2|\bar{S}|\frac{1}{2}(\frac{\delta\bar{u_i}}{\delta x_j}+\frac{\delta\bar{u_j}}{\delta x_i}) \tag{3.16}$$

where C_s is a constant and Δ is the cell size.

As such, the cell size used in large eddy simulation defines the level at which the smaller scale eddies are filtered and thus modelled.

The sub-grid scale model is relatively simple compared to the full equations for the k-ϵ model. However, the difficulties lie in implementing the model and the computational resources required. A range of factors must be accounted for to ensure that LES is implemented correctly. Firstly, all spatial and temporal discretisation must be at least second-order, as lower-order discretisation can generate errors larger than the sub-grid scale model. Additionally, the cell size must be small enough to ensure that the turbulence below that scale is truly isotropic, which can require a very fine mesh at higher Re values.

The simulation must be run for a sufficient period to ensure that the initial conditions are not influencing the solution. From there, the simulation must be run for an additional length of time to generate meaningful average values. Finally, unlike with a RANS model, all boundary conditions must be time-dependent to ensure that incoming turbulence is accurately represented. These restrictions mean that the computer resources required are at least an order of magnitude greater than required for a RANS simulation.

DNS

Of the methods described, DNS provides the most accurate representation of turbulence. This is done by resolving the non-linear governing equations using extremely fine grids, smaller than the Kolmogorov length scale, and solving for very small time steps in order to resolve the smallest length and time scales of turbulence. This results in an extremely large number of cells and run times of years for practical flows.

However, for DNS, the spatial resolution required is around $Re^{9/4}$ with a similar temporal resolution, limiting the Re values, which can be considered an order of magnitude around 10^5. This makes the DNS method prohibitively expensive for most uses based on current, widely available computers.

On this basis, this investigation will use the two-equation k-ϵ turbulence model with standard wall functions applied to predict turbulence in the system. This is due to the relative simplicity of the flow regime being investigated and the large number of permutations that are required.

3.5 HRSG Model

Integrating a UHTS system with an HRSG could significantly enhance thermal efficiency and improve its environmental performance, offering promising avenues for energy optimisation. Understanding the physical limitations of this integration is necessary. As such, an investigation is carried out on the feasibility of integration to determine whether this is possible in practice. This section outlines the model through which heated air from a UHTS system is introduced into the inlet of an HRSG.

A HRSG is often designed with a specific GT in mind, and as such, they are produced to operate under the conditions seen in the exhaust of that GT (Wuryanti and Jadmiko, 2021). Such design specificity necessitates a thorough evaluation of the UHTS integration impact, ensuring compatibility without compromising the HRSG's performance or longevity. During the operation of a CCGT, off-design conditions caused by variations in the gas flow can significantly impact the efficiency of the steam generator. This variation may also lead to increased corrosion and fouling of tube walls. Consequently, an investigation must be conducted to determine the effect of introducing an additional heated flow to the system. The most significant effect of this change will be seen in the primary superheater tube bank (SP1). This is where the proportional change in the flow conditions will be greatest, as beyond this, tube banks will act to stratify and cool the gas. In such instances, key parameters that must be investigated are the peak temperatures and the flow velocity at the foremost surface of SP1.

This work investigates the flow on the gas side of a heat recovery steam generator. A computational simulation is carried out using Ansys Fluent. As discussed in Section 3.3.3, it is established in technical literature that CFD is a frequently used tool to investigate flow, mixing and heat transfer in HRSGs. This model was produced to simulate the effect on mass, momentum, and energy conservation caused by introducing air heated by a UHTS system. The HRSG geometry and the simulation boundary conditions are taken from a typical industrial HRSG fed by GT exhaust gases. Numerical results for a range of realistic UHTS retrofit designs are compared to those for the HRSG standard operation point.

It should be noted that if UHTS were being considered for a new build case, the design and

integration of the system would likely differ significantly from a retrofit scenario. For instance, space for the flow to develop could be provided using a longer duct, ensuring that the flow is evenly distributed.

3.5.1 Model Setup

The equations presented above are solved using the Ansys Fluent 19.1 code. This software discretises the governing equations using the Finite Volume Method, the pressure-based solver, and the second-order upwind scheme. Pressure velocity coupling of momentum and continuity equations is obtained using the SIMPLE algorithm. The gradients are calculated using the Least Squares Cell Based method, and second-order spatial discretisation of the advective terms is performed for all variables. The gas is assumed to follow ideal gas behaviour, with density, viscosity and thermal conductivity varying with temperature. A pseudo-transient model is used for implicit relaxation whilst capturing greater detail than the standard steady-state method. The calculations are conducted on an Intel Core i5-8365U CPU computer with 4 cores and 16 GB of RAM. The selection of Ansys Fluent and the model setup aligns with industry standards, providing a robust framework for accurate simulation outcomes.

3.5.2 HRSG Geometry

The HRSG used in this model is a Hangzhou H Class Heat Recovery Steam Generator from a deployed CCGT. The HRSG geometry was constructed by Silva et al. (2020) using Ansys Workbench. Due to the large number of tubes and the significant disparity in the length scales of the diameter and height of each tube, they chose not to represent each tube individually to reduce mesh complexity. Instead, each heat exchanger was modelled as a porous medium.

This section describes the geometry of the heat recovery steam generator in the present work. The HRSG is a triple-pressure equipment (HP, IP, LP) with 14 heat exchangers divided into six modules. Modules 1 and 2 contain one superheater and one reheater (respectively, HPSH2, RH2 and HPSH1, RH1), and module 3 contains one evaporator-drum set and one economiser (HPEV, HPEC3). Module 4 holds two superheaters, one economiser, and one evaporator-drum set (IPSH, LPSH, HPEC2, IPEV). Module 5 includes two economisers and one evaporator-drum set (HPEC1, IPEC, LPEV). Finally, Module 6 contains a single low-pressure economiser (LPEC). The geometry of the HRSG can be seen below in Figure 3.14. As this geometry is representative of a real system, there are inactive zones both above and below the central region where the exhaust gas does not flow.

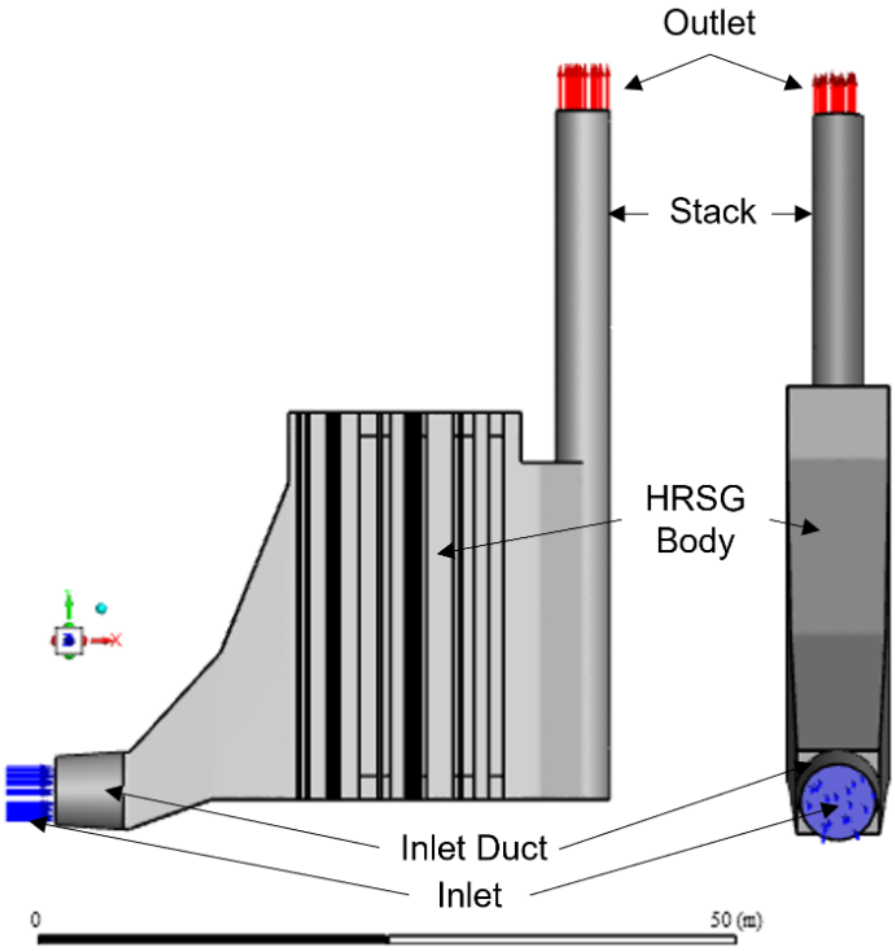


Figure 3.14: Labelled geometry of HRSG.

Though the heat-exchanging properties are not modelled in this investigation due to computational limitations and their minimal effect on the upstream flow, the tube banks must still be accounted for due to their effect on the flow. As the tubes would require significant computational power to model individually and would negatively impact the mesh quality, each bank of tubes is represented as a porous medium. This simplification balances the need for computational efficiency with the requirement to accurately capture the flow dynamics within the HRSG.

As for the additional inlets applied for the UHTS system inlet used in the alternative cases, two modifications are investigated. The first is a multi-pipe inlet around the circumference of the HRSG inlet, and the second is a continuous annular inlet around the circumference.

These inlets were sized based on the method of retrofit: either supplementation or full conversion. The supplementation system provides an additional 10 % to the overall mass flow through the system, whereas the full conversion system maintains the pre-retrofit mass flow rate.

As the SP1 is the area of investigation here, a plane was set up at the inlet-facing surface so that the properties of the flow which make contact could be investigated. The position of

this plane can be seen in Figure 3.15, highlighted in red.

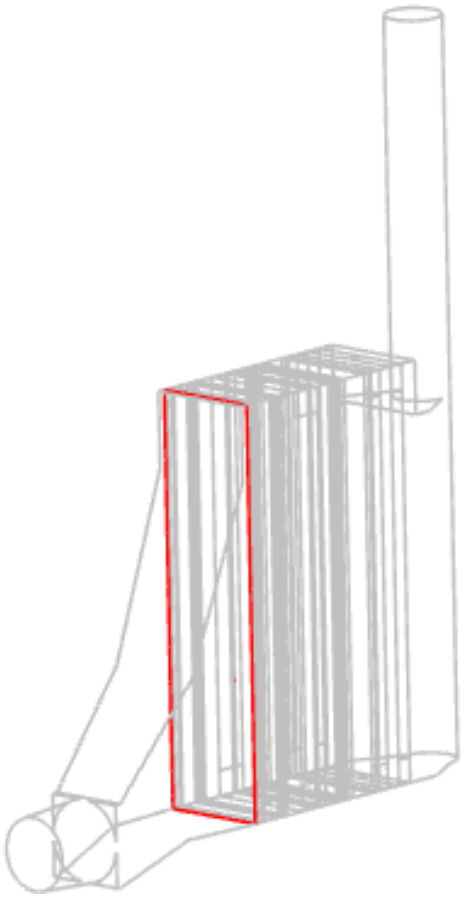


Figure 3.15: Outline of HRSG geometry with the surface of interest highlighted.

3.5.3 Boundary Conditions

The velocity profile is defined using a predetermined profile at the inlet duct section of the HRSG, leaving from the GT exhaust. The distribution used was from data for a GE Gas Turbine Exhaust Axial Velocity Distribution plot (Vytla, 2005). The applied inlet velocity contours are shown in Figure 3.16. The temperature of the exhaust gas is set to 883.75 K. The inlet temperature from the store was set at 1750 K, based on the maximum possible outlet temperature of the system. The outlet at the top of the stack is set to atmospheric pressure with a backflow temperature of 364 K, which represents the design stack outlet temperature. The HRSG walls are adiabatic, so there is no heat transfer to the ambient.

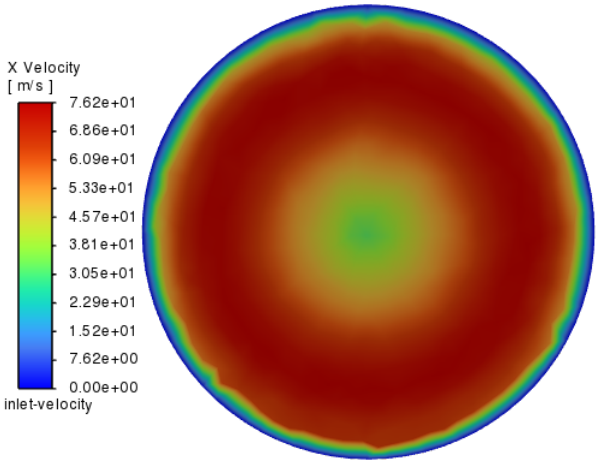


Figure 3.16: Outlet velocity profile of GT into HRSG.

The simulations were conducted with the following conditions for the exhaust gas. The actual temperature, pressure, and velocity profiles of the physical systems were obtained and implemented. The exhaust gas composition is shown below in Table 3.1. The chosen profiles for temperature and velocity are based on empirical data from GE GTs, ensuring that the simulations accurately reflect operational conditions.

Table 3.1: Gas turbine exhaust gas composition (Sharif Ahmadian, 2016).

Component	Concentration (% m/m)
Carbon Dioxide	6.21
Water Vapour	6.03
Nitrogen	73.76
Oxygen	14.00

The effects of UHTS integration at the SP1 in the HRSG are investigated here through simulations of a range of cases. Four core retrofit cases were investigated, each with subdivisions. The first two are sized for a mass flow of 10 % of the primary inlet, whilst the second two are sized to fully replace the inlet flow. These are compared to the typical operational point of Case 0. The simulation cases are as follows:

- Case 0 – Corresponds to the standard operation of the HRSG whilst at base load with respect to the GT exhaust gas flow, which enters the HRSG.
- Case 1-a – Identical to Case 0, except for 8 air inlets incorporated into the GT exhaust flow. These inlets are evenly spaced, with an inlet angle of 30° to the primary inlet surface.
- Case 1-b – Identical to Case 1-a, except the inlets are at an angle of 60° to the primary inlet surface.
- Case 1-c – Identical to Case 1-a, except the inlets are at an angle of 90° to the primary inlet surface.

- Case 1-d – Identical to Case 1-a, except the inlets are reversed at an angle of 120° to the primary inlet surface.
- Case 2-a – Identical to Case 0, except an annular inlet is incorporated into the GT exhaust flow. This inlet is at a 30° angle to the primary inlet surface.
- Case 2-b – Identical to Case 2-a, except the annular inlet is at an angle of 60° to the primary inlet surface.
- Case 2-c – Identical to Case 2-a, except the annular inlet is at an angle of 90° to the primary inlet surface.
- Case 2-d – Identical to Case 2-a, except the inlet is reversed at an angle of 120° to the primary inlet surface.
- Case 3 – Identical to Case 1, except the inlet diameters are increased, and there is no bulk flow from a GT. Inlets are sized to allow for the complete conversion of HRSG to stored heat. Temperature is set to 883.75 K.
- Case 4 – Identical to Case 2, except the inlet diameters are increased, and there is no bulk flow from a GT. Inlets are sized to allow for the complete conversion of HRSG to stored heat. Temperature is set to 883.75 K.

All the geometries each have additional sub-variations. These vary the area of the inlet surface to allow an alteration of the inlet velocity. The velocities investigated are 100 m/s, 200 m/s and 300 m/s. Table 3.2 shows each separate system that will be investigated, with each system given a name.

Table 3.2: Case names for each HRSG model.

	v	Multi-Pipe Inlet Angle				Annular Inlet Angle			
	(m/s)	30°	60°	90°	120°	30°	60°	90°	120°
Supplementary	100	1-a-100	1-b-100	1-c-100	1-d-100	2-a-100	2-b-100	2-c-100	2-d-100
	200	1-a-200	1-b-200	1-c-200	1-d-200	2-a-200	2-b-200	2-c-200	2-d-200
	300	1-a-300	1-b-300	1-c-300	1-d-300	2-a-300	2-b-300	2-c-300	2-d-300
Conversion	100	3-a-100	3-b-100	3-c-100	3-d-100	4-a-100	4-b-100	4-c-100	4-d-100
	200	3-a-200	3-b-200	3-c-200	3-d-200	4-a-200	4-b-200	4-c-200	4-d-200
	300	3-a-300	3-b-300	3-c-300	3-d-300	4-a-300	4-b-300	4-c-300	4-d-300

An example of the geometries of these additional inlets at each angle for both the multi-pipe and the annular designs can be seen in Figure 3.17. Each is positioned so that there is a 3 m space between the wall of the retrofit inlet and the entrance to the body of the HRSG to ensure a consistent mixing region. Due to this, it was not possible to generate a feasible geometry for Case 3-a-100 as there was an insufficient surface area on the inlet duct to maintain a 3 m distance without altering the geometry.

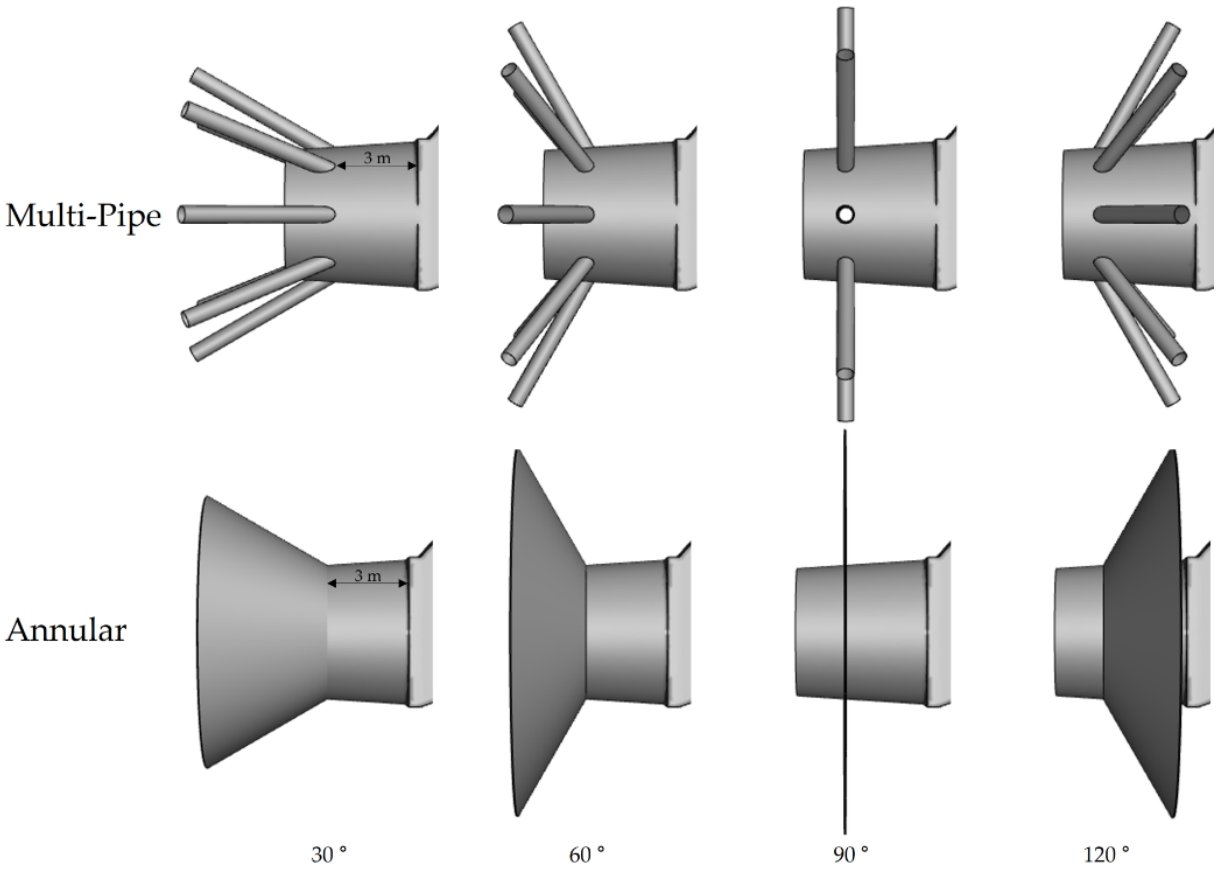


Figure 3.17: Example of the inlet geometry angles employed.

These inlet modifications aim to optimise the flow distribution within the HRSG, enhancing heat recovery and overall system efficiency, whilst minimising emissions.

3.5.4 HRSG Mesh Independence

As the mesh utilised in this study was generated by Silva et al. (2020) for a previous model, it has already undergone an initial mesh independence analysis to establish the numerical solutions insensitivity to variations in cell numbers and locations. Subsequently, a secondary mesh independence study was conducted to corroborate these findings. Three distinct meshes, designated as MI1, MI2 and MI3, were constructed with identical geometry and boundary conditions. Here, MI1 is the base mesh, MI2 a reduced density mesh, featuring just over half the number of cells as MI1 and MI3, an increased density mesh with slightly over 3.5 times the number of cells. The velocity, temperature and turbulence profiles at the surface of SP1 were recorded and subjected to analysis for each mesh configuration. Table 3.3 presents a comparative evaluation of both the average and peak velocity, temperature, and turbulence at the area of interest.

Table 3.3: Mesh independence comparison at the primary superheater in a HRSG for MI1, MI2, and MI3.

Variable	MI1	MI2	MI3	MI2 Diff (%)	MI3 Diff (%)
Cell Size	0.3	0.45	0.15	150	50
Total Cells	5,659,807	3,102,073	20,139,768	-45.2	255.8
Run Time (h)	6.3	14.1	63.5	122.4	904.7
Average Velocity (m/s)	5.6	5.6	5.6	0.0	0.0
Peak Velocity (m/s)	23.0	21.4	23.3	-7.1	1.4
Average Temperature (K)	883.6	882.8	883.7	-0.1	0.0
Peak Temperature (K)	883.9	887.1	883.8	0.4	0.0
Average Re (-)	2,950,000	2,770,000	3,020,000	6.3	2.2
Peak Re (-)	5,930,000	5,790,000	6,060,000	-2.4	2.2
Average TKE (J/kg)	66.4	76.9	64.9	15.8	-2.3

Examining results between MI1 and MI3 revealed a maximum percentage differential of 2.3 % with a notable temperature difference of 0.0 % to one decimal place. It should also be noted that the time to complete 1000 iterations significantly increased between these two mesh studies. The small difference in values substantiates the mesh independence of MI1, affirming the reliability and robustness of the numerical solutions. Furthermore, the significant time requirement difference for a small change in accuracy means that an increase in mesh density would not be worth the computational cost.

However, when additional flow is introduced, the mixing region must be able to model the increased complexity generated by this sufficiently. As such, a further mesh independence study was carried out to ensure that the detail within this region was captured and to check if this affected the overall results. As this study had not been conducted previously, an increased number of meshes were tested.

Five separate meshes were investigated for a mesh independence study with impinging jets, named MIJ1, MIJ2, MIJ3, MIJ4 and MIJ5. Here, MIJ1 is the initial mesh, without any alterations in the bulk flow path, apart from at the outlet of the additional flow inlet region. It should be noted that the area that connects the inlets to the main HRSG inlet has a mesh sizing of 0.100 m in the base case - MIJ1. MIJ2, MIJ3, MIJ4 and MIJ5 each have a sphere of influence in the mixing region with various cell sizes applied. These are 0.150, 0.100, 0.075 and 0.050 respectively. It was not possible to reduce the cell size further due to the limited available computational power.

The sphere of influence, the area in which mesh refinement occurs, has a radius of 3.6 m to ensure the entire mixing region, along with the inlet to the body of the HRSG is investigated. This can be seen in Figure 3.18.

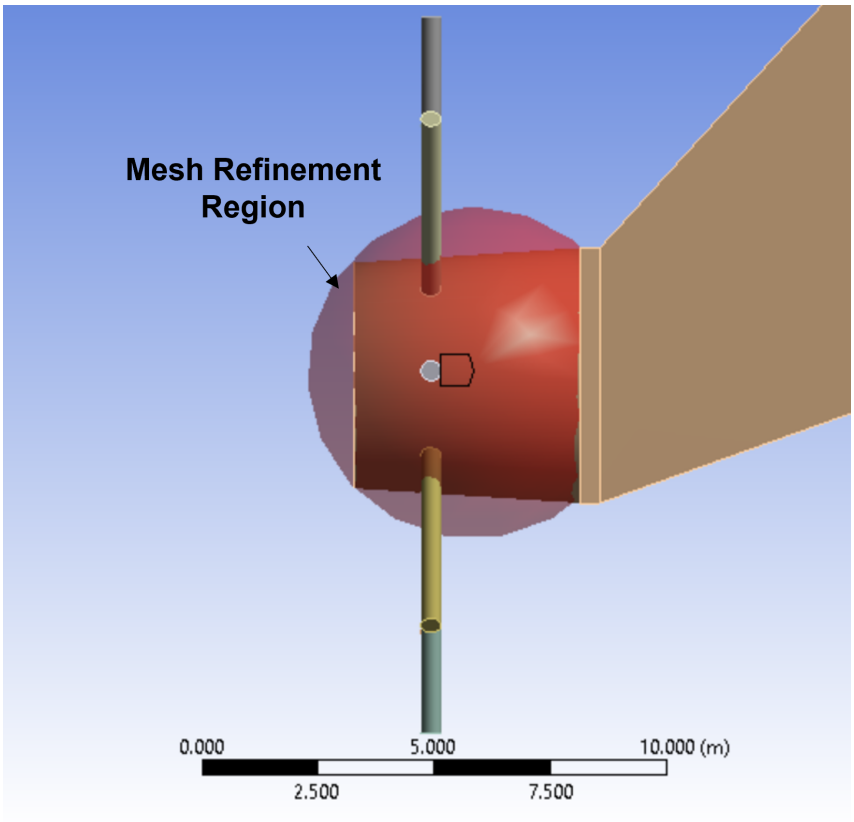


Figure 3.18: Volume of mesh density variation.

The velocity, temperature and turbulence profiles at the face of SP1 were recorded for each of the five mesh configurations. Table 3.4 presents a comparative evaluation of both the average and peak variables at the plane of interest.

Table 3.4: Mesh independence comparison at the primary superheater in a HRSG for MIJ1, MIJ2, MIJ3, MIJ4, and MIJ5.

Variable	MIJ1	MIJ2	MIJ3	MIJ4	MIJ5
Average Velocity (m/s)	7.0	7.0	7.0	7.0	7.0
Peak Velocity (m/s)	29.1	27.4	28.1	29.13	28.5
Average Temperature (K)	971.6	971.7	970.5	971.5	970.2
Peak Temperature (K)	997.0	994.1	1001.5	1001.1	1006.3
Average Re (-)	3,000,000	2,920,000	3,000,000	3,000,000	3,190,000
Peak Re (-)	5,880,000	5,520,000	5,520,000	5,660,000	5,490,000
TKE (J/kg)	75.2	91.0	94.1	95.0	95.1

These values can also be seen plotted in Figure 3.19 below, with error bars showing a 2.5 % variation from the calculated value. This shows, that despite minimal variation between these results, the values for TKE are significantly affected when there is no mesh restructuring within the mixing region, MIJ1. Furthermore, the results become increasingly more stable as the mesh density increases. However, MIJ3 matches MIJ5 in the majority of variables of interest with a significantly reduced computational cost. As such, the methodology of MIJ3 is implemented into all systems in which an additional flow is introduced into the inlet duct. The established

mesh independence ensures that the simulation results are accurate, robust and reflective of physical realities.

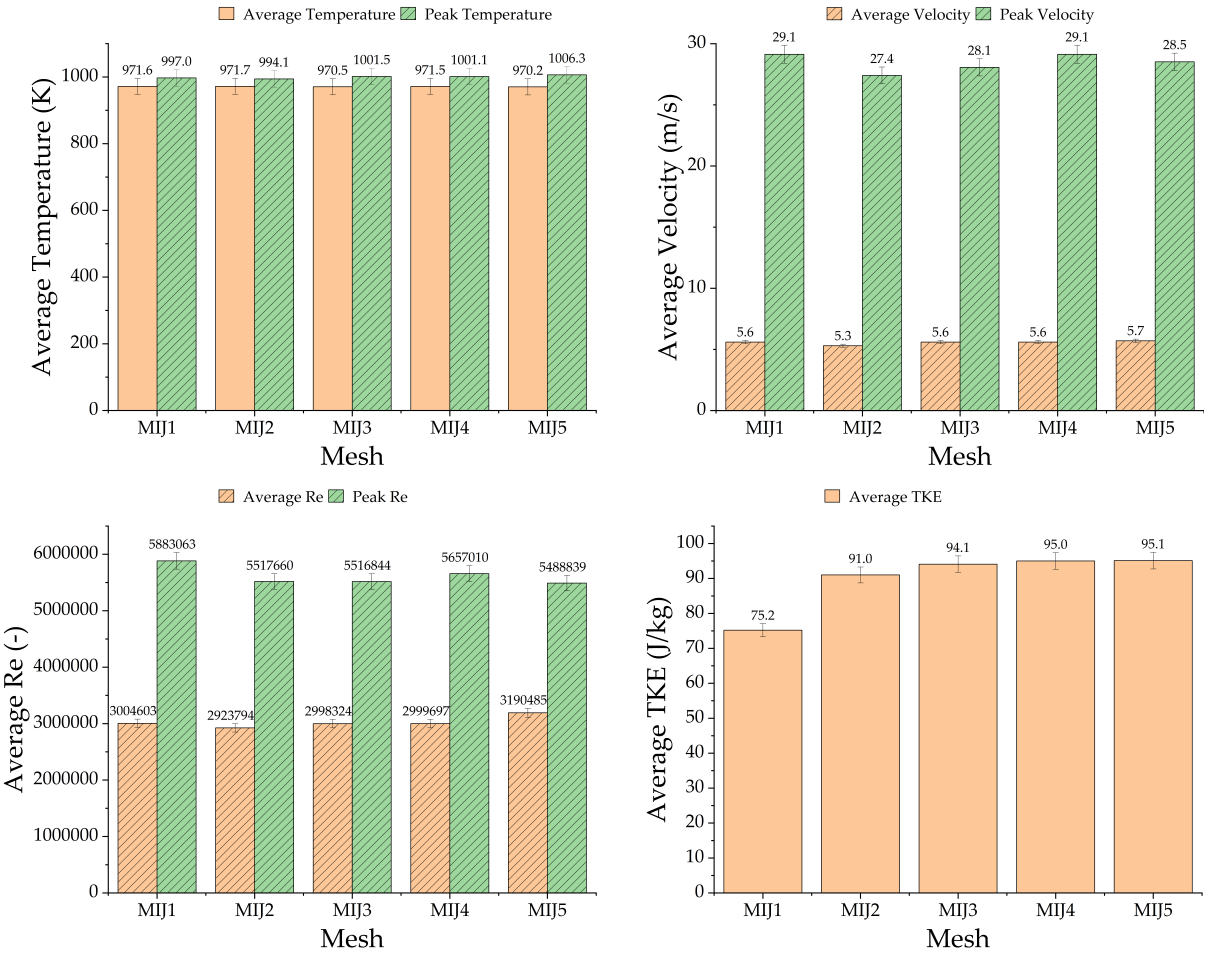


Figure 3.19: Meshing sphere density variable comparison at the primary superheater.

With the mesh validated to ensure accuracy and reliability, the settings utilised to represent the flow, which have been optimised based on published data and validation studies, are outlined in Table 3.5 below. These settings were chosen to achieve a balance between computational efficiency and solution accuracy.

Table 3.5: Overview of HRSG Model Settings

Parameter	Setting
Solver Type	Pressure-Based
Turbulence Model	k-ϵ (Standard)
Time Stepping	Pseudo-Transient
Spatial Discretisation	Second-Order Upwind
Convergence Criteria	10^{-6}
Walls	No-Slip Condition
Inlet Velocity	Varied
Outlet Pressure	Ambient

Continued on next page

Table 3.5 continued from previous page

Parameter	Setting
Wall Boundary	Adiabatic
Mesh Type	Structured
Total Cells	5,659,807
Density	Temperature Dependent (Polynomial)
Viscosity	Temperature Dependent (Polynomial)

3.6 HRSG Integration Feasbility

Having confirmed the viability of the mesh, it is applied to investigate the integration of stored heat from a UHTS system into a HRSG. The geometry used is representative of the HRSG type that is commonly found in CCGTs. This section presents a detailed analysis focusing on the impact on temperature, velocity, turbulence, and pressure requirements. This analysis employs a comprehensive CFD model, gauging the efficacy of integration by examining critical flow metrics.

The integration of heated air was investigated at a range of angles, inlet velocities and inlet geometries. Within this investigation, two distinct integration methods are investigated. The first introduces heat to supplement the flow from the outlet of a GT, increasing the mass flow rate passing through the HRSG by 10 %, an addition of 44.7 kg/s. The second fully replaces the flow from the GT, matching the mass flow rate entering the HRSG. A scenario where the GT flow is partially displaced is not tested here as this would involve varying the operating conditions of the GT, which would affect the overall efficiency of the combined cycle. However, it would be beneficial to investigate these conditions in the future as the addition of heat may increase overall efficiency by allowing the HRSG to operate at its baseload temperature.

Whilst these systems will not be the most efficient integration mechanisms for the introduction of flow, they are substantially easier to implement retroactively to a pre-existing system. This is due to the external nature of the engineering work not requiring full disassembly of the system. As previously discussed, additional heat could be added to the system through the same inlet system as found in supplemental combustion systems, but this requires significant engineering work, especially in accounting for the increased flow rates associated with heated air input, rather than a fuel inlet.

As such, the flow must be suitably mixed and redirected within the inlet duct. Impinging flows are widely used industrially to enhance fluid mixing as a velocity shear is created between the fluid from the jet entering the bulk fluid (Chu et al., 2023; Kashinskii et al., 2016). The dynamic interaction between impinging jets and the bulk fluid significantly influences heat transfer rates and flow uniformity, necessitating an understanding of flow dynamics and optimisation strategies for impingement angles.

The effect of introducing air via a range of retrofit designs on the flow characteristics of temperature, velocity and turbulence at a plane located at a cross-section at the surface of SP1 is discussed below. Additionally, the effect this has on the required inlet pressure is also discussed. These are compared against a system which has no retrofit implemented, to ensure that the integration of additional flow does not damage the HRSG.

3.6.1 No Retrofit Case

The Case 0 model of the HRSG gives values for the system when no alteration is made to the geometry, inlet flow temperature, or mass inlet. Therefore, the temperature, velocity and turbulence values are considered to be within the design parameters for the HRSG. Any change in these variables, when a retrofit is introduced, can be compared with these values to establish if the retrofit is likely to cause a failure in the system.

Temperature, velocity, Re, and Turbulent Kinetic Energy are primary factors at SP1 as they not only directly influence the heat transfer efficiency but also affect the physical integrity of the system. Any retrofit should aim to match or improve these parameters in order to optimise or enhance thermal performance, structural integrity, and operational efficiency of the HRSG.

The results at the plane of investigation for Case 0 are given in Table 3.6.

Table 3.6: Case 0 HRSG results at the primary superheater.

Bulk v	Peak v	Bulk T	Peak T	Bulk Re	Peak Re	Bulk TKE
m/s	m/s	K	K	-	-	J/kg
5.6	23.0	883.6	883.9	2,950,000	5,930,000	66.4

Figure 3.20 below shows the distribution of temperature, velocity, Re and TKE over the face of SP1. Due to the uniformity of the temperature, contour lines have been used to show where there is any minor temperature variation. These distributions are discussed below the figure.

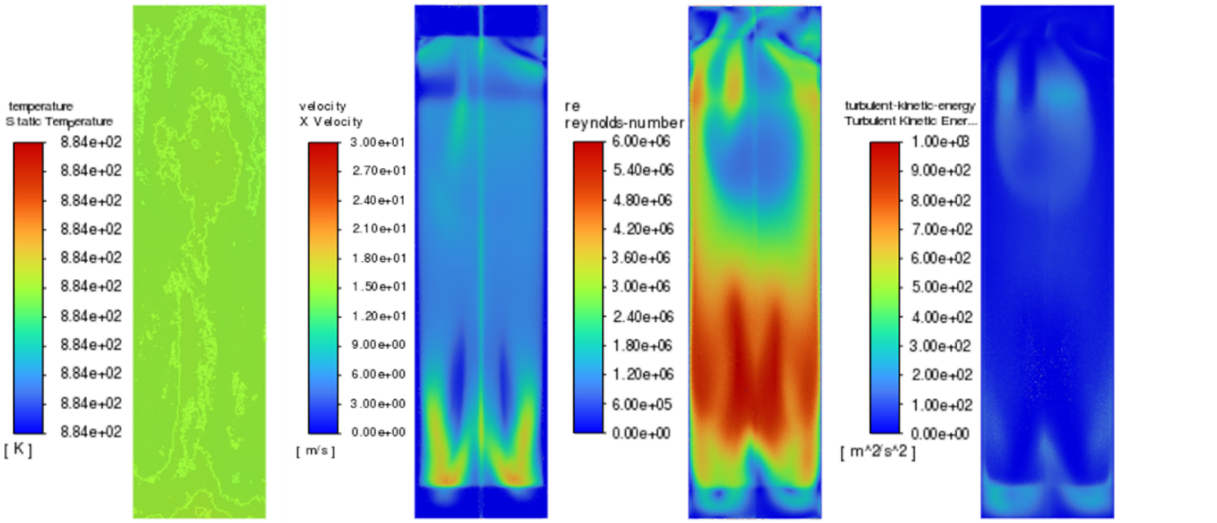


Figure 3.20: Contours of temperature, velocity, Reynolds Number and Turbulent Kinetic Energy at the primary superheater for Case 0.

The temperature contour reveals a high level of homogeneity across the superheating surface. The expansion in the geometry reduces the velocity of the exhaust gases, which promotes heat transfer due to increased residence time (Chantasiriwan, 2024). The absence of

distinct thermal layers indicates effective thermal mixing, a desired characteristic within the superheater for uniform tube metal temperatures and reduced thermal stresses (Nawaz et al., 2023). The homogeneity indicates that the flow expansion and distribution are well-tuned to promote uniform steam temperatures and mitigate thermal stress risks within the superheater tubes.

The velocity contour shows some variation across the surface, with a higher velocity in the region aligned with the GT inlet. This is expected due to the driving force of the GT exhaust flow. However, this variation is minimal, indicating a well-balanced flow distribution that allows for uniform convective heat transfer. As the HRSG geometry expands upwards from the inlet, flow deceleration occurs, increasing the uniformity of flow velocity and minimising the impact of the inlet at SP1. The homogeneity of the temperature distribution shows that the HRSG design actively manages the velocity over the surface of the tube bank, ensuring that the velocity does not significantly impact the heat transfer to the steam.

The high Re indicates a fully turbulent flow at SP1, ensuring effective mixing of the hot gases and contributing to the uniformity in temperature (Zametaev and Lipatov, 2021). Due to the consistent geometry and uniform temperature, the higher velocity at the inlet region would contribute directly to a higher Re in the same region since velocity is a multiplier in the Re formula.

The turbulent kinetic energy appears to be well distributed across the superheating surface, apart from a slight increase near the top of the region. This is caused when the flow encounters the tube bank, which changes the direction of a section of the main flow path. Recirculation zones result in increased TKE values in these areas, where the flow is perpendicular to the tube bank (Zhang et al., 2020). The recirculation regions acts to stabilise the downstream flow at the superheater surface, damping fluctuations and contributing to the low TKE observed in high Re regions. This stabilisation effect is crucial in maintaining efficient heat transfer and flow stability across the superheater surface. This also further demonstrates that the porous media approach, used to simulate the superheater tubes, effectively maintains a high level of turbulence across the superheater section. This is reflected in the uniform turbulent kinetic energy distribution, which correlates well with the observed temperature homogeneity.

3.6.2 Select Retrofit Cases

The results of this study illustrate the potential opportunities and challenges involved in integrating a UHTS system with a HRSG. However, the integration of a UHTS system into the inlet duct of a HRSG is deemed to be viable and provides the ability for power generators to boost their operational efficiency and environmental sustainability.

Retrofit Case 1-b-100 is a promising option for straightforward flow supplementation integration, requiring minimal structural modifications, thereby offering a practical solution for existing power plants. Conversely, Retrofit Case 3-d-300, although more intricate in implementation, presents an opportunity for significant environmental benefits with a full flow replacement. Table 3.7 shows the conditions in each of these two cases.

Detailed insights of these findings are outlined in the following section. They outline viable pathways for upgrades while highlighting the necessity of meticulously evaluating system dynamics alongside environmental considerations.

Table 3.7: Flow conditions at SP1 of optimal retrofit cases for a supplementation retrofit and a replacement retrofit.

Model	Temperature (K)	Velocity (m/s)	Re (-)	TKE (J/kg)
Base	883.6	5.6	2,950,000	66.4
Supplement	972.5	7.0	2,720,000	89.4
Replacement	883.6	5.6	1,470,000	645.0

Flow Supplementation

Cases 1 and 2, which introduce supplementary heated flow from the UHTS into a bulk flow from the outlet of a GT are explored to investigate their impact on the temperature, velocity, Re and turbulent kinetic energy at SP1 and the required inlet pressure. A comparison of these values is given in Table 3.8.

Table 3.8: Primary superheater surface flow properties with flow supplementation.

Case	T (K)		v (m/s)		Re (-)		TKE (J/kg)	P (Pa)
	Average	Max	Average	Max	Average	Max	Ave	Inlet
0	883.6	883.9	5.6	23.0	2,950,000	5,930,000	66.4	6,250
1-a-100	971.5	1,025.9	7.0	24.6	2,780,000	5,610,000	79.4	9,654
1-a-200	967.2	1,024.5	7.0	29.9	2,980,000	5,810,000	70.0	9,478
1-a-300	966.8	1,009.3	7.0	33.1	2,950,000	5,520,000	85.6	9,392
1-b-100	972.5	1,013.6	7.0	22.7	2,720,000	5,120,000	89.4	9,714
1-b-200	968.7	1,006.7	7.0	28.1	3,160,000	5,450,000	48.9	9,552
1-b-300	967.5	996.7	7.0	29.8	3,370,000	5,270,000	4.3	9,466
1-c-100	970.9	1,013.2	7.0	23.3	2,250,000	5,620,000	211.8	9,948
1-c-200	971.6	997.0	7.0	27.1	3,000,000	5,880,000	75.2	9,859
1-c-300	970.1	992.4	7.0	28.6	3,370,000	5,840,000	46.4	9,827
1-d-100	969.2	995.9	6.9	21.2	1,480,000	4,330,000	14.7	10,263
1-d-200	967.7	990.7	6.9	25.0	2,000,000	5,990,000	308.2	10,358
1-d-300	962.7	984.1	6.9	19.1	1,910,000	6,160,000	366.7	10,686
2-a-100	977.2	1,098.2	7.0	31.5	3,280,000	5,900,000	40.0	9,715
2-a-200	964.2	1,075.0	7.0	41.9	3,380,000	6,000,000	61.6	9,507
2-a-300	963.5	1,036.0	7.0	42.7	3,180,000	7,000,000	128.3	9,320
2-b-100	974.0	1,056.5	7.0	29.2	2,960,000	5,760,000	59.3	9,835
2-b-200	964.2	1,059.3	6.9	31.5	3,340,000	5,730,000	56.2	9,481
2-b-300	962.7	1,067.3	7.0	46.5	3,520,000	6,530,000	97.1	9,712
2-c-100	971.3	1,025.6	6.9	38.8	3,530,000	8,770,000	196.3	10,994
2-c-200	968.9	1,010.6	7.0	54.4	3,330,000	9,730,000	310.4	11,624
2-c-300	964.7	1,001.7	7.0	50.4	3,510,000	12,400,000	442.7	12,225
2-d-100	967.3	1,015.9	7.0	45.0	3,800,000	10,300,000	255.9	11,334
2-d-200	968.9	1,010.6	7.0	46.4	3,460,000	9,730,000	310.4	12,473
2-d-300	967.8	993.7	7.0	63.0	3,570,000	13,300,000	517.1	13,556

The wide range of variations in flow conditions of each of the systems in Cases 1 and 2 illustrates the precision required in retrofitting HRSG systems, where the objective is to augment existing capabilities rather than to fundamentally re-engineer them. Based on this, Case 1-b-100 is identified as the retrofit strategy that best integrates with existing operational parameters, matching the Case 0 parameters without exceeding the allowable temperature.

This is seen as there is less than a 5 % variation in velocity, Re, TKE whilst producing a bulk temperature increase of 85.1 K without exceeding the maximum allowable temperature. This is vital where preserving the integrity and established efficacy of the existing system is essential, ensuring that the supplementary retrofit components are suitably integrated, thereby enhancing, rather than disrupting, the established flow and thermal patterns.

Based on this, the benchmark for supplementary flow integration systems utilises a multi-pipe inlet with a 60° inlet angle and a lower 100 m/s flow velocity. This indicates that it is possible to boost the outlet of a HRSG using a UHTS system by generating a bulk increase in temperature that may increase the output of the HRSG whilst maintaining adherence to design flow conditions to prevent system damage. This makes it an attractive option for power plants looking to upgrade with minimal downtime, offering a feasible upgrade path that enhances efficiency while being conscious of environmental and operational constraints.

The findings from Retrofit Case 1-b-100 demonstrate minimal velocity change, suggesting this approach could be integrated into existing HRSG systems with minimal structural modifications, making it attractive for power plants looking to upgrade with minimal downtime.

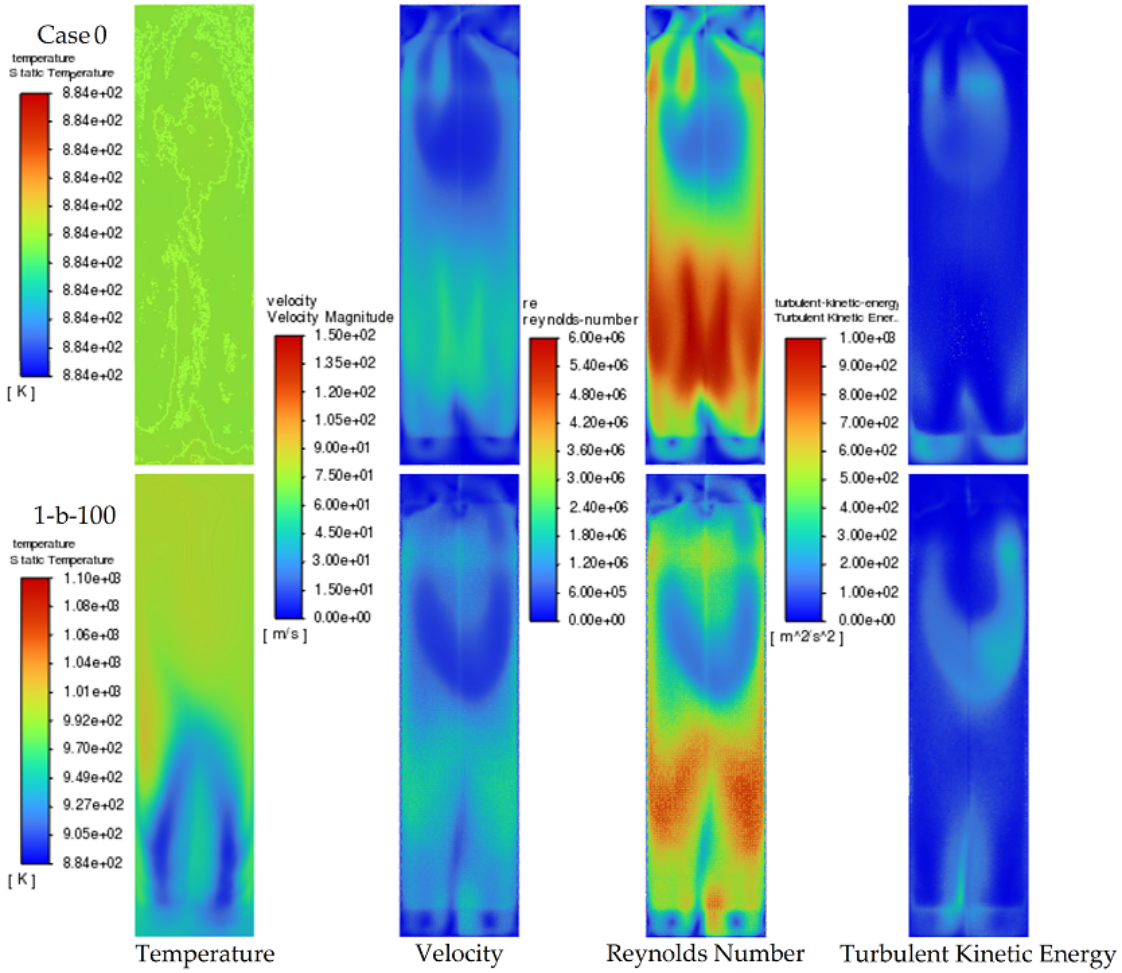


Figure 3.21: Comparison between Case 0 and Case 1-b-100 of flow properties at SP1 when supplementing the GT outlet flow.

However, there is a significant temperature variation between the bulk and peak temperatures caused by hotspots, which pose challenges in thermal stress management, potentially impacting the longevity and reliability of the HRSG system. The greatest temperature variation is found centrally in the bottom section of the HRSG. This aligns with the inlet duct and is caused by the incomplete mixing of the heated additional air into the cooler flow from the GT outlet. The lack of mixing here is caused by the jet effect as the flow exits the inlet and enters the main body of the HRSG. This jet will tend to maintain its velocity and direction due to its momentum, leading to a potential increase in velocity in the regions that align with the outlet. These are highlighted in Figure 3.21.

Regions of elevated temperatures, or hot spots, such as those seen here may require an additional retrofit. Strategically placed thermal blankets could help manage these temperature variations, thereby reducing thermal stress and enhancing the system's operational stability.

This heterogeneity of the temperature suggests there is insufficient mixing to produce a uniform distribution. This results in variations in material properties and affects heat transfer rates and system performance. The non-uniform temperature distribution in Case 1-b-100 can lead to areas of heightened thermal stresses, potentially compromising the integrity of the system and the quality of the output. Therefore, this case would benefit from an enhancement in mixing to achieve a more homogeneous temperature profile to optimise the process efficiency and safety. Enhancing mixing could involve the introduction of baffles to promote better thermal homogeneity.

Additional upgrades may be required to enhance thermal homogeneity. In a retrofit system, these may include an expansion and contraction in the duct in the form of a diffuser, or an increase in duct length by curving the duct away from the inlet to the HRSG before bringing it back. If the distance between the GT and HRSG could be increased, moving the retrofit further from the HRSG inlet would allow for more in-duct mixing, increasing thermal homogeneity. However, each of these systems would increase pressure losses which would have to be accounted for.

Overall, Retrofit Case 1-b-100 presents a balanced approach, offering a feasible upgrade path that enhances efficiency. Moreover, this retrofit aligns well with current environmental regulations, offering a pathway to reduce carbon footprint while maintaining operational efficiency. Additional upgrades to enhance mixing, and their effect on the pressure drop should be examined in further work.

Complete Replacement

Cases 3 and 4 fully replace the outlet flow from a GT using a UHTS. When converting a HRSG from a GT-driven system to a fully renewably driven system, although the inlet is redesigned, the rest of the HRSG will remain the same. As such, the flow from the UHTS is diluted in order to maintain the same temperature as the GT outlet. The same flow limitations that apply to Cases 1 and 2 also apply to Cases 3 and 4. As mentioned previously, a geometry for Case 3-a-100 was unable to be produced due to the limited available area on the inlet duct. A comparison of these values is given in Table 3.9.

Table 3.9: Primary superheater surface flow properties with complete flow replacement.

Case	v (m/s)		Re (-)		TKE (J/kg)	P (Pa)
	Average	Max	Average	Max	Ave	Inlet
0	5.6	23.0	2,952,568	5,930,856	66.4	6,250
3-a-100	N/A	N/A	N/A	N/A	N/A	N/A
3-a-200	5.6	34.2	2,030,000	10,100,000	508.3	6,717
3-a-300	5.6	35.7	1,820,000	10,700,000	799.0	7,241
3-b-100	5.6	37.0	2,940,000	7,960,000	177.8	7,316
3-b-200	5.6	27.8	1,390,000	7,640,000	520.7	7,524
3-b-300	5.6	57.8	1,750,000	9,670,000	795.5	8,307
3-c-100	5.6	46.8	2,990,000	8,510,000	205.0	7,810
3-c-200	5.6	26.5	1,670,000	7,620,000	557.8	7,588
3-c-300	5.6	41.1	1,660,000	8,510,000	733.7	7,698
3-d-100	5.6	40.5	2,990,000	9,270,000	273.5	8,379
3-d-200	5.6	17.4	1,250,000	4,060,000	404.0	7,483
3-d-300	5.6	27.0	1,470,000	6,220,000	645.0	7,717
4-a-100	5.6	37.4	2,540,000	9,030,000	351.2	12,318
4-a-200	5.6	58.7	2,900,000	13,300,000	513.4	29,471
4-a-300	5.7	84.9	3,210,000	16,000,000	604.6	59,665
4-b-100	5.7	99.3	3,140,000	20,300,000	963.3	23,162
4-b-200	5.7	149.9	4,190,000	28,300,000	1,462.0	66,363
4-b-300	5.7	161.2	5,610,000	34,300,000	1,377.2	140,952
4-c-100	5.7	114.9	3,310,000	23,200,000	1,124.6	28,288
4-c-200	5.7	149.6	4,970,000	30,800,000	1,428.4	69,218
4-c-300	5.7	152.4	3,490,000	30,800,000	2,859.3	181,267
4-d-100	5.6	82.1	2,810,000	19,900,000	1,151.1	23,954
4-d-200	5.7	121.4	3,190,000	25,000,000	1,931.4	68,218
4-d-300	5.7	178.6	4,920,000	32,500,000	1,859.6	144,267

For Cases 3 and 4, unlike the supplemental cases, temperature uniformity is achieved in these scenarios due to the flow entering uniformly at 883.75 K, negating the need for temperature evaluation.

The assessment of these full conversion systems thus pivots on understanding how the retrofit influences velocity and turbulence within the HRSG. The impact of velocity and Re provides critical insights into the operational impact of these comprehensive system changes, enabling a focused analysis of fluid dynamics and turbulence characteristics. This approach is crucial in these scenarios, where the alterations are more radical compared to the supplemental cases. This facilitates the identification of the most suitable full conversion retrofit option that aligns with operational efficiency and mechanical integrity objectives.

The case offering the most favourable overall flow properties, and thus recommended for implementation, is identified as 3-d-300. This is because the peak values for velocity and Re show the second least and least divergence from Case 0 respectively, with bulk Re below that of Case 0. This suggests that the alterations made in Case 3-d-300 will likely be the most manageable, as a bulk variation in flow conditions is much easier to monitor than a localised peak. However, even though this system is highlighted as the most suitable for retrofit, the bulk Re shows a significant divergence from the baseline Case 0. A comparison between Case 0 and the selected case is presented in Figure 3.22.

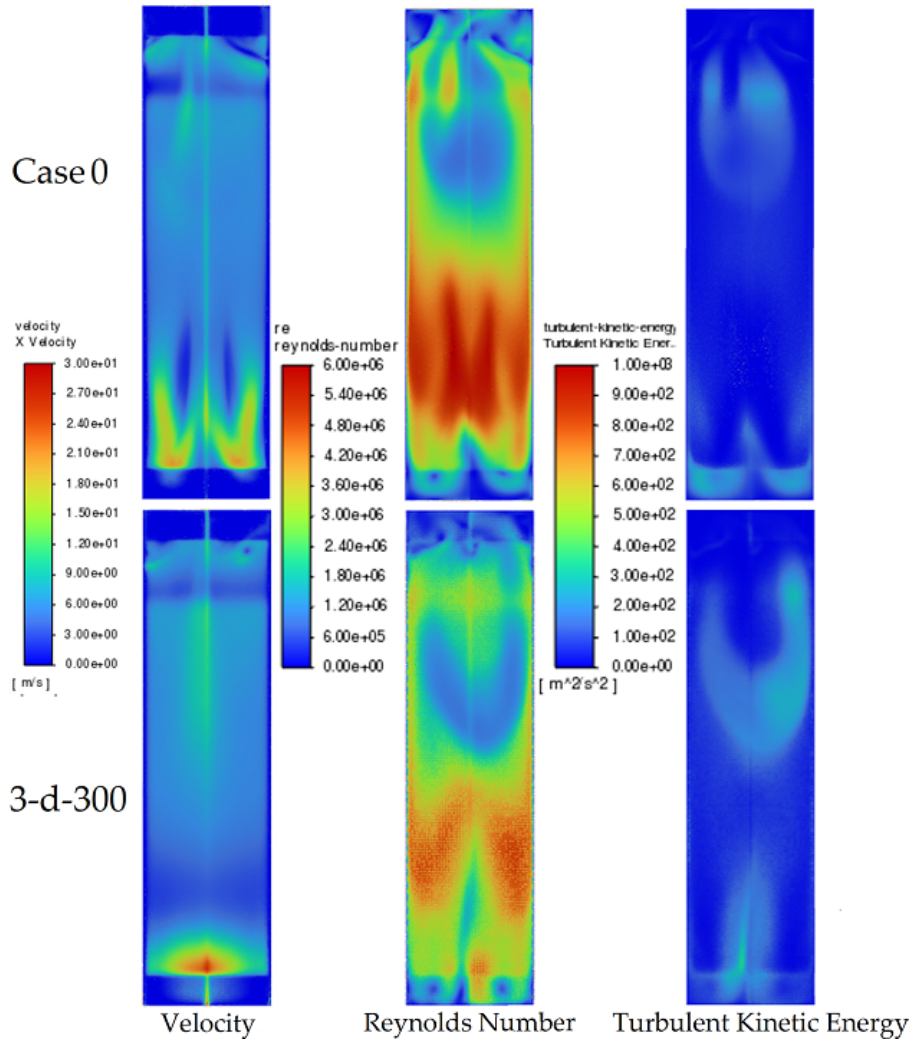


Figure 3.22: Comparison between Case 0 and Case 3-d-300 of flow properties at SP1 when fully converting to heat from the UHTS.

Whilst a multi-pipe inlet is still found to be preferable, a counter-current inlet at 300 m/s is utilised to increase mixing, which minimises the peak values that would be otherwise elevated due to the lack of bulk flow. Case 3-d-300, representative of full conversion systems, portrays a more ambitious retrofit strategy, where the emphasis shifts from augmentation to comprehensive system transformation.

While the case demonstrates some success towards this objective, it does not entirely succeed in fully replicating the baseline conditions. Deviations in average flow conditions, evidenced by higher bulk Re, indicate a marked departure from Case 0. However, it is noteworthy that the peak performance metrics in Case 3-d-300 are efficiently managed, reflecting a targeted strategy to prevent damage caused by high regions of Re. This illustrates a scenario where the retrofit, despite its ambitious goals, encounters limitations in fully mirroring the baseline conditions, especially in average operational states.

As such, the implementation of Retrofit Case 3-d-300 may require a significant redesign of existing systems, posing challenges in terms of cost, time, and technical complexity. Whilst

peak values of the flow conditions do not require attention, an additional retrofit of adjustable dampers may be used to address the low bulk Re. These would allow for more precise control of flow conditions, adapting to different operational demands and enhancing overall system responsiveness. Though this is a significant retrofit, the resulting increase in efficiency would be a valuable outcome, ensuring that the HRSG operates optimally across a wider range of operational conditions, ultimately enhancing system performance and longevity.

However, the economic implications alongside the environmental benefits of fully converting a HRSG to be driven by a UHTS system must be balanced against the expected efficiency gains, with a detailed cost analysis necessary to determine feasibility. A comprehensive cost analysis should be undertaken to encompass both the initial retrofitting expenses and projected long-term operational savings, providing a clearer picture of the payback period and return on investment. This should also account for the future savings of reducing CO_2 emissions by 100 %, aligning it with broader sustainable energy objectives.

3.6.3 Notable Effects

The interplay between the inlet flow from the UHTS and its effects on the temperature, velocity, and turbulence at specific points within the HRSG, along with the associated pressure losses, is a subject of significant importance in optimising the performance and reliability of power generation systems.

Whilst the integration of these retrofits has been seen to be viable, based on the replication of the Case 0 conditions, further analysis of the physical causes of these results is required to highlight the interactions that significantly impact integration.

This analysis sets a foundation of important integration factors for subsequent studies in sustainable HRSG system design.

Improvements in Mixing With A Multi-Pipe Inlet A primary design characteristic that can improve integration is the selection of an appropriate inlet geometry. This is seen in the investigated cases as the geometry of the additional inlet has a noticeable effect on the feasibility of integration. By altering the spatial configuration of the inlet, the mixing profiles and downstream flow distribution can be optimised to enhance heat transfer efficiency and minimise potential flow-induced wear on the superheater tubes.

The geometric configuration of the supplementary flow inlet is pivotal in determining the thermal distribution across the HRSG. The multi-pipe inlet systems are found to enhance the mixing of incoming fluid with the bulk flow, making them considerably more suitable for use in a retrofit situation.

This is facilitated by the generation of thicker, more structured impinging jets that maintain their momentum over a longer distance, ensuring a broader interaction surface with the bulk flow. This is because they are less easily diverted and therefore penetrate further into the bulk flow before the vector of their momentum changes. The greater impingement distance allows the jets to penetrate further into the bulk flow before dissipating their energy, increasing the volume of the mixing region. This results in an equalised dissipation of momentum which reduces localised high-velocity zones and allows for increased flow integration. This greater

flow penetration generates a larger surface area contact between the heated impinging fluid and the bulk flow preventing the formation of a high-velocity core or jet.

An increase in mixing is a primary factor to ensure the feasibility of the integration of additional heated air as it directly impacts both the bulk and peak temperature at SP1. The extent to which the flow mixes before reaching the tube bank will directly affect both the bulk and peak temperatures at the tube surfaces, as greater mixing promotes stable and predictable heat transfer. The temperature distribution within the HRSG is a critical determinant of the system's thermal efficiency and the structural integrity of its components.

An increase in mixing within the inlet duct markedly influences the peak temperature due to more effective thermal blending. Increased mixing of the incoming fluid with the bulk flow ensures the thermal energy is more effectively redistributed throughout the system. This causes hot and cold regions within the HRSG to be more effectively homogenised, preventing the formation of localised hotspots.

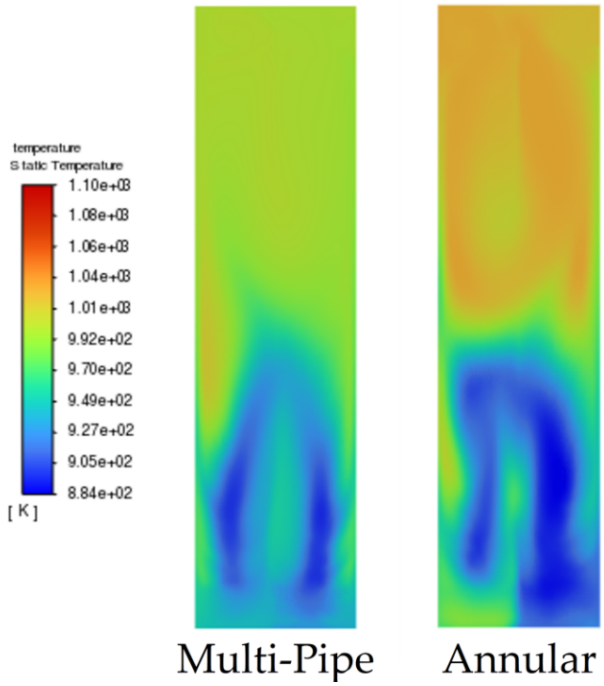


Figure 3.23: A comparison of temperature homogeneity at SP1 for multi-pipe inlet against annular inlet geometries.

The effect of this increased mixing on temperature is presented in Figure 3.23. The annular system shows two discrete temperature regions, with high-temperature flow over the upper half of the tube bank. This demonstrates a significant improvement in mixing using the multi-pipe inlet, resulting in a reduction in regions of elevated temperature and a more uniform thermal profile.

Flow Stratification Caused By An Annular Inlet As outlined in previously, there is a significant reduction in mixing with the annular inlet. If this were to be implemented into a HRSG, it would be detrimental to the tube banks, increasing the likelihood of thermal fatigue.

This reduced mixing exhibited is attributed to the reduced flow penetration from annular inlets, resulting in flow stratification. Flow stratification results in a high-velocity core flow, surrounded by a layer of unmixed flow from the annular inlet.

As the annular inlet system concentrates the flow into a narrower region, it maintains increased velocities as it travels through the duct and into the HRSG. This is a major contributing factor to the decrease in flow mixing. As such, there is a less even flow distribution over the cross-sectional area of the HRSG, resulting in the continuity of high momentum flows and increased localised high-velocity zones, contributing to higher peak velocities.

This prevents the heated inlet air from efficiently normalising with the bulk flow. As a result, a significant thermal gradient produces a heated, low-velocity ring around a cooler core flow, which generates the large temperature variations seen in Figure 3.23.

As a result of these high peak velocities, there is greater downstream turbulence, as this is heavily impacted by velocity. Elevated velocities often increase the Re, corresponding to an intensification of turbulence characteristics (Antonia et al., 2000). Greater variations in temperature caused by the reduction in mixing also influence fluid density and viscosity, thereby further affecting the turbulence. Whilst this is especially pronounced in flows with substantial thermal gradients, where temperature-induced buoyancy effects can give rise to complex turbulence structures (López-López et al., 2019), the changes will have a significantly lesser effect than the high-velocity peaks caused by flow stratification.

Figure 3.24 presents the velocity profile at the transition between the inlet duct and the HRSG body, highlighting the channelling effect produced that results in decreased mixing.

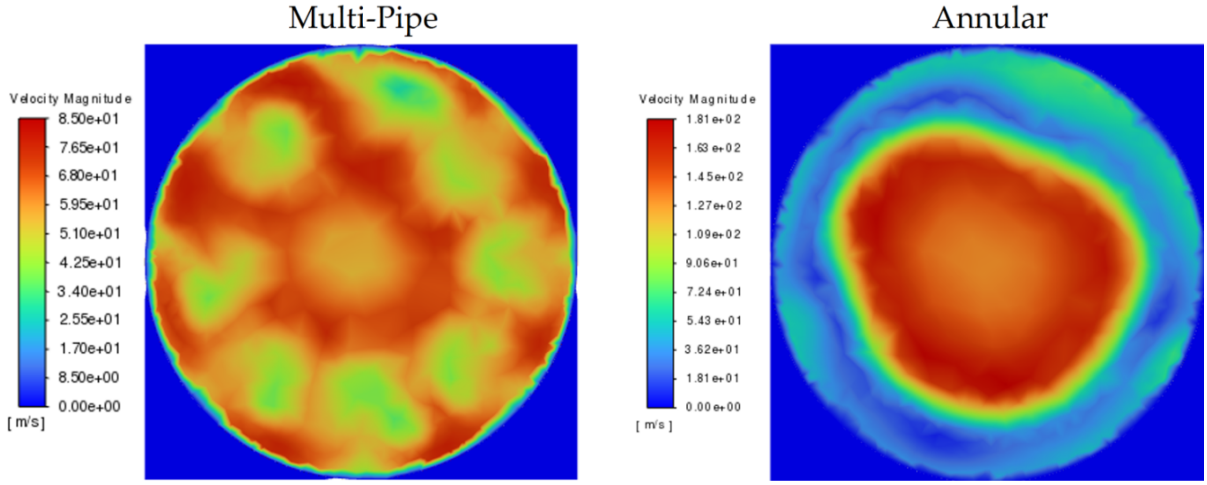


Figure 3.24: Comparison of the duct outlet velocity profile created by a multi-pipe inlet and an annular inlet, with a 90° inlet angle and a 300 m/s inlet velocity.

Whilst an increase in velocity and turbulence will improve the heat transfer at the tube banks, this must be carefully monitored and controlled to prevent damage. These factors create flow-induced vibrations within the tubes and, if at a great enough magnitude, can cause tube failure (Prakash and Ramesh, 2020).

Differing Inlet Angles For Application When flow impinges into a duct, the manner in which the fluid streams collide, interact, and redistribute energy is a crucial determinant of

the downstream viability of the retrofit. Angles that align with the natural flow path can enhance aerodynamic efficiency, while angles that oppose the flow direction may introduce turbulence and energy dissipation. This phenomenon aligns with findings from Liang et al. (2023), indicating that the supplementary flow, integrating with the established flow, increases the overall turbulence.

As such, when considering flow supplementation, the 60° inlet is found to most accurately recreate the downstream flow conditions of Case 0 and minimises variation between bulk and peak quantities. This indicates that, of the inlet angles tested, a 60° inlet produces the optimal angle of attack to minimise flow separation. This inlet provides a smooth transition into the bulk flow, producing fewer disturbances, hence greater flow uniformity.

The moderate inlet angle of 60° creates a balanced distribution of shear forces along the impinging surface. This balance contributes to a more homogeneous flow profile. Additionally, at this inlet angle, the flow is less likely to separate from the impingement surface compared to steeper angles due to a reduction in TKE, allowing the boundary layers to remain thicker. This helps to maintain a more stable boundary layer and induces a less abrupt boundary layer disruption, resulting in a more uniform flow distribution. In contrast, more extreme angles can introduce a range of issues such as non-uniform shear forces; flow channelling and boundary layer disruption, which generate flow instabilities that would not be present in the developed flow from the GT outlet.

Jet Interactions When considering the full conversion system, due to the lack of entraining flow, the interactions between the inlet flows and the walls become far more significant. A critical factor that affects these interactions is the effective flow area. The effective flow area refers to the portion of the cross-sectional area through which the fluid can pass before encountering a redirecting surface. When there is an inlet angle into a duct, the effective flow area is affected by the deviation of the flow direction from the axial direction of the duct. With a more perpendicular inlet angle, the area through which the fluid can flow effectively in the axial direction is reduced. The more the inlet angle aligns with the flow direction, the less energetic interaction the flow has with the opposite duct walls. This is depicted in Figure 3.25. As such, a more perpendicular inlet angle reduces the effective flow area, affecting the fluid velocity and pressure.

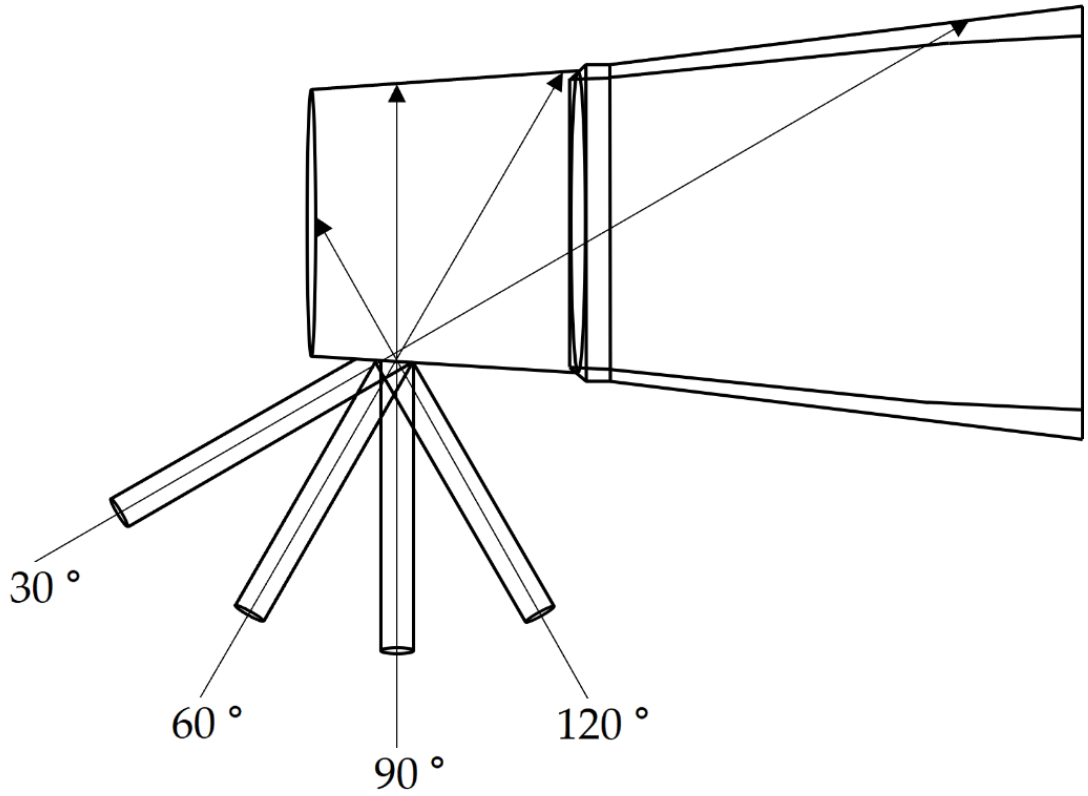


Figure 3.25: Visualisation of flow area for each inlet angle.

Additionally, when the inlet angle is closer to 90 degrees, the incidence angle between the incoming streams from the opposite side of the duct decreases. This promotes a more intensive mixing of the fluids, as their interactions are significantly more energetic due to the more direct nature of the particle collisions. This causes an increase in the magnitude and rate of vortex formation. Additionally, the magnitude of the transverse component of the inlet flow is also greater, requiring more energy for redirection. These interactions result in pressure losses caused by frictional effects and the dissipation of energy from turbulent vortices.

At steeper inlet angles, the flow jets merge, maintaining higher downstream velocities. This induces greater mixing, but results in increased average turbulence, that can cause damaging vibrations within the tube banks.

However, these systems result in a decrease in peak turbulence due to the chaotic nature of the flow interactions. This leads to energy dissipation and reduced peak velocities. Due to the inherent relationship between velocity and turbulence, the downstream tube banks experience lower peak turbulence, which is less likely to cause damage due to the lower localised intensity.

The annular inlet system generates fewer jet interactions, due to the reduced penetration distance, as outlined in Section 3.6.3. This is particularly prevalent at lower inlet angles as the flows are not actively directed at each other. As such, systems with these inlet geometries do not experience the effects of jet interactions as keenly as the systems utilising the multi-pipe inlet geometry. This promotes stratified flow distribution with higher peak velocities and turbulence.

Viability of High Angle Inlets Obtuse angles, such as the 90°or 120°inlets cause an increase in pressure losses. As such, these inlet angles are intuitively less appealing when considering integration into a system which aims to minimise energy losses in order to maximise efficiency.

These pressure losses occur as, when fluid streams collide, the flow direction is disrupted, causing the fluid to separate from the boundary layer. Such impingement leads to the formation of vortices, the creation and sustenance of which require energy from the fluid flow. The generation of turbulence via these pathways dissipates energy and results in pressure losses.

Further energy losses can be attributed to the conservation of momentum when redirecting the impinging flow. The inlet pipes distribute the momentum of the supplementary flow across a wide area within the inlet duct. This flow reversal is seen in Figure 3.26.

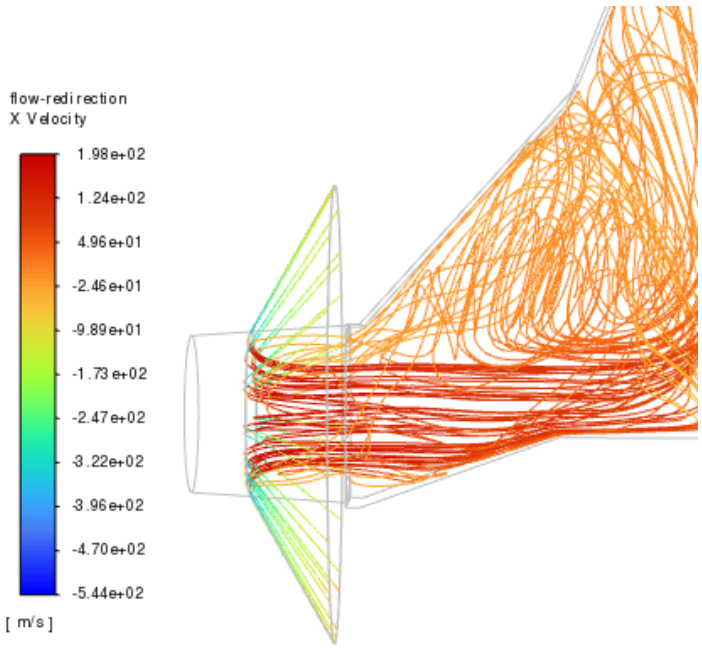


Figure 3.26: Velocity pathlines showing flow reversal from a counter-current inlet when redirected by a bulk flow.

Additionally, the kinetic energy of the fluid streams is also partially converted into other forms of energy, such as heat, due to inelastic collisions between fluid particles and interactions with the duct. This energy dissipation contributes to the overall pressure drop in the system.

When using an inlet angle of 120°, a combination of these phenomena can dissipate sufficient energy to cause a reduction in peak velocity at SP1 when compared to Case 0. This would result in a reduction in heat transfer at the tube bank surface.

In addition to the velocity reduction, the shear forces introduced by the 120° inlet lead to a less stable flow, resulting in uneven velocity distributions. This can be seen when comparing the Re and TKE as, though the 120° inlet results in a reduced velocity and thus a lower Re, the increase in fluctuations results in a greater TKE at the surface of interest. Case 1-d-100 is depicted in Figure 3.27. The increase in turbulence also results in greater pressure losses throughout the system.

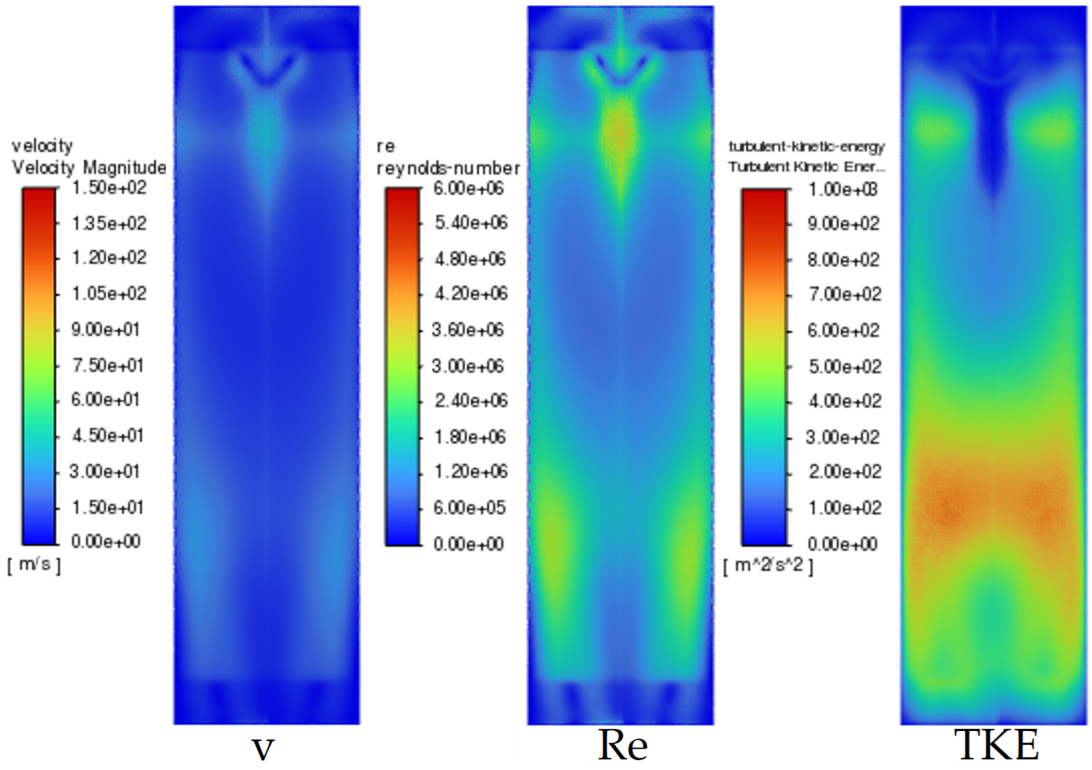


Figure 3.27: Comparison of contours of velocity, Reynolds Number and Turbulent Kinetic Energy at the primary superheater.

The pressure losses generated by these systems make them non-viable for implementation in a flow supplementation system. This is because an increase in pressure loss in the exhaust path from the GT to the HRSG can lead to back pressure on the GT. Back pressure can decrease the exhaust flow, reducing the GTs efficiency as the turbine would have to work against an off-design pressure differential. This would lead to increased fuel consumption for the same power output.

Additionally, increased pressure losses affect the operational flexibility of the system. The ability to ramp up or down quickly in response to changing demand could be hampered, as the system will respond more slowly to changes in operational settings due to the inefficiencies introduced by the increased pressure losses. The combined effect of reduced efficiency, increased fuel consumption, and decreased flexibility would have a significant economic impact on the operation of the combined cycle, affecting the competitiveness of the plant in the electricity market.

However, this is not the case for a full conversion system. In this case, the inlet flow completely replaces the outlet of a GT. Without the influence of an entraining mass flow from the GT outlet, the flow is driven by the pressure differential throughout the system. As such, the overall efficiency would not be reliant on a highly optimised GT system. Therefore, an increased pressure drop can be accounted for with additional inlet pressure. Though this would require additional energy, it would not affect any upstream operations.

The angle of flow impingement directly influences the thermal boundary layer development

and the heat transfer characteristics at the superheater surface. Angles promoting more effective impingement can enhance heat transfer rates but may also increase thermal stresses.

Residence Time:Mixing Balance Increasing the inlet velocity of co-current flow impacts the heat transfer and mixing within the duct. Higher inlet velocities promote turbulence in the impinging flow which enhances the mixing efficiency of the impinging jets. This is caused by an increase in shear forces within the fluid. Shear forces contribute to the generation of turbulence by causing fluid layers to move at different speeds. As inlet velocity rises, the intensity of shear forces increases, leading to higher TKE. An inlet velocity increase facilitates the transfer of energy across different length scales in a turbulent flow field. A greater inlet velocity contributes to a higher overall energy input into the system, which can cascade down to smaller scales, leading to increased TKE throughout the flow.

Additionally, increased inlet velocity causes a thinning in the thermal boundary layers at the heat exchange surfaces. Thinner boundary layers facilitate more efficient heat transfer by reducing the insulating effect of stagnant fluid layers near the surface (Venkateshan, 2021). This ensures that the heat is transferred more effectively, reducing the temperature differential between the surface and the bulk flow.

In co-current configurations, however, elevated inlet velocities also heighten both bulk and peak flow velocities. Though this is more pronounced in the annular systems, it is the case regardless of inlet geometry. This is primarily driven by kinetic energy conservation and fluid dynamics principles. When the supplementary flow enters the inlet duct at an elevated velocity, it has greater kinetic energy, directly proportional to the square of its velocity. The conservation of energy dictates that this excess kinetic energy must be distributed within the system. As the supplementary flow mixes with the primary flow, a portion of its kinetic energy is transferred to the bulk flow, increasing downstream velocity.

When the inlet velocity is increased, the flow moves through the inlet duct more quickly. This translates to shorter residence time, meaning the fluid spends less time within the inlet duct. While higher velocities can enhance turbulence and improve thermal mixing by creating more chaotic flow patterns, the benefits are negated by the fact that there is less time for this mixing to occur. Consequently, despite the intensified mixing actions, the overall flow within the duct may not achieve a uniform velocity and turbulence profile at SP1. This lack of uniformity can lead to areas within the flow that are not well mixed, impacting the efficiency of heat transfer processes downstream and also causing structural damage.

Furthermore, when jets of fluid enter the duct at high velocities, particularly when directed at acute angles, their momentum makes them less likely to blend with the slower-moving bulk flow. In such scenarios, the high-velocity jets tend to maintain their speed and direction longer, exiting the duct without significantly imparting their momentum to the surrounding fluid. This resistance to dissipation means that the energy carried by the supplementary flow is not effectively transferred to the primary flow, causing localised regions of high velocity as the flow progresses toward SP1. These peak velocities indicate areas within the flow where the velocity is significantly higher than the surrounding fluid, potentially leading to inefficiencies in the system, as the flow is not uniformly mixed and energy transfer between the jets and the bulk flow is suboptimal.

Bulk Flow Interactions

When comparing the profiles at SP1 between the supplementary retrofit systems (Cases 1 and 2) to the full conversion retrofit system (Cases 3 and 4), the bulk flow has a significant impact on the downstream flow field.

With a supplement to the bulk flow from a GT, an increase in velocity is expected as the mass flow rate is greater than Case 0. This is due to the additional flow entering the system introducing more energy into the closed system, contributing to a higher total momentum and, therefore, a greater downstream bulk velocity.

However, where supplementary flow is added, the resultant mixing dissipates energy and creates a uniform composite flow field. This is because the pre-existing bulk flow has a tempering effect which dilutes jet-induced turbulence. As such, the overall turbulence levels do not reach the heights observed in full conversion scenarios.

Without the flow tempering effect in the full conversion systems, the jets maintain coherence and momentum for a longer distance within the duct. The jetting effect creates distinct high-velocity regions that persist further downstream from the inlet, with no pre-existing flow to dissipate or redirect it. This prevalence of persistent jets reduces the mixing within the system, generating a greater differential between the bulk and peak flow properties (Wang et al., 2017).

This non-uniformity in the flow results in greater pressure loss. As such, flow integration efficacy in the full conversion systems is solely shaped by the inlet conditions. If these inlet parameters are not optimally designed, the system will experience increased flow disturbances, separation, and inefficient flow patterns, further impeding the development of higher downstream velocities.

3.6.4 Comparison of Supplementary and Full Conversion Retrofit Systems

When analysing the retrofit strategies for a HRSG, a comparison focuses on the effect on flow dynamics, such as temperature, velocity and turbulence. Both retrofit strategies aim to achieve a balance between the operational and mechanical implications of the modifications and system efficiency. In the case of supplementary retrofits, the focus is on optimising within the constraints of the existing system, whereas full conversion aims to replicate Case 0 without generating a flow that would require significant structural changes and cause potential operational disruptions.

When comparing the retrofit systems for their effect on flow temperature, the full conversion system was implemented with the aim of maintaining the pre-retrofit inlet temperature by diluting the output of the UHTS with cool air. Consequently, the full conversion system is not designed to increase power output, which is a significant point of difference from the supplementary system. In contrast, the supplementary retrofit consistently demonstrated a substantial increase in temperature, with a minimum rise of 79.1 K noted across all cases. This increase directly enhances the energy input into the HRSG.

However, the full conversion system presents a unique flexibility in temperature control. By modulating the extent of dilution with cool air, the inlet temperature could be elevated. When compared to the supplementary system, this would create a more uniform temperature

distribution within the HRSG. This uniformity arises from the pre-mixed nature of the inlet flow, contrasting with the supplementary retrofits where thermal gradients are more pronounced due to the requirement to mix with the bulk flow within the inlet duct. Note that exploring the full potential of this temperature adjustment in the full conversion system was not covered in the current research, indicating a valuable direction for future studies.

The supplementary system results in smaller velocity variations than the full conversion system. This can be seen in Table 3.10, which shows the average variation in velocity measurements from Case 0 after implementing the retrofit.

Table 3.10: Comparison of average absolute velocity variation from Case 0 between supplementary retrofit, and full conversion retrofit systems.

	Multi-Pipe		Annular	
Re	Supplementary	Full	Supplementary	Full
Bulk v Variation (%)	24.6	0	24.4	1.2
Peak v Variation (%)	17.6	63.2	88.9	403.8

The variation of Re is considerably greater in full conversion retrofits due to the more substantial changes in the flow dynamics and the lack of bulk flow to dampen turbulent effects. While a slight increase in turbulence can aid in heat transfer efficiency, excessive turbulence leads to increased pressure drops and higher energy requirements, along with the potential to cause mechanical damage. Additionally, distinct differences in the impact on turbulence are observed, with the full conversion system causing much larger variations in both bulk Re and peak Re. A table comparing Re deviation between the supplementary and full conversion systems can be seen below in Table 3.11.

Table 3.11: Comparison of average absolute Re variation from Case 0 between supplementary retrofit, and full conversion retrofit systems.

	Multi-Pipe		Annular	
Variation	Supplementary	Full	Supplementary	Full
Bulk Re (%)	16.1	66.3	15.4	36.0
Peak Re (%)	7.2	44.1	185.6	298.2

These results indicate that, when considering the flow properties of velocity and turbulence, the full conversion system will produce a considerably larger variation from Case 0 than the supplementary system.

As such, the integration process of the supplementary retrofit requires comparatively little modification to the existing HRSG infrastructure. The addition of inlet pipework is designed to complement the current setup, allowing for enhancements in performance while retaining the fundamental system configuration and its connection with the GT.

Conversely, the integration methodology in full conversion retrofitting is more complex due to the requirement for a larger inlet flow and detachment from the GT. This detachment is a complete overhaul of the inlet system, fundamentally changing the flow dynamics and requiring an alteration to the control and operation of the system. This approach necessitates a thorough re-engineering of the system, potentially offering further opportunities for optimisation, but would require a more comprehensive implementation strategy.

The use of advanced control systems in both integration methods would enhance the adaptability of the HRSG to fluctuating operational conditions, optimising performance through real-time adjustments to flow rates, temperatures, and pressures.

From an economic standpoint, supplementary retrofits likely require lower investment, which can be attributed to the limited scale of modifications. They represent a cost-efficient method for bolstering system efficiency with renewable energy without necessitating significant capital. Conversely, full conversion retrofits require a higher initial investment but can yield greater long-term economic benefits. Particularly when the retrofit aligns with strategic goals of enhancing efficiency and sustainability, these investments offer potentially higher returns in the long run and are likely to be favoured for their zero-carbon nature. Exploring the scalability of retrofit solutions and the potential for modular implementations could facilitate phased upgrades, allowing for incremental investments and adaptability to future technological advancements.

The environmental benefits derived from supplementary retrofitting are realised through efficiency gains within the constraints of the existing system design. These improvements, though noteworthy, are intrinsically limited by the pre-existing architectural framework of the HRSG system. Regarding the full conversion retrofit, this system offers a substantial opportunity for environmentally sustainable power generation. It leads to a full elimination of emissions and facilitates the integration of renewable energy sources by eliminating the GT and the need for NG combustion.

In summary, when comparing the supplementary and full conversion retrofit approaches, each exhibits unique influences on system dynamics. The supplementary retrofit, requiring fewer modifications, generally impacts the velocity and turbulence less, enabling the increased temperature to enhance efficiency while maintaining structural integrity. This contrasts with the full conversion retrofit, which entails a more significant system reconfiguration and leads to larger variations in flow parameters. Economically, supplementary retrofits are cost-effective for immediate efficiency gains, while full conversions demand higher initial investments due to their increased complexity but offer potentially substantial long-term benefits, especially when integrated with renewable energy sources. Environmentally, both strategies contribute to sustainability goals, with the full conversion approach having a more pronounced impact due to its potential for significant emissions reduction. Assessing the potential for integration with the electrical grid and demand response systems could further enhance the value of retrofitted HRSGs, contributing to grid stability and facilitating the integration of intermittent renewable energy sources.

3.7 Summary of HRSG Integration Feasibility

This chapter explores the integration of a UHTS system into a HRSG, focusing on the impact of various retrofit systems. The CFD model used provides insights into the effects of variations in inlet geometry, angle, and velocity and their effects on downstream flow conditions within HRSG systems.

The flow analysis quantifies thermal and fluid dynamic parameter deviations in various retrofit scenarios that aim to enhance system efficiency and environmental sustainability. This

approach shows how inlet condition alterations influence downstream flow patterns, turbulence characteristics, and HRSG efficiency.

Inlet geometry significantly impacts flow distribution within the system. Varying geometries create different flow dynamics, with multi-pipe inlets improving mixing and flow distribution and enhancing thermal management within the HRSG. Conversely, annular inlets cause flow stratification, leading to higher peak velocities and lower uniformity, emphasising the necessity of precise inlet geometry selection for operational optimisation.

The inlet angle is also a key factor in controlling the velocity profile and flow turbulence. An optimal inlet angle contributes to energy efficiency and system longevity. Acute inlet angles increase flow channelling, and obtuse angles increase turbulence and pressure losses, both detrimental to HRSG performance.

The impact of inlet velocity on downstream conditions is evident. Higher velocities in annular systems increase downstream velocities, reducing velocity uniformity and increasing the likelihood of mechanical wear. This underlines the importance of calibrating inlet velocities for a balance between enhanced heat transfer and mechanical integrity.

It should be noted that the interplay between these inlet parameters is complex, where each factor influences and is influenced by the others, creating a dynamic flow environment within the HRSG.

Cases 1 and 2 explore the UHTS integration using a supplementary flow regime, whereas Cases 3 and 4 fully convert the HRSG to be driven by the thermal store. Case 1-b-100, a multi-pipe inlet, at a 60 $^{\circ}$ inlet angle, introducing air at 100 m/s, is identified as the optimal design to effectively boost bulk temperature. This enhances performance while most closely aligning with existing flow conditions.

Conversely, for a more ambitious full conversion, Case 3-d-300, with a 300 m/s, counter-current inlet of a multi-pipe design, produces optimal results. Although this system maintains peak flow characteristics, it faces challenges in replicating the bulk flow properties found in Case 0. This highlights the complexity of retrofitting HRSG systems whilst maintaining ideal flow parameters, though the partial success of this case in replicating baseline conditions gives insight into this retrofit process. As such, future research should focus on developing retrofit strategies that balance performance enhancements with practical system dynamics and operational constraints, and consider incorporating flow control systems to minimise the flow alterations caused by the change of inlet flow.

However, as the heat-exchanging properties of the HRSG are not modelled, it is not possible to quantify the effect on power output due to the implementation of these retrofits. Further work should incorporate this into the model so that the changing flow properties can be directly linked to the thermal efficiency of the system.

These findings emphasise the need for bespoke retrofit strategies that align with specific system objectives, whether supplementation or full transformation. It is crucial to consider the mechanical integrity of the existing system and the effect of variations in the established flow and thermal patterns in HRSG systems. Consequently, the challenges in retrofitting complex systems must be acknowledged. This research demonstrates that achieving replication of baseline conditions with an ambitious retrofit may not always be feasible, however, a viable path toward decarbonisation is highlighted. Retrofit applications are preferred because they utilise existing infrastructure, significantly reducing costs and complexity. As outlined in Section 2.1.5,

retrofitting is much cheaper compared to constructing new systems from scratch. Additionally, retrofitting allows for quicker implementation, minimising downtime and disruption to ongoing operations.

Chapter 4

Brayton Cycle Integration

4.1 Brayton Integration Overview

This chapter seeks to explore the integration of UHTS into the Brayton Cycle, focusing on reducing emission production during combustion. By displacing fuel with renewably sourced heat, the chapter seeks to demonstrate how UHTS can be effectively incorporated into existing gas turbine GT systems, particularly in the context of reducing emissions from NG combustion.

To achieve these goals, CFD is employed to model a hybrid combustion process within a GT combustion chamber. The analysis allows for understanding the impact of preheating combustion air on fuel requirements and emissions of CO_2, CO, and NOx. By examining the effects of varying inlet air temperatures, the chapter identifies how preheating can reduce pollutant emissions while maintaining the required turbine inlet temperature (TIT). The simulations provide insights into the thermal and fluid dynamic behaviour of GT combustion chambers under various displacement scenarios, enabling the evaluation of the feasibility of UHTS integration.

This is achieved by initially modelling a Tay combustion chamber to validate the combustion model against experimental data. This model is then transitioned from the Tay system to the GE DLN 2 series combustion chamber, which is representative of a heavy-duty, power-generating gas turbine. This transition allows for a comprehensive analysis of UHTS integration in a modern and industrially relevant context, highlighting the potential for significant environmental improvements in the currently deployed power generation system.

4.2 Introduction

A large portion of the UK's current peaking plants are NG-fired GTs, accounting for 40.9 % of generation in 2021 (Harris et al., 2022). Their widespread deployment is due to their high efficiencies (up to 64 %) when operating using a combined cycle. Additionally, the UK began transitioning to GTs from coal during the 1990s due to their lower cost and emissions when compared with coal. However, to meet the previously mentioned UK emissions targets, pollutants from GTs must be significantly reduced. The UK government has stated that this transition to a more diverse generation mix will also increase energy security (DECC, 2011).

The primary pollutants related to NG combustion in GTs are CO_2, CO, and NOx. These have a range of environmental impacts, including acting as or contributing to the formation of GHGs. CO is produced from the incomplete combustion of hydrocarbons. Though CO itself is a weak GHG, it readily reacts with hydroxyl radicals ($\cdot$OH) to produce further CO_2, also reducing the $\cdot$OH availability to break down methane (CH_4), another strong GHG (ESSEA, 2015). Commonly referred to as NOx, nitrous oxide and nitrous dioxide are produced when N_2 dissociates in the high-temperature environment of combustors. As air, composed of ~75.5 wt % N_2, is often used to oxidise fuel, this is prevalent in GTs. As with CO, NOx indirectly acts as a GHG, enabling atmospheric reactions to produce photochemical smog containing ozone (O_3) and other organic compounds, contributing to the greenhouse effect. Additionally, NOx reacts with atmospheric water, causing the deposition of acidic substances in the environment, commonly referred to as acid rain.

Due to the existing infrastructure surrounding GTs, there is a focus on retrofit technologies that may mitigate emissions. One method includes Exhaust Gas Recirculation (EGR) and pollutant capture systems. EGR is utilised to increase the concentration of pollutants in the exhaust gas, improving the efficiency of a separation plant. Experimental work done by Evulet et al. (2009) shows that modern Dry Low-NOx (DLN) combustors can currently recirculate up to 35 % of their exhaust gas without modification. With modifications, it is predicted that over 40 % EGR may be achieved. However, major modifications to a GT would require significant time and economic investment to ensure the system efficiency remains uncompromised by altering the combustion chemistry and outlet temperature. Post-combustion retrofit technologies, such as selective catalytic reduction, are also used to convert NOx to N_2.

GT modifications can use renewably sourced heat to produce electricity via a hybrid system. This allows heat-to-electricity conversion utilising the high efficiency of modern combined-cycle power plants. One method to achieve a hybrid system is preheating the compressed air as it exits the compressor to match the design TIT, allowing the turbines to run partially or entirely from renewable heat. This displaces the heat input from combustion with renewably sourced heat and minimises the release of pollutants. Proposed alteration methods include Direct Solar Integration (DSI), using concentrated solar energy to heat air discharged from the compressor, bringing it closer to the required temperature (Spelling et al., 2014). Though these technologies are not mature, they allow renewably sourced heat to be efficiently integrated into GTs.

Due to the cyclic nature of solar energy, this system cannot provide on-demand dispatchable power to ensure the security of supply. Integration with a UHTS system provides the ability to store excess renewable energy produced at times of lower demand or during periods of curtailment. They then dispatch renewable energy when required to smooth both the inherent intermittency associated with RES and the overall demand curve, minimising the use of NG backups (Garvey, 2015).

UHTS systems may be combined with a GT in a similar manner to that used in DSI, through the discharge of heat on demand to make the process dispatchable. A process flow diagram of a UHTS system integrated into the GT can be seen in Figure 4.1. Furthermore, they can be designed to discharge at a required temperature, providing greater control than DSI (BEIS, 2016). Based on this, UHTS may provide high-grade heat to pre-existing GTs, achieving a 57 % electric-to-electric round-trip efficiency when discharged via a modern combined-cycle GT. Additionally, four further concepts for implementing TES systems into GTs are presented by

Holy et al. (2021).

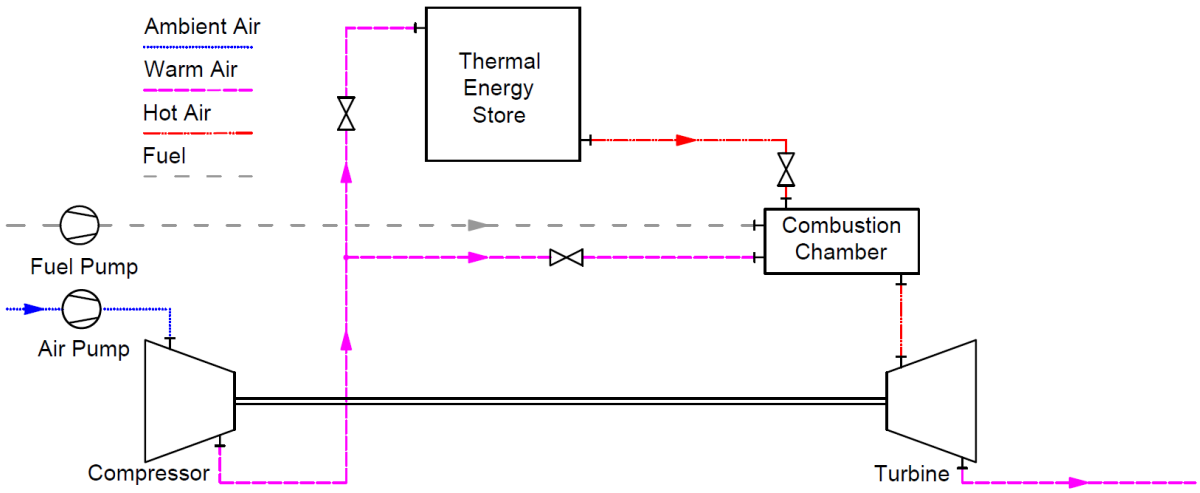


Figure 4.1: Process flow diagram of a thermal storage system integrated with a GT for complete conversion or hybrid operation.

The heat from the UHTS can be introduced directly into the combustion system, displacing fuel. To fully replace the combustion process, the energy store would be required to supply a working fluid to a GT at the required TIT. However, with work being undertaken to reach TITs of 1974 K, the 1800 K store cannot provide sufficient heat to reach the design TIT in all situations (Hada et al., 2015). This is also the case when the UHTS has partially depleted, resulting in a lower storage temperature. These current limitations in the UHTS system prevent the system from becoming combustion-free via 100 % fuel displacement. Although it is not possible to achieve total fuel displacement, this should not limit the ability of UHTS integration to achieve zero-carbon operation if NG can be replaced with a zero-carbon storage fuel such as H_2 or NH_3.

In this case, the GT should be powered using hybrid combustion, where the working fluid is heated as far as possible using thermal storage, and any additional energy requirement is met through the combustion of fuel to increase plant availability (Grange et al., 2013). A process flow diagram of the storage system integrated into the GT can be seen in Figure 4.1. This study does not consider part load operation with a lower TIT, however, the results would be applicable to a part load system that operated by fully utilising a reduced number of combustion chambers within the can-annual configuration.

Though not addressed in this research, when altering the flow of fluids entering a GT combustion chamber, it is important to consider the side effects this will have. Significant changes to temperature and flow rates would likely require a combustion chamber redesign. For example, a primary concern is the increase in air temperature prevents it from cooling the combustion chamber liner, which must maintain a temperature equal to or below that of the initial compressor outlet temperature. It may be necessary to explore the implementation of existing techniques used elsewhere in GTs, such as active cooling from compressor bleed, thermal barrier coatings, advanced combustion chamber materials or film cooling (Long et al., 2023; S. Can Gülen, 2019; Robinson, 2018) to ensure the integrity of the combustor. It should

be noted that some of these thermal control systems have an associated energy cost, which must be limited to an acceptable level. Due to the above, a GT retrofit would likely require a complete combustor redesign to allow hybrid burning/storage integration.

Furthermore, reduced flow rates of the fuel when high preheating is adopted would require a redesign of the swirler and both the primary and secondary air flows, as the change in flow rate would affect the functionality of inlet swirlers, reducing their effectiveness and affect the mixing with the air flows. This could cause issues with combustion stability due to a change in the air:fuel mixing (Bhuvana et al., 2018).

For example, excessive mixing could result in autoignition close to the fuel inlet of this retrofit system as the time for autoignition to occur decreases with an increasing temperature of the unburned air:fuel mixture (Huth and Heilos, 2013). Excessive swirling caused by inappropriate swirler design is also capable of causing flashback as they can create recirculation zones that generate negative velocity in the swirler region, allowing the flame front to progress back into the inlets (Shelil, 2009). Whilst these issues are important and combustion chamber design issues are critical in the physical implementation of UHTS integration, they are outside the scope of this chapter, which focuses on emissions reduction and the maintenance of GT output through consistent combustor outlet conditions, rather than combustion chamber design.

Historically, there has been extensive experimental work on GT combustion chambers to produce a more efficient system that minimises pollutants. Computational methods such as CFD can now produce models that replicate experimental results accurately (Kutlumukhamedov et al., 2021). The models allow for a detailed view of the complex internal processes within a combustion can, providing greater insight into their functionality. Though many of these numerical methods are complex and computationally expensive, they remain preferable to experimental setups due to their adaptability and low cost. As such, they can be employed in the investigation of turbulent combustion (Lila, 2021).

In GTs, the combustion reaction occurs in the form of a highly mixed turbulent flow. Due to shear stresses generating vortices, there are inherent velocity fluctuations leading to instability in properties such as temperature and flow composition. These fluctuations can alter reaction rates due to an increased heating period or reaction quenching. This produces a highly complex system which is difficult to model.

Emissions production for lean combustion has been studied using CFD in various cases (Hermeth et al., 2013; Brewster et al., 1999; Zheng et al., 2013; De Robbio, 2017). Using the RANS analysis, Laranci et al. (2011) investigated a combustion chamber with fuel switching from natural gas to syngas. The non-adiabatic PDF (Probability Density Function) approach was used to account for the NOx formation mechanisms. This model was suitable for predicting NOx formation, even at the increased temperatures present during hydrogen combustion.

A further study by Shih and Liu (2010) investigated the emissions and flame temperature distribution within a micro GT using the k-ϵ model and a PDF table to account for the chemical interactions between fuel and air mixtures. The results demonstrated an accurate prediction of the flow, temperature, and emissions concentration produced by the model.

Investigations have been undertaken into the preheating of compressed air before entering the combustion chamber. Dabwan et al. (2022) state that the preheating of the compressed air results in a reduction in fuel consumption and CO_2 emissions. However, this method is limited by the compressor outlet temperature and, as such, requires the integration of heating

into inter-cooled turbine cycles, increasing the complexity of a retrofit. Analysis by Behar (2017) shows that solar preheating of compressed air is feasible but depends on the compression ratio and atmospheric temperature. To overcome these limitations, they recommend the implementation of TES to provide a constant temperature. Whilst these results indicate the benefits and limitations of air preheating, they do not study the chemistry within a combustion chamber when the heated air is introduced.

Due to the widespread deployment of GTs and the global shift towards renewable power generation, numerical modelling will be fundamental to the adaptation of existing systems to fit in the next generation of power generation technologies. However, a primary issue with modelling realistic combustion is reaction time scales. As combustion processes proceed at rates that may be orders of magnitude apart, it can be difficult to accurately predict the outcome of all of these across the range.

This study employs CFD to predict the flow dynamics and chemical reactions within a GT combustion chamber using a hybrid system with preheated combustion air. In turbulent combustion modelling, it is essential to resolve both flow turbulence and mixture composition. The Ansys Fluent 19.1 code (Ansys Inc, 2018) is utilised to solve the governing Navier-Stokes equations through a finite-volume method (Sharif Ahmadian, 2016). These equations, which describe turbulent flow and energy continuity, were detailed in Chapter 3. Therefore, this section will focus solely on the combustion modelling process.

In summary, integrating renewably sourced heat into GTs via UHTS systems marks a significant step towards reducing emissions in power generation. This chapter will delve into UHTS integration techniques and their effects on combustion chemistry, using CFD models to predict flow characteristics and chemical interactions accurately. The main goal is to evaluate how varying levels of combustion air pre-heating influence combustion stability and emissions in a heavy-duty GT combustion chamber. This involves analysing the impact of changing inlet air temperature while maintaining the outlet flow rate and TIT. The study will assess fuel requirements and the production of CO_2, CO, and NOx within the combustion chamber, aiming to address a gap in the literature regarding the chemical application of stored heat in GT combustion.

4.3 Computational Combustion Modelling

To model gaseous phase turbulent combustion and emissions generation within a can-style combustor within a GT using UHTS to provide heat, CFD was used again.

CFD has been used to predict turbulent mixing and, when paired with a suitable chemical model, the chemical reactions and associated heat release during combustion. Due to the intrinsic connection between reacting chemistry and turbulence, modelling turbulent combustion is a complex challenge. The outlined combustion models refer to the RANS framework.

Combustion modelling within CFD focuses on the closure of the chemical reaction source terms in the governing equations. When modelling a reacting flow, it is required to represent the species mass fraction conservation. This is done using Equation (4.1) to track the progress during a reaction.

$$\frac{\partial}{\partial t}(\rho Y_\alpha) + \frac{\partial}{\partial x_i}(\rho u_i Y_\alpha) = -\frac{\partial}{\partial x_i}(J_{\alpha,i}) + \dot{\omega}_\alpha \tag{4.1}$$

Here, the reaction rate is given as $\dot{\omega}_\alpha$.

When modelling a combustion process, the chemical source term is not resolved as the process occurs at scales smaller than that of the mesh. As such, it is necessary to implement a suitable combustion model. This means that the process for modelling combustion for RANS and LES is derived from the same method.

When modelling a flame, classifications are used to assign suitable models for different types of combustion. The three primary classifications, each of which is required to use its own modelling methodology, are premixed, non-premixed and partially premixed flames.

Evidence shows that introducing turbulence into a combustion system is preferable for more rapid combustion (Lefebvre et al., 2010). As such, turbulent combustion systems are utilised in GTs and will be further explored for this study.

4.3.1 Premixed Combustion

A well-known example of a premixed flame is that produced by a Bunsen burner. The fuel and oxidiser are uniformly mixed within such a flame before reaching the combustion region, and the flame front propagates into the gas mixture.

Most models for turbulent premixed combustion assume isobaric conditions, an adiabatic system, and a unity Lewis number (Poinsot and Veynante, 2005). The primary variable used when modelling premixed combustion in Fluent is a progress variable, c, to parameterise the reaction's progression. During combustion, quantities such as species concentration and temperature can be used to calculate the state of a reaction at a given point. When used in a combustion model, these values are normalised, so a progress variable of 0 indicates the mixture is yet to undergo a reaction, and a progress variable of 1 indicates the components have fully combusted. As such, c is used to determine the location of the flame front within the system using the local mixture fractions of species involved with the combustion process. The progress variable can be expressed using Equation (4.2).

$$c = \frac{\sum_{i=1}^{n} Y_i}{\sum_{i=1}^{n} Y_{i,eq}} \tag{4.2}$$

Here, Y_i represents the mass fraction of the product species i and Y_i, eq represents the equilibrium mass fraction of species i.

The transport equation must be solved for c when modelling premixed turbulent combustion. As premixed combustion often takes place in a thin flame sheet, the combustion is divided into a burnt and unburnt region, separated by the flame. The propagation of the flame front is found using Equation (4.3).

$$\frac{\delta}{\delta t}(\rho c) + \nabla \cdot (\rho u c) = \nabla \cdot (\frac{\mu_t}{Sc_t}\nabla c) + \rho S_c \tag{4.3}$$

where Sc_t is the turbulent Schmidt number, and S_c is the reaction progress source term.

The reaction source term can be found using Equation (4.4).

$$\rho S_c = \rho_u U_t |\nabla c| \tag{4.4}$$

where ρ_u is the unburnt mixture density, and U_t is the turbulent flame speed.

The turbulent flame speed (U_t) is influenced by variables such as composition, temperature, surrounding geometry and the pressure of the unburnt mixture due to their impact on the laminar flame speed. It is further affected by the deformation of the reaction zone, known as wrinkling or thickening. An increase in turbulence increases flame speed due to the distortion and wrinkling of the flame front. Due to these factors, it is difficult to define the turbulent flame speed using experimental results. To account for this, models such as the Zimont Turbulent Flame Speed Closure Method are used to define a value Zimont et al. (1997). The Zimont closure method finds the flame speed with Equation (4.5).

$$U_t = Au'(\frac{\tau_t}{\tau_c})^{\frac{1}{4}} \tag{4.5}$$

where A is a model constant (often 0.52), u' the root-mean-square velocity, τ_t the turbulence time scale and τ_c, the chemical time scale.

The model is applicable for a thin reaction zone combustion region, which assumes the smallest turbulent eddies are smaller than the flame thickness. This region is quantified by a Karlovitz number (Ka) greater than unity.

4.3.2 Non-Premixed Combustion

In non-premixed combustion, fuel and oxidiser are introduced into the system separately and are required to mix via turbulent transport or diffusion before combustion can occur. This combustion process is found in GT combustors.

The modelling of non-premixed combustion can utilise simplifications such as the mixture fraction approach, simplifying the process to that of the mixing of two gases. To predict the reaction process for non-premixed combustion, the process mixture fraction, (Z), is used to derive species concentrations. The value always remains between 0 and 1 and represents a ratio of the mass of fuel to the mass of oxidiser within the flow. This gives a value of 1 when the mixture has no oxidiser and a value of 0 when the mixture has no fuel remaining. As the flow within combustion chambers is designed to be turbulent to improve mixing, it can be assumed that each species has an equal diffusivity as turbulent convection dominates over molecular diffusion (Pierce and Moin, 2004). Assuming that the diffusion coefficients for each species are equal, Z is calculated using Equation (4.6).

$$Z = \frac{Z_i - Z_{I,ox}}{Z_{i,f} + Z_{I,ox}} \tag{4.6}$$

where Z_i is the mass of element i and the subscripts ox and f are the masses at the oxidiser and fuel inlets, respectively.

To accurately predict slow-forming species such as NOx and low-temperature CO and phenomena such as flame quenching, the species should be considered to be in global chemical non-equilibrium. Whilst the mixture fraction provides insight into the fuel and oxidiser distribution, the flamelet model simplifies the turbulent combustion by representing the turbulent flame as a collection of laminar flamelets. Each flamelet, defined by specific mixture fraction and scalar dissipation rate conditions, captures the essential features of the local flame structure within the turbulent flow.

The concept of flamelets is a well-established approach in combustion modelling, particularly for turbulent flames. It simplifies the complex interaction of chemistry and turbulence by assuming that at any point in the flow, the local structure of the flame is similar to a laminar flame, which is defined by the local mixture fraction and scalar dissipation rate. This approach is especially useful for modelling non-premixed combustion where the flame structure can be significantly influenced by the local mixing of fuel and oxidiser.

In turbulent combustion modelling, flamelets are employed to assess the formation of slow-forming species, using their ability to simplify the intricate interaction between turbulence and chemical kinetics (Hu et al., 2017). The Flamelet Model conceptually represents the local structure of a turbulent flame as a series of laminar flamelets, thereby delineating the effects of fluid mechanics from chemical reactions. This approach is instrumental in addressing chemical non-equilibrium conditions typical in turbulent flames, where species like NOx do not attain chemical equilibrium rapidly (Kim et al., 2001). Utilising key parameters like mixture fraction and scalar dissipation rate, flamelet models effectively the formation of slow-forming species by accurately simulating temperature and species concentration within each flamelet (Li et al., 2023). Integrated into numerical simulations, these models facilitate the efficient computation of slow-forming species in complex flow fields, predominantly by employing pre-computed and tabulated flamelet properties within CFD frameworks (Kundu et al., 2020). This methodology enhances accuracy in turbulent combustion and significantly improves computational efficiency, which is crucial for advanced combustion studies.

A further factor affecting this flamelet model's solution is the scalar dissipation rate (χ). As χ varies in space within the combustion region, the flamelets must account for this. In order to track the transport of the mass-weighted, non-diffusive Eulearian particles for a given flamelet, l, Equation (4.7) is used.

$$\frac{\delta \bar{\rho} \tilde{I}_l}{\delta t} + \nabla \cdot (\bar{\rho} \tilde{I}_l \tilde{\mathbf{v}} - \nabla \cdot (\bar{\rho} \frac{\nu_T}{Sc_l} \nabla \tilde{I}_l) = 0 \tag{4.7}$$

where ρ is the density, I_l the mass fraction of particle l and $\mathbf{v}$ the velocity vector. Bar is the ensemble average, and tilde is the Favre ensemble average. ν_T is the turbulent viscosity coefficient and Sc_l the turbulence Schmid number.

The flamelet surface-averaged value of χ at a stoichiometric mixture can then be found based on the mixture fraction for particle l. This is given by Equation (4.8).

$$\hat{\chi_{st}}(l) = \frac{\sum\limits_{V} \tilde{I}_l(\mathbf{x}) \bar{\rho}(\mathbf{x}) \chi_{st}^{\frac{3}{2}}(\mathbf{x}) pdf(Z_{st}) dV'}{\sum\limits_{V} \tilde{I}_l(\mathbf{x}) \bar{\rho}(\mathbf{x}) \chi_{st}^{\frac{1}{2}}(\mathbf{x}) pdf(Z_{st}) dV'} \tag{4.8}$$

The number of flamelets required depends on the size of variation in χ as each particle can only cover a limited range. The combustion process is modelled from this as a group of discrete flamelets.

Once these flamelets have been calculated, density-weighted mean scalar values are calculated from the PDF of the mixture fraction and the progress variable. The reaction chemistry and PDF integrations are pre-processed to produce look-up tables for interactions between turbulence and chemistry (Razeghi et al., 2020). This allows the thermochemistry to be looked up during the simulation rather than directly calculated, reducing the computation load.

4.3.3 Partially Premixed Combustion

A partial premix of fuel and air is utilised within current GT DLN combustors. Here, fuel and a portion of the oxidiser are introduced for a limited time before they are ignited within the combustion region. As the fuel and oxidiser enter the combustion system at different temperatures, the model is run under non-adiabatic conditions to allow heat transfer between the different inlet streams.

The use of partially premixed combustion causes the laminar flame speed to change with the reaction composition as the combustion process progresses. The partially premixed combustion species model accounts for this variation by fitting curves produced by Göttgens et al. (1992) to a piecewise-linear polynomial.

When employing the partially premixed combustion model, the region ahead of the flame is assumed to be mixed, and as such, variables are calculated based on the mixture fraction. Behind the flame, laminar flamelets are used. Within the flame itself, a combination of the two is used based on the reaction progress variable, using a linear weighting (Hu and Kurose, 2018).

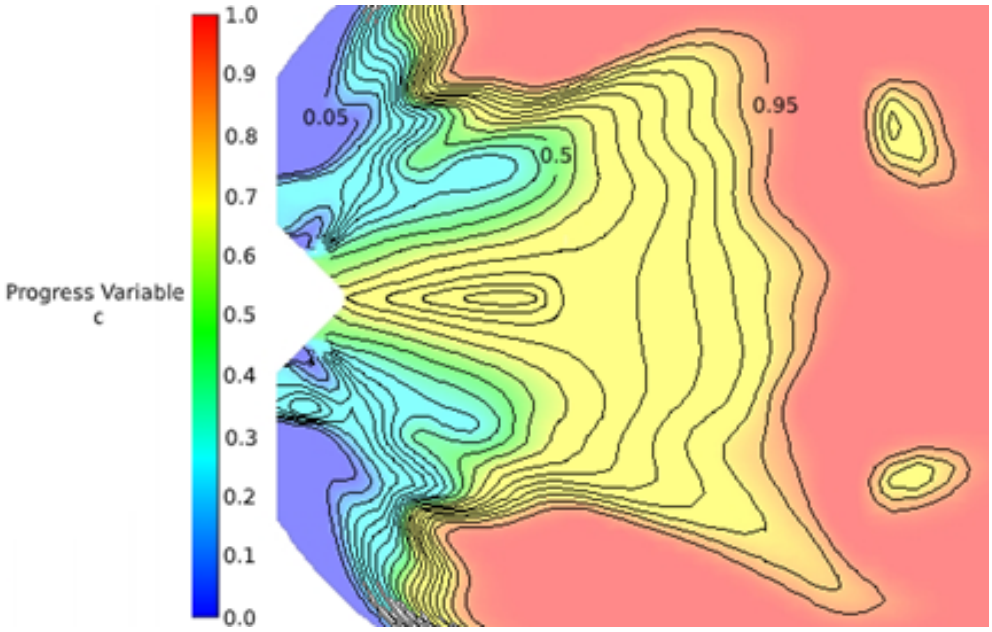


Figure 4.2: Combustion model transition throughout flame from the Tay validation model (When c=0: non-premixed, 1: premixed).

Figure 4.2 displays how the progress variable evolves from the fuel inlet, with the results produced when modelling the combustion region of the Tay combustion chamber. The values of $c > 0$ and < 1 indicate the combustion region. The laminar flamelet mixture fraction solution is employed behind the flame (c=1) and ahead of the flame (c=0), and properties are calculated based on the unburnt mixture fraction. The flame front position is determined by the reaction progress variable. Using the Fluent non-premixed and premixed combustion models efficiently closes the calculations, minimising computational cost.

To calculate the density-weighted scalars ($\bar{\phi}$) within this system, a probability density function (PDF) of the mixture fraction and the progress variable is utilised. When assuming combustion produces a thin flame, this is given by Equation (4.9). As with the non-premixed model, the pre-processing of look-up tables is performed.

$$\bar{\phi} = \bar{c} \int_0^1 \phi_b(Z) p(Z) dZ + (1 - \bar{c}) \int_0^1 \phi_u(Z) p(Z) dZ \tag{4.9}$$

where subscripts b and u are burnt and unburnt, respectively.

4.3.4 Thermophysical Interaction

The thermophysical properties of the mixture and flame are calculated as a function of the temperature using the Fluent default thermodynamic database (Kee et al., 2000).

When considering the detailed 1D chemistry, the GRI-Mech 3.0 CHEMKIN chemical kinetics mechanism (Smith et al., 1999) is often employed. This is a software tool designed to simulate fast, complex chemical reactions and kinetics in systems such as combustion by solving a pre-defined set of differential equations based on chemical mechanisms, thermodynamic data and flow properties. Here, scalars of interest such as species mass fractions, reaction rates and temperature are tabulated as a function of controlling variables such as the local mixture fraction, progress variable and enthalpy and are used in conjunction with calculated flamelets. This library is composed of 325 chemical reactions and their associated rate coefficient expressions, as well as the thermochemical parameters of the 53 intermediate species. The use of these databases has the advantage of being able to use detailed chemical kinetics with low computational requirements (Raman et al., 2005).

The formation of NOx is typically modelled within commercial CFD codes using post-processing models. In these, transport equations for species involved in NOx chemistry, such as N_2O and HCN, are solved using the resolved velocity, temperature and local concentration of other species. The source terms are found from rate expressions based on various NOx-producing pathways such as thermal, prompt and N_2O intermediate formation.

Thermal NOx is predicted using rate constants from experimental studies to produce an overall equation for the rate of formation based on concentration and temperature (Jiang and Campbell, 2005; Russo et al., 2007). There is both a partial equilibrium and an equilibrium method. The partial equilibrium method accounts for the concentration of oxygen atoms, which are under-predicted in an equilibrium model, minimising errors (Stiehl et al., 2020).

Prompt generation is based upon the carbon concentration in a given volume, enabling the intermediate production of compounds such as amines, which then react to form NOx. Due to

this, prompt NOx production is predicted based on the fuel carbon number and equivalence ratio (ϕ) (Jiang and Campbell, 2005).

During the combustion process, thermal radiation must be considered to account for the transmission of energy over temperature gradients. This is critical as peak temperatures affect the production of NOx due to its dependency on areas of high temperature. The most commonly utilised radiation models within Fluent are Discrete Ordinates (DO), P-1 and Discrete Transfer Radiation Model (DTRM). Radiation from combustion in GTs is often predicted using the P-1 and DO models, as seen in Karyeyen (2018); Sharma et al. (2014).

The Discrete Ordinates model is generally considered the most comprehensive radiation model (Sen and Puri, 2008), achieving heightened solution accuracy through improved discretisation and ensuring a thermal energy balance. However, the computational demand increases when resolving situations with a broad range of angles, presenting a limitation, especially regarding CPU intensity.

The P-1 model is used where the radiative heat transfer equations incorporate the assumption of direction independence. This allows for the ease of solving the radiation heat transfer equation with minimal CPU usage. P-1 is more appropriate for systems with large optical thicknesses, such as combustion processes, and can be applied to more complex geometries without a large computational demand. (Sazhin et al., 1996; Hosseini et al., 2020). However, P-1 may produce inaccuracies in low-thickness geometries.

4.4 Combustion Chamber Model

This CFD model is designed to predict the combustion system for various combustion air preheat temperatures. The effect on fuel requirements and pollutant production of integrating the UHTS system with NG into a GT will be assessed. The emission concentrations of carbon dioxide (CO_2), carbon monoxide (CO), and nitrous oxides (NOx) are to be investigated, and the pathways by which their production is affected will be discussed.

As the model is run at a steady state, the pressure-velocity coupling may be solved using the Semi-Implicit Method for Pressure-Linked Equations (SIMPLE) algorithm as it has been shown to provide accurate results in similar models (Xi et al., 2022; Andrić et al., 2017).

Swirl intensity generated at the inlet is a critical factor of flow behaviour within a GT combustion chamber. Due to the highly turbulent swirling, the seven-equation RSM is used to solve the Reynolds Stress values. In swirling flows, RSM has produced more accurate results than two-equation turbulence models (Aspden et al., 2021). RSM can account for critical anisotropic behaviours in complex flows, such as swirl and recirculation, which are prevalent in combustion chambers (Benim et al., 2016; Nanduri et al., 2007; Prieler et al., 2015). These values are used in the Reynolds Averaged Navier-Stokes (RANS) to close the momentum equations, modelling the flow turbulence within the system. Though Large Eddy Simulation (LES) or Direct Numerical Simulation would also be suitable, RANS has been used due to the significant computational expense associated with these models.

Regarding the chemistry, the GRI-Mech 3.0 mechanisms were used alongside the Fluent thermodynamic database to account for the reactions occurring during combustion. The combustion itself was modelled using the partially premixed combustion model. The non-

adiabatic PDF approach was used to account for the generation of NOx. The mechanisms used accounted for both thermal and prompt NOx.

A second-order upwind scheme is used to improve the spatial accuracy of the momentum, turbulence kinetic energy, turbulence dissipation rate, energy, and all species equations. The convergence criteria are set to 10^{-5} for all transport equations and when temperature profiles within the system reach steady-state.

4.4.1 Combustion Chamber Geometry

In GT systems, air is drawn into a compressor, increasing the pressure and raising the temperature due to the isentropic nature of the process. In modern combustors, air is split to enhance performance, efficiency, and emissions control. A small portion of the air is directed into the primary combustion zone for mixing with fuel, ensuring stable and efficient combustion at high temperatures. The majority of the air bypasses the primary zone and is introduced downstream via dilution holes to cool combustion gases to temperatures that turbine blades can withstand. This split air approach is also employed to reduce the formation of NOx by moderating peak temperatures. Air is also used to introduce a swirling component which enhances fuel-air mixing. A portion of the air is also utilised to cool the combustion chamber walls via film cooling, creating a protective layer that shields the walls from the heat of combustion, ensuring the durability and longevity of the chamber.

Within a Tay-type GT, the complete combustion system comprises ten individual combustion chambers with curved vane swirler inlets arranged in a can-annular configuration with pseudo transpirational wall cooling (Wilson, 1988). In this study, a single combustion chamber is simulated in 3D. Figure 4.3 shows a diagram of the Tay system. The purpose of focusing on the Tay-type combustion chamber is because there is published experimental data on the combustion process which can be used for model validation. This allows for a more accurate and reliable assessment of the combustion model.

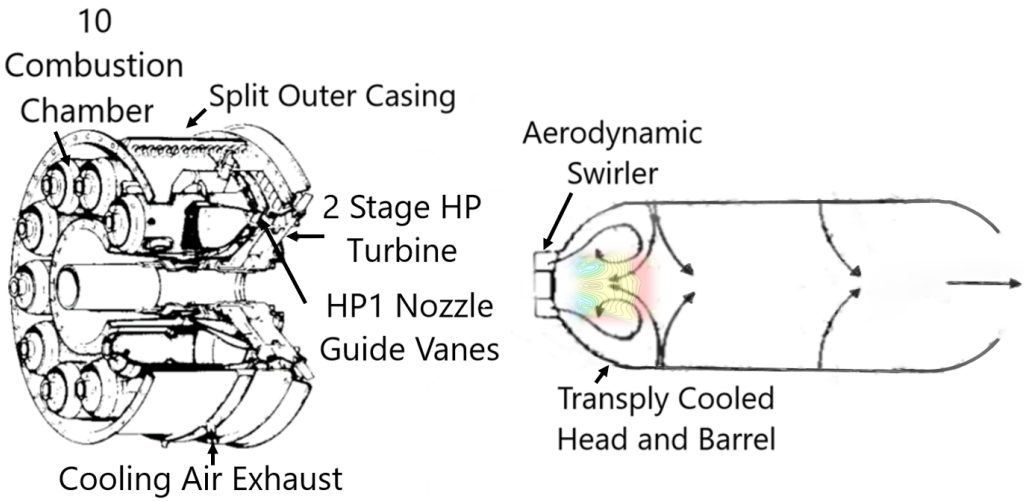


Figure 4.3: A) Tay Combustion System Arrangement (Wilson, 1988). B) Individual Tay Can-Annular Combustor (Wilson, 1988).

A $\frac{3}{4}$ scale combustion chamber mesh consisting of 1,198,832 hexahedral cells developed by Zhang (2017) based upon the Tay-type GT is used (geometry in Figure 4.4). This mesh was employed for model validation as it was published previously, demonstrating its capability to suitably capture the required detail for validation against experimental data. Although this combustion chamber is from an aeronautical turbine, it may still be used to model a generic combustion system similar to one within a heavy-duty industrial turbine, as both systems rely upon mixing produced from a swirler and the introduction of secondary air.

Key differences between the two turbine types are their maximum power output relative to size, weight limitations around an aeronautical turbine, and the mass of air utilised. The size and weight limitation results in very compact combustors for aeronautic applications. Much larger combustors are used in stationary GTs, with longer residence times. These factors can influence CO reactions. It should be noted that within the combustor, two key factors affect pollutant production, especially NOx formation. These are the pressure in the combustion chamber and the peak combustion temperature.

The generation of this mesh is described in detail, along with a mesh independence study by Zhang (2017). Experimental data for combustion in this geometry is available based on the works of Bicen et al. (1990). This data is used to validate the simulation method outlined. The results of this may be seen in Section 4.5. This model is used as the author is unaware of suitable experimental analysis published regarding a heavy-duty GT due to the commercial sensitivity of the data.

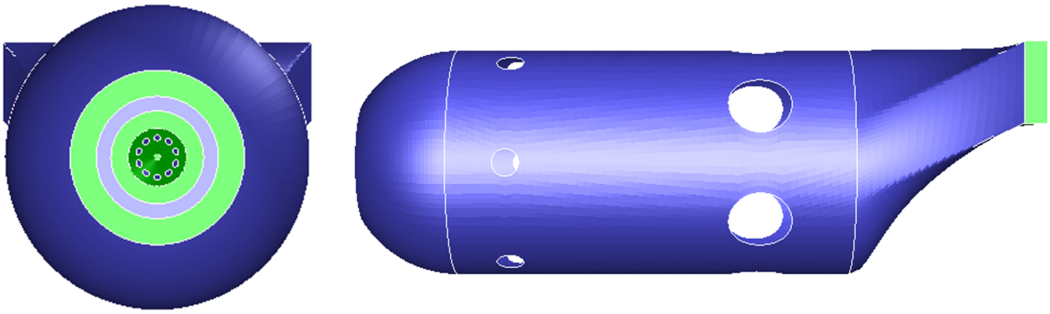


Figure 4.4: Geometry of Tay combustion chamber (Green: Wall, Blue: Porous Wall, Clear: Gas Inlet/Outlet).

4.4.2 Boundary Conditions

As the Tay system is used to validate the solution method, the boundary conditions are set to match those published from the experimental setup. Thus, the total mass flow rate of air is set at 100 g/s, and the fuel is set to 1.76 g/s. The total air is split as follows: 6.9 % injected through the swirler, 13.6 % through primary holes, 53.3 % through dilution holes, 6.6 % through the porous head, 13.8 % to the porous barrel, and 5.8 % to the discharge nozzle which would attach to the transition piece. The initial overall air:fuel ratio (AFR) is 164.9, and ϕ at the fuel inlet is calculated as 1.02.

Dirichlet boundary conditions are imposed on the inlets and are set in terms of mass flow rates. The outlet uses a Neumann boundary condition and is based on static pressure set at

atmospheric pressure. The combustor wall is defined as a solid, no-slip, adiabatic surface with a roughness height of 0 to indicate the smooth walls within a combustion chamber. Modelling no wall roughness is common practice due to the high-velocity flows and elevated temperatures, which minimise the impact of surface roughness on the flow characteristics. Additionally, the walls of GT combustion chambers are engineered to be very smooth, further reducing the impact of roughness on the flow. This simplification helps in focusing computational resources on critical aspects of combustion and flow dynamics.

The fuel inlet is kept at a constant 318 K, and the swirl angle at the swirler inlet is kept constant at 45° using tangential and axial flow components. Fuel is represented as C_3H_8, and the air is composed of 76.7 % N_2 and 23.3 % O_2 by mass, as is standard practice (Vilag et al., 2019; Gamil et al., 2020; Krieger et al., 2015). The inlet pressures are also kept constant at t 1.10 bar. The outlet boundary condition is set at 1.01 bar to match the experiment, which outlet to the atmosphere (Bicen et al., 1990).

Once the model was validated (see Section 4.5) and initial results were produced using the Tay system, the model was rerun with CH_4 as the fuel, a 23 bar inlet pressure, and an initial air temperature of 760 K and an outlet pressure of 21.85 bar based upon published pressure drop values in a heavy-duty combustor (Boyce, 2012). This ensured that the model still converged using boundary conditions for more modern GTs.

4.4.3 Mesh Transition

Once a combustion model is built and validated against experimental data using the Tay geometry, it can be transitioned to the combustion chamber of a heavy-duty, power-generating GT. The previous mesh was required as there is no published experimental combustion data for this combustion chamber. As such, the combustion model is applied to the mesh of a GE DLN 2 series combustion chamber consisting of 1,111,154 mixed cells (geometry in Figure 4.5). This geometry is produced by Hasini et al. (2016) from a 3D scan of an industrial combustion chamber. Like the Tay combustion chamber, the heavy-duty combustion chamber geometry is composed of a main burner, swirl air inlet, secondary air inlet, diffusion air inlets, and the outlet to the transition piece. As this geometry does not allow for diffusion through the wall to provide cooling air, secondary air provides both the combustion diffusion air and the cooling air for the combustion liner. As previously mentioned, this combustion chamber is significantly larger than the Tay combustion chamber as it is designed to accommodate a greater mass flow rate (x55.78 the flow rate per combustion chamber) and, therefore, requires an extended combustion region. Additionally, as the outlet of this system would be attached to a turbine with back pressure, the outlet pressure is set to 21.85 bar to match the operating pressure of a real heavy-duty gas turbine combustion chamber (Boyce, 2012).

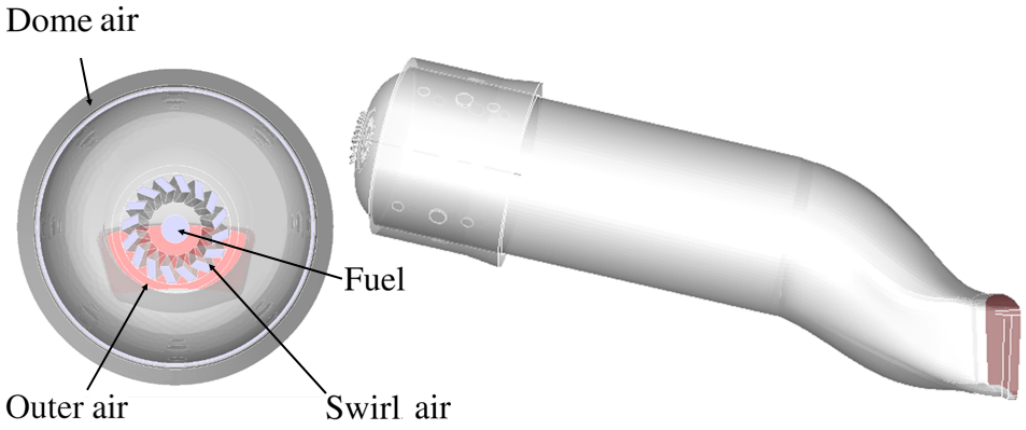


Figure 4.5: Geometry of GE DLN 2 Series Industrial combustion chamber.

It should be noted that the author was unable to find the specific flow and temperature conditions for this model of combustion chamber. However, this chapter aims to present potential pollutant reductions at state-of-the-art temperatures and pressure ratios. As there is no access to the flow rate data and geometries of these combustion chambers, the flow rate, TIT and pressure ratio of a typical J-series GT (Yuri et al., 2013) are used with the available geometry.

4.4.4 Combustion Chamber Mesh Independence

As this mesh was produced by Hasini et al. (2016), a mesh independence study had already been conducted to demonstrate that the solutions are independent of the number and location of the cells. To verify, a secondary mesh independence study is completed. To ensure that the solutions are unaffected by further refinement, two meshes are created: MI1 and MI2, with identical geometry and boundary conditions. MI2 had eight times the number of cells as MI1. The downstream velocity and temperature profiles are recorded and analysed for each mesh. Table 4.1 compares the average velocity and temperature across the profile at various locations downstream of the fuel inlet. When the results from MI1 and MI2 are compared, the maximum velocity difference is less than 1.9 %, and the maximum temperature difference is less than 0.2 %, proving that MI1 is sufficiently mesh-independent.

Table 4.1: Mesh independence comparison between average velocity and temperature at various z locations for MI1 and MI2.

z position	Velocity (m/s)			Temperature (K)		
(m)	MI1	MI2	Difference (%)	MI1	MI2	Difference (%)
0.00	108.69	108.20	0.45	750.19	750.15	0.01
0.10	94.24	94.18	0.06	751.30	751.34	0.01
0.20	11.18	11.37	1.69	757.87	757.08	0.10
0.30	10.98	11.15	1.55	758.00	757.14	0.11
0.40	10.84	11.05	1.89	758.09	756.98	0.15
0.50	10.97	11.14	1.48	758.16	757.01	0.15
0.60	11.11	11.15	0.33	758.22	757.19	0.14

4.5 Model Validation

Model validation appropriate for complex, swirling flows alongside reaction chemistry requires precise experimental measurements and accurate, well-defined geometry and boundary conditions. Studies such as those conducted by De Santis (2016); Anisimov et al. (2015); Lippert et al. (2004) achieve this through the use of experimental apparatus, through which models can be recreated experimentally.

Additionally, the reported settings used in the previously mentioned studies were investigated to ensure the model was suitable for this study. For example, each used finite-volume method discretisation and the GRI 3.0 mechanism was employed to simulate the chemistry of the combustion process. Where reported, the SIMPLE algorithm managed the pressure-velocity coupling, and a second-order upwind scheme was used for the momentum equation. A range of turbulence models were used, and it was reported that the RSM model produced similar results to those presented (De Santis, 2016).

Due to the novel nature of this hybrid storage integration, there is no published experimental data available for validation. Reheat combustion was investigated due to the introduction of heated gases into the combustion region. However, the lack of availability of boundary conditions, experimental data, and an accurate test rig geometry made these studies unsuitable for validation. As such, model validation was achieved using the Tay combustion chamber.

To enable validation, 2-dimensional cross-sections are used to take measurements within the scaled Tay combustion chamber at 4 locations. Using the numerical model, boundary conditions, and geometry described in Section 4.4, the modelled data is compared with experimental data. Due to the experimental sampling process, the experimental data has an error of $\pm$10 % for temperature and $\pm$8 % for species concentration.

These cross-sections are taken across the central horizontal plane at various distances from the inlet (z=0.02 m, 0.05 m, 0.08 m, 0.13 m). The location and distribution of these cross-sections are displayed in Figure 4.6.

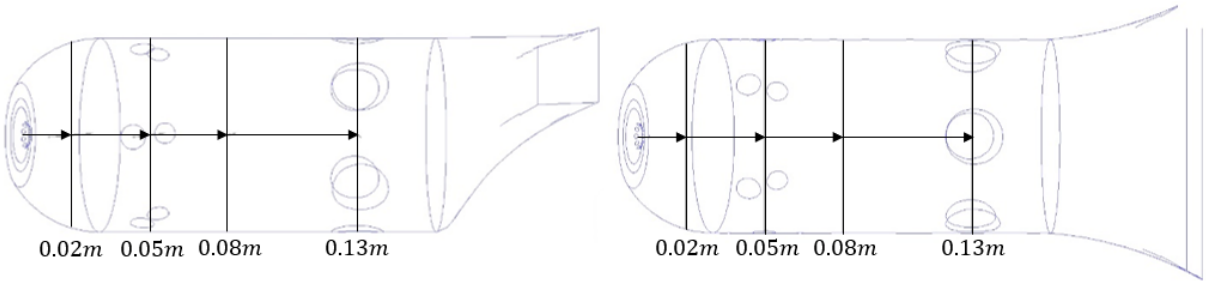


Figure 4.6: Locations of horizontal cross-sections used to measure data throughout scaled Tay combustion chamber.

A comparison of the temperature throughout the Tay combustion chamber is presented in Figure 4.7. These figures compare values produced by the combustion model with those reported from experimental data, and the variation is quantified in Table 4.2, with the difference given as a percentage change.

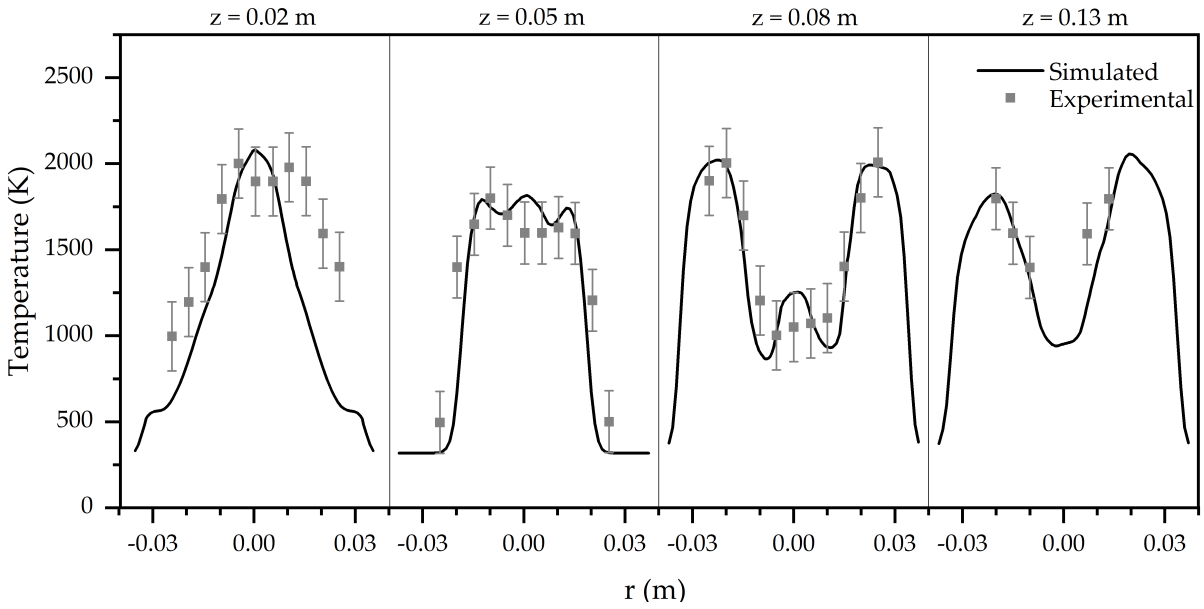


Figure 4.7: Comparison of experimental (Bicen et al., 1990) and simulated temperature data at horizontal cross-sections throughout the Tay combustion chamber.

Table 4.2: Comparison of experimental (Bicen et al., 1990) and modelled temperature.

	z=0.2 m			z=0.5 m			z=0.8 m			z=1.3 m		
r	Exp	Sim	Diff	Exp	Sim	Diff	Exp	Sim	Diff	Exp	Sim	Diff
(m)	(K)		(%)	(K)		(%)	(K)		(%)	(K)		(%)
-0.025	997	614	-38.46	496	321	-35.3	1902	2007	5.5	-	-	-
-0.020	1197	840	-29.8	1400	635	-54.6	2005	1977	-1.4	1797	1823	1.4
-0.015	1400	1127	-19.5	1648	1666	1.1	1700	1452	-14.6	1597	1638	2.6
-0.010	1795	1432	-20.2	1800	1754	-2.6	1205	900	-25.3	1398	1328	-5.0
-0.005	2001	1881	-6.0	1701	1719	1.0	1003	1036	3.3	-	-	-
0.000	1897	2079	9.6	1598	1811	13.3	1051	1252	19.1	-	-	-
0.005	1897	1962	3.4	1598	1729	8.2	1072	1105	3.0	1593	1182	-25.8
0.010	1979	1516	-23.4	1630	1677	2.9	1104	933	-15.4	-	-	-
0.015	1898	1158	-39.0	1596	1671	4.7	1403	1280	-8.7	1797	1690	-6.0
0.020	1594	836	-47.6	1207	655	-45.7	1802	1949	8.2	-	-	-
0.025	1402	614	-56.2	501	321	-35.8	2009	1984	-1.2	-	-	-

The second validation point is the ability to predict the concentration of O_2, CO, and CO_2 within the combustion chamber. This demonstrates the ability of the model to predict the chemical process throughout the system. This comparison is shown in Figure 4.8.

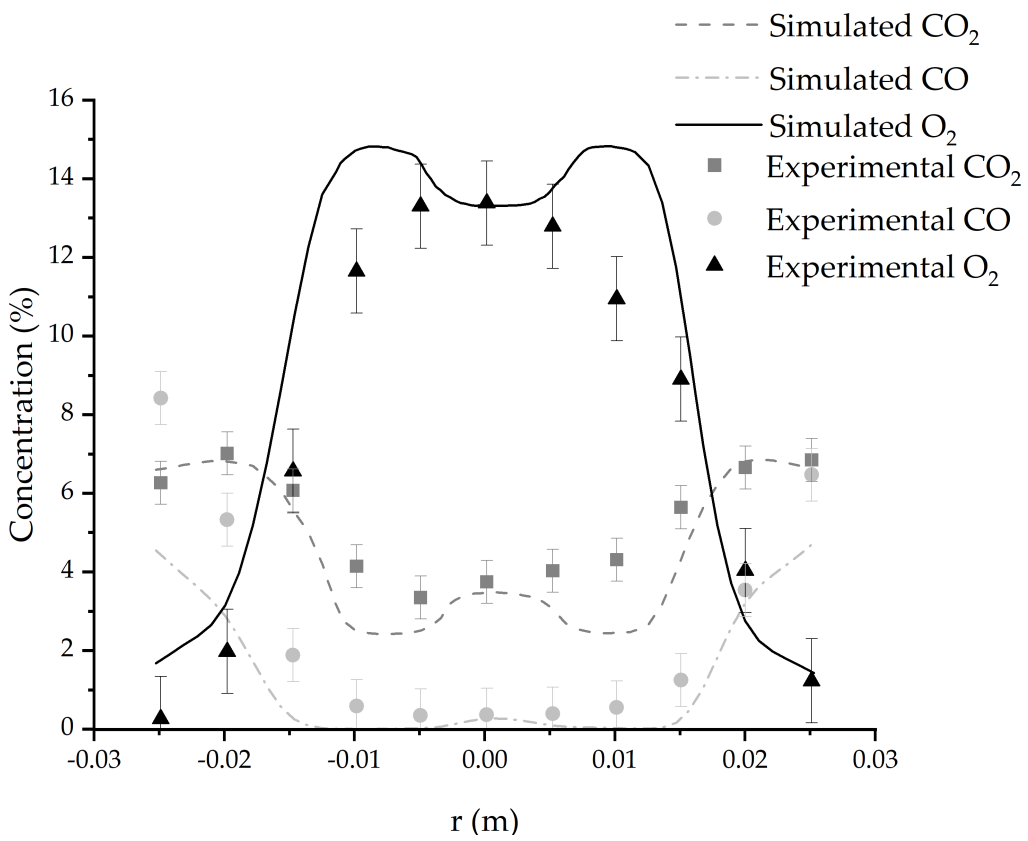


Figure 4.8: Comparison of experimental (Bicen et al., 1990) and simulated concentrations of O_2, CO_2 and CO at horizontal cross-sections 0.8 m from the fuel inlet of the Tay combustion chamber.

Table 4.3: Comparison of experimental (Bicen et al., 1990) and modelled component concentrations.

r	O_2 (%)			CO_2 (%)			CO (%)		
(m)	Exp	Sim	Diff	Exp	Sim	Diff	Exp	Sim	Diff
-0.025	1.73	1.73	0.00	5.82	6.61	-0.80	6.77	6.71	0.06
-0.020	2.36	3.12	-0.76	6.53	6.82	-0.29	4.50	4.36	0.15
-0.015	6.35	9.86	-3.51	5.74	5.73	0.01	2.35	0.70	1.65
-0.010	11.93	14.71	-2.78	3.76	2.54	1.23	0.84	0.02	0.82
-0.005	14.32	14.44	-0.11	2.57	2.51	0.06	0.71	0.06	0.66
0.000	14.08	13.32	0.76	2.68	3.48	-0.80	0.68	0.40	0.28
0.005	13.67	13.67	0.00	2.93	3.12	-0.19	0.70	0.17	0.53
0.010	12.91	14.81	-1.90	3.35	2.45	0.90	0.78	0.03	0.74
0.015	9.83	11.11	-1.28	4.70	4.26	0.45	1.06	0.26	0.80
0.020	4.75	2.76	2.00	6.20	6.82	-0.62	2.09	3.21	-1.12
0.025	1.99	1.48	0.51	6.25	6.65	-0.40	5.93	5.97	-0.04

From the comparison of the temperature and component concentration distribution for the numerical and experimental results, it is clear that the numerical model has accurately predicted the behaviour of the combustion system. However, heat release in some zones is slightly under-predicted. This is a radial positioning error, with accurate temperatures predicted

less than 5 mm from the experimental location. The peak temperatures, a critical factor in emissions generation, fall within the error bars of the experimental data with a maximum variance in the combustion region of 9.6 %. Furthermore, the general trend of the temperature profile has been captured, though due to the limited number of experimental points, the finer details cannot be seen.

Additionally, the simulation predicted the concentration of pollutants produced from the combustion. The maximum variation from the experimental data was 2 %, indicating a valid model. Furthermore, the model shows sustainable combustion with a high-temperature inlet gas. It has been demonstrated in various scenarios that CFD is capable and valuable for validating this (Tsuji et al., 2002; Su et al., 2012).

Future work should include experimental testing to improve the accuracy of validation to improve confidence further.

With both the mesh and combustion model validated, the settings utilised to represent the flow and chemistry are outlined in Table 4.4 below.

Table 4.4: Overview of GT Model Settings

Parameter	Setting
Solver Type	Pressure-Based
Turbulence Model	RSM
Time Stepping	Steady-State
Spatial Discretisation	Second-Order Upwind
Convergence Criteria	10^{-5}
Walls	No-Slip Condition
Inlet Mass Flow	Varied
Outlet Pressure	23 bar
Wall Boundary	Adiabatic
Mesh Type	Mixed
Total Cells	1,111,154
Density	Temperature Dependent (Polynomial)
Viscosity	Temperature Dependent (Polynomial)
Fuel Inlet Temperature	318 K
Combustion Model	Partially Premixed Combustion
Chemical Kinetics	GRI-Mech 3.0
Radiation Model	P-1

4.6 GT Hybrid Combustion

Having validated the numerical model, it is applied to investigate the integration of air preheating within a heavy-duty combustion chamber via a UHTS system. The combustion chamber geometry used is representative of the type used in CCGTs.

The degree of air preheating tested ranged from 760 K to 1750 K. Greater temperatures are not tested here as, although the maximum store temperature of the type proposed by Robinson (2017, 2018) is 1800 K, the extraction temperature from the store will reduce due to losses and heat transfer effectiveness.

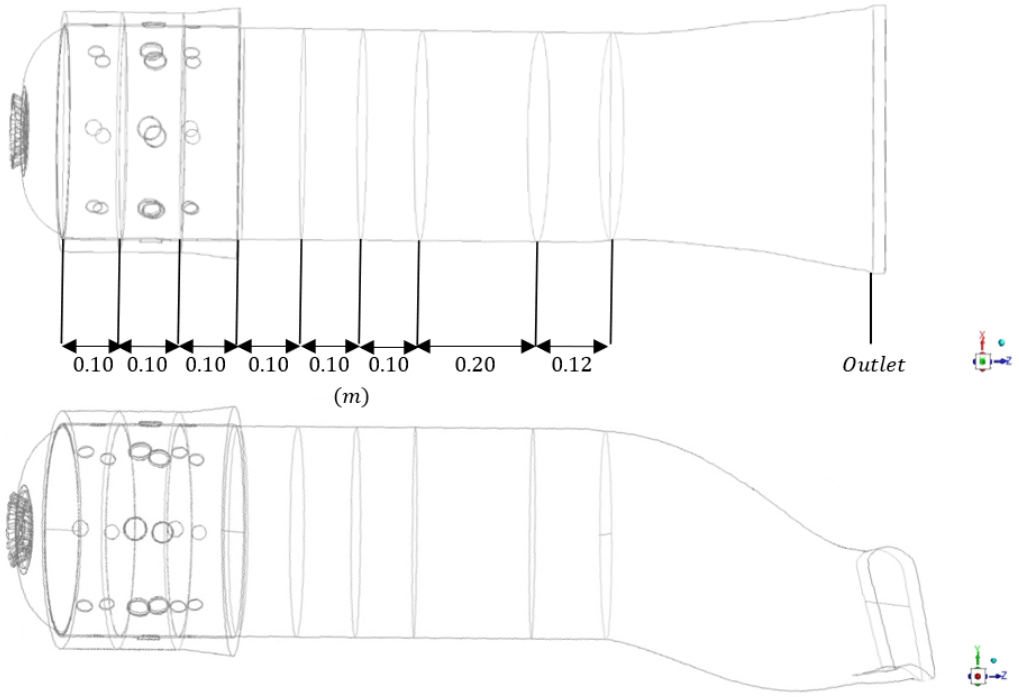


Figure 4.9: Locations of horizontal cross-sections (dashes) and interior faces used to measure data throughout the combustion chamber.

The effect of preheating the combustion air on the fuel requirements and emissions of CO, CO_2, and NOx are discussed below. These results are taken from a series of faces outlined in Figure 4.9. The faces are taken as planes at cross-sections of various z-distances from the inlet.

4.6.1 Fuel

The greatest TIT required in a current heavy-duty GT is 1873 K (Yuri et al., 2013). To achieve this at different air preheat temperatures, the fuel requirement varies. In order to maintain a constant inlet mass flow rate, the air inlet must also vary. The ratio of air that enters through each boundary is kept constant.

The fuel requirement is initially predicted based on the sensible heat equation. However, these predictions fail to account for energy losses due to the partial combustion of fuel and the varying thermal properties of air, combustion products, and their intermediates. These cause inaccuracies in predicting a realistic fuel requirement, resulting in under-predictions. In the GT simulations, using a thermodynamic database provides accurate properties for all components (Kee et al., 2000). The boundary conditions below were found using these properties by adjusting the fuel and air flow rates in an iterative manner, maintaining the AFR, to find the flow rate of fuel required to match the design TIT.

The fuel requirement decreases as inlet air temperature increases. This is due to the hybrid system providing a significant portion of the energy required to meet the TIT. This is seen in Table 4.5.

Table 4.5: Boundary conditions producing 1873 K outlet in the heavy-duty combustion chamber.

Air Temperature		Mass Flow				
Combustor Inlet (K)	Increase Required (K)	Air (Outer) (kg/s)	Air (Swirl) (kg/s)	Air (Dome) (kg/s)	Fuel (kg/s)	ϕ (-)
760	1113	21.255	2.733	2.530	0.162	1.02
1000	873	21.280	2.736	2.533	0.131	0.83
1250	573	21.308	2.740	2.537	0.096	0.60
1500	273	21.337	2.743	2.540	0.059	0.37
1750	123	21.372	2.748	2.544	0.016	0.10

The combustion location within the combustion chamber for each system can be seen in Figure 4.10. The combustion region moves closer to the inlet with an increased preheat air temperature as the fuel reaches its auto-ignition temperature faster (Ye et al., 2014) and requires less mixing to achieve a suitable AFR.

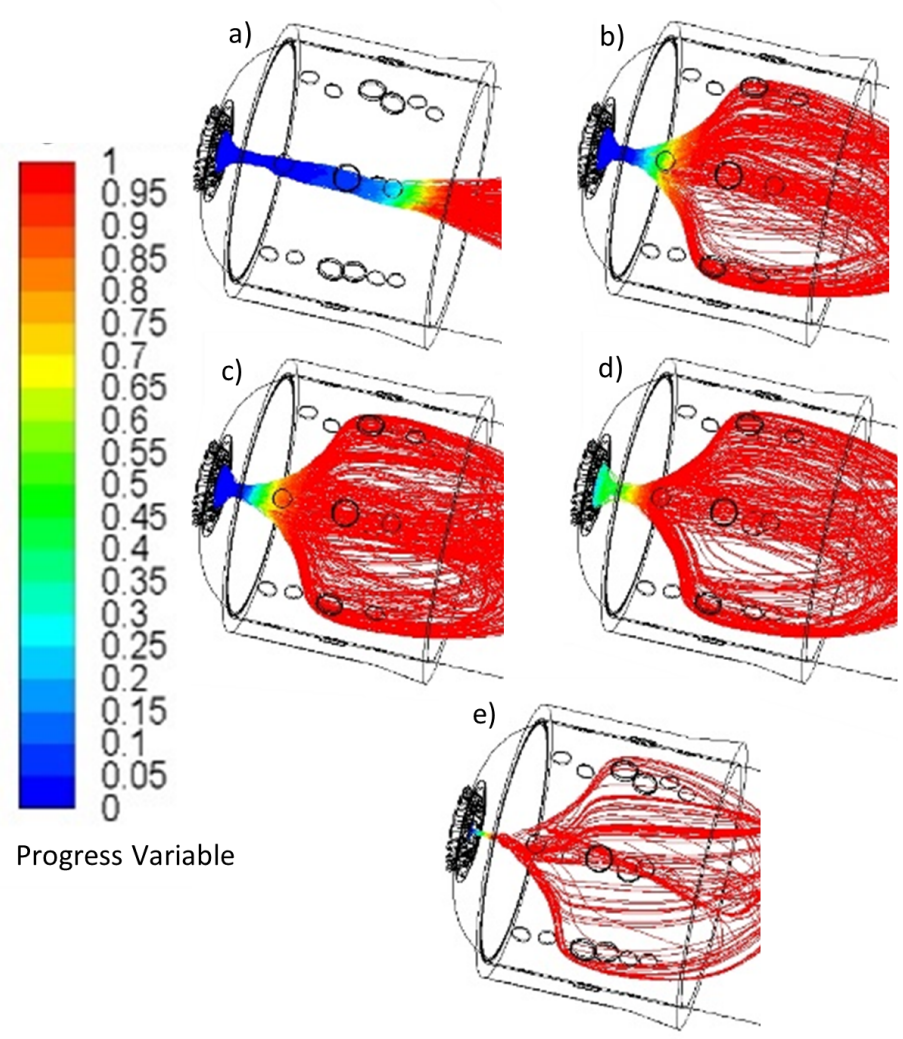


Figure 4.10: Combustion progress variable along the length of the combustion chamber for different systems a) 760 K, b) 1000 K, c) 1250 K, d) 1500 K, e) 1750 K.

Whilst the movement of the combustion region towards the fuel inlet does not present any chemical issues, it should be noted that the change may have adverse effects physically. As cooling air is inlet to maintain material temperatures around the initial combustion region, there would be insufficient cooling around the new combustion region. As such, the chamber would require a redesign to introduce cooling air closer to the fuel inlet. Wall temperature is not modelled in this investigation due to the increase in complexity, and therefore computational requirements.

These results confirm that the system with the highest preheat temperature requires the least fuel. The required mass to maintain an 1873 K outlet temperature was reduced from 0.162 kg/s to 0.015 kg/s. With the implementation of a 1750 K air preheat, the fuel requirement is reduced to 11.1 % of the initial mass.

4.6.2 Carbon Dioxide

The CO_2 production in the system is primarily due to the complete combustion of the fuel. Any change in the mass of fuel entering the system will directly affect the CO_2 at the outlet. The concentration of CO_2 at the system exit is displayed in Figure 4.11.

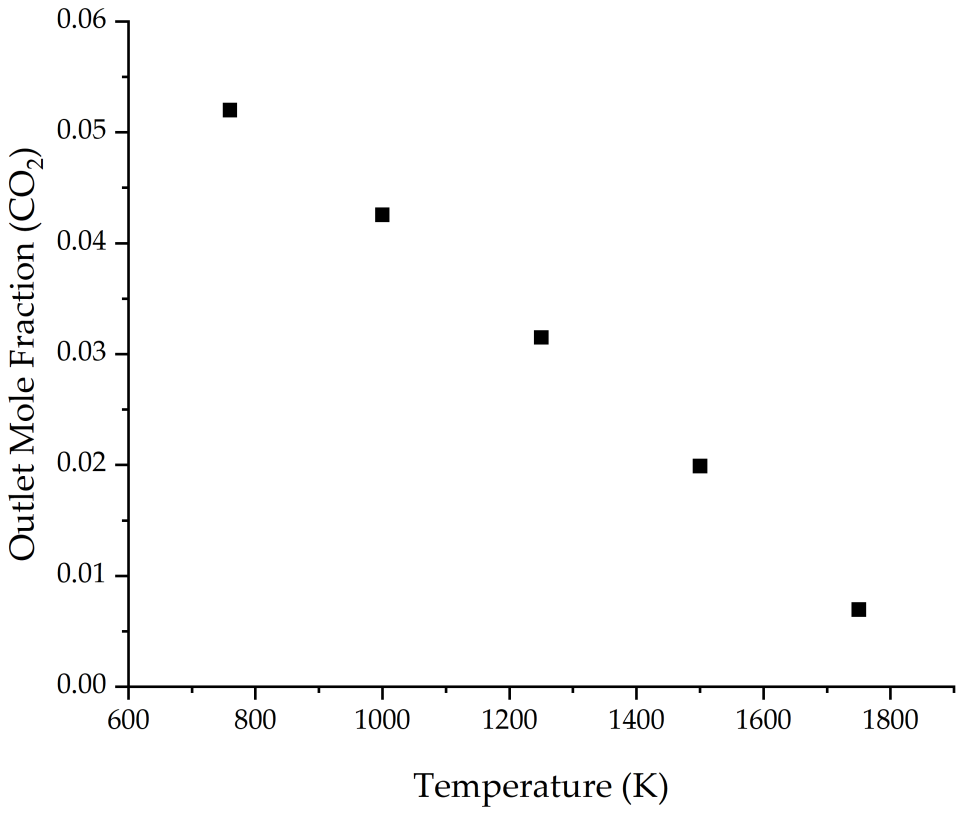


Figure 4.11: Mole fraction of CO_2 at the system outlet for various inlet temperatures.

These results show that the system with the least fuel produced the lowest CO_2 concentration

at the outlet. Implementing an air preheat to 1750 K resulted in the CO_2 mole fraction lowering to 13.4 % of its initial value, reducing from 0.052 to 0.007. However, this is not a directly proportional reduction, as fuel mass is just 11.1 % of its initial value. This slight increase is discussed in Section 4.6.4.

4.6.3 NOx

The nature of NG-air combustion leads to regions of high temperature or hot spots that cause NOx production (Nemitallah et al., 2022). As a result, temperatures throughout the combustion chamber are raised above that of the required average TIT.

With preheating of the working fluid, there is a reduced requirement for combustion. This causes the size of the combustion region to decrease and, thus, minimises hot spots within the system. This is seen in Figure 4.12.

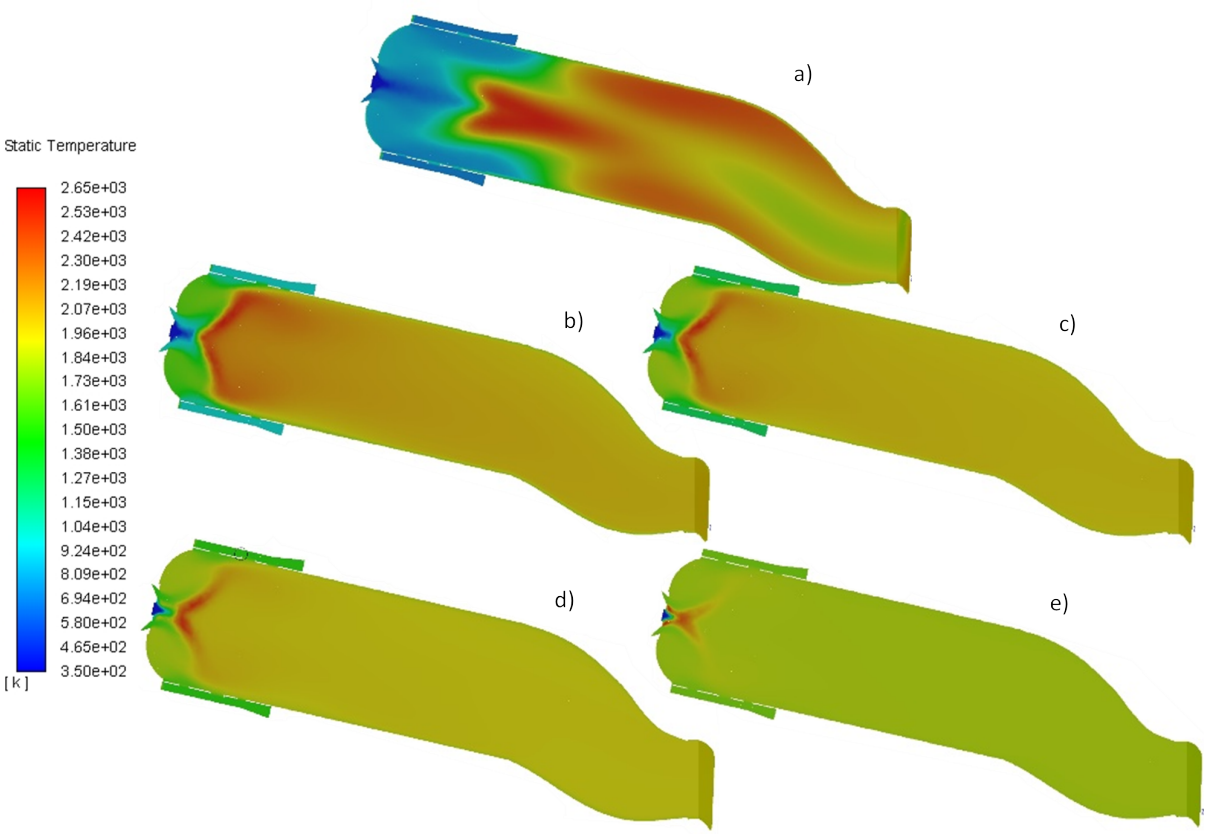


Figure 4.12: Temperature contours for four models along a vertical cross-section at the fuel inlet axis for different air inlet temperatures: a) 760 K, b) 1000 K, c) 1250 K, d) 1500 K, e) 1750 K.

The initial conditions, using 760 K air, produce a combustion region approximately 0.2 m from the fuel inlet, similar to the location found by Hasini et al. (2013). It should be noted that this results in the combustion region moving closer to the fuel inlet. As the initial design does not account for significant combustion in this region, a combustor wall redesign may be required to ensure material temperatures are controlled. This reduces the ease of retrofit.

Further pilot-scale work would be necessary to confirm the flame behaviour and identify any barriers to long-term operation.

Above 1800 K, NOx is produced primarily through the thermal pathway, caused by the dissociation of N_2 and O_2 (S. Can Gülen, 2019). Thermal NOx production is an exponential function of the flame temperature. Generation begins at around 1700 K and increases exponentially, becoming significant at 1850 K (Egil Røkke et al., 2003). Due to this, the hot spots within the combustion chambers are significant when considering the production of NOx.

As the volume of hot spots decreases with an increase in inlet air temperature and a reduction in fuel combusted, N_2 and O_2 molecules spend a reduced period at high temperatures. As a result, the production of NOx occurs across a significantly smaller region. It should be noted that as the preheat temperate increases and the combustion region moves closer to the combustor inlet, the residence time in the combustion chamber at the TIT increases. However, the subsequent increase in NOx production is insignificant compared to that produced in regions of elevated temperature due to increased combustion. A comparison of NOx production regions can be seen in Figure 4.13 below.

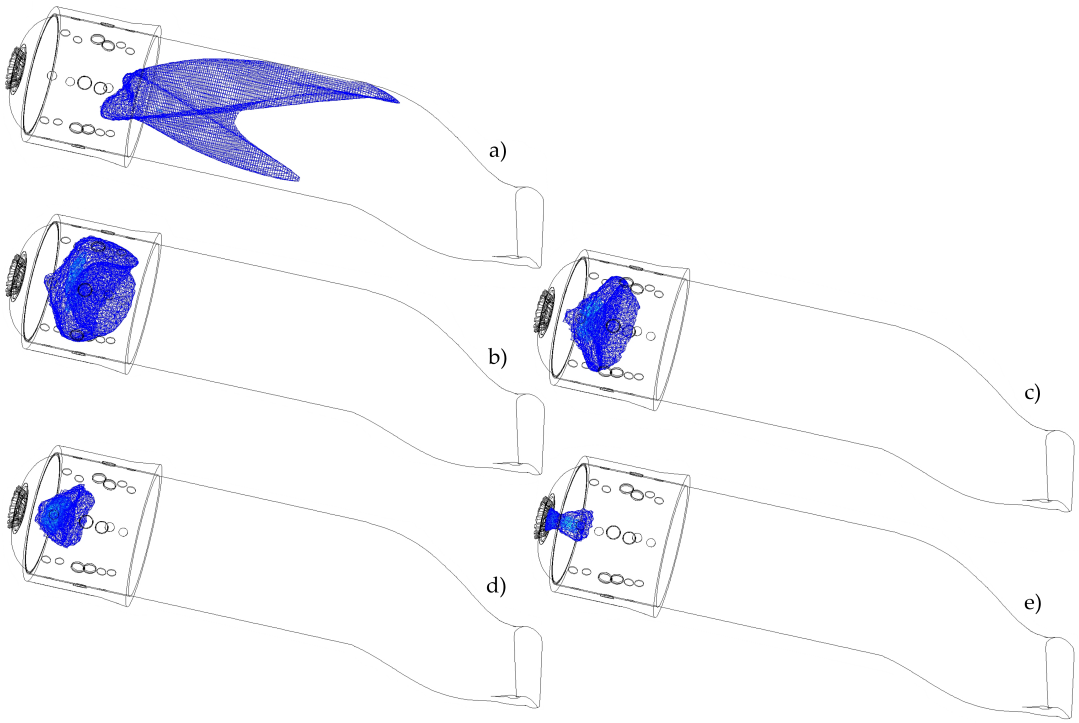


Figure 4.13: Volume of the region in which NOx is produced in the combustion chamber at various air inlet temperatures, based on Fluent Rate of NOx production a) 760 K, b) 1000 K, c) 1250 K, d) 1500 K, e) 1750 K.

For each inlet air preheat temperature, the average NOx mole fraction is reported at faces throughout the combustion chamber to show production within the system. These results are displayed in Figure 4.14, and the mole fractions at the outlet are displayed in Table 4.6.

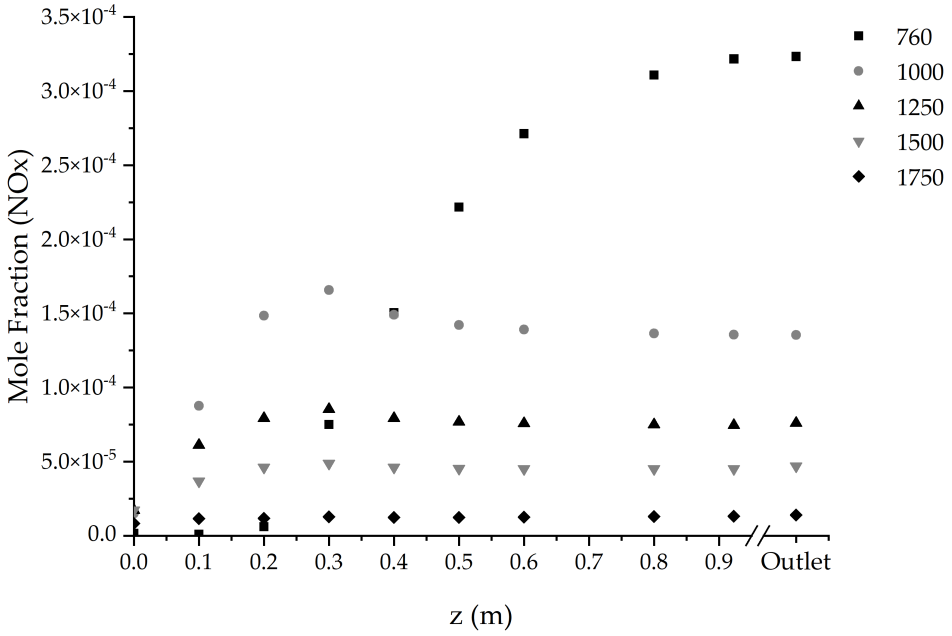


Figure 4.14: NOx mole fraction at nine cross-sections down the length of the combustion chamber with various inlet air temperatures.

Table 4.6: Mole fraction of NOx at outlet face of the combustion chamber.

Air Temperature (K)	Outlet Concentration (ppmvd [@ 15 % O_2])
760	128
1000	92
1250	67
1500	64
1750	53

These results confirm that the system with the highest preheat temperature combusted the least fuel, produced the smallest hot spot area and, as such, generated the least NOx. The mole fraction at the combustion chamber outlet reduced from 2.28x10^{-4} to 0.14x10^{-4}. With a 1750 K air preheat implementation, NOx is reduced to 6.2 % of the mole fraction produced by the system without preheating.

4.6.4 Carbon Monoxide

CO production within a GT is a function of the incomplete combustion of hydrocarbons. When the fuel has insufficient O_2 for complete combustion, incomplete combustion occurs. CO is produced as there is insufficient O_2 to convert the carbon to CO_2 fully.

In current GTs, there is a trade-off between NOx and CO (Hung, 1993), attributable to NOx-controlling technologies reducing the flame temperature. If the flame temperature is reduced too far, this can result in the quenching of the combustion, resulting in CO formation.

During ultra-lean combustion without a UHTS system, the peak combustion temperatures are significantly lowered. Whilst this reduces the formation of NOx, the cool air can result in

quenching as there may be insufficient heat to sustain the reaction. In hybrid systems, the likelihood of quenching is reduced as the air is heated, reducing its cooling effect on the flame. This increases the probability of complete combustion, the primary mechanism by which the production of CO is limited.

Additionally, as the mass inlet of fuel decreases, there is a lower point concentration. As such, less fuel is required to mix to attain a suitable AFR for combustion, which causes the bulk of CO to be generated further upstream. Resultantly, any CO produced via incomplete combustion has a greater residence time.

As there is an increase in the abundance of O_2 at high temperatures in hybrid systems, CO is further oxidised to form CO_2. This causes the slight increase in CO_2 concentration, highlighted in Section 4.6.2. The CO concentration at the system outlet may be seen in Figure 4.15.

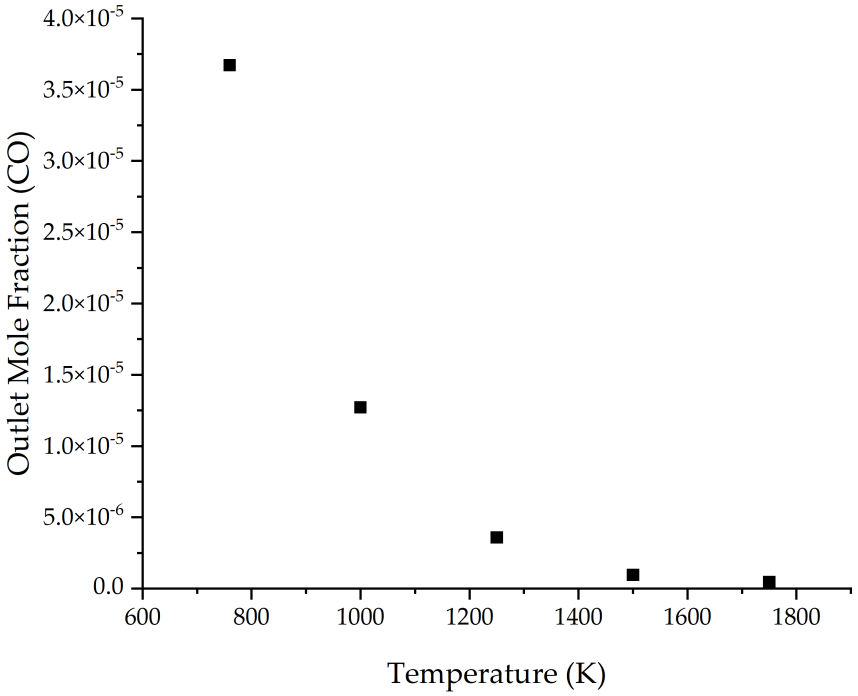


Figure 4.15: Mole fraction of CO at the system outlet for various inlet temperatures.

These results confirm that the system with the highest preheat temperature produced the least CO. The mole fraction at the combustion chamber outlet reduced from 3.67×10^{-5} to 0.046×10^{-5}. Implementing a 1750 K air preheat reduces CO to 1.35 % of the mole fraction produced by the system without preheating.

4.7 Summary of GT Integration

In this chapter, a numerical analysis of a partially premixed combustion chamber of a >440 MW GT has been carried out. The primary aim is to find how converting a conventional GT to a hybrid burning system affects pollutant emissions. Fuel requirements and outlet concentrations of CO_2, NOx, and CO are assessed.

An initial investigation is undertaken to validate the CFD model by evaluating and comparing it with available experimental data. The results showed that both the chemical and physical behaviours are modelled accurately. The Tay geometry was used for initial validation due to the availability of experimental data, while the heavy-duty GE DLN 2 series combustion chamber was used for further analysis as it is representative of a power-generating GT combustion chamber.

A range of temperatures at which the air is introduced to the combustion system has been simulated. The AFR varies to maintain a constant outlet temperature and mass flow rate. In these conditions, the preheated air displaces the combustion requirement to reach the required TIT. As such, there are fewer localised regions of high flame temperatures. The primary factor is the reduction in fuel combustion, which prevents gases from spending prolonged time at high temperatures.

While working in a validated CFD model provides some confidence in results, they must be confirmed. As such, further work is required to investigate an optimal combustion chamber design for integrating high-temperature air. As outlined, issues associated with combustion chamber liner material limitations, autoignition and flashback mitigation and combustion stability should be investigated through further CFD alongside experimental validation. This may be achieved by altering combustion chamber geometries, swirler design and air-split ratio alterations.

An increase in air preheating resulted in a significant decrease in the emissions of CO_2, NOx, and CO. The reduction of CO_2 is directly based upon the reduction of carbon-based fuel entering the system. NOx is then affected by the minimisation of hotspots, reducing the production of NOx via the thermal pathways. Finally, CO emissions are reduced due to an increase in complete combustion due to a reduction in combustion quenching and an increase in further oxidation to CO_2.

An increased outlet temperature from a UHTS system may achieve 100 % fuel displacement. When the TES system is depleted and unable to output at the required TIT, it may be possible to maintain a constant output from the generator without CO_2 production by replacing NG with H_2. Further study is required to investigate fuel switching. A pilot-scale study may examine the flame behaviour of highly diluted H_2 combustion.

Reducing pollutant release from conventional GTs allows for cleaner power generation using highly efficient heat-based systems. Air preheating may enable the continued operation of these systems as emissions regulations become more stringent to meet the 1.5 $^\circ$ C warming target. Grid-scale UHTS integration will allow for a low-emission dispatchable power system driven by renewable energies, ensuring supply security.

Chapter 5

Economic Analysis

5.1 Integration Economics Overview

This chapter investigates the economic and environmental impacts of integrating a UHTS system into GTs, HRSGs, IBs. The analysis is conducted through the development of a dispatch model for individual UHTS systems discharging to maximise either system profitability or sustainability.

Two separate economic dispatch models were produced: the arbitrage model and the fuel displacement model. The arbitrage model evaluates the profitability of charging the UHTS system during periods of low electricity prices and discharging during high-price periods, taking advantage of market fluctuations to maximise revenue. The fuel displacement model, on the other hand, focuses on the environmental benefits of using UHTS to displace conventional fuels in thermal processes, thereby reducing carbon emissions.

These models are utilised to explore past and future networks using historical market data from 2018 to 2022 and forecasts up to 2050. This aims to highlight the potential long-term benefits and challenges of UHTS integration in a transitioning energy market. A sensitivity analysis is performed to investigate the impact of varying model parameters, such as system efficiency, temporal optimisation periods, and settlement period lengths. This aims to identify the key factors affecting the accuracy of the economic models, providing insights into potential areas for improvement.

By providing an analysis of both the arbitrage and fuel displacement models, this chapter offers insights into both the economic feasibility and environmental impact of UHTS integration into the current and future energy network, with the goal of supporting energy resilience and decarbonisation.

5.2 UK Energy System

The UK energy market is evolving to enhance grid reliability in the face of increasing renewable integration, with market-driven mechanisms playing a pivotal role. The introduction of carbon pricing through emissions trading schemes has influenced electricity pricing dynamics, incentivising and accelerating the shift towards low-carbon generation.

This chapter will investigate the economic and environmental effects of the integration of the 10,800 MWh TES system proposed by Robinson (2017) into a 650 MW_e Gas Turbine and a 250 MW_e Heat Recovery Steam Generator-driven steam turbine for electricity production and a 3 MW_{th} Industrial Boiler for steam generation. This will be achieved by generating a dispatch model of individual UHTS systems attached to each of these discharge technologies, supplying high-temperature air, with no interaction with each other.

Whilst this will be based on a UK network, the model aims to be adaptable and applicable to various international networks. The UK is used in this study due to its readily accessible data on the electricity market and published projections for the future energy landscape, which will be discussed in greater detail later in this chapter.

5.2.1 Opportunities within the Electricity Network

The emergence of aggregators and Virtual Power Plants (VPPs) is a response to this change in system dynamics, representing a strategic approach to managing the variability and decentralisation of RES. By pooling resources from smaller generators and demand sources, these entities act as cohesive, flexible units, contributing significantly to grid stability (Rouzbahani et al., 2021). Virtual Lead Parties (VLPs) utilise VPPs by instructing short-notice and short-duration increases and decreases in consumption in response to fast-moving changes in the needs of the network (Elexon, 2021). Figure 5.1 shows a simplified flow diagram of a VPP participating in the energy market using distributed assets.

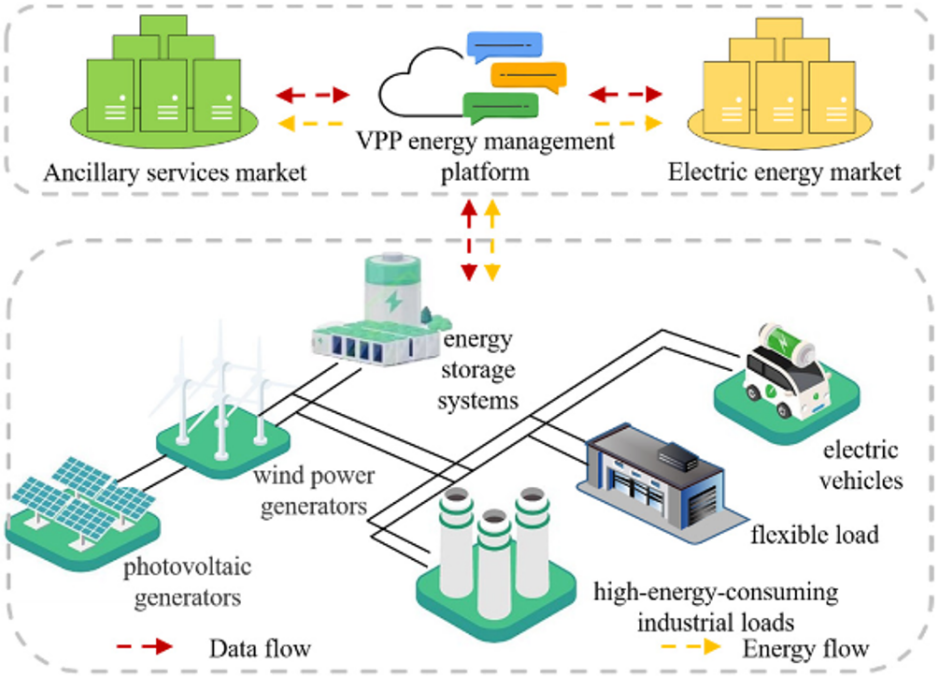


Figure 5.1: Integration of distributed assets into the network via a Virtual Power Plant (Wang et al., 2023).

As such, VLPs such as Flexitricity provide demand-side response, using industrial, commer-

cial, and distributed resources to help balance supply and demand in the GB electricity system. This is achieved by monitoring and controlling flexible industrial load, small generation, and battery storage in response to the needs of the electricity networks, providing reserve, frequency response, peak reduction and other balancing services. This provides businesses with access to flexibility markets regardless of their energy supplier.

When considering their use with ES, VPPs ensure that systems are charged using the lowest cost and greenest electricity available, by accessing flexible electricity opportunities such as the Balancing Mechanism, spot electricity markets and Local Constraints Market. These markets provide revenue which offsets the business's fuel and network operating costs.

This growth is driven by the profit potential of balancing the grid as it evolves to incorporate higher levels of variable renewable energy sources (Denholm et al., 2021). UHTS systems offer the potential for extended ES periods and provide an adaptable output that can offer high-grade heat to various industries. This positions UHTS as a focal point of research in developing energy resilience and network decarbonisation in the UK's energy transition (Datas et al., 2018). This is particularly relevant in the UK, where ES is predicted to play a pivotal role in mitigating wind and solar power variability, thus ensuring a stable and reliable energy supply amidst the nation's dynamic weather patterns (Ryland and He, 2023).

Independent ES systems can utilise low-cost electricity for charging. Conversely, they release electricity back to the grid during periods of high energy demand, capitalising on higher prices. This is known as arbitrage. The profitability of these services has been proven by mechanical storage systems such as PHS and CAES. These storage systems are mature technologies used primarily for time-shifting and supply capacity (Soini et al., 2019) and provide capacities large enough to enter into the markets alone. These technologies have high Technology Readiness Levels (TRL) and have been proven commercially. An overview of TRL for various ES technologies is shown in Figure 5.2. As UHTS technologies are currently entering TRL 5 and 6, the economic aspects of these systems require thorough investigation.

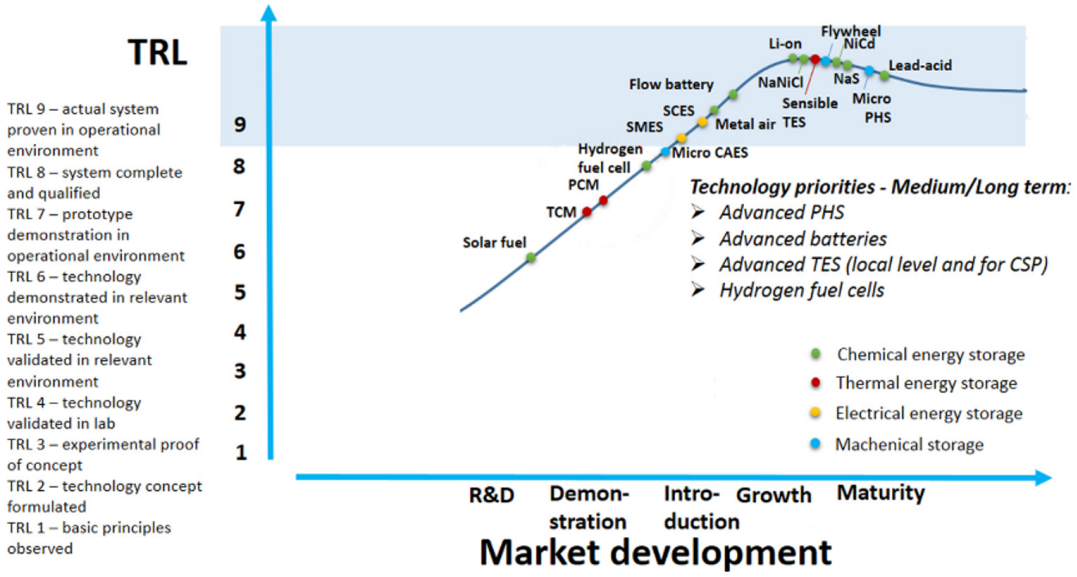


Figure 5.2: Technology Readiness Level and maturity of various energy storage technologies (adapted from Nguyen et al. (2017)).

Due to the versatile nature of UHTS systems, a range of discharge technologies must be considered when investigating the economics of the system. In addition to being used in time-shifting applications such as arbitrage, UHTS can also provide economic advantages by displacing or replacing fuel used in conventional thermal processes, as seen in Chapter 3 and Chapter 4. This secondary utility is economically incentivised through a reduction in operational costs associated with fuel and, in some cases, carbon taxes.

5.2.2 Current Economic Models

A majority of existing techno-economic assessments use a top-down approach when investigating TES systems (Rathgeber et al., 2015; Puschnigg et al., 2021; Rathgeber et al., 2016; Bradbury et al., 2014). While top-down assessments provide a broad perspective, they often overlook factors such as grid requirements, technical parameters specific to the energy sector of the region, and local policies such as carbon taxes. It is vital to include technical parameters affecting the store's operation, such as thermal mass, storage temperature, storage material, outlet temperature, and thermal losses. Similarly, the extraction system's parameters - including system efficiency, heat exchange effectiveness, start-up time and the effective system capacity based on the minimum temperature requirement - must be accounted for. Furthermore, in the context of the UK's industrial sector, which is under increasing pressure to reduce CO_2 emissions, the benefits in terms of operational cost savings must be quantified. As such, a model must also be designed to account for varying carbon tax credit prices. These parameters are often overlooked in similar studies (Kriechbaum et al., 2018).

Therefore, it is necessary to develop a suitable economic model that can account for all of these parameters to provide suitable insight into the economics of UHTS deployment. The bottom-up method uses engineering principles to calculate the required parameters based on system specifications, making the model transparent and the results reproducible. As such, this research employs a bottom-up approach, allowing for a detailed analysis of UHTS systems' economic viability against the backdrop of the UK's unique energy challenges and opportunities (Prina et al., 2021).

Studies conducted by Schoenung and Eyer (2008) and Schoenung (2011) for the US Department of Energy both demonstrate this concept, using a variety of data sources to study a range of types of modular electrochemical storage technologies. Models have also been produced to evaluate the cost-effectiveness of commonly used battery storage technologies, using manufacturer-provided data (Abrams et al., 2013). While valuable, such methods must be adapted to account for the specificities of UHTS technologies. Their potential integration with existing generation sites is crucial to achieving energy resilience and carbon neutrality within the UK's strategy.

Modelling and conducting techno-economic analyses on ES systems are complex, due to the need for assumptions regarding the rates and timing of charging and discharging operations. This complexity is amplified by the UK's dynamic energy market, where factors such as fluctuating renewable output, variable energy demand, and evolving policy incentives must be captured in order to accurately assess the value of ES solutions like UHTS (Ademulegun et al., 2021).

Additionally, the operation of ES systems is influenced by market conditions and the physical

capabilities of the storage devices. There are two main models for analysing the performance and value of ES: unit commitment models; and price-taker models (Martinek et al., 2018). Unit commitment models balance the grid whilst optimising the dispatch of all generators and storage within a grid to minimise overall system costs by considering demand, reserve requirements, and system constraints (Martinek et al., 2018). Conversely, price-taker models optimise the operations of individual storage systems based on known market conditions, without the ability to impact the market, to maximise value. Price-taker models offer higher fidelity and more rapid solution times. However, they do not consider the impact of these operations on the grid, which can limit these models for studying grid development (Lin and Magnago, 2017).

When considering energy arbitrage, the price-taker model offers a best-case scenario for estimating revenue for ES systems. This approach assumes stable electricity prices that are unaffected by the discharge of an ES system. This may not reflect real-world scenarios as prices will fluctuate based on the usage of an ES system. However, for larger systems such as national scale grids, the capacity of the store is comparatively small. As such, this method can still provide a reliable estimate of operational value. A study by Martinek et al. (2018) demonstrated that the price-taker approach could accurately estimate the value of solar power systems with TES. This approach was found to be effective, even when compared to more complex production cost models, highlighting its utility in evaluating system value within large electricity grids.

5.2.3 Energy Market Factors

With respect to the wider energy system, NG costs, electricity pricing, and carbon taxation, each influence the economics of a UHTS system. This is because NG plays a significant role in the current energy mix, providing a base-load energy source and being used for heat generation in various industries. Similarly, the dynamics of electricity pricing directly affect the economic landscape for industrial energy consumers and the opportunities presented by arbitrage. Additionally, carbon taxation mechanisms are affecting the economic feasibility of many systems.

The dynamics of the pricing of NG, electricity and of carbon taxation shape the economic viability of introducing a UHTS system. The fluctuating prices of NG have direct implications regarding the potential savings produced through fuel displacement. Additionally, as the cost of emitting CO_2 increases, the savings associated with fuel reductions will increase in turn. Finally, as the store is charged via the grid, electricity market prices further affect the economics of system operation.

Real data should be sourced regarding historic NG, electricity, and carbon tax prices to account for these factors in an economic model. The factors which influence these prices are examined below.

Natural Gas Price

In anticipation of future decarbonisation required to reach net-zero, the UK is phasing out unabated coal-fired power generation, positioning NG as a transitional, cleaner fuel source to ensure the security of supply against the intermittent availability of renewables. As such, when

modelling the integration of UHTS systems into existing infrastructure, it is likely to be NG that is replaced or displaced. It is therefore necessary to account for the price of NG within the UK.

The UK's NG market is based on a dynamic trading system which revolves around the trading and distribution of NG, facilitating its supply to various sectors of the economy (Moore et al., 2003). The UK market relies on an array of sources. The North Sea has historically been a primary reservoir of domestically produced NG. However, as production from these gas fields has tapered due to maturation, the market has developed a greater reliance on imports. This shift is underpinned by the infrastructure of pipelines connecting the UK to neighbouring countries such as Norway, Belgium, and the Netherlands.

These pipelines facilitate the import of NG, enhancing the country's energy security. This is further supplemented by Liquefied Natural Gas (LNG) terminals which bolster supply capabilities, enabling the reception of LNG shipments from global suppliers, and providing flexibility and resilience to the NG supply network.

Within the UK's NG market, consumption is distributed across diverse sectors, of which the industrial, commercial, and residential are all significant contributors. Of note, residential and commercial heating demand surges during colder months, posing seasonal challenges to the market's supply-demand balance.

The structure of the NG market is characterised by its emphasis on competition and market-driven operations. Key participants include NG producers, suppliers, transmission companies, and end consumers. The Office of Gas and Electricity Markets (Ofgem) oversees the market to safeguard NG supply security.

Pricing mechanisms in the UK NG market are influenced by factors including global NG prices, supply-demand, and currency exchange rates. The National Balancing Point (NBP) is central to these pricing mechanisms, acting as the primary NG trading hub. Prices at the NBP are determined based on market forces, making it a key resource for market participants (National Grid, 2017).

Regulation by Ofgem is integral to the function of the NG trading sector by establishing regulations that promote competition, maintain pricing fairness, and ensure the market's stability. This is based on the 1986 Gas Act and subsequent legislative acts (UK Parliament, 1986).

However, the price fluctuation of NG during unexpected supply disruptions, such as that triggered by the war in Ukraine, remains a challenge for energy security, which is compounded by a reduction in domestic UK production. Despite efforts to diversify sources and increase storage capacity, the reliance on international supplies leaves the market vulnerable to geopolitical disruptions (Maneejuk et al., 2024). This underscores the importance of a robust energy strategy to mitigate the impact of such disruptions on NG prices and, as such, energy security.

Electricity Price

The variability of NG prices - which provide a large portion of the baseload - alongside the variability in renewable generation, significantly impacts the electricity system in the UK. While crucial for sustainability, the shift towards RES introduces volatility in electricity prices due to their intermittent nature. This volatility impacts industrial operations, particularly those with

intensive energy demands, such as UHTS, which relies on electrical resistance for charging. This must be accounted for in any model looking at operational economics.

Electricity pricing within the UK is governed by market mechanisms, regulatory policies, and network charges. Industrial users are subject to the same wholesale market prices as other consumers. The electricity market operates on a bid system where generators and users bid to buy or sell electricity at a set price per unit. Based on this supply and demand principle, prices fluctuate around on the availability of generation and the level of demand (Liu et al., 2022). During periods of high renewable output and low demand, prices can fall, sometimes even becoming negative, which is beneficial for industrial facilities during these periods. Conversely, reliance on NG increases during low renewable generation and high demand periods, causing wholesale prices to surge, particularly if accompanied by high NG prices (Halbrügge et al., 2024).

The transmission and distribution network also influences the overall electricity pricing structure. Network charges cover the maintenance and upgrade of grid infrastructure and differ by region due to the distance between generation and consumption variation. Industrial facilities are significantly affected by these network charges and, given the substantial energy consumption of industrial operations, these charges can constitute a considerable portion of their electricity costs.

Policy measures aimed at decarbonising the energy sector, including levies to fund renewable subsidies and promote energy efficiency, add another layer of costs for industrial users (Watson and Bolton, 2023). While these policies are essential to facilitate a transition to a sustainable energy system, they can increase the cost and complexity of energy procurement for industrial operations.

The price of electricity can also vary throughout the day beyond the usual temporal fluctuations. The real-time nature of the UK electricity market requires a managed system that is dynamic in order to guarantee grid stability. Without this, a disparity between generation and consumption can affect system reliability. A difference between electricity produced and electricity consumed, known as the system imbalance, can directly result from a range of factors, including unexpected changes in demand, a variation in RES generation, or anomalies such as plant failures.

Over the course of one day, electricity is traded in 30 minute sections, referred to as Settlement Periods (SPs). Each day (Settlement Day) is split into 48 SPs, with SP 1 equivalent to 00:00 to 00:30, SP 2 to 00:30 to 01:00, and so on, through to SP 48 (23:30 to 00:00). Each SP is settled in isolation from the SPs around it. Within a SP, the National Grid Electricity System Operator (ESO) observes the actual electricity generation and consumption and calculates the grid imbalance price (Elexon, 2020). This serves as a market-driven mechanism to incentivise participation in balancing supply and demand during each SP, with generators either increasing output or high-consumption industries reducing power usage.

The calculation of imbalance prices is underpinned by the following key principles, which play out in sequential order (Fairbairn, 2020):

1. **Supply-Demand Differential**: Initially, the difference between actual electricity supply and demand within each Settlement Period (SP) is found.

2. **Bid and Offer**: Market participants, such as generators and consumers, submit bids

to alter their operation during that SP. Consumers may pay for additional electricity, whereas generators can receive compensation for additional electricity generation. These submitted bids and offers determine imbalance price.

3. **Price Calculation**: The imbalance price is established by matching the lowest offer with the highest bid. This selection reflects the cost associated with either generating additional electricity or curtailing consumption to restore grid balance.

4. **Market Clearing**: The market operator determines the imbalance price that clears the market. This is when there is a balance between supply and demand for electricity. This clearing price is typically set at the level where the supply-demand differential is reduced to zero.

Following each SP, settlements are conducted based on the disparities between their contracted positions and the imbalance price. Generators that produce surplus electricity relative to their contractual obligations and sell it at a high price imbalance receive financial reimbursements. Conversely, consumers who exceed their contracted consumption and purchase electricity at a high imbalance price incur financial costs.

Therefore, the imbalance price serves as a critical financial instrument within the UK electricity market. It provides both an economic incentive for generators and consumers to contribute to grid balancing actively and enforces financial accountability based on the grid conditions during each SP.

Carbon Taxation

One of the primary systems in the UK to mitigate CO_2 emissions is the carbon tax system. This assigns a financial cost to GHG emissions by levying a tax on the use of fossil fuels, creating an economic incentive to reduce the carbon footprint of a system. The rate of this tax is set per tonne of carbon dioxide equivalent (CO_2e) emitted. As a result, the operating cost of high-carbon sources such as NG increases. This directly links the tax to the carbon intensity of an electricity generation process or other significant industrial process. In this context, the integration of UHTS systems presents a compelling case for displacing traditional fuel requirements and thus minimising the financial burden of carbon taxes on energy producers and consumers. As such, any economic model should quantify the savings associated with this reduction in the outlet of CO_2.

The levy initially introduced was the Carbon Price Floor (CPF) scheme, structured to complement the European Union Emissions Trading System (EU ETS). This was in place until 2021 when it transitioned into the UK Emissions Trading Scheme (UK ETS) (UK ETS Authority, 2023), and is a critical component of the UK's transition towards a low-carbon energy system.

Under the UK ETS, a cap-and-trade mechanism limits the total emissions mass of certain GHGs. Systems that fall under the purview of the levy must hold allowances equivalent to their emissions, which they can either receive as a free allocation, purchase at auction or trade with other participants. This creates a market-driven approach to reducing emissions, where the cost of emitting CO_2 becomes a variable factor in operational decision-making processes.

The primary objective of the UK ETS is to provide a clear economic signal to carbon-intensive sectors to invest in cleaner, lower-carbon technologies, such as UHTS systems. The cap on emissions is intended to decrease over time, aligning with the UK's broader climate targets, including achieving net-zero GHG emissions by 2050. This is seen in practice as, in 2022, approximately 81 million allowances were available for auction, while in 2023, around 79 million allowances were allocated, with a slight adjustment to account for increased aviation operator entitlements. Looking ahead to 2024, under the new net-zero consistent cap, the expectation is that approximately 69 million allowances will be auctioned, reflecting a commitment to a more stringent emissions reduction trajectory (Department for Energy Security & Net Zero, 2024a).

At auctions, typically held on a weekly basis, allowances are sold to the highest bidders, and the auction clearing price sets the cost for those allowances. This auction price is influenced by factors such as current and anticipated demand for allowances, overall economic conditions, fuel prices, and regulatory policies. Notably, an auction reserve price is set at £22, below which bids are not accepted, to maintain a price floor (Department for Energy Security & Net Zero, 2024b). Prices can fluctuate on the secondary market based on trading activities. Participants trade allowances based on their individual needs. During the primary auction, if the bid price is significantly below the secondary market price, the auction clearing price is adjusted to align with the market. An example of this was seen in October 2021, where there was a 1,038,500 excess in allowances as these were valued under the clearing price of £60. This partial clearance, a first for the UK ETS, was due to bids below £60 being considered significantly lower than the prevailing secondary market price, leading to the remaining allowances being redistributed to subsequent auctions (Department for Energy Security & Net Zero, 2024a).

The UK ETS is also designed with mechanisms to provide both price stability and predictability to the market. A Market Stability Mechanism (MSM) can be triggered if the total number of allowances in circulation surpasses a certain threshold, leading to the adjustment of auction volumes to manage the market supply of allowances. For instance, if an auction offers 1 million allowances and the aggregate demand from all bids at or above a certain price level is for 1.5 million allowances, the clearing price would be set at the lowest bid price within that aggregate demand of 1.5 million, ensuring that all 1 million allowances are sold (Department for Energy Security & Net Zero, 2023).

Figure 5.3 displays an example of this system, published by the Department for Energy Security & Net Zero (2024a), where: PA is the price at which the number of bids exceeded the allowances; PB is the secondary market price; and PC is the auction clearing price. PA would usually be the clearing price; however, because PA is significantly below PB, PC is used as the clearing price. Additionally, QA is the number of allowances, QB is the number of allowances bid at the secondary market price, and QC is the number of allowances sold. P_{min} is the reserve price.

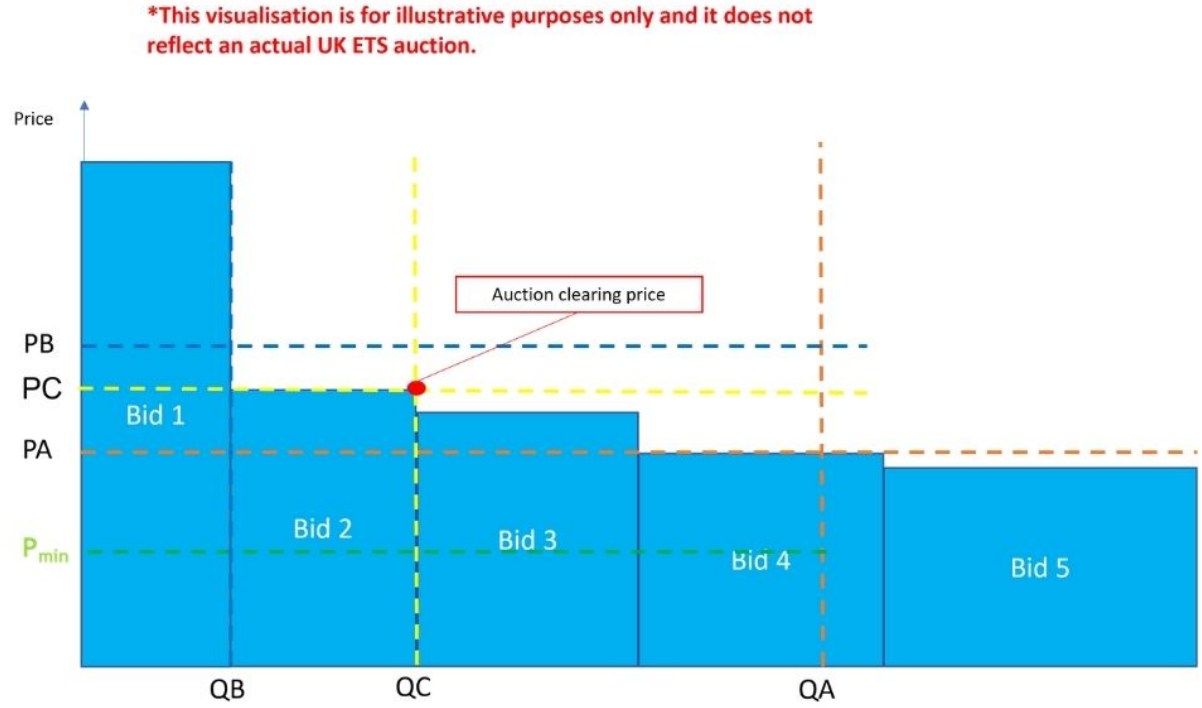


Figure 5.3: Published example of the auction clearing price calculation (Department for Energy Security & Net Zero, 2024a).

The UK ETS dynamically adjusts in response to market conditions, ensuring it generates a reduction in emissions. It is important to note that the UK ETS works alongside other climate policies to drive change and provide a framework for decarbonising the UK. As such, the variability of the carbon tax price must be accounted for within the economic model.

5.2.4 Future Network Prediction

When predicting profitability looking forward, the same system cannot be used due to the uncertain nature of future markets. Although a few studies look at future predicted markets, these tend to be on a shorter term. As UHTS systems are designed for extensive operational lifetimes, the potential climate for these systems should be investigated going forward decades. Leveraging the historical data of the UK's energy market can provide valuable baseline scenarios for modelling the future performance of UHTS systems amidst the country's transition to a low-carbon energy system.

PyPSA is an open-source Python-based package that can simulate and optimise modern electrical power systems over multiple time steps based on marginal costs (Lyden, 2022). It can be used for operational studies (optimal linear, non-linear, and security-constrained power flow) and investment studies (total energy system least-cost investment optimisation). Model implementations of PyPSA include the European transmission system (Hörsch et al., 2018) and global coverage models, which have been validated over the African continent (Parzen et al.,

2023). PyPSA is suited to modelling studies requiring high spatial and temporal resolution.

The transmission network operator for the UK, the National Grid, annually publishes a report titled Future Energy Scenarios (FES) (National Grid, 2023), on their modelling of the UK's pathway to net-zero. This is divided into four scenarios:

- Falling Short
- System Transformation
- Consumer Transformation
- Leading The Way

The Falling Short scenario falls short of targets whereas the other three scenarios reach net-zero. The modelling used to inform the FES involves numerous modelling methods applied to different sections of the energy system to determine the evolution of the energy system to 2050. Figure 5.4 below outlines the four scenarios and elaborates on how quickly they will lead to a reduction in CO_2 output and how much societal action is required to achieve this.

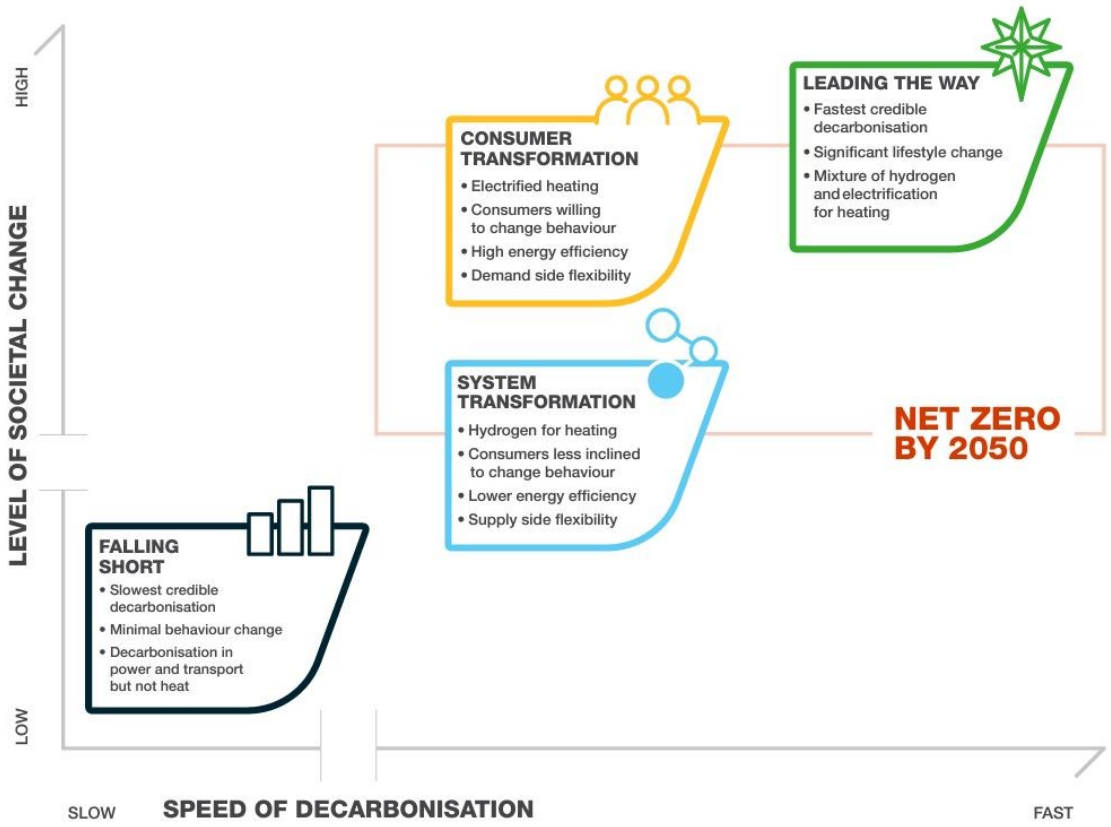


Figure 5.4: FES Net-Zero scenarios (National Grid, 2019).

PyPSA-GB is a power dispatch model of the Great British (GB) power system encompassing future years up to 2050 based on National Grid's FES. The NG prices in this model are projected to continuously increase, reaching a maximum of 25.18 £/MWh in 2050, as seen in Figure 5.5. Note that the gap from 2022 to 2029 is due to licence agreements preventing this data from being published.

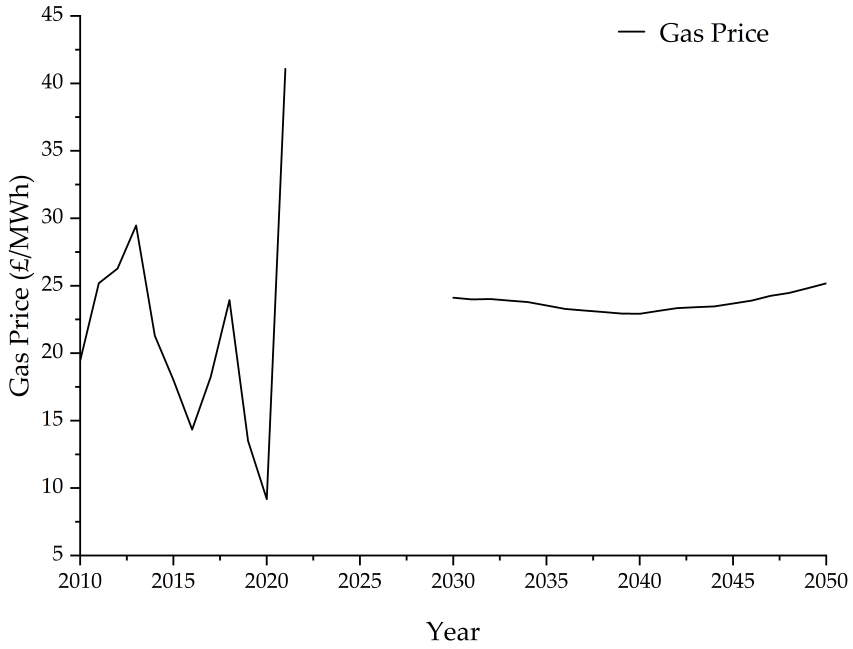


Figure 5.5: GB total NG price projection [adapted from National Grid (2023)].

As for the source of future carbon prices, FES publishes predictions. As of February 2024, the price is currently fluctuating around 34 £/tnCO_2, indicating that these prices are potentially overpredicted, and the most likely outcome is the low-case scenario. However, these carbon prices make it attractive to reduce the carbon intensity of NG-generated thermal electricity. This prediction is shown in Figure 5.6 up to 2050.

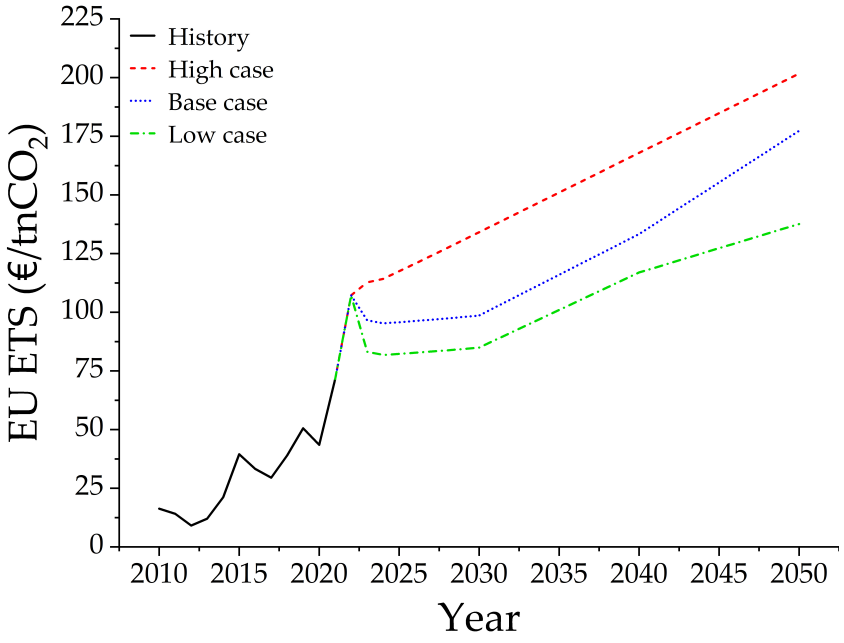


Figure 5.6: Carbon price projection for EU ETS (National Grid, 2023).

PyPSA-GB models the GB power system with high spatial and temporal resolution and incorporates historical data and both commitments and published predictions regarding future years. This links long-term energy transition pathway outputs from FES with high-resolution operational/dispatch models. More details on this model can be found within its documentation (Lyden, 2022).

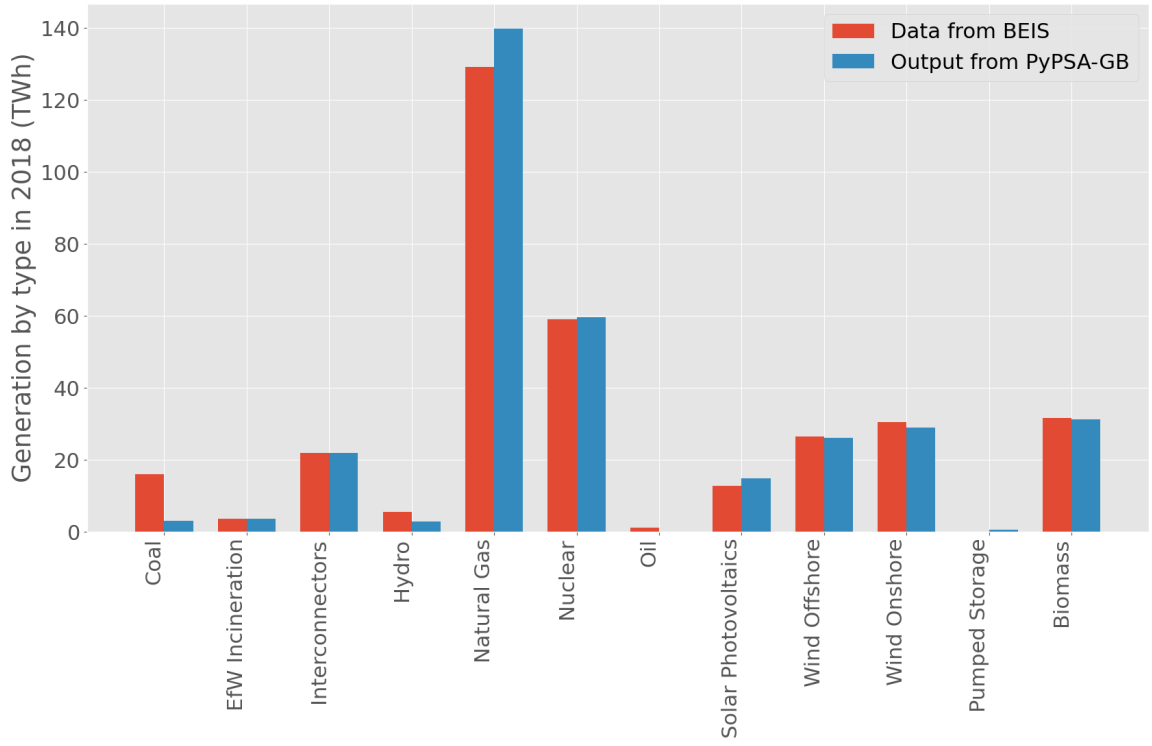


Figure 5.7: Comparison of PyPSA-GB generation with actual generation - 2018 (Lyden (2022)).

To verify the accuracy of the model, it was run to simulate the 2018 year, to provide confidence in the predictions that this model can produce. Figure 5.7 shows a comparison between the generation predicted and the actual generation as reported by BEIS. It can be seen that the two match with a high accuracy, thus giving confidence that this model can be used to estimate future electricity prices.

Due to the commercial sensitivity of the data, there is a lack of information on the future of UHTS systems, including all the appropriate parameters to evaluate their techno-economic feasibility for various applications. This chapter aims to fill this research gap by developing a comprehensive dispatch model, optimised to provide an economic assessment to evaluate the cost-effectiveness of a large-scale UHTS technology based upon the system described by Robinson (2017, 2018). This model will then be employed to compare the profitability of three discharge technologies – GT combustion chambers, HRSGs, and Industrial Boilers (IBs). The selection of these technologies is informed by their widespread deployment in the UK.

The results will then be compared using various discharge system efficiencies in one or both application scenarios - arbitrage profits and carbon taxation savings - between 2018 and 2050. The specific objectives of this study are to:

- Produce a set of historical data which will allow the modelling of potential economic benefits;
- Produce a data set which predicts future commodity prices up to 2050;
- Develop bottom-up economic models for two UHTS discharge systems;
- Compare the economic feasibility in two implementation scenarios – arbitrage and carbon tax savings; and
- Conduct sensitivity analysis to determine the effects of variability in input parameters on output results.

5.3 Data Acquisition

Modelling the profitability of a UHTS system necessitates an understanding of various economic and environmental factors. Electricity prices, NG prices, carbon tax prices, and emissions factors play crucial roles in evaluating the economics of integration. Multiple sources for this data should be examined when possible to ensure the model is robust, allowing for an in-depth understanding of the operational and environmental economics of UHTS systems.

5.3.1 Electricity Prices

In the UK, wholesale electricity prices are influenced by various factors and are sourced from different platforms. Two main suppliers of wholesale pricing data are EPEX and Nord Pool, which provide comprehensive data for market participants. These platforms play a crucial role in the dynamic trading ecosystem, facilitating the supply and pricing of electricity across different sectors of the economy.

Ofgem also provides insights into wholesale market indicators, offering a snapshot of data collected and analysed to assess the wholesale energy market. These indicators derive from Ofgem's monitoring framework and include wholesale forward delivery contracts price trends and day-ahead contracts price trends, which reflect the prices suppliers face when buying NG or electricity to supply their customers.

For modelling a system that takes advantage of selective price fluctuations for arbitrage, both Day-Ahead Electricity Prices and Imbalance Prices may be utilised. A comparison of these two prices over the same day is given in Figure 5.8.

Imbalance prices offer a unique arbitrage opportunity by capitalising on real-time fluctuations, which might be more pronounced due to rapid changes in supply and demand. Unlike Day-Ahead Prices, which are set in advance and reflect expected market conditions, imbalance prices can provide opportunities for higher returns in volatile markets, especially when renewable energy sources lead to unpredictable generation. Figure 5.8 also shows the effect of this on prices, where the imbalance price produced more fluctuation along with higher peaks and lower troughs.

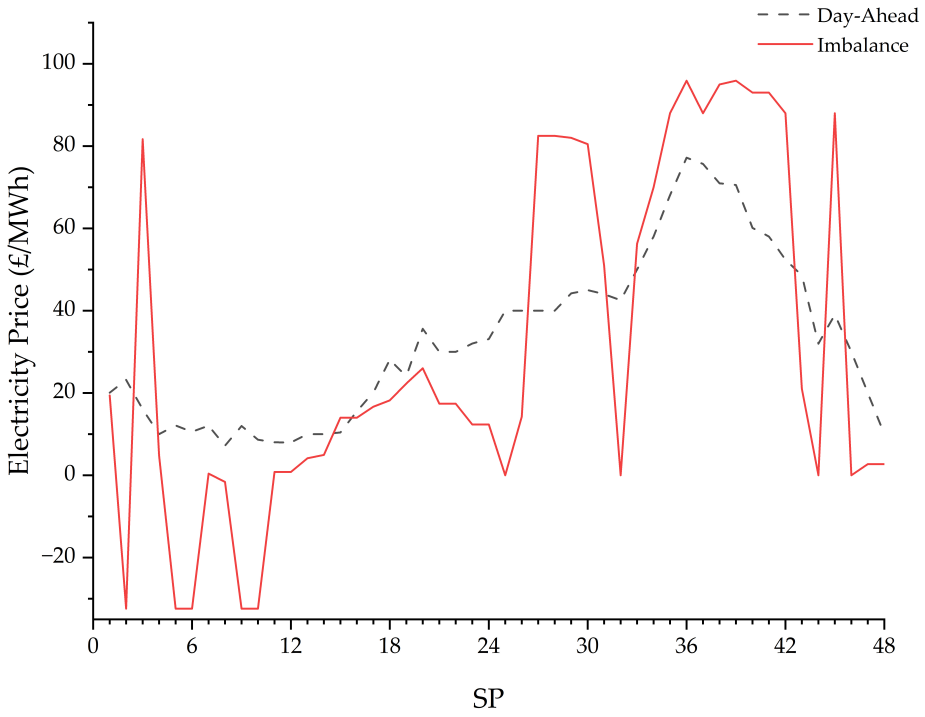


Figure 5.8: Comparison of Day-Ahead Auction Price against System Sell and Buy Imbalance Prices (Elexon, 2024; Montel, 2024).

This real-time approach allows for potentially higher profits but requires sophisticated systems capable of quick response to market signals. It should be noted that Day-Ahead Prices offer a safer strategy for investment due to their predictive nature, allowing for strategic planning around expected price changes.

If the model were to use Day-Ahead electricity prices, the suitability of each source must be considered. While Nord Pool and EPEX provide granular data on wholesale electricity prices, with updates available for smaller time steps such as hourly or half-hourly, Ofgem's approach to data publication is notably different. Ofgem aggregates and presents wholesale electricity price data in a summarised format, often providing averages over longer periods (Ofgem, 2024). This method of data presentation reflects Ofgem's role in monitoring and reporting on market trends rather than facilitating trading decisions. While the aggregated monthly averages offered by Ofgem provide valuable insights into longer-term market trends, they are not suitable for modelling the operation of a reactionary system, which requires more immediate data provided by platforms like Nord Pool and EPEX (Nord Pool, 2024; EPEX, 2024).

However, accessing the detailed, granular data necessary for modelling from Nord Pool and EPEX is prohibited by cost, as these platforms require subscriptions in excess of 1000 €. This factor limits the accessibility of real-time, highly specific market data for many users, potentially impacting the feasibility of conducting in-depth arbitrage analysis and modelling.

When considering the use of Imbalance Pricing, the data can be accessed for each SP from the Balancing Mechanism Reporting Service (BMRS) published by Elexon. This data is accessible by the Settlement Day and includes the System Sell Price (SSP) and the System Buy

Price (SBP) in £/MWh (Elexon, 2024). Elexon operates under Ofgem's regulatory framework, managing the Balancing and Settlement Code (BSC) in a more operationally focused role, ensuring efficient market operation within the guidelines set by Ofgem.

Based on its availability and suitability, the Imbalance Price values are used as the wholesale electricity prices. Using this data gives over 17,000 data points for each year analysed, and an example of this price fluctuation over 2021 can be seen in Figure 5.9.

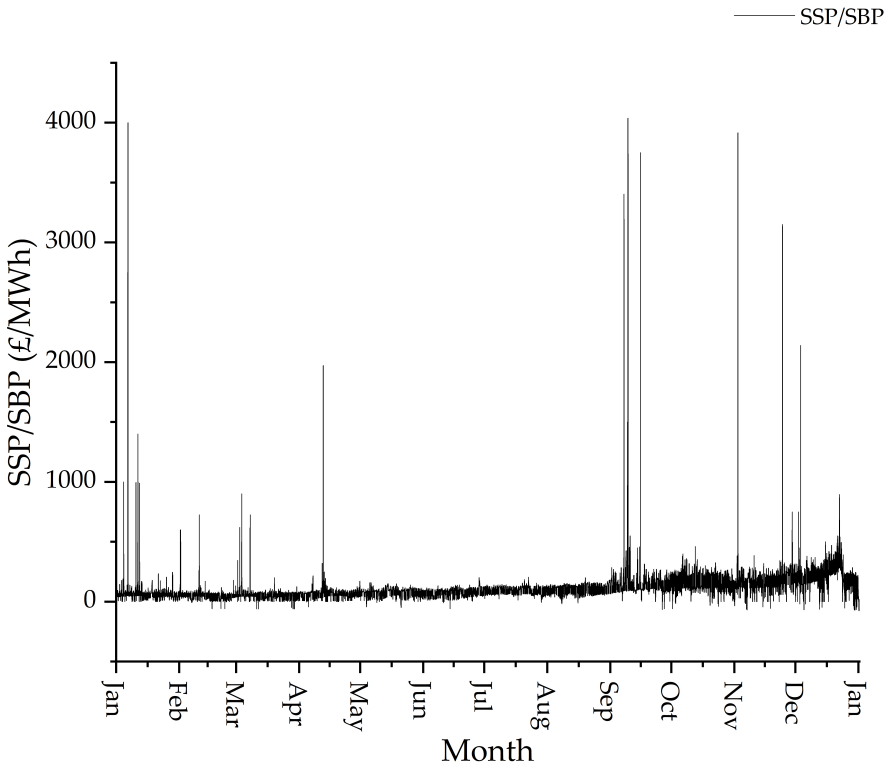


Figure 5.9: Example of imbalance price variation over each SP in the 2021 year (Elexon, 2024).

This provides electricity price data for the historic dates investigated. However, to predict future profitability, an estimation must be made of future SP electricity prices. To do this, the open-source PyPSA-GB model is used (Lyden, 2022). PyPSA-GB predicts the optimal network deployment to match demand going forward to 2050. This may be used alongside published data from Elexon regarding bid values to predict an overall system price.

5.3.2 Natural Gas Prices

For UK industrial users, the NG supply is pivotal due to its use for heating and power generation, accounting for 39.3 % of electricity generation in 2022 (Department for Energy Security & Net Zero, 2023). The market's structure allows for various purchasing mechanisms, including long-term contracts and spot market purchases, providing flexibility and security of supply.

Wholesale NG prices can vary based on the exchange it is sold on. The majority of the NG is bought and sold on the Intercontinental Exchange (ICE), though others, such as PEGAS,

are used. These use the National Grid-led National Balancing Point (NBP) as a virtual trading post to trade Natural Gas Futures. These are financial contracts for the delivery of NG and play a significant role in the NG market.

The NBP gas market allows prices to be set for same-day delivery (within-day), day-ahead, months, quarters, summers, winters, and annual contracts. With the use of the Montel Online Portal, a platform offering insights into energy market dynamics, market data is available (Montel, 2024). This provides a comprehensive platform for tracking wholesale NG prices from the NBP, offering both historical and real-time data. Regarding the UK specifically, Montel offers data from ICE, PEGAS, Spectron and GFI exchanges, though the latter two are behind a paywall and are, therefore, unavailable (Intercontinental Exchange, 2024; Montel, 2024).

ICE provides a global platform for trading a variety of commodities, including specific energy contracts relevant to the UK market, making it an ideal choice for models focused on UK ES economics. The most granular data accessible regarding NG prices in this market is daily DA prices, though there is no trading over weekends, and as such, there is no data. On the other hand, PEGAS offers extensive access to the European NG market, with its high liquidity and wide coverage being key for models that require an in-depth understanding of European NG trading dynamics. Additionally, within-day data is available, down to prices updating as frequently as every minute. However, this exchange only joined NBP in 2023, meaning that there is insufficient data for detailed historical investigations.

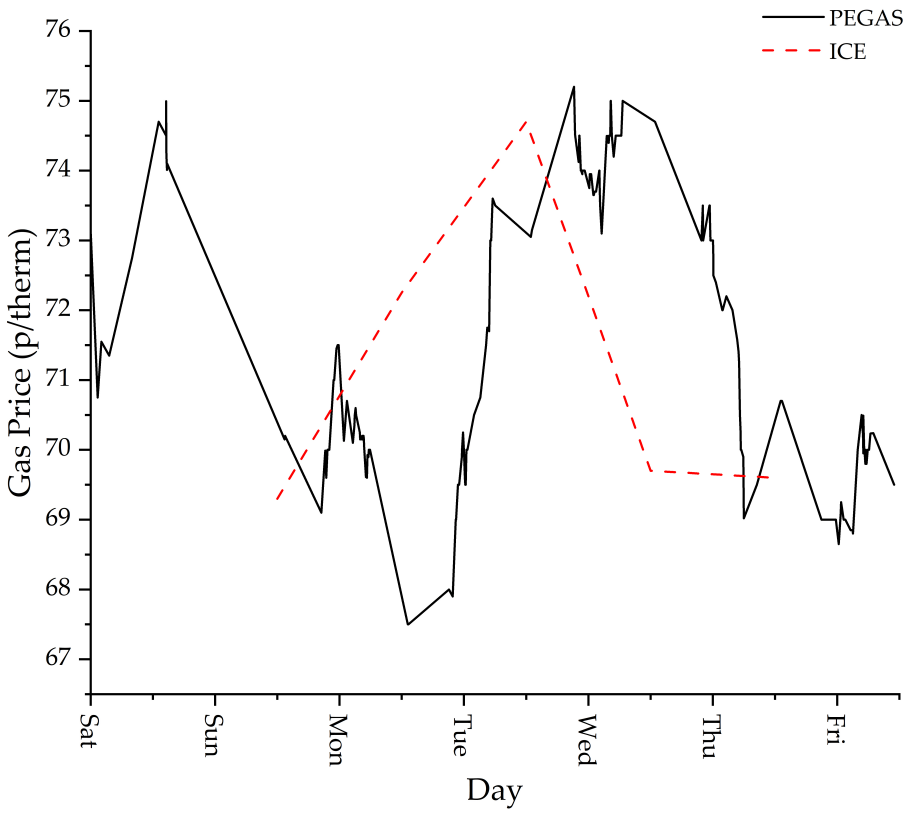


Figure 5.10: Comparison of UK Natural Gas prices based on market (Montel, 2024).

For a model focused on the economical use of ES in the UK, ICE is more suitable due to

its extensive coverage of UK-specific energy products, resulting in a greater granularity in the data. Figure 5.10 shows the varying prices associated with ICE and PEGAS over the course of a day. Note the significant increase in data points when sourcing from PEGAS.

5.3.3 Carbon Tax Prices

Carbon pricing assigns a cost to emitting CO_2. The EU ETS, Carbon Price Support and the UK ETS schemes are market-based approaches that financially incentivise emitters to reduce their GHG output (European Commission, 2022; Department for Energy Security & Net Zero, 2024; Hirst, 2018).

The EU ETS prices were sourced through the Montel Online Portal (Montel, 2024). This includes both real-time and historical data on EU ETS prices. Exchange rates between the Euro (EUR) and the British Pound (GBP) also play a significant role in the financial analysis of carbon pricing when the EU ETS is applied. Historic prices of the EUR to GBP exchange rate were sourced from Investing.com (2023). This is crucial for converting EU ETS prices into GBP for an accurate comparative analysis in the UK context.

The CPF levy used in conjunction with the EU ETS was found based on reports from the UK Government (Hirst, 2018). The values of this carbon price support (CPS) from its inception in April 2013 are given in Table 5.1.

Table 5.1: Carbon Price Support rates over time (HM Revenue & Customs, 2024).

Effective Date	CPS Rate (£/tCO_2)
April 2013	4.94
April 2014	9.55
April 2015	18.08
April 2016	18.00

Initially, the CPS was planned to rise each year until 2020 to a target price of £30/tCO_2. However, to limit the competitive disadvantage this induced, the Government capped the price at a maximum of £18/tCO_2 from 2016 to 2021. When the UK ETS replaced the EU ETS, the CPS price was rolled into the UK ETS, creating one single price. As such the auction reserve price, currently set at £22/$tnCO_2$, could be seen as the latest iteration of the CPS.

Similarly, the UK ETS prices are also sourced through Montel Online, providing continuous data for carbon pricing in the UK market, without any interruption through the transition from EU ETS to UK ETS.

Figure 5.11 shows the progression of EU ETS prices, EU ETS with CPF and the UK ETS.

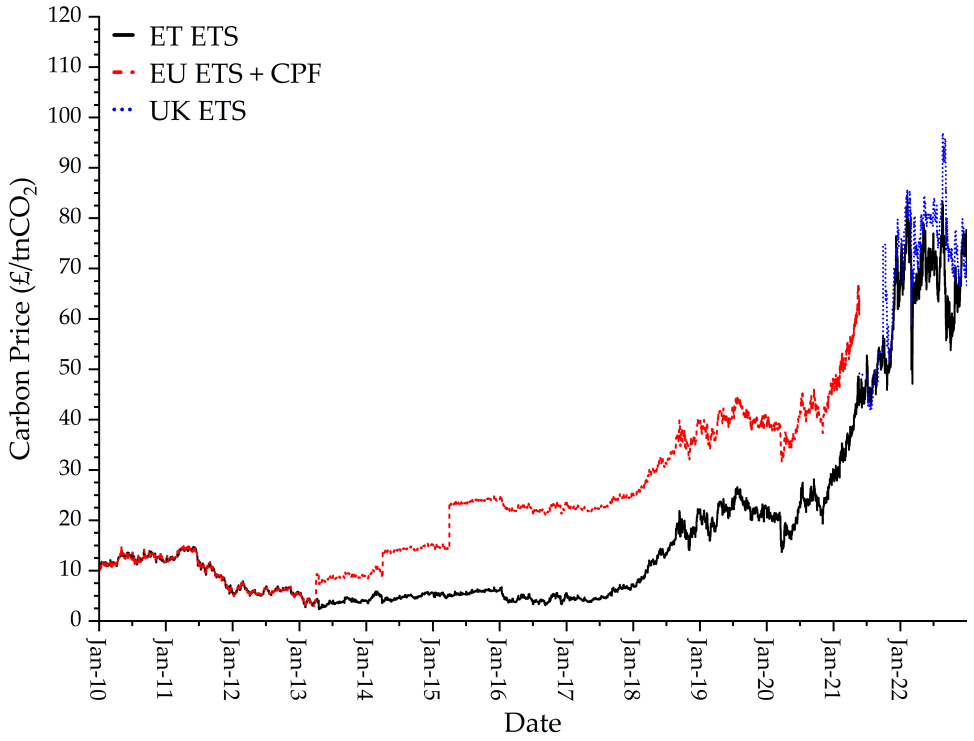


Figure 5.11: Comparison of the different carbon emissions taxes seen in the UK (Investing.com, 2024).

5.3.4 Carbon Output

Emissions factors for power generation are pivotal in calculating the CO_2 output when fuel is combusted. These factors, typically expressed in mass of CO_2 equivalent emitted per unit of energy produced (often $kgCO_2e/kWh$), provide a quantifiable measure of the GHG emissions associated with the combustion of fuels, such as NG, coal, or oil. UK Emissions factors are published annually by the Government (currently the Department for Energy Security and Net Zero) to reflect changes in technology, fuel quality, energy mix, and environmental policies, ensuring that the calculations of GHG emissions are as accurate and current as possible (UK Government, 2023).

To find the CO_2e produced from the combustion of fuels, the thermal energy required to produce the desired electrical output is used alongside the emissions factor associated with the energy source used. This allows for the assessment of the emissions output of different power generation methods. Historical emission factor values for NG, coal and fuel oil are displayed in Figure 5.12, which shows how they vary over time, and the differing scales associated with each fuel.

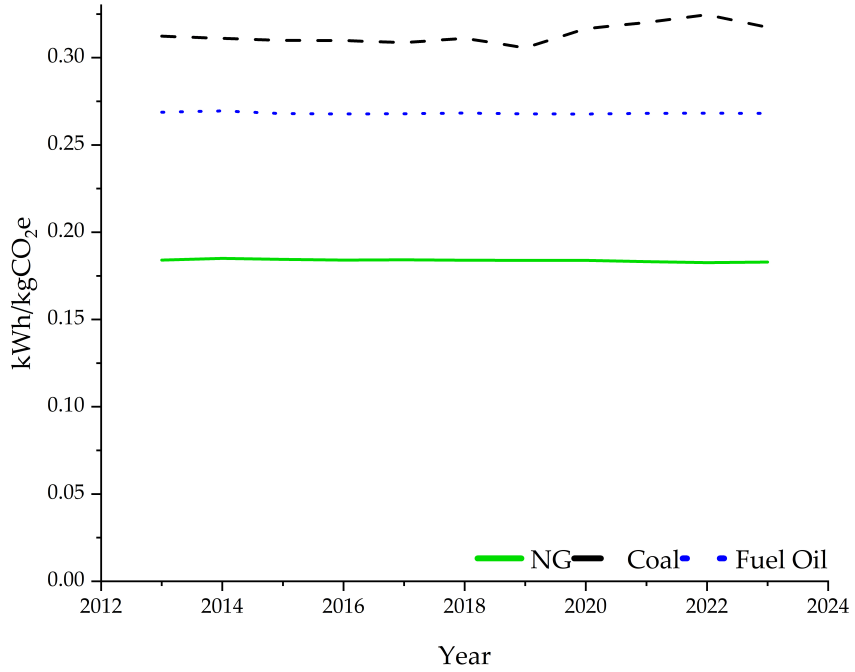


Figure 5.12: Comparison of conversion factors for NG, coal, and fuel oil.

5.3.5 Future Data

Future electricity prices are estimated using PyPSA-GB, which adopts the 'Leading the Way' pathway. This pathway signifies the most rapid decarbonisation pace combined with substantial societal change. This scenario was used as it produces the most rapid transition to a fully renewable system, and as such, provides a worst-case scenario for the model due to the associated reduction in electricity prices.

The Linear Optimal Power Flow (LOPF) functionality optimises the dispatch of generation and storage to meet demand which must be met in all time steps. The LOPF minimises the total system cost based on the capacities of generation and storage, along with the parameters of the transmission network. Further information can be found in the 'Future Years' section of the PyPSA-GB documentation (Lyden, 2022). Figure 5.13 shows a future generation mix produced through this optimisation method.

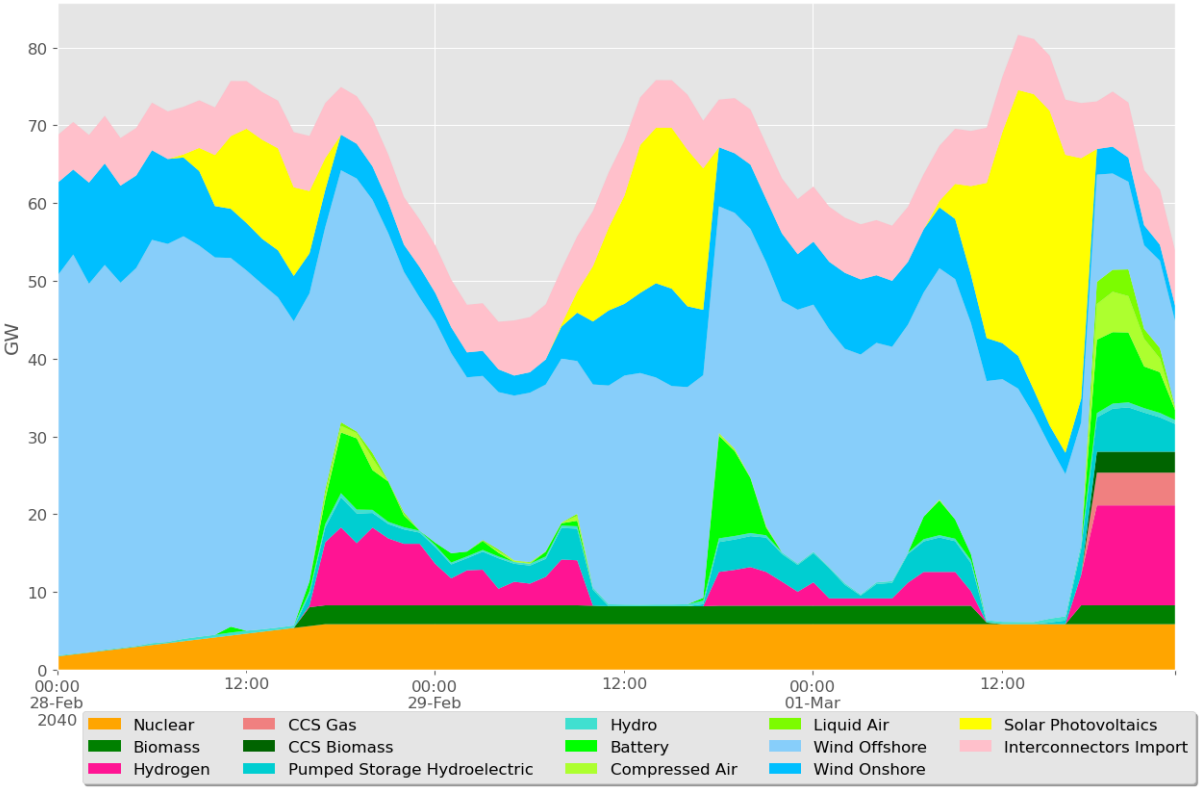


Figure 5.13: Modelled generation mix over a 3-day period in 2050 (Lyden, 2022).

Based on the optimised network, the energy mix for a given time step is found. The peak marginal cost is found based on the most expensive method of generation which is supplying the grid during a given time step. Based on this cost, the spark spread value is added. The spark spread quantifies the profitability of NG-fired power plants by calculating the difference between the revenue and cost of the NG needed to generate that electricity. It serves as an indicator to assess market conditions and the profitability of running a power plant. This data is published by Ofgem, with the high-efficiency spark value used (Ofgem, 2024). The addition of these two values produces a network cost of electricity. Monthly historic spark and dark spreads are displayed in Figure 5.14. The boundaries around the spark spread indicate the effect of high and low-efficiency generators, with high-efficiency systems producing an increased spark spread due to their greater output per unit of fuel. The dark spread quantities the profitability of coal generation.

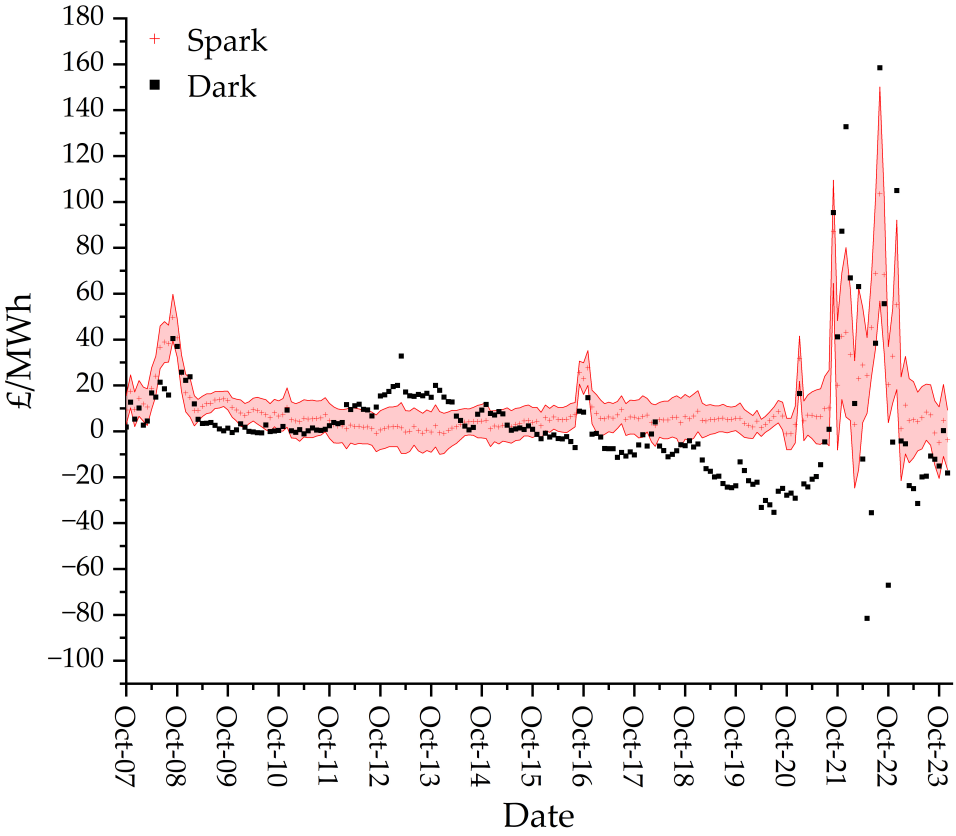


Figure 5.14: Historical variation in spark spread and dark spread.

It should be noted that this model is not capable of producing extreme peaks in electricity prices. These may be produced by, for example, a weather event which prevents wind turbines from operating, causing the grid to rely on GTs resulting in a high balancing price, or an excess of wind requiring power to be offloaded, resulting in negative pricing.

There are models of economic unpredictability which aim to predict events that affect market prices using stochastic modelling. These models can forecast energy prices by accounting for random fluctuations in market variables. Alarcón et al. (2023) discusses the integration of a scenario-based economic-stochastic model predictive control (SCMPC) strategy for microgrid management. This approach focuses on addressing the unpredictability associated with RES by incorporating uncertainty prediction into the energy management system. SCMPC accounts for the probabilistic nature of disturbances, enhancing the system's flexibility and response to unpredictability. Complex systems such as these could be used to predict the effect of future market events on the energy system, producing volatile price changes.

However, due to the complexity of these models, it is not possible to incorporate them into PyPSA-GB to predict future extreme weather events. As such, they are excluded from the study. The result of this is highlighted as a potential reduction in calculated profitability as the peak prices are ideal opportunities for ES systems to generate income.

5.4 UHTS Utilisation Model Development

In this study, data-intensive techno-economic models were developed to assess the viability of UHTS deployment. The creation of computational codes was necessitated to accommodate the complexity of factors influencing the economic and technical feasibility of UHTS implementations. Developing a bespoke model was essential due to the proprietary nature and high costs associated with existing models, making them inaccessible. Additionally, existing models lack the necessary tailoring for TES and the capability to integrate with future market predictions generated using PyPSA-GB.

A critical component of the modelling process involved the incorporation of commodity and carbon price variabilities. These elements are pivotal in determining the economics within which UHTS systems operate. Commodity prices, encompassing electricity and NG for UHTS, exhibit volatility influenced by market dynamics, geopolitical events, and regulatory policies. Carbon price rates pertaining to CO_2 emissions and energy production introduce additional layers of economic consideration, affecting the operational costs and profitability of UHTS installations.

Moreover, the computational framework was designed to encapsulate the technical constraints inherent to UHTS technologies. This encompasses the physical attributes of the storage media, such as thermal capacity, energy density, and resilience to degradation over repeated cycles of use. The efficiency and capacity limitations of the systems through which the UHTS discharges, whether for power generation or industrial heating applications, were also evaluated. This included the examination of heat exchanger effectiveness, operational thresholds of equipment, and the potential for energy losses during energy conversion phases.

The development of these techno-economic models and the requisite computational codes serve as a fundamental element of this research. It enables a detailed analysis of the feasibility, operational efficiency, and economic viability of deploying large-scale UHTS systems within both current and future energy frameworks. By integrating a broad range of variables and constraints, the models aim to produce a comprehensive understanding of the potential contributions and challenges of UHTS technology in the context of advancing sustainable ES solutions.

5.4.1 Language Selection

The selection of a programming language is pivotal in developing techno-economic models for UHTS systems. Python is an open-source, interpreted, general-purpose language known for its simplicity (Python Core Developers, 2023). It is characterised by its readability and object-oriented design. As such, Python creates code that can be readily understood.

Python's readability and adaptability make it ideal for the development of this techno-economic model. Its ability to support complex analytical tasks aligns with the challenges of modelling large-scale UHTS systems. The adoption of Python in this study leverages these strengths, contributing to the creation of robust and adaptable models.

It is also highly adaptable due to its library of modules, making it ideal for the diverse needs of techno-economic modelling. The approach adopted involves using various data sources and tools, including Excel workbooks for data input and the generation of numerical outputs. Python's capability to integrate with these using libraries such as Pandas ensures an efficient

workflow from data input to model execution and output analysis (pandas development team, 2024). This enables the adaptation of the models to evolving data and analysis requirements.

While Python is a strong choice for developing techno-economic models, other programming languages could also be considered. MATLAB is a popular alternative, especially in engineering and scientific communities. It offers built-in functions for numerical computation, making it efficient for complex mathematical modelling. However, MATLAB is proprietary software, which can be costly and is therefore less utilised within industry compared to open-source alternatives like Python.

Additionally, Julia is known for its high performance in numerical and scientific computing. Julia's syntax is similar to MATLAB, but it is open-source and designed for high-speed execution, which can be advantageous for large-scale simulations. However, Julia's ecosystem is not as mature as Python's, and it has fewer libraries and less community support.

C++ is a powerful language that could be used for developing techno-economic models. Known for its high performance and efficiency, C++ is particularly well-suited for computationally intensive tasks and handling large datasets. It can quickly perform complex calculations, making it suitable for modelling large-scale UHTS systems. However, C++ has a steeper learning curve and is less readable compared to Python, which can make development more challenging and less accessible for industrial deployment. Despite these challenges, C++ remains a viable option where performance and efficiency are important.

However, there are also drawbacks associated with using Python. One potential issue is performance, as Python can be slower than compiled languages like C++ or even Julia for certain computationally intensive tasks, though this can be somewhat mitigated by using optimised libraries such as NumPy. Despite these concerns, Python's extensive libraries, ease of use, and strong community support make it a robust choice for techno-economic modelling.

5.4.2 Technical Requirements

This section introduces the technical requirements essential for the operational analysis of a UHTS system, focusing on the key variables critical to system performance. These include the properties of the storage system and discharge systems, system design parameters, and operational conditions. Understanding these variables is fundamental for modelling the ES and discharge capabilities of the system, thereby informing the techno-economic assessment of UHTS implementations.

UHTS Store Independent Variables

In the exploration of the UHTS system's dynamics, certain fixed variables are established as foundational parameters to facilitate the computation of dependent variables tailored to the specific system being analysed. These parameters include the system dimensions, materials, and operational limits, which are critical for simulating real-world scenarios.

For instance, the UHTS system under consideration designates the maximum storage temperature at 1,800 K, reflecting the operational thermal limit due to material limitations. The core mass is also specified at 24,800,000 kg, a figure critical for assessing the capacity of a TES due to the linear relationship between storage capacity and thermal mass.

Furthermore, these fixed definitions extend to encompass the material used as the HTF and the thermal core to allow for the material properties and thermal characteristics to be defined, which are crucial for evaluating the system's heat transfer effectiveness. This approach ensures a holistic understanding of the thermal dynamics within the UHTS, from heat absorption to energy dispatch. In this case, the HTF used is air as it can easily integrate into a wide range of discharge systems, and the material used for the core is aluminium. The selection of aluminium as the core material, due to its high thermal conductivity and specific heat capacity, significantly impacts the system's thermal response and ES efficiency, underpinning the UHTS system's ability to achieve high-temperature gradients and rapid charging/discharging cycles.

A further definition required is the losses associated with the inefficiency in the transfer from the core to the HTF, which must be accounted for. This includes both conductive and convective losses, which occur because the HTF that the system outputs may not match the storage temperature due to thermal gradients within the core itself. To account for this, a heat-exchanger effectiveness value is defined, causing the outlet temperature to be lower than that of the core itself. This is given as 0.9 for this model.

A further factor that must be defined when considering a thermal storage system is thermal losses from the store itself. At such high temperatures, radiation drives these losses associated with the storage system over time. Based on data from Robinson (2017), these are set at 0.5 % of the total stored energy per day of storage. The model accounts for this by reducing the stored energy by just over 0.01 % for every 30 minute settlement period (SP), reducing the available stored energy to be extracted from the system to sell when discharging every 30 minutes.

The UHTS system is assumed to have a grid connection capable of supplying sufficient energy to reach peak temperature within 30 minutes for a full charge in one SP. This requires a connection capable of supplying a power supply double that of the storage capacity.

While not always feasible due to deployment location and storage capacity, this assumption is applied across all modelled cases, based on the likelihood of larger storage systems being deployed near power generators, which are likely to have high-power connections installed or can directly feed the store.

Discharge Technology Independent Variables

For the UHTS system's discharge technologies, thermal efficiency is crucial. Thermal efficiency varies over different discharge technologies, ranging from values as low as 29 % for a HRSG to 95 % for an IB. As previously mentioned, the IB outputs heat, whereas HRSGs and GTs generate electricity. This results in a large efficiency difference. In addition, efficiency is also affected by each system, based on the equipment's design and modernity. This must be accounted for to ensure sufficient energy is provided by the UHTS system.

A further factor when considering discharge systems is the inlet temperature requirement, which will vary for different processes which use high-grade heat. GT, HRSG, and boilers each require a specific temperature input in order to operate most efficiently, necessitating precise output control within the UHTS system. This characteristic is vital in the operation of a thermal store, as if the storage temperature drops below this value, it can either no longer supply the energy to the discharge system, or the outlet must be supplemented to maintain

peak efficiency. For example, the GT mentioned in Chapter 4 requires a temperature greater than 1700 K entering its turbines to operate at optimal efficiency.

The HTF inlet temperature also affects the operation of the system. This parameter directly influences energy transfer effectiveness from the storage medium to the discharge system, necessitating careful control and monitoring. Whilst this is often atmospheric temperature, the air is supplied from the compressor outlet for systems such as the GT. For example, the compressor in the GT systems mentioned produces an air temperature of 760 K. This is dependent on the discharge system and impacts the operation of the core itself as limitations like these mean that though the UHTS system may store a given maximum energy when fully charged to 1800 K, it will not be possible to extract all the stored energy due to the lower temperature limit.

Similarly, each system has variable requirements for the inlet flow rate of the heat transfer. This must be defined in order to prevent damage to the discharge system, some of which are outlined in Chapter 3. This can vary depending on the operational parameters, whether the fuel is being fully replaced, partially displaced or augmented.

Finally, the operating hours for these technologies are tailored to specific industry requirements or energy demand patterns. This adaptability is key to aligning the UHTS system's operation with fluctuating demand profiles, enhancing its value in a dynamic energy market. As such, the model required the input of these hours to ensure that the system would only discharge when required. Whilst a power generating system may be utilised 24 hours a day, an industrial system may only require heat during the working day.

Dependent Variables

The fixed variables for the storage and discharge systems outlined above produce some dependent variables which must be considered.

The calculation of the specific heat capacity of the storage medium in the system is pivotal for assessing its ES potential. This is based on the storage medium material. The model employs a polynomial approach, allowing for a more nuanced representation of the specific heat capacity as a function of temperature, capturing the material's changing thermal properties across different temperature ranges. The polynomial model enhances the accuracy of the heat capacity calculation, which is crucial for precise ES and release estimations, contributing to the reliability and efficiency of UHTS systems. Equation 5.1 shows the polynomial model used.

$$C_{p,Core}(T) = a_0 + a_1 T + a_2 T^2 + a_3 T^3 + \ldots + a_n T^n \tag{5.1}$$

where $C_{p,Core}(T)$ is the specific heat capacity (J/kg· K) at temperature T, T is the core temperature (K), $a_0, a_1, a_2, \ldots, a_n$ are the coefficient values specific to the storage medium material and n is the degree of the polynomial.

Similarly, the specific heat capacity of the HTF must be found using a polynomial, with the median temperature between the HTF inlet and the discharge temperatures taken for the temperature of the fluid, as shown in Equation 5.2.

$$C_{p,HTF}(T_{median}) = b_0 + b_1 T_{Median} + b_2 T_{Median}^2 + b_3 T_{Median}^3 + \ldots + b_m T_{Median}^m \tag{5.2}$$

where $C_{p,HTF}(T_{Median})$ is the specific heat capacity of the HTF at the median temperature T_{Median}, which is the average of the HTF inlet and discharge temperatures. Here, $T_{Median} = \frac{T_{Inlet} + T_{Discharge}}{2}$, and $b_0, b_1, b_2, \ldots, b_m$ are the coefficient values specific to the HTF material, with m being the degree of the polynomial.

The maximum stored energy in a TES system like UHTS is determined by the system's capacity to absorb, retain, and release heat. This capacity is calculated based on the thermal mass, the specific heat capacity of the storage material, and the peak temperature of the storage medium, as depicted in Equation 5.3. This reflects the amount of thermal energy the system can store and subsequently make available for use, which is critical for applications requiring energy supply during periods when direct energy generation is not possible.

$$E_{Max} = m_{Core} \cdot C_{p,Core} \cdot (T_{Peak} - T_{Initial}) \tag{5.3}$$

where E_{Max} is the maximum stored energy in the system (J), m_{Core} is the mass of the storage material (kg), $C_{p,Core}$ is the specific heat capacity of the storage material (J/kg· K), T_{Peak} is the peak temperature of the storage medium (K), and $T_{Initial}$ is the initial temperature of the storage medium before ES begins (K).

However, not all the stored energy will be usable. Based on the discharge system temperature requirement and using the same correlation as previously mentioned, this temperature can be converted to a level of energy in the store, below which the system cannot be used. This allows for the calculation of usable stored energy, which is the difference between the stored energy and the lower limit of usable energy, as detailed in Equation 5.4

$$E_{Usable} = E_{Stored} - E_{Min} \tag{5.4}$$

where E_{Usable} is the usable stored energy in the system (J), E_{Stored} is the total stored energy in the system (J), and E_{Min} is the lower limit of usable energy, corresponding to the minimum operational discharge temperature of the system (J). The E_{Min} can be calculated as

$$E_{Min} = m_{Core} \cdot C_{p,Core} \cdot (T_{Min} - T_{Initial}) \tag{5.5}$$

where T_{Min} is the minimum operational discharge temperature (K).

It should be noted that the outlet temperature of the system will not be the same as the core temperature. Based on the temperature of the core and the effectiveness of the heat exchanger, the outlet temperature of the UHTS system can be found. This accounts for the temperature difference between the core and the incoming HTF, the specific heat capacity of the core material and the HTF, the mass flow rate of the HTF, and the heat exchange effectiveness. The exponential term, determined by the ratio of the mass of the core and its specific heat capacity to the HTF flow rate and its average specific heat capacity, reflects the rate of temperature change. This ensures a realistic simulation of thermal energy transfer dynamics, resulting in an accurate outlet temperature, as shown in Equation 5.6.

$$T_{Outlet} = (T_{Store} - T_{Inlet}) \cdot e^{\left(-\frac{\Delta t}{\left(\frac{m_{Core} \cdot C_{p,Core}}{\epsilon \cdot \dot{m}_{HTF} \cdot c_{p,HTF}} \right) + T_{Inlet}} \right)} \tag{5.6}$$

where T_{Outlet} is the outlet temperature of the system (K), T_{Store} is the storage or core temperature of the system (K), T_{Inlet} is the inlet air temperature (K), Δt is the time step (s), ϵ is the efficacy of the heat exchanger and $\dot{m}_{HTF}$ is the mass flow rate of the incoming air (kg/s).

The actual outlet temperature of the UHTS system, alongside the specific heat capacity of the HTF, can then be used to find the energy discharged from the system per unit of time. This calculation forms the basis for determining the operational efficiency and energy delivery potential of the UHTS system in real-world applications and allows for the stored energy to be continuously updated. Based on the updated stored energy, the temperature of the core is updated, as illustrated in Equation 5.7:

$$E_{Discharged} = \frac{(\dot{m}_{Air} \cdot \Delta t) \cdot C_{p,HTF} \cdot (T_{Outlet} - T_{Inlet})}{3600} \tag{5.7}$$

where $E_{Discharged}$ is the energy provided by the UHTS system (Wh) and Δt is the time step (s).

If a specific power to the discharge system is required alongside a constant HTF flow rate, the air may be split to allow only a portion to be heated by the UHTS. Here, the flow splits with a percentage passing through the UHTS and the remainder of the airflow bypassing, maintaining its initial temperature. Post-heating, the two air flows - heated and bypassed - recombine, resulting in a mixed final temperature. This ensures the thermal generator receives the appropriate energy from the store, tailored to the current core temperature. This requires the air split to dynamically adjust to the core temperature, the HTF flow rate and its physical properties.

However, as the only fixed variables are the mass flow rate of the HTF and the required energy, this becomes more complex as the outlet temperature of the UHTS system is required in order to calculate the energy provided to the discharge system after the heated flow and the bypass flow recombine, as outlined in Equation 5.8:

$$T_{UHTS,Out} = \frac{E_{Required}}{(SAP \cdot \dot{m}_{HTF}) \cdot C_{p,\text{HTF}}} + T_{Inlet} \tag{5.8}$$

where $T_{UHTS,Out}$ is the outlet temperature of the heated flow (K), $E_{Required}$ is the total required energy to be provided by the combined flow (J) and SAP is the Store Air Percentage (-).

As such, the value of SAP can be iterated between 0 and 1 to find the required air split that outputs $E_{Required}$. If this value cannot be found, it indicates that the store temperature is too low to provide the required energy.

If this value is equal to 1 and the energy provided is insufficient, additional energy may be added through the combustion of fuel. The mass of fuel required is found using the differential

between the supplied energy and the required energy, alongside the calorific value of the fuel used, as shown in Equation 5.9:

$$m_{fuel} = \frac{E_{Required} - E_{Supplied}}{CV_{Fuel}} \tag{5.9}$$

where m_{fuel} is the mass of fuel required (kg), $E_{Supplied}$ is calculated based on the UHTS discharge dynamics (J), representing the energy actually supplied by the UHTS system after the heated flow and the bypass flow recombine, and CV_{Fuel} is the calorific value of the fuel used (J/kg).

5.4.3 Optimised Storage Use Model Description

The framework of the model is described in this section. This data-intensive techno-economic model was developed for large-scale UHTS systems, though it may be adapted to apply to a range of ES systems. For this, a model is required which can account for commodity price fluctuations and the technical parameters and limitations of the storage and discharge systems, as outlined previously.

A time step resolution that aligns with the granularity of the available market data is employed to account for these price fluctuations. This ensures that each step accurately reflects real-world conditions, whilst also allowing for abnormal variations to be accounted for, such as extreme price spikes, to ensure realistic system behaviour. The state of the ES system is updated at each time step, incorporating the effects of charging, discharging, and thermal losses, to provide a dynamic and temporal representation of system performance.

The collated economic variable data is read from an Excel workbook to build data frames within Python. The modelling tool procedurally executes operations, processing ES system simulations through defined functions and iterative loops. This is outlined in Figures 5.15 and 5.17 later in this section. It uses time step data for price evaluations and system technical parameters to run models. This script directly invokes functions and manipulates data structures to assess system performance and optimise profit based on commodity prices and system characteristics at each time step. This can be applied over a range of operational methodologies outlined here. The outputs of this are in the form of numerical outputs printed by Python. Each of the different operation method models is described below.

It should be noted that the following models optimise based on historical data with no uncertainty regarding upcoming prices over the investigated range. The ability to account for upcoming prices, ahead of the current time step means these models produce best-case scenario results.

As this work optimises based on historical data, it currently cannot be applied to a future-facing model in its current state. However, by analysing the optimised results from historical price data, the model could predict optimal Charge Trigger (CT) and Discharge Trigger (DT) prices to maximise profitability. Applying this model to published day-ahead prices may optimise based on market trends, enhancing strategy for UHTS deployment.

With increased use of this model, it can be further enhanced. To achieve this, trends in optimal CT and DT prices over a continued should be collated. With this, machine learning based on historic weather data can be used to further enhance predictions of suitable CT

and DT, enabling the optimisation of system deployment by utilising future weather forecast predictions.

This predictive capability allows operators to adjust their strategies to capitalise on market fluctuations and optimise profitability.

Additionally, this model does not incorporate non-commodity costs such as network benefits and charges, as well as income from flexibility services. These include elements such as:

- Transmission Network Use of System Charges (TNUoS) - A payment to cover the cost of installing and maintaining the transmission system (National Grid, 2024);
- Distribution Use of System Charges (DUoS) - A charge applied to every connection to the distribution network to cover the cost of building, operating and maintaining the network (Scottish & Southern Electricity Networks, 2023);
- Balancing Settlement Use of System Charges (BSUoS) - A fee to cover the cost of maintaining a balanced transmission system (National Grid, 2019); and
- Demand Flexibility Service (DFS) - A payment to suppliers and industrial users to incentivise voluntarily flexing the time when electricity is used (National Grid, 2023).

These are not included as model universality is preferred. This simplification makes the model more generally representative, allowing for it to be employed over a range of global markets. It should be noted, that due to the bottom-up approach used, these could be implemented without major changes.

Arbitrage Model

When operating under arbitrage conditions, the storage system can discharge to 'boost' the output of an active system, with capacity available for additional energy extraction. For example, a GT producing 650 MW may have the capacity for a 5 % increase in output. In this case, when discharging, the thermal store would supply the energy required to achieve an output of 682.5 MW, a 32.5 MW output increase.

A flow chart of the logic used within the code is shown in Figure 5.15. In this diagram, red text indicates code variables, blue indicates a process being undertaken, and purple indicates a value taken from the associated data file.

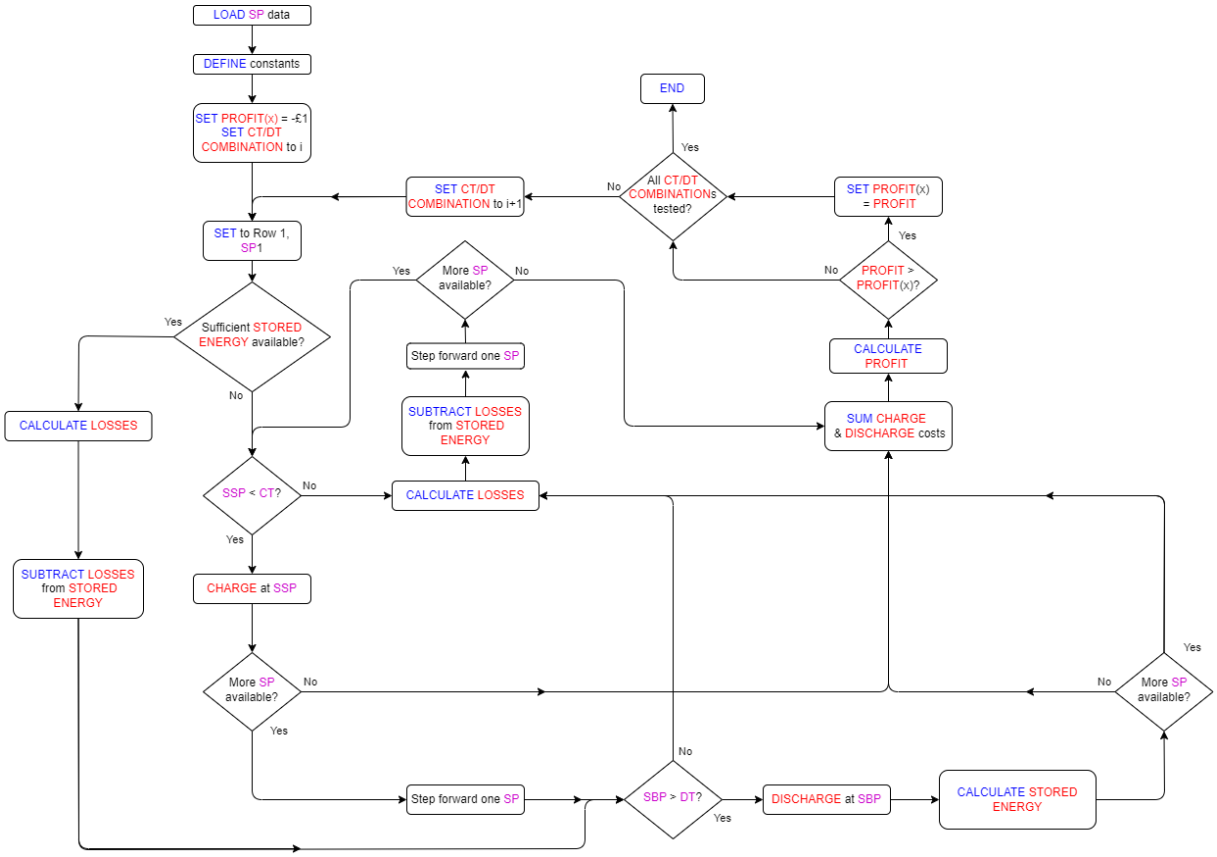


Figure 5.15: Flowchart of the logic process for arbitrage optimisation.

The script starts by iterating over possible values for CT and DT. Limits for the CT and DT values are specified to fall in the range where the system will never discharge when using fuel is cheaper. For each combination, it checks if the CT is greater than or equal to the DT. If it is, it skips the rest of the loop and moves on to the next combination.

To quantify the profitability of the arbitrage system, the script then marches down over each 30 minute time step. For each time step, it checks if the SSP is less than or equal to the CT and if the SBP is greater than or equal to the DT. If these conditions are met, it records the SSP or SBP for that time step.

At each time step, the code performs a number of calculations related to the storage system, such as calculating the energy into and out of the storage system and the cost of charging and discharging. Additionally, the model reduces the stored energy at each step to account for the energy lost through thermal losses and will recalculate the storage temperature.

If the SSP is less than the CT, the storage system will calculate the energy required to reach its full charge based on its current charge level and buy electrical energy for that 30 minute SP to heat the system. The required recharge level is based on how much the system has discharged and lost through heat since the last charging instance.

When the SBP is greater than the DT, the store can provide the pre-defined energy requirement based on the required boost. If the stored energy is less than the required energy, only the available energy is discharged. The updated total stored energy is then calculated,

accounting for the efficiency of the discharge system.

Note that, due to the variable temperature of the core, a controlled dilution system is required to maintain both a consistent mass flow rate and temperature input into the system. This is done using a defined total flow rate, which is added to the system, and a function to find the HTF split between the storage system and the cooling bypass.

This function uses an iterative process to adjust the split of HTF through the store and bypass, thus minimising the energy difference between the energy provided to the system and the desired plant boost. The function calculates the corresponding mass flow of HTF to store and to the bypass based on the split and estimates the outlet temperature based on various parameters such as the current storage temperature, incoming air temperature, and specific heat capacity of the materials. Subsequently, the function iterates through split values between 0 and 1, updating the system operating parameters and calculating the energy discharged.

Central to this function is the calculation of the energy difference, which quantifies the disparity between the system discharged and the design energy boost, determined by the operating parameters at each HTF split. The function returns the absolute value of this energy difference to facilitate the minimisation process.

The optimal percentage of HTF to be passed through the storage system is determined using an optimisation process aimed at minimising the energy difference between the desired energy added from the store and the actual energy provided by the system. This begins by defining a function that calculates the absolute value of this energy difference, which depends on the percentage of the additional air passing through the store. The Nelder-Mead optimisation method iteratively adjusts the HTF split between the storage and the bypass to find the minimum energy difference. During each iteration, a new outlet temperature is based on the current HTF split, the temperature of the stored energy, and the air inlet temperature. It then adjusts the HTF split to minimise the difference between the energy increase provided by the adjusted outlet temperature and the desired energy boost. The optimisation process continues until the optimal HTF split, which results in the smallest absolute energy difference, is found. This value is then used to set the mass flow of HTF through the storage system, ensuring that the system delivers the required energy boost. Once the temperature has reduced to the point where the required flow through the store would exceed 100 %, the store will no longer discharge as it is unable to output the required energy with the set HTF flow conditions.

Based on the electricity price and the charge/discharge volumes at each time step, the operating costs/income is calculated for each time step.

After the final time step, the total charging costs and the total income from discharging are calculated, and the difference between them is found. This gives the overall arbitrage profit from that period based on the total output boost.

From this point, the system then optimises to maximise profitability. To achieve this, the initial system arbitrage profit is set as £-1, and the model performs an iterative grid search process for each combination of CT/DT. For each calculated arbitrage profit, the script checks if the value is greater than the best profit seen so far. If it is, it updates the CT/DT combination, the best profit and other associated variables. The best profit value is not updated if the next combination gives a lesser profit value. This continues through the grid of potential CT/DT combinations until all pre-defined combinations have been attempted. The combination that produces the greatest profit is the final output. This is visualised in a simplified form in Figure

5.16 below, with the cross showing the point at which the CT/DT ratio gives the optimum profit.

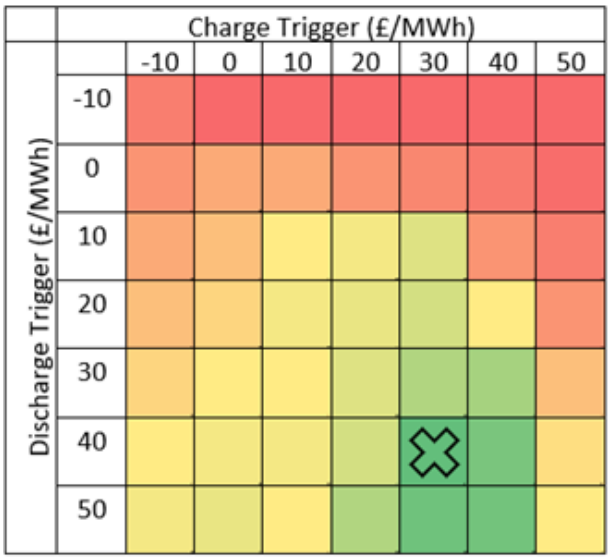


Figure 5.16: Simplified visualisation of the grid search process in which the CT/DT combination with the greatest output is marked.

Fuel Displacement Model

The second operational scenario is based on producing savings when operating the system. This is achieved by displacing the fuel required to drive the discharge system. Savings are produced by a reduction in the fuel required to drive the generator, alongside a reduction in CO_2 produced, minimising carbon tax fees.

When discharging in the fuel displacement scenario, the system is configured so that the thermal store displaces as much fuel as possible without making the system more expensive to operate than if it were to use its initial fuel source solely. Again, initial CT and DT values are set to achieve this, as with the arbitrage model.

Here, instead of boosting the output of the system, the store discharges the stored energy to replace or displace the primary fuel source, depending on the required energy. If the energy extracted is less than required to maintain a constant output of the discharge system, the additional energy required is calculated. The energy discharged is calculated based on the flow rate of the HTF through the store. Again, after each SP, the stored energy is updated, and the model then continues to step forward until another buy or sell opportunity, repeating until the end of the dataset.

Temperature plays a key role in the energy discharge process of the UHTS system. As the store discharges energy, the outlet temperature of the HTF decreases, decreasing the volume of energy extracted. To maintain a constant energy outlet, the required flow temperature is found, based on the HTF thermal properties and flow rate. Similarly to the arbitrage model, the energy provided by the HTF entering the discharge system is adjusted by altering the flow that bypasses the UHTS system. This adjustment uses a function to minimise the difference

between this overall outlet temperature and the target temperature. The minimisation employs the L-BFGS-B algorithm from SciPy (Virtanen et al., 2020), a method well-suited for problems with bounded constraints. This algorithm is efficient for large-scale problems, making it suitable for this complex optimisation. Other options could have included the Nelder-Mead or Conjugate Gradient methods, but L-BFGS-B's ability to handle large datasets and bounded constraints makes it preferable.

Unlike the arbitrage system, once the temperature drops below the required temperature, the store will continue to discharge up to the minimum allowable store temperature. As such, though the model optimises over CT and DT values, the CT is the primary focus. The energy shortfall is calculated for each SP and the required input of supplemental fuel to make up for this is calculated. The store will not simultaneously charge and discharge.

When optimising the UHTS system, the total fuel cost to run the system without a thermal store is calculated based on its fuel use, the efficiency of the discharge system, the calorific value of the fuel displaced, and the required output of the system. The total fuel supplement cost and the sum of costs to charge the store produce a total operating cost to drive the discharge system. The difference between these values is operational profit, and the income will remain constant.

From this point, the system is then able to optimise to maximise displacement without incurring additional operational expense. To achieve this, another iterative grid search process is performed to maximise the percentage of energy supplied by the store. After each combination of CD/DT, the model checks two parameters. Firstly, the operational profit must be equal to or greater than 0. This ensures that the cost to run the system is not greater than when it ran solely using its carboniferous fuel. If this is the case, the model then checks the replacement percentage of that iteration. The initial replacement percentage is set as -1. If the new replacement percentage is greater than the current saved best replacement percentage, the optimal CT/DT combination, replacement percentage, and other associated variables are updated.

As thermal systems with a total rated thermal input greater than 20 MW_{th} are required to participate in the emissions trading scheme (Department for Energy Security & Net Zero, 2024b), any reduction in CO_2 output results in additional savings. With the volume of fuel displaced calculated, the savings associated with the reduced CO_2 output due to the displacement of fuel can be found. In order to quantify these savings, the reduction in the mass of CO_2 emitted must be quantified. Using the conversion factors discussed in Section 5.3.4, the mass of CO_2 produced by a given fuel per kWh_{therm} is found. From this value, the carbon trading scheme in use in the UK during the time frame being studied is used to find the savings produced. This can be achieved down to the fidelity of the coarsest set of data, which in many cases is the emissions trading scheme auction prices. Figure 5.17 shows a flow chart of the logic used within the code.

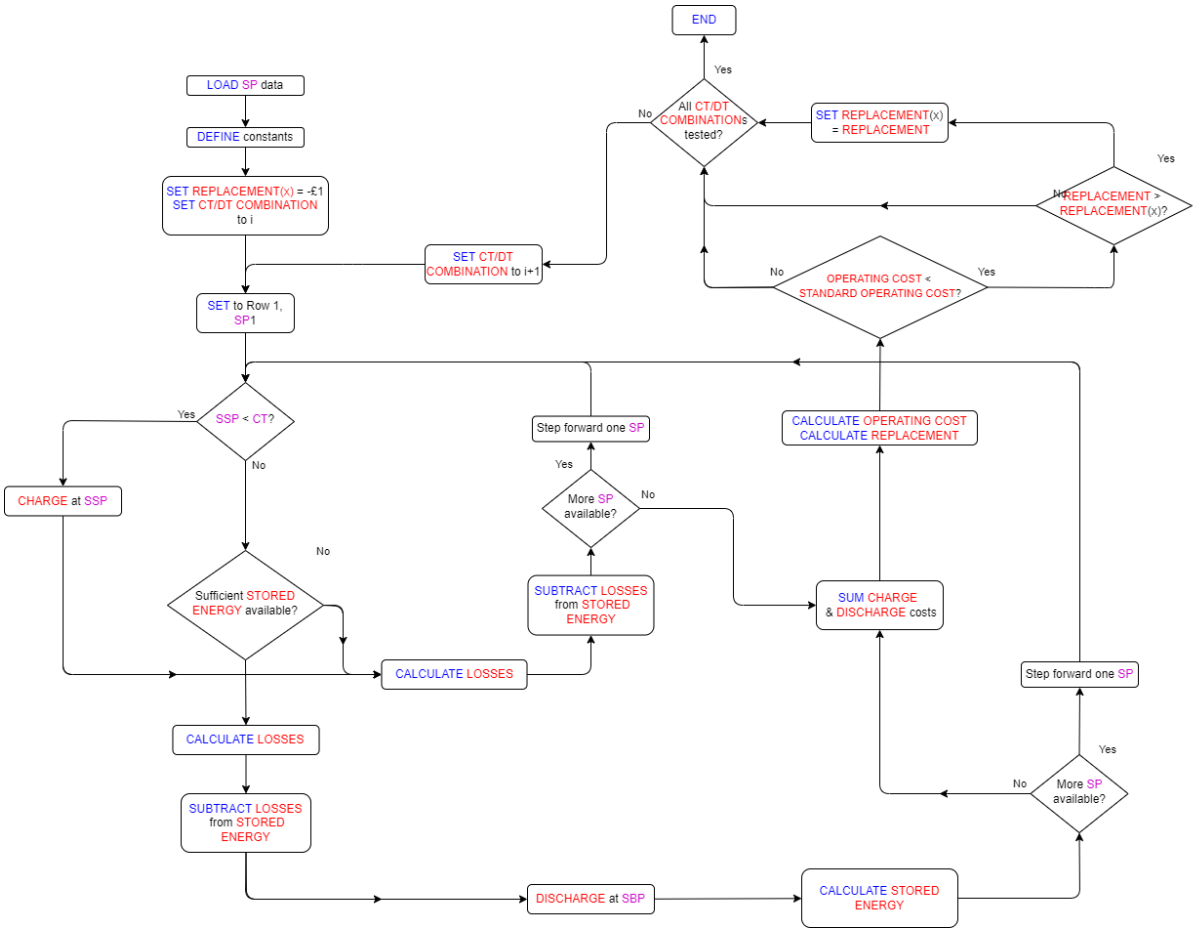


Figure 5.17: Flowchart of the logic process for savings optimisation.

Model Specific Inputs

Model-specific parameters define the variation in the operation of a UHTS system when implemented into different discharge technologies. Table 5.2 outlines these essential inputs, which are fundamental in driving the model simulations and obtaining realistic and applicable results.

Table 5.2: Operational parameters for UHTS system implementation across various discharge technologies.

Model Input	GT	HRSG	IB
Efficiency Range (%)	55-65	35-45	85-95
Power Output (MW)	650	250	3
Required Temperature (K)	1800	883	723
Mass Flow Rate (kg/s)	765	765	6.5
HTF Inlet Temperature (K)	760	760	288
HTF	Air	Air	Air
Start Time	00:00	00:00	08:00
Operating Hours	24	24	10

These inputs are instrumental in establishing the operational limits and performance

capabilities, offering a detailed and granular basis for the techno-economic model simulations, and exploring various scenarios under different operational methodologies.

This facilitates a comprehensive techno-economic analysis by factoring in technical parameters alongside the economic variables outlined previously to assess potential savings or income generated by the system. These inputs and their ease of variation allow the accurate simulation of UHTS system implementation into larger energy systems.

5.5 Application of Economic Models

The economic and environmental performance of a UHTS system implemented into GTs, HRSGs, and IBs is evaluated. This utilises historical market data from 2017 to 2022 and forecasts produced by PyPSA-GB increase in 5-year increments from 2025 to 2050. Both the arbitrage and fuel displacement models are used to assess the system performance up to 2050. The investigation highlights the UHTS system's capability to enhance viability within a fluctuating market.

Results are produced using the base arbitrage and fuel displacement models from 2017 to 2050, optimised over individual months. Sensitivity analysis is then performed over the single year of 2021 to investigate the impact of varying model parameters. These parameters are:

- A variation in system efficiency for each discharge technology. This is done in two steps of efficiency reductions of 5 %;
- A variation in the temporal optimisation period. This is done by optimising over an annual data set and a year's worth of weekly data sets; and
- . A variation in SP length. This is done by increasing the time step from 30 minutes to 60 minutes.

5.5.1 Model Verification

In order to verify the model, two primary methods were utilised: white box and black box testing.

White box testing was applied to the economic dispatch model to ensure its internal mechanisms functioned as intended. This approach involved several key steps: a review of the model's code to verify the accurate implementation of algorithms for all calculations; examination to identify any logical errors; tracking the flow of data to confirm correct processing and accurate output generation; testing individual components in isolation to verify their correctness; and evaluating the model's performance to ensure efficient operation, particularly when processing large datasets. Visual Studio Code was utilised to complete this process, utilising code breaks and the ability to observe calculated variable values at these breaks. By employing white box testing, a comprehensive understanding of the internal logic of the model was achieved, ensuring its correct and efficient operation.

Once the white box testing was completed, the model then progressed to black box testing to provide further validation, leading to a robust and reliable economic dispatch model. With

the internal logic accounted for, black box testing was employed to evaluate the fidelity of the economic dispatch model over a single-month dataset. This dataset had been manually optimised iteratively to demonstrate the best possible deployment for both the arbitrage and savings models. This approach involved treating the model as an opaque entity, focusing solely on the input-output relationship without delving into the internal mechanics. The primary objective was to ascertain whether the model's outputs could replicate and align with the expected results derived from manual calculations. By comparing the model's outputs against the manually obtained benchmarks, discrepancies were identified and analysed. This ensured that the model's external behaviour was consistent with optimal operation. This method proved instrumental in validating the model's accuracy and reliability, highlighting areas for further refinement and ensuring robust performance under specified conditions.

5.5.2 Model Validation

Model validation for the economic dispatch model presented challenges due to the lack of publicly available data specific to TES dispatch. To address this, scenario analysis was performed using GTs, HRSGs, and and IBs as discharge systems. This involved simulating the model under different configurations to evaluate its performance and adaptability. Each discharge system presented unique operational characteristics and constraints, allowing for a thorough examination of the model's versatility. By comparing the model's outputs across these different scenarios, the research validated the ability of the model to handle a range of operational conditions and its applicability to real-world situations.

In addition to scenario analysis, a sensitivity analysis was conducted. This analysis involved varying key parameters such as discharge efficiency, optimisation periods, and time step length to assess their impact on the model's performance. By systematically altering these variables, the robustness of the model was tested under different conditions, ensuring that it could reliably predict outcomes across a range of scenarios. This approach helped identify the key factors affecting the accuracy of the model, and provided insights into potential areas for improvement. This dual approach of scenario and sensitivity analysis demonstrates the reliability of the models.

5.5.3 Base Model Results

Using the base models, the system utilisation was investigated from 2017 to 2022 using historical data. Future implementation was evaluated using predictions from PyPSA-GB for the years 2025, 2030, 2035, 2040, 2045, and 2050. The efficiencies used were 65 % for the GT, 45 % for the HRSG via a Rankine power plant throughput and 95 % for the thermal output of an IB. The models optimise over individual months, using 30 minute SP lengths.

Arbitrage Performance

The arbitrage implementation of a UHTS system boosts the output of conventional thermal generators by providing additional heat. These results are presented in terms of profitability. Figure 5.18 illustrates the monthly profit trends for each discharge technology both without a storage retrofit and UHTS boosted operation. It is evident from the time series that the

UHTS boosted operation consistently outperforms the pure fuel operation in terms of monthly profit. This underscores the effectiveness of the UHTS system in enhancing the operational profitability of thermal systems.

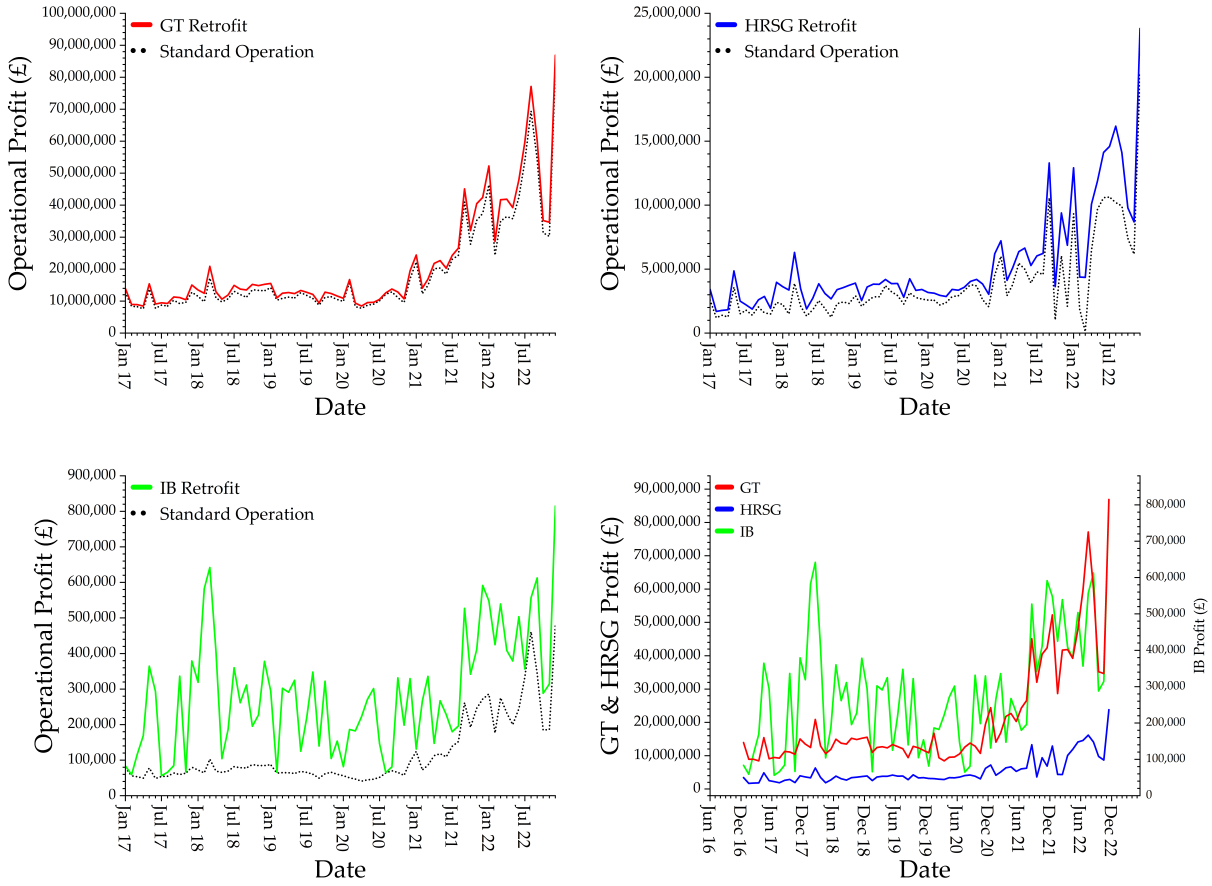


Figure 5.18: Gross profit differential from the standard operation of a GT, HRSG, and IB against that produced during boosted operation, under the arbitrage model.

An analysis of monthly profit differentials, defined as the differential between UHTS-boosted and normal operating profits, is also carried out. Figure 5.19 presents the profit differentials for each month over six years. This is shown cumulatively for GT integration, stacking the profit for that month for each year. This offers a visual representation of the UHTS system's financial impact on operation. The stacked bars indicate cumulative profit differentials, delineated by year, providing a comparative perspective across the observed temporal range.

This indicates variability in profit differentials between months, with discernible trends that could be attributed to operational performance and market demand fluctuations. Cooler winter months generally exhibit higher profit differentials, suggesting these months benefit significantly from the UHTS system, potentially due to climatic influences on energy demand. During the summer, a general trend of lower profit differentials is seen, indicating a seasonal decline in the benefits from the UHTS system. This is likely due to the greater input of solar sources during these months, reducing the variability of the imbalance prices due to a more stable and predictable supply.

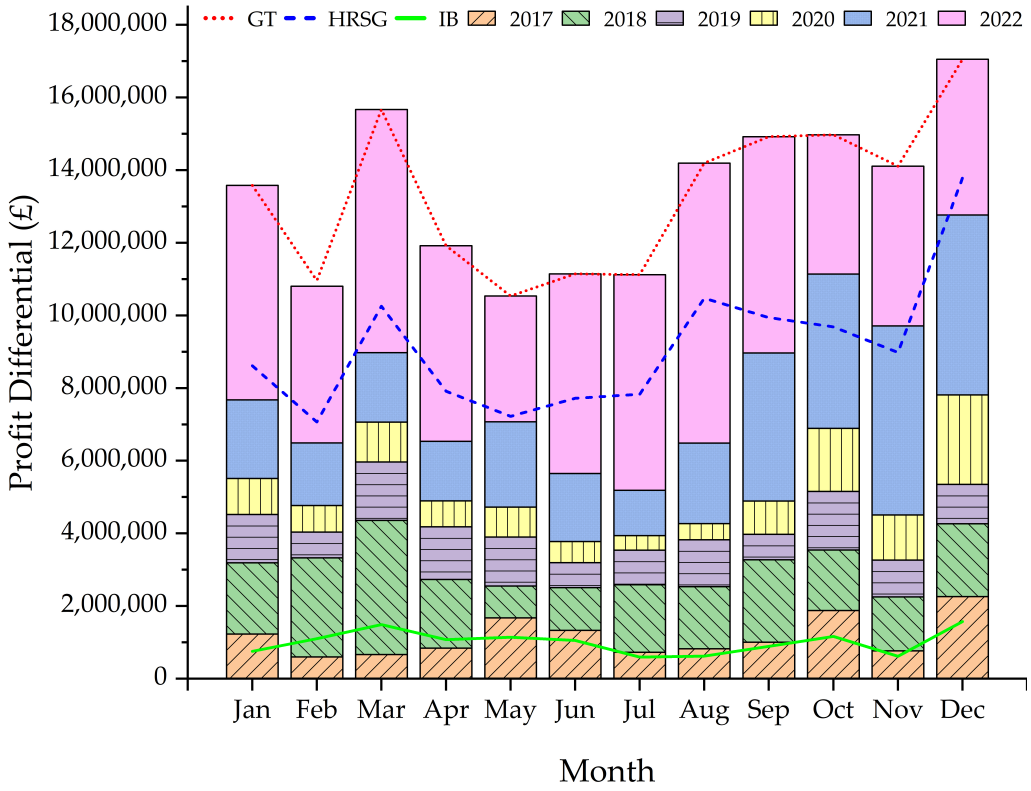


Figure 5.19: Cumulative annual profit differential from the standard operation of a GT, HRSG, and IB, under the arbitrage model.

Abnormal spikes in profit differential can be caused by an increase in the imbalance price that is not expected, affecting multiple SPs. For example, consistently low wind generation over an extended period of time results in fewer balancing options. Consequently, there is a greater proportion of high-value bids from NG-driven units during times, which must be accepted due to the short nature of the system. The system is short where the electricity supply within the grid is insufficient to meet the demand, potentially leading to power outages or, if not addressed, necessitating load shedding. An increased reliance on NG systems to balance the grid leads to an increased marginal price. Situations such as these underscore the value of a suitably situated UHTS system, which can respond to demand-supply imbalances when cheaper generation sources like wind are underperforming.

Profit differentials on a year-on-year basis often reflect the interplay of strategic operational decisions and market dynamics. For instance, the downturn in profitability observed in 2020 can largely be attributed to the diminished energy demand resulting from the UK's COVID-19 containment measures. In contrast, the subsequent upswing in profit margins during the latter part of 2021 into 2022 coincides with a period of escalating fuel costs. This uptick in fuel prices was significantly influenced by geopolitical tensions that culminated in the Russian invasion of Ukraine, underscoring how international incidents can impact energy markets. It is vital to note that these external factors, while pivotal, are part of a broader array of variables that influence profit differentials, including changes in consumer behaviour, regulatory adjustments, and shifts in energy production and distribution efficiencies.

The integration of a UHTS system demonstrates a variable impact on profit margins across different technologies. The average monthly profit increase is most pronounced in the case of an IB, while the GT configuration exhibits the smallest percentage increase. This variation can be attributed to the differential in power output required to drive the thermal generator, which influences the profitability enhancement.

This occurs as the lower power discharge systems take a longer period of time to fully discharge the store. When the UHTS system reaches a fully discharged state less frequently, the system undergoes fewer recharge cycles. Consequently, this allows for optimised operation, capitalising on lower charging costs while maintaining its availability to provide heat at high price periods. Table 5.3 details the impact of UHTS adoption on operational profits.

Table 5.3: System profitability comparison for a GT, HRSG, and IB under the arbitrage model.

System Profit	GT	HRSG	IB
Base (£)	18,940,000	3,830,000	120,000
Boosted (£)	21,160,000	5,350,000	280,000
Increase (%)	11.9	98.6	200.2

The volatility of the energy market, particularly in periods of price spikes, demonstrates the strategic advantage of the UHTS system when operating under arbitrage conditions. The data presented from the operational profits, both with and without UHTS retrofit, distinctly shows that periods of high market volatility directly correlate with increased profitability for UHTS systems when operating in an arbitrage-led manner. If the UHTS operator can rapidly respond to market signals, the systems can leverage these situations to boost profitability. Over an extended timeline, the UHTS's ability to augment profits appears robust against the backdrop of the broader energy market volatility. The seasonal trends and year-on-year shifts reflected in the multi-year data analysis further illustrate how UHTS systems are well-suited to adapt to changing market conditions.

These results demonstrate the necessity for strategic operational planning, such as conducting any required maintenance during the summer months when the system profitability is lower.

Fuel Displacement Performance

The fuel displacement model is designed to utilise the UHTS to replace fuel with energy from the UHTS while ensuring that operational costs do not surpass those of the base GT operation. As with the arbitrage optimisation, the model will charge the thermal store when imbalance prices are low and discharge via a thermal generator when they are high, maximising fuel savings and CO_2 displacement.

Fuel Savings The operational savings are determined by the cost differential, which factors in the costs of charging the UHTS system and any additional fuel required to supplement the UHTS outlet to reach the temperature required for the thermal generator to operate. These are present in Figure 5.20 for each discharge system. The inlet energy displaced by the store is measured as a proportion of the total energy that would have conventionally been supplied

by the combustion of fuel, which has instead been replaced by heat from the UHTS. This displacement is a direct indicator of the efficacy in reducing fuel consumption and, by extension, operational costs.

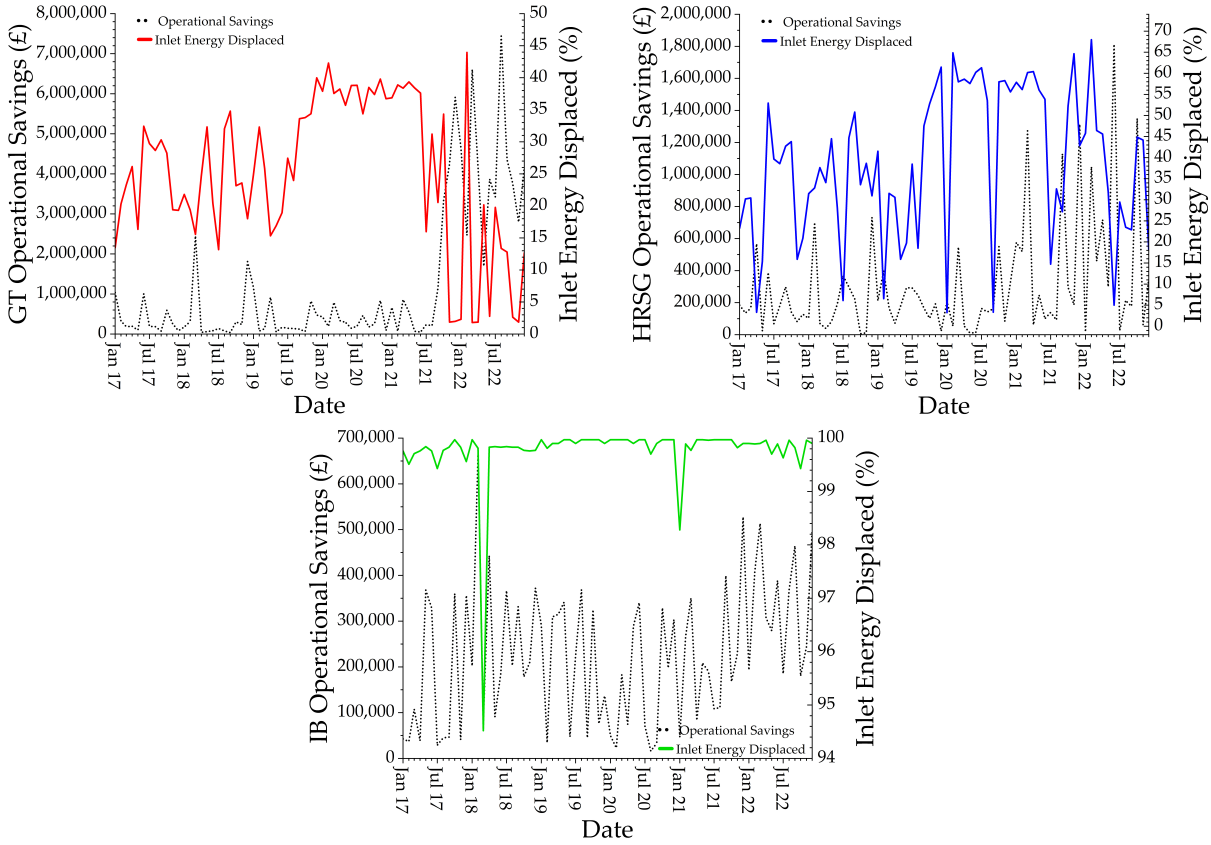


Figure 5.20: Inlet energy displacement percentage and operational savings for a GT, HRSG, and IB under the fuel displacement model.

Results confirm that energy displacement correlates with operational costs. The integration of the thermal store introduces a variable cost factor that is influenced by the cost-effectiveness of charging and discharging cycles, which correspond to the fluctuations in imbalance prices. However, there are instances where lower inlet energy displacement coexists with higher operational savings. This counterintuitive occurrence is caused by instances with extremely high imbalance prices.

For example, this was seen in March 2018. During this month, there were 127 SPs in which the imbalance price was greater than 100 £/MWh, more than 20 % of the occurrences for the year. This peaked at a price of 990 £/MWh, five times the average for the quarter and the highest seen in all of 2018. In these SPs, the system was short due to the weather event nicknamed the 'Beast from the East', in which there was a reduction in wind generation due to infrastructure damage and a drop in temperature (Thornton, 2020). This pushed electricity demand up 10 %, with the evening peak demand on March 1st being the highest in three years. Events such as these demonstrate that during high-price periods that last on the scale of a few days, the UHTS system is able to produce significant savings. This also shows that, even with

a lower percentage of energy displacement by the thermal store, the cost of supplemental NG required during discharge remains economically advantageous due to the higher price offset achieved during these peak pricing periods.

These observations demonstrate that the extent of inlet energy displacement is not the sole determinant of operational savings. Instead, the timing of UHTS utilisation, in response to the fluctuations in energy pricing, critically influences the cost-effectiveness of the system, even when operating under the fuel displacement model.

Carbon Savings The financial savings associated with carbon reduction do not increase linearly with fuel displacement as the carbon tax price varies due to the process through which they are traded.

The optimisation logic generates variable operational savings, based on the interplay between fuel prices, electricity prices, and the charging-discharge cycles of the thermal store. When fuel is displaced, this results in a reduction in CO_2 emissions which in turn means the generation system requires fewer carbon credits.

Figure 5.21 shows the savings associated with a reduction in CO_2 production, along with the mass of CO_2 displaced each month, from 2017 to 2022.

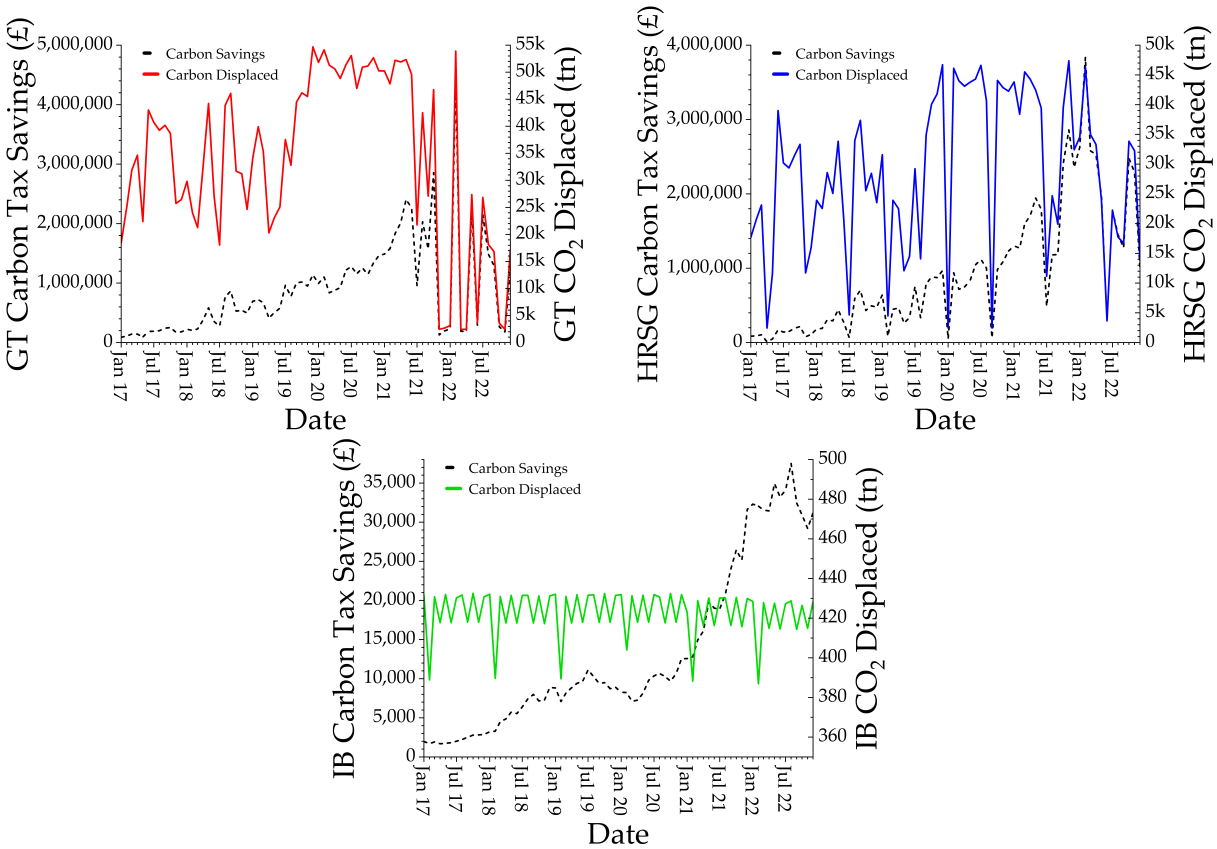


Figure 5.21: Carbon tax savings and CO_2 displaced for a GT, HRSG, and IB under the fuel displacement model.

It can be seen that initially, the carbon tax savings and CO_2 displacement show a consistent

correlation. There is a change in this from early 2021, with an increase in tax saving per unit mass of CO_2 produced. This is due to policy shifts as the UK transitioned from the EU ETS to the UK ETS after Brexit at the beginning of 2021. These results indicate that policy shifts can have a noticeable impact on the savings the UHTS system can produce, and can be seen most clearly in the IB case due to the fairly consistent CO_2 displacement.

When discharging via a GT, an inverse relationship is observed between NG prices and CO_2 displacement. As mentioned in Section 5.5.3, NG prices increase at the tail end of 2021, heading into 2022. This results in increased charging costs. As the model prioritises not incurring an increased operational cost, these prices reduce the frequency of charging as fewer low-price SPs can be used to charge the UHTS system.

This indicates that models which require additional fuel to meet the energy requirement of the discharge system are sensitive to changes in imbalance prices due to the constraints which prevent operational costs from exceeding that of normal operation. The higher prices result in the model reaching this limit more frequently. This results in the store spending more time fully discharged, reducing the system availability, which is reflected in a reduction of fuel displacement, and as such, CO_2 displacement. Further work may be required to produce an optimisation model designed for when there are fewer low-value SPs that the UHTS system can use to charge.

On the other hand, the IB system maintains a relatively constant CO_2 displacement. This occurs as the UHTS system rarely fully discharges and therefore, does not rely on the use of additional NG to boost the output. Additionally, implementation into smaller systems with reduced operating hours is less susceptible to market fluctuations due to the lower frequency of charging required, allowing them to continuously generate savings.

As the system rarely fully discharges, this suggests that the storage capacity is oversized for integration into an IB and is therefore inefficiently deployed. This suggests a tailored approach to matching TES system sizes with discharge technologies is necessary. By analysing the discharge patterns and energy requirements of different technologies, it is possible to optimise storage capacities to ensure efficient utilisation and avoid the inefficiencies associated with oversized storage systems.

Future Performance

To evaluate the future integration of the UHTS system, both the arbitrage and fuel displacement models are applied to future years. This is achieved using 30 minute SPs for the years 2025, 2030, 2035, 2040, 2045 and 2050. These are selected to give a progressive evaluation, without an excessive computational requirement. These results demonstrate how the evolving energy market affects the UHTS performance.

Arbitrage Prediction When considering the future viability of the UHTS system, Figure 5.22 demonstrates that the system is likely to continue to produce profits up to 2050.

Under arbitrage conditions, the UHTS profit differential from integrating with a GT and HRSG is expected to increase until 2040 and then decline. With RES capacity continuously increasing, it drives the rising cost of NG-fuelled generation, which causes a decrease in reliance on traditional thermal generators.

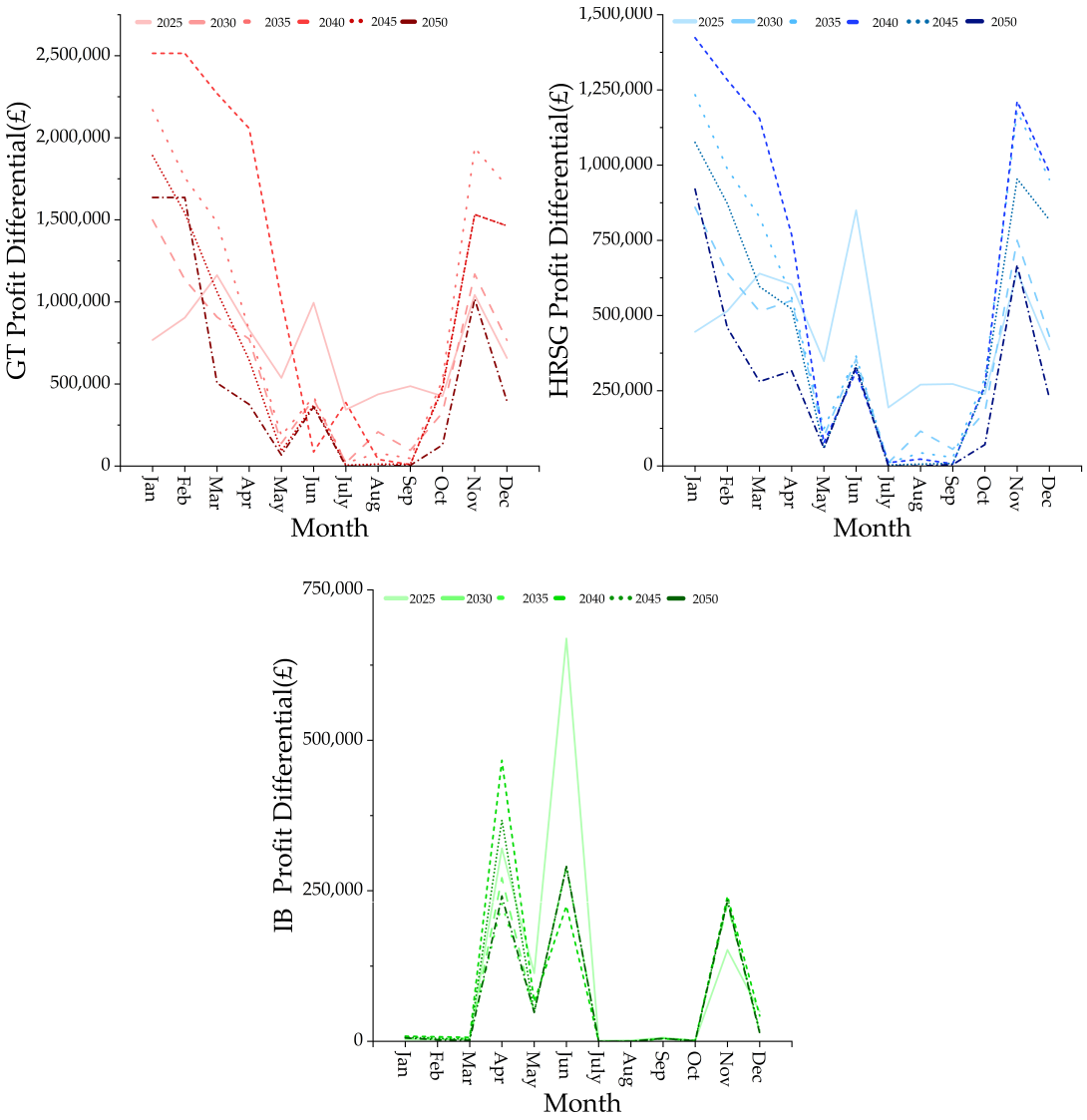


Figure 5.22: Projected future profit differentials from 2025 - 2050 for a GT, HRSG, and IB under the arbitrage model.

This is highlighted in August and September of 2050, where there are no points in which the UHTS system increases profitability. These months see greater utilisation of installed solar PV resulting in an influx of cheap, renewable energy which meets a greater portion of the reduced demand seen when heating requirements are lower. Moreover, despite lower wind utilisation outside of winter months, increased installed capacity means wind generation and storage can still meet much of the demand affordably.

Low energy prices coupled with the significant marginal cost of NG-driven generation, a result of a combination of both high NG prices and high carbon tax prices, means that generation through retrofitted thermal units is priced out of the energy mix. However, looking ahead to this date, the implementation of a UHTS system retrofit would likely see out the life of all but the newest generation systems, based on their designed life cycles of around 25 years (Singh et al., 2011).

In contrast, the IB's profitability spikes in certain months, driven by periods of negative imbalance prices. The lower power requirement of an IB leads to a smaller arbitrage profit differential, yet imbalance payments acting as a sink for excess grid energy can yield a significant income when suitably utilised. This indicates that the future of arbitrage for a UHTS system retrofitted to an IB presents greater profit opportunity by primarily acting as a sink for excess power on the grid, which can be utilised in the IB boiler as a secondary benefit.

It should be noted that, as mentioned previously, the future model is unable to predict price spikes caused by geopolitical pressures or abnormal weather patterns, and as such, future models will miss extreme price events which would make the UHTS system more profitable.

These findings demonstrate UHTS's suitability for boosting the output of thermal generators. The outperformance of base operation profitability underscores the potential of UHTS for deployment optimisation, presenting a case for its broader adoption in the energy sector. These results also outlined the necessity for strategic operational planning, such as conducting required maintenance during the summer months when the system profitability is lower.

Fuel Displacement Prediction When considering the future viability of the UHTS system, the impacts of escalating energy prices and carbon taxation vary depending on the discharge system. GTs and HRSGs show greater sensitivity to economic factors, resulting in a reduction in fuel displacement as time progresses. This is displayed in Table 5.4.

Table 5.4: Fuel displacement percentages each month from 2025 - 2050 for a GT, HRSG, and IB under the fuel displacement model.

Fuel Displaced (%)		Jan	Feb	Mar	Apr	May	Jun	Jul	Aug	Sep	Oct	Nov	Dec	Ave
GT	25	14.3	15.8	17.6	19.7	19.9	23.7	14	16.1	38.0	13.1	19.4	12.4	18.7
	30	10.3	9.7	13.1	12.5	12.1	30.4	11.9	13.4	39.5	9.1	11.7	15.4	15.8
	35	7.7	8.4	9.9	12.4	9.1	24.9	12.5	12.9	31.5	10.8	8.8	9.7	13.2
	40	7.0	8.6	11.5	14.4	8.9	19.0	11.4	9.9	21.4	11.6	11.8	9.3	12.1
	45	7.9	9.2	12.2	12.4	9.4	20.5	8.6	11.6	18.5	12.5	9.3	8.1	11.7
	50	8.6	9.9	13.5	11.1	7.7	16.6	5.7	9.7	14.7	12.5	8.1	9.9	10.7
HRSG	25	18.8	20.1	24.7	30.8	24.0	42.6	19.8	28.4	58.1	13.9	28.0	18.5	27.3
	30	16.1	11.6	18.5	21.0	17.0	50.1	17.2	22.1	65.4	8.8	16.9	27.5	24.4
	35	14.2	9.8	16.3	21.8	14.1	47.8	22.1	20.9	47.8	8.3	14.3	19.1	21.4
	40	11.5	11.7	14.6	24.4	14.6	36.2	17.9	16.5	37.9	8.8	18.9	14.8	19.0
	45	9.2	11.5	19.6	20.1	13.8	37.2	13.2	16.9	30.6	10.4	14.9	13.3	17.6
	50	9.3	13.4	3.2	18.3	11.8	32.8	9.5	15.6	24.4	12.1	13.8	12.9	14.8
IB	25	99.8	99.8	99.8	99.8	99.8	99.8	99.8	99.8	99.8	99.8	99.8	99.8	99.8
	30	99.8	99.8	99.8	99.8	99.8	99.8	99.8	99.8	99.8	99.8	99.8	99.8	99.8
	35	99.8	99.8	99.8	99.8	99.8	99.7	99.8	99.8	99.8	99.8	99.8	99.8	99.8
	40	99.8	99.8	99.8	99.7	99.8	99.8	99.8	99.8	99.8	99.8	99.8	99.8	99.8
	45	99.8	99.8	99.8	99.8	99.8	99.8	99.8	99.8	99.8	99.8	99.8	99.8	99.8
	50	99.8	99.8	99.8	99.8	99.8	99.8	99.8	99.8	99.7	99.8	99.8	99.8	99.8

This reduction in fuel replacement is caused by the model limitation that prevents the system from simultaneously charging and discharging. This is representative of realistic deployment as, if the price were low and the system fully charged, it would be more economically prudent to directly heat air, removing any inefficiencies associated with heating air via the store. Due to the reduction in price fluctuations as RES capacity increases, the model encounters extended

periods when the price is below the CT. As such, it will not discharge during these periods. This indicates that in these instances, it would be beneficial to use direct electrical heating of the HTF, rather than passing it through the UHTS.

IBs, however, maintain steady performance in fuel displacement, underscoring their operational efficiency due to their ability to rely on much less common, lower charging prices. Only 0.2 % of their time is spent charging, as a fully charged store can drive a 3 MW IB with the heat for extended periods, without reaching a state of insufficient stored heat.

However, even with the decrease in fuel displacement looking forward, this does not directly correlate with a decrease in carbon tax savings. Though less CO_2 is displaced, the savings per tonne of displacement increase due to the escalating carbon tax rates. This serves as an economic incentive for the adoption of UHTS to reduce CO_2 emissions.

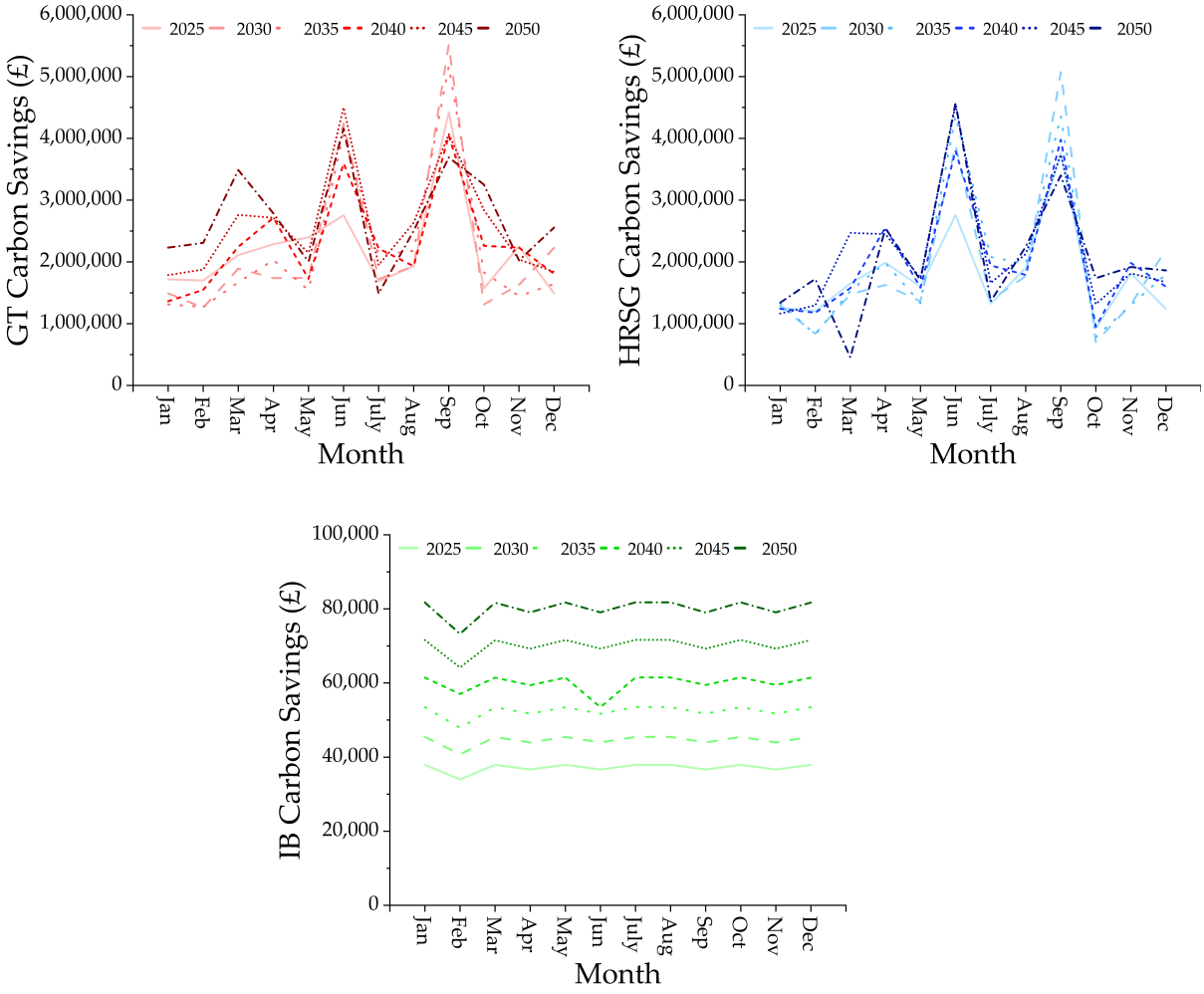


Figure 5.23: Projected future carbon tax savings from 2025 - 2050 for GTs, HRSGs, and IBs under the fuel displacement model.

GTs and HRSGs demonstrate substantial carbon tax savings, reflecting their higher fuel requirement resulting in larger baseline carbon footprints. However, these savings are not consistent over the course of a year. With the increasing frequency of low prices which prevent

the model from discharging, the CO_2 displaced fluctuates over the course of a given year, resulting in inconsistent savings on a monthly basis. A balance between the reduced fuel replacement and the increased carbon tax price results in the carbon savings remaining relatively consistent as years progress. Figure 5.23 demonstrates that the system is likely to continue to produce carbon savings up to 2050.

In contrast, IBs exhibit consistent yet relatively lower carbon tax savings, owing to their already high efficiency and lower carbon intensity. Due to their ability to displace a high percentage of the required fuel, the impact of increasing carbon tax prices can be seen clearly.

The results show both environmental and economic benefits when integrating UHTS systems within power generation systems with the rising NG costs and increasing carbon taxation, alongside the decrease in electricity prices predicted going forward. The difference across GTs, HRSGs, and IBs highlights the importance of a technology-specific approach. This allows for the optimal deployment of the storage systems.

The integration of UHTS systems into existing thermal generators has the potential to be a pivotal technology in the transition towards sustainability. This transition is supported by the economic viability of displacing conventional fuels, reducing CO_2 emissions, and thus generating carbon tax savings.

5.5.4 Discharge System Efficiency Variation

The economic feasibility of integrating a UHTS system with existing power generation infrastructure will vary based not only on the type of discharge system implemented but also on the efficiency of that system.

Similar technologies with different designs, ages, and physical locations can have a wide range of thermal efficiencies, affected by numerous factors. When varying the efficiency of the discharge systems, there is an impact on the profitability of the UHTS system due to a variation in discharge dynamics. As such, this section discusses the effects of system efficiency in the discharge mechanisms of UHTS and the relationship between thermal efficiency and the system economics.

Arbitrage - Efficiency

The arbitrage scheme capitalises on the disparity between high and low electricity prices. This will be affected by the efficiency of discharge due to the pivotal role of efficiency in determining the amount of energy released from the UHTS and consequently, the power output during peak price periods, understanding this relationship is crucial.

An inverse relationship is apparent between the operational efficiency of each discharge system and the profit differential. As the efficiency decreases, the profit differential correspondingly increases. This trend indicates the UHTS system's enhanced value at lower discharge cycle efficiencies. For example, the profit differential at 55 % thermal efficiency was consistently higher compared to that at 60 % and 65 % efficiencies across all months, with the sole outlier of December for the 65 % efficient system. This is visualised in Figure 5.24.

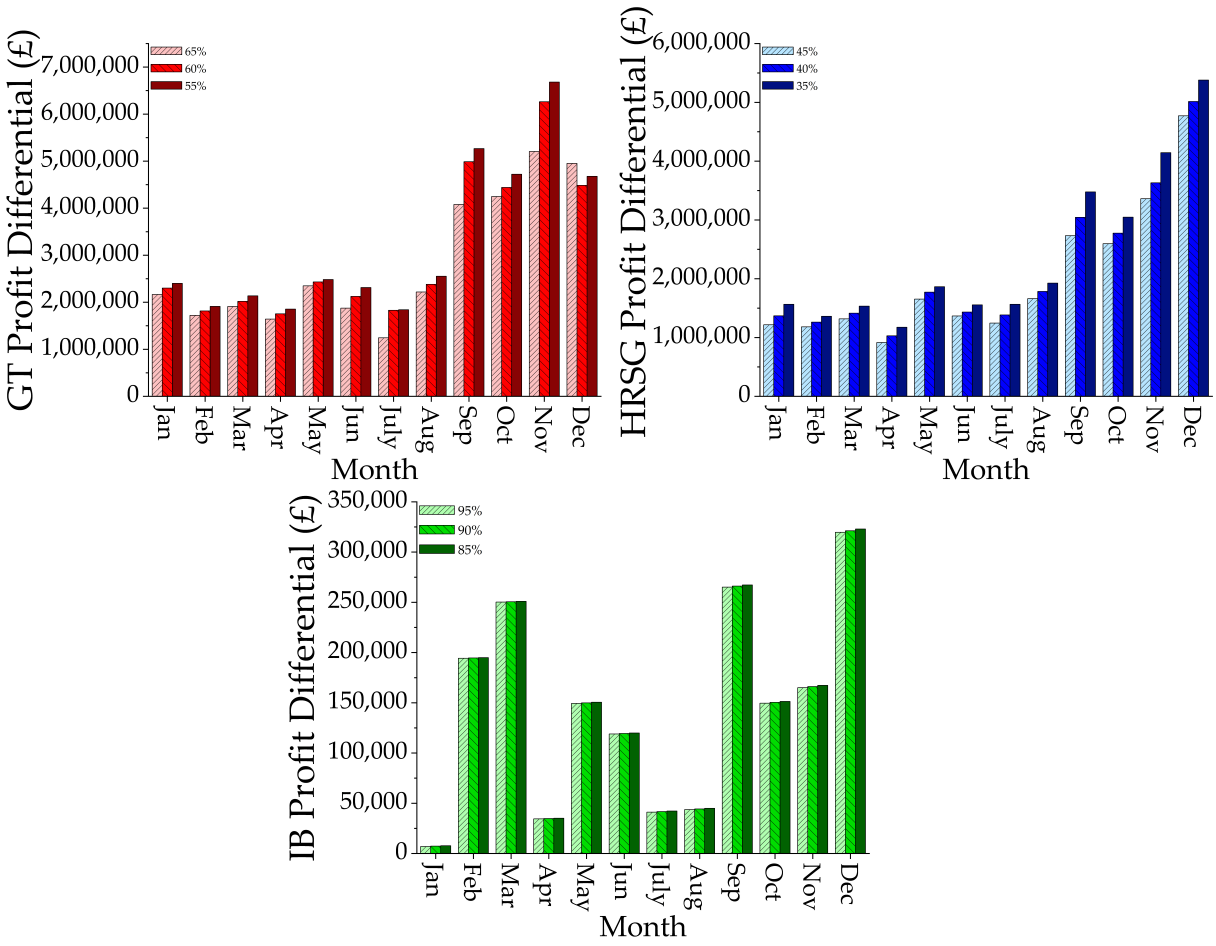


Figure 5.24: Profit differentials per month in 2021 for GTs, HRSGs and IBs operating at differing efficiencies, under the arbitrage model.

This outlines the advantage of deploying the UHTS system, particularly with less efficient systems or during times of lower efficiency operations, such as start-up. This is quantified in Table 5.5, which gives the mean profit differential for each discharge system.

Table 5.5: Comparison of mean profit differential for a GT, HRSG, and IB under the arbitrage model.

		Profit (£)		
		Base System	Retrofit System	Differential
GT	65%	24,775,046	27,575,607	2,800,562
	60%	26,404,849	29,474,074	3,069,225
	55%	23,592,473	26,828,996	3,236,523
HRSG	45%	4,681,445	6,683,014	2,001,569
	40%	2,683,731	4,842,931	2,159,199
	35%	115,242	2,497,809	2,382,567
IB	95%	157,114	301,977	144,863
	90%	152,068	297,597	145,529
	85%	146,427	292,701	146,274

This trend occurs as systems with lower efficiencies inherently incur higher fuel costs per

unit of electricity generated due to their less effective conversion of fuel to power. Consequently, without a UHTS retrofit, these systems operate at reduced profitability. The introduction of UHTS alters the profit potential of these systems by allowing them to make use of arbitrage, leveraging the differential between peak and off-peak energy prices.

The UHTS retrofit in this study supplies a 5 % boost in output. As such, whilst the higher efficiency systems still provide the optimal profit when the UHTS operates under arbitrage deployment, the lower-efficiency systems offer a more substantial differential profit margin by maximising effective thermal efficiency during high-price periods.

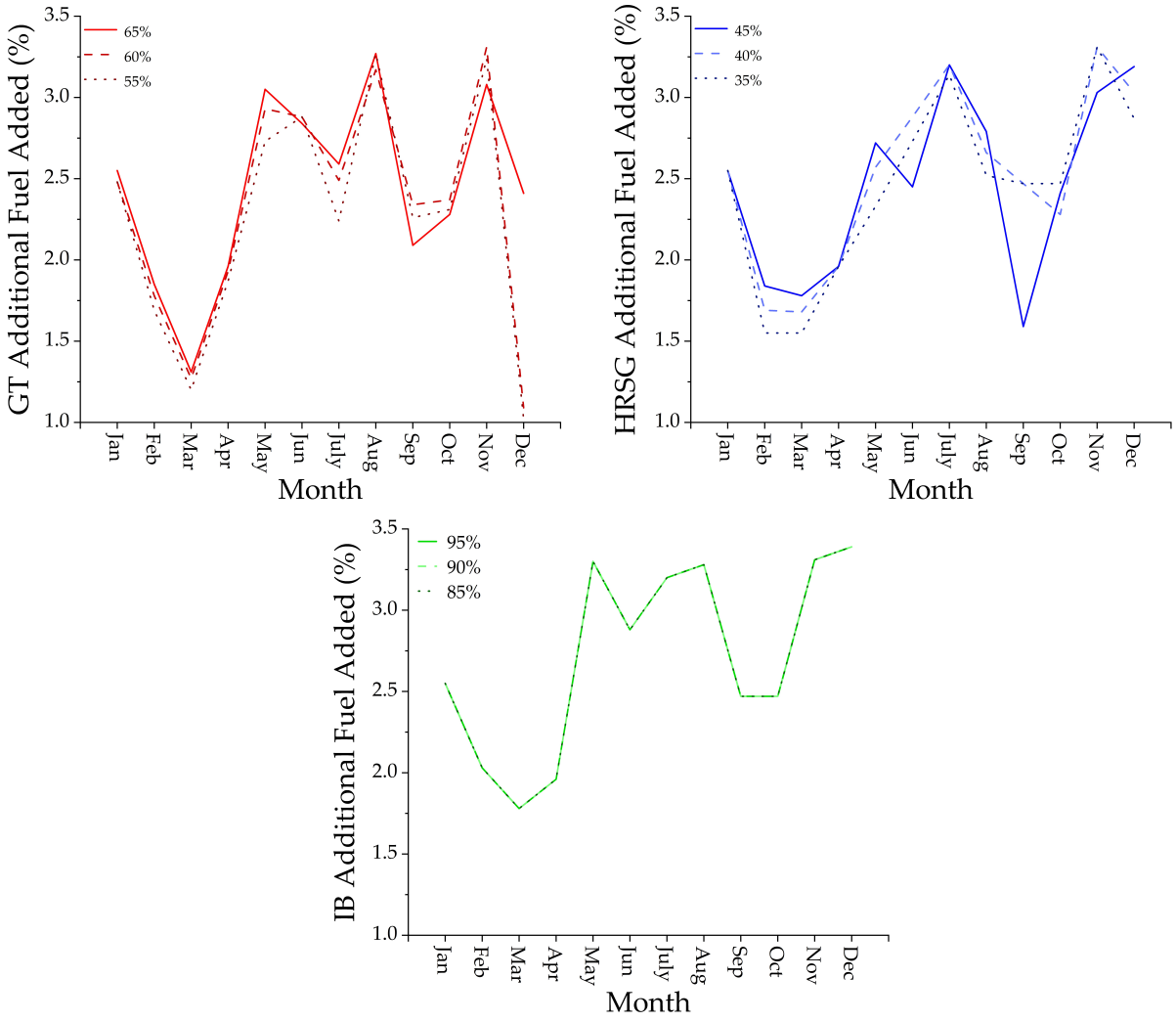


Figure 5.25: Boost percentage per month in 2021 for GTs, HRSGs and IBs operating at differing efficiencies, under the arbitrage model.

During arbitrage operation, the augmented output is quantified as the net percentage increase in the energy output of the discharge system, attributed to the energy released from the UHTS store. Assuming an ideal scenario where the UHTS possesses unlimited capacity, this augmentation aligns with the predetermined boost value, set at 5 % for this analysis. The efficiency of the GT and HRSG discharge systems plays a pivotal role in this context. Greater

system efficiency results in an overall increased energy boost, as more efficient discharge cycles require less energy from the UHTS to achieve the targeted 5 % output increase during discharge periods, and as such, the store will discharge less quickly. The resultant boost percentages for each system are displayed in Figure 5.25.

However, this direct relationship between system efficiency and energy boost changes in months when electricity prices reach higher peaks. During these periods, the increase in boosted energy for high-efficiency cycles is not consistently observed. This anomaly can be attributed to the elevation of the DT, a response to the heightened electricity prices. In these scenarios, a more efficient system capitalises on its ability to generate increased profits by minimising the frequency of full-store discharges. It conserves stored energy for periods when electricity prices peak, discharging at these times to optimise profit margins. This operation underscores the ability of a highly efficient discharge system to enhance profitability through a reduced number of discharge cycles, demonstrating the balance between system efficiency, discharge frequency, and market dynamics in maximising arbitrage opportunities.

This is particularly prevalent in the month of September, which shows a reduction in boost percentage for the most efficient GT and HRSG systems. The cause is peak values of imbalance prices throughout the month that are outliers to the bulk prices. A larger disparity between mean (177.46 £/MWh) and median (110.13 £/MWh) imbalance prices, indicates a positively skewed distribution, indicative of a non-uniform distribution, caused by a few high price anomalies during the month.

Contrastingly, the IB systems maintain a consistent boost percentage, regardless of variations in efficiency. This uniformity is attributed to the higher thermal efficiency of an IB, combined with its significantly lower energy demand from the UHTS. As such, the likelihood of the UHTS depleting to its minimum temperature is reduced. This results in the discharge capability of the IB systems not being affected by differences in efficiency. In this scenario, the efficiency of the IB system does not limit its ability to discharge; rather, the operational dynamics of these systems are based on the CTs and DTs. Once the model has optimised these triggers to produce the maximum arbitrage profit, these triggers are found to remain consistent over each efficiency of IB, demonstrating the importance of optimising the deployment strategy.

Fuel Displacement - Efficiency

As for the fuel displacement model, a change in efficiency will impact the emissions profile of a generator. The fuel displaced by each system, alongside the CT, is shown in Figure 5.26.

For the GT, due to the large volume of energy required to drive the system, a lower-efficiency discharge system can result in an increased CT. This shows that the model has optimised to prioritise displacement over economic profit, as a small increase in the CT will allow for an extra charging SP, boosting the displacement at the cost of greater operational expense. These increased CT values are available to the lower efficiency systems as the operational cost that the retrofit system must stay below is greater due to the increased fuel requirement the lower efficiency necessitates.

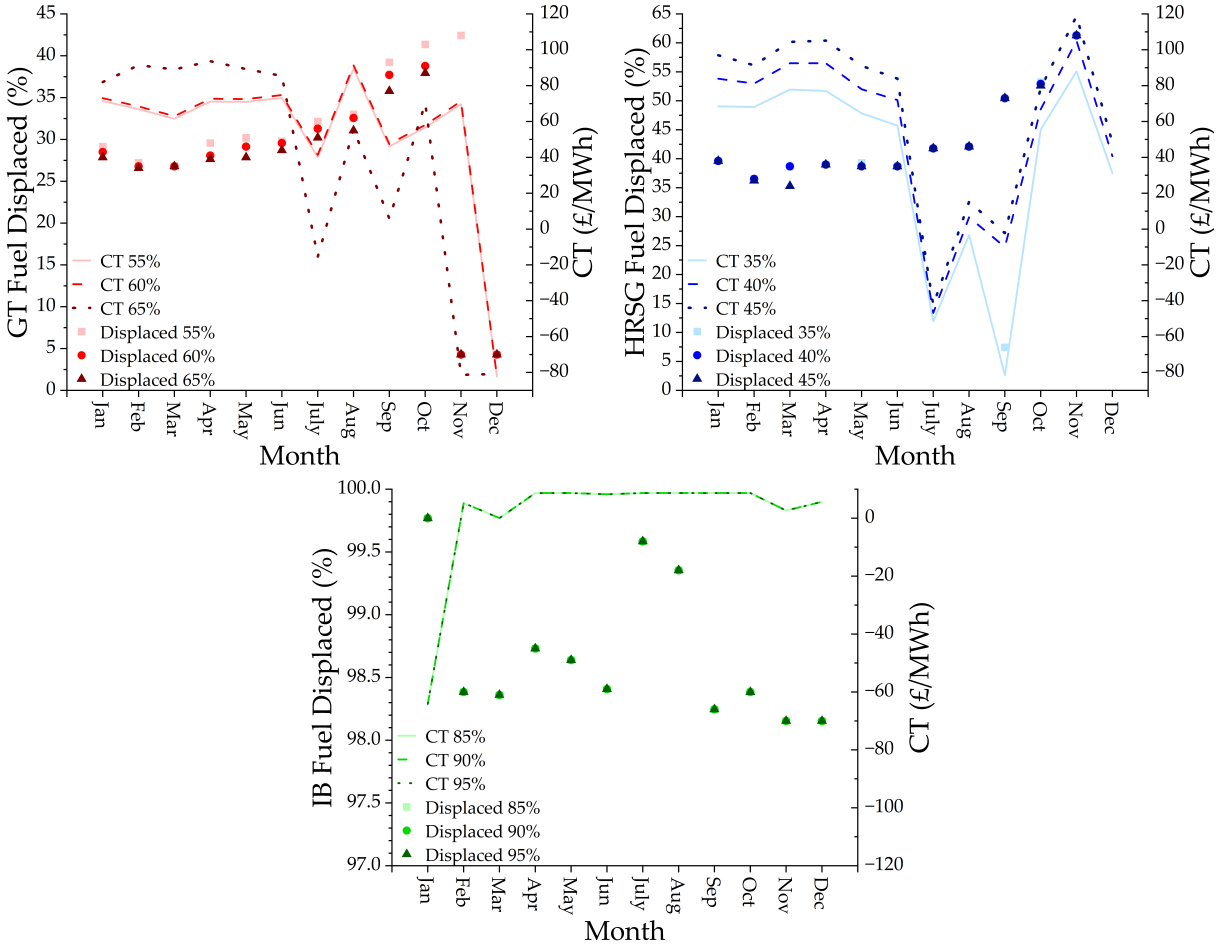


Figure 5.26: Fuel displacement percentage and associated Charge Trigger per month in 2021 for GTs, HRSGs, and IBs operating at differing efficiencies, under the fuel displacement model.

This is not seen as frequently in the HRSG, as the lower range of Rankine cycle efficiencies requires lower CT values to match the original operating costs. As instances of these lower values are less common, there are fewer opportunities for the CT to increase marginally without becoming too expensive to operate. As such, when the efficiency of the HRSG decreases, the percentage of fuel replaced also decreases. This is due to the more efficient systems requiring less fuel to be displaced by the UHTS system to achieve the same output, expending energy from the store less rapidly.

An anomaly during September should be noted. Here, with the lowest efficiency system, the CT falls considerably in order to allow the system to be able to charge whilst still operating at an equal or lower cost to that of normal operation. Due to this, the system charges less frequently, and there is a resultant drop in fuel displacement when compared to higher-efficiency systems. When compared to the 45 % and 40 % efficient systems, this causes displacement to fall by 24.6 % and 22.2 % respectively, compared to an average of 7.3 % and 3.9 % for the other months. This highlights that operating efficiency can have a severe impact on the operational viability of a system if the market conditions change slightly.

As for the IB, due to its reduced energy requirement and high efficiency, the replacement

percentage remains steady over each system. This simply occurs as so few recharges are required to ensure the system can constantly supply energy when required, the system does not get close to matching its original operating cost and therefore, can maximise its fuel replacement.

The mass of CO_2 emitted increases with a decrease in efficiency. As thermal systems require less fuel to produce a constant output at higher efficiencies, the baseline CO_2 emissions are lower. Therefore, even though the percentage of fuel replacement by the UHTS system may be lower, the reduction in CO_2 emissions represents a larger proportion of the total emissions and each unit of energy supplied by the UHTS system offsets a larger quantity of CO_2 than it would under lower efficiencies. These results are displayed in Figure 5.27. This indicates that the UHTS system has the potential to extend the lifetime of high-output generators with lower efficiency, that would otherwise be phased out sooner due to emissions limits.

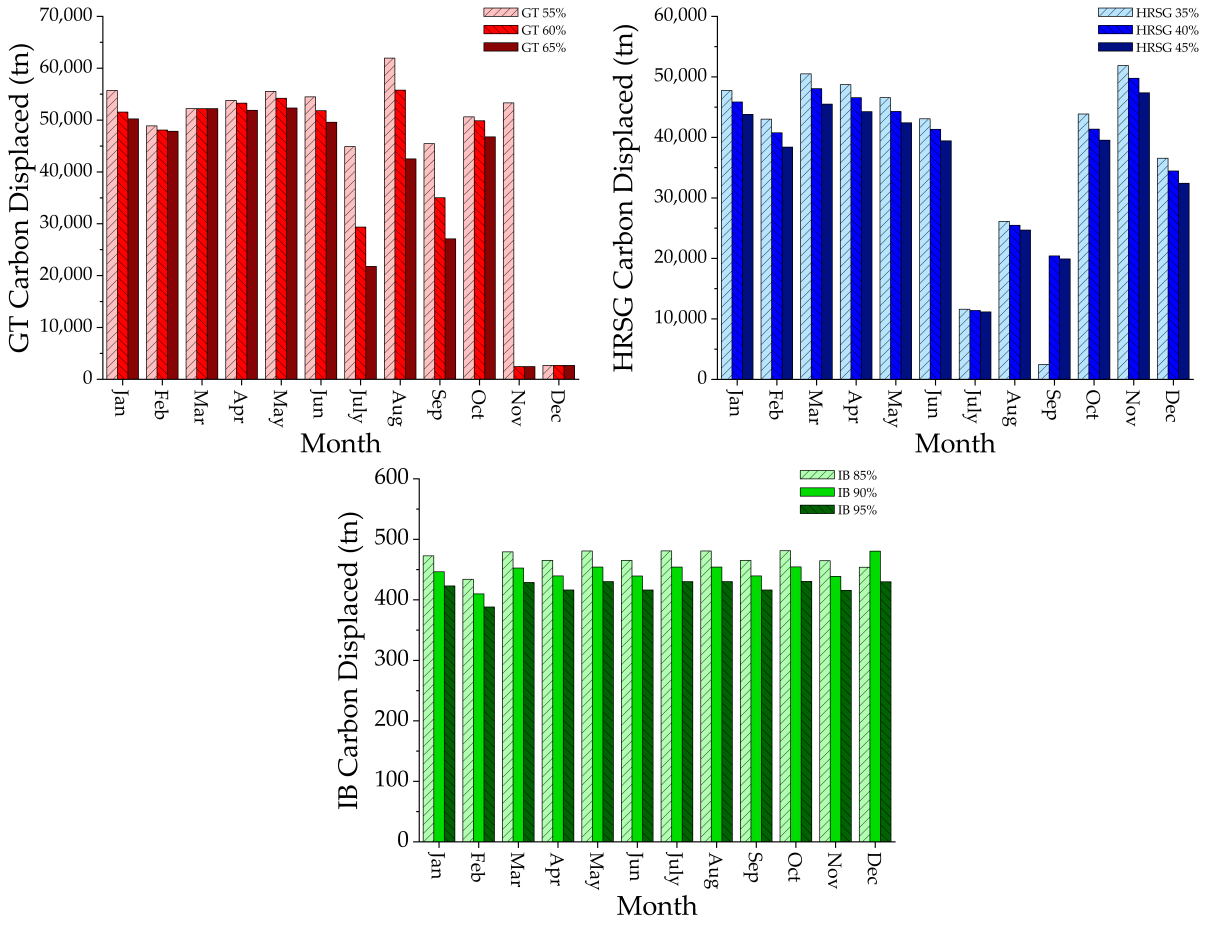


Figure 5.27: Mass of CO_2 displaced per month in 2021 for GTs, HRSGs and IBs operating at differing efficiencies, under the arbitrage model.

There was low CO_2 in November and December for the GT system. This is due to the significant increase in NG prices resulting from the 2021 UK Energy crisis, specifically the suspension of approval for Nord Stream 2 in November, which resulted in a 17 % price increase. This surge in NG prices led to a hike in imbalance pricing, with noticeably fewer low-price

periods, making it more expensive to operate the UHTS system due to high charging costs. Consequently, the utilisation of a UHTS system discharging via a GT was low during this period. This is due to the model limitation that restricts UHTS discharge to ensure that operating costs do not exceed those of normal operation without a TES system. However, lower efficiency systems such as the HRSG, which require more gas per MW_e, were less affected by the price increase due to their higher baseline operating cost and therefore maintained better utilisation rates. This highlights the effect of fuel efficiency and operational costs when integrating UHTS with different discharge technologies.

5.5.5 Temporal Optimisation Period Adaptation

The economic viability of deploying a UHTS system is influenced by the granularity of the dataset used, as a greater data period gives a larger insight into the range of available prices. Previously, the operation of the UHTS system was optimised on a monthly basis, with these results combined to assess annual profitability. This section introduces a variation in approach by exploring the effects of transitioning from monthly datasets to weekly datasets, as well as considering an entire annual dataset for optimisation.

The temporal resolution of the dataset plays a crucial role in capturing the dynamics of electricity pricing and demand patterns, which directly impacts the discharge strategy and, subsequently, the profitability of the UHTS system. By examining the effects of changing the optimisation period from a monthly basis to more frequent weekly intervals, alongside a single year-long interval, the relationship between the temporal granularity of datasets and the economic performance of UHTS is highlighted.

Arbitrage - Optimisation Period

The arbitrage strategy is inherently sensitive to the temporal resolution of the dataset used for system optimisation. Adjusting the optimisation timeframe introduces a new dimension to the operational strategy of UHTS systems in arbitrage markets. Table 5.6 highlights some key figures from changing this timeframe over 2021. This shows that a shorter optimisation period enables a more profitable arbitrage operation.

Table 5.6: Variation in key performance indicators of the arbitrage model with varying temporal granularity of datasets.

	KPI	Weekly	Monthly	Annual
GT	Average CT (£/MWh)	-11	8	5
	Average DT (£/MWh)	57	95	105
	Discharge SPs	14,401	5,845	5,436
	Charge Cost (£)	-3,005,790	-435,278	-953,089
	Discharge Income (£)	46,134,131	33,171,460	27,516,745
HRSG	Average CT (£/MWh)	-14	-32	-31
	Average DT (£/MWh)	51	95	105
	Discharge SPs	15,276	8,645	3,929
	Charge Cost (£)	-2,286,663	-401,708	-8,291,121
	Discharge Income (£)	26,344,616	19,198,336	19,504,892

Continued on next page

		Weekly	Monthly	Annual
IB	Average CT (£/MWh)	-18	-43	-15
	Average DT (£/MWh)	46	93	105
	Discharge SPs	13,364	9,550	6,954
	Charge Cost (£)	-571,628	-1,617,391	-2,138,591
	Discharge Income (£)	136,773	120,961	106,558

The weekly optimisation optimises over a narrower range of CT and DT prices, whilst taking advantage of a lower average CT. This means that the weekly system is more selective regarding when it charges, and the reduced range of data allows the system to maximise its discharge income, without retaining charge for later SPs. This also results in a lower DT for the weekly optimisation model, as it is charging more cheaply, which allows the system to sell back to the grid at a lower price and maintain a profit.

Due to this, there are substantially more discharge SPs in the weekly optimisation than in the other optimisation systems. This higher frequency of discharging is a result of the lower DT, providing more opportunities for the system to discharge.

This more frequent discharging schedule enhances profitability. Weekly optimisation produces a profit of £3,005,790 when charging due to its reduced reliance on higher price SPs to charge. To further increase the profitability of the weekly optimisation, this methodology yields a significantly higher discharge income of £46,134,131 due to the increased number of discharging SPs, producing a greater overall income.

This aligns with the understanding that a more granular temporal resolution can uncover niche operational strategies that maximise the economic potential of UHTS systems in arbitrage markets.

Future research should enhance the model to remove an inherent advantage seen in shorter temporal optimisation systems. As each new optimisation cycle begins with the thermal store full, each dataset essentially starts with a 'free' charge. As such, the model should be updated to read the output of the previous optimisation cycle, finding the remaining stored energy and using that as its initial charge volume.

Fuel Displacement - Optimisation Period

The fuel displacement model shows a similar result when changing the optimisation period. A reduction in the data set size over which the system optimises produces favourable results. Table 5.7 quantifies this effect.

Table 5.7: Variation in key performance indicators of the fuel displacement model with varying temporal granularity of datasets.

	KPI	Weekly	Monthly	Annual
GT	Average CT (£/MWh)	44	30	34
	Total CO_2 Displaced (tn)	462,740	447,351	374,025
	Average Fuel Displaced (%)	29.1	27.9	23.2
HRSG	Average CT (£/MWh)	56	50	50
	Total CO_2 Displaced (tn)	463,199	428,879	382,497
	Average Fuel Displaced (%)	52.2	48.2	42.7

Continued on next page

		Weekly	Monthly	Annual
IB	Average CT (£/MWh)	-17	-47	2
	Total CO_2 Displaced (tn)	5,042	5,055	4,993
	Average Fuel Displaced (%)	99.3	99.8	98.0

However, the data averages over the year fail to outline the full benefits of this change in operation. As Figure 5.28 shows, when optimising over a weekly period, the model produced a greater consistency in CO_2 displacement, compared to the monthly model for the GT and HRSG. The weekly model is less affected by price fluctuations, producing a more predictable operating pattern. This is attributed to the weekly model more effectively responding to market conditions, resulting in a more uniform performance in terms of CO_2 displacement and fuel savings.

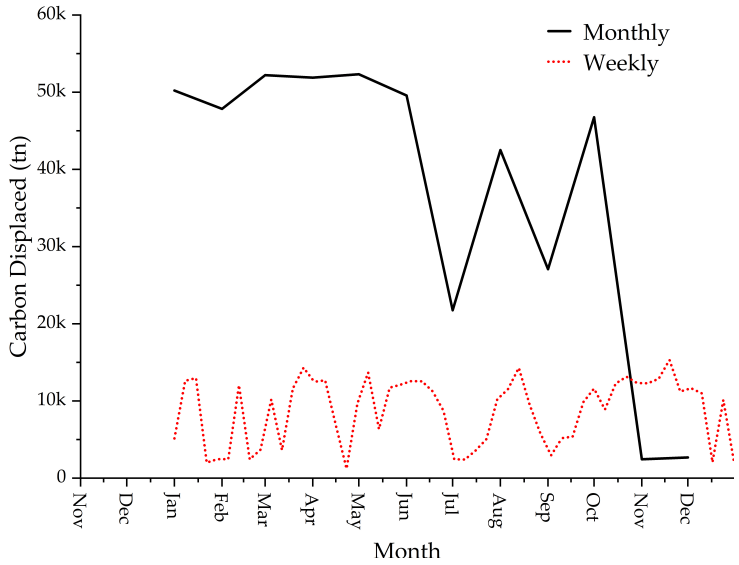


Figure 5.28: Comparison of the mass of CO_2 displaced per optimisation step over the course of 2021, when discharging via a GT.

However, the weekly model resulted in reduced displacement for integration with an IB. As discussed in Section 5.5.3, a reduction in price variation can result in the discharge of the UHTS being limited due to its inability to simultaneously charge and discharge. This occurs in this instance as the weekly optimisation has a reduced range of price fluctuation than the monthly optimisation data set. As such, there are slightly more instances in which the discharge is limited by this model rule.

5.5.6 Time Step Adaptation

Not all countries use 30 minute Settlement Periods, with European nations SPs alone utilising SP lengths of 15, 30 and 60 minutes. The economic viability of integrating a UHTS system with the existing power generation framework is also influenced by the temporal granularity of grid prices. A critical variable in this context is the time step of the SPs, which dictates the frequency of changes in the imbalance prices. Whilst the SPs in the UK are set at 30 minutes, this section explores the effects of extending the time step to 60 minutes.

The frequency of price variation affects the ability of the UHTS system to respond to fluctuations in electricity prices caused by changes in demand, thereby impacting its profitability. A longer time step, for example, 60 minutes, alters the operational dynamics by providing a broader window for charging and discharging at a given price. The impact of an increase in SP length on UHTS profitability will be investigated through a comparison of the standard 30 minute period with a 60 minute period.

Arbitrage - Time Step

During operation under arbitrage conditions, the time step of SPs plays a crucial role. The extension from a 30 minute to a 60 minute time step results in a shift in the operational process of a UHTS system due to its effect on the ability of the system to capitalise on short-term price spikes.

Comparing the 30 minute and 60 minute SP time steps reveals an impact on the profitability of UHTS integration, primarily when discharging via a HRSG and an IB, as seen in Figure 5.29.

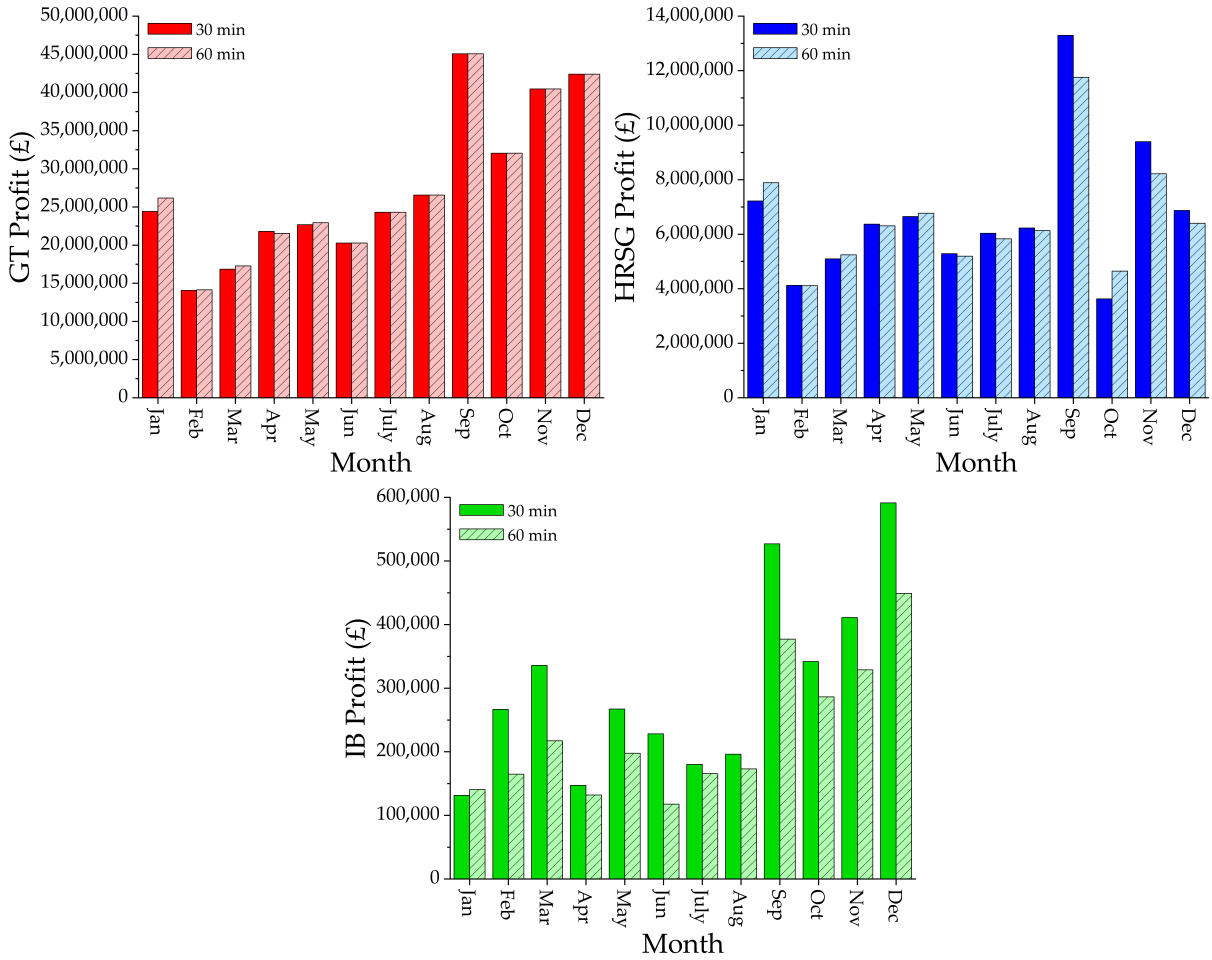


Figure 5.29: Profitability per month in 2021 for GTs, HRSGs, and IBs optimised over 30 minute and 60 minute SPs, under the arbitrage model.

Notably, when integrating into a GT, a transition to the 60 minute time step produced

either equal or increased system profits. The increased profits were seen in the earlier months, which displayed lower imbalance prices. This is because, in months when the difference between the average and median market prices is lower, the market is more stable with fewer price spikes. A 60 minute time step results in reduced volatility, allowing the UHTS to exploit longer duration's of marginally higher-than-average prices. A longer SP enables the UHTS system to take advantage of bulk energy trading, where larger volumes of energy are traded less frequently. This is suitable for less volatile periods as there are fewer peak prices, so profit is generated from consistent income from periods of prices slightly above average, rather than short-term peaks. This highlights that the UHTS system can benefit from the smoothing out of volatility over a 60 minute period.

However, with a longer SP, if prices are higher for extended periods, as was the case in the latter months of 2021, this can still be exploited effectively. A 60 minute SP offers a more sustained window to harness high energy prices, thereby elevating the potential profit per cycle.

This trend was not seen as prominently in the HRSG and IB integration. The HRSG technology displayed a mixed response to the change in time step. While some months showed a slight increase in profit when transitioning to a 60 minute time step, other months exhibited negligible differences or even a slight reduction in profit. This behaviour indicates that HRSG systems have a different sensitivity to an increase in time step length.

IBs showed the least positive outcome to the change in time step among the technologies evaluated. For example, in February 2021, the profit difference between the two time steps fell to £164,672 in the 60 minute time step when compared to £266,660 in the 30 minute time step, indicating specific periods where shorter time steps might offer slightly better arbitrage opportunities. This indicates that the operational profitability of an IB is less dependent on the granularity of imbalance prices.

This variability highlights the importance of tailoring operational strategies to specific discharge technologies and indicates that the time step may be altered to optimise arbitrage profits. There is a stronger correlation between an increase in profitability and a change in time step from 30 minutes to 60 minutes when the discharge system requires the UHTS to output greater volumes of energy per time step.

The change in time step also affects the operational triggers for the UHTS system. With an increase to a 60 minute time step, the CT increases across the different technologies. This indicates a reduction in lower-priced charging opportunities when there is an increase in the time step. As a result, the CT must increase to ensure the system does not deplete itself before high-price SPs to maintain optimal operation.

In contrast, all but one of the DTs remain unchanged, indicating that the optimal price point for energy release is independent of the time step duration. This suggests that, with a reduction in the number of SPs when operating under a 60 minute SP, it becomes economically beneficial to conserve UHTS charge for use during high-priced SPs, rather than discharging more frequently at a lower price. In the first three panels of Figure 5.30, the no-operation zones (shaded areas) between the CT and DT for integration with a GT, HRSG, and IB respectively, are presented. These show how a variation in the time step affects the optimal values for these. The final panel integrates the no-operation zones from all methods, illustrating overlaps and method-specific constraints. This aggregated view highlights the similarities, particularly in the DT, over the various discharge systems.

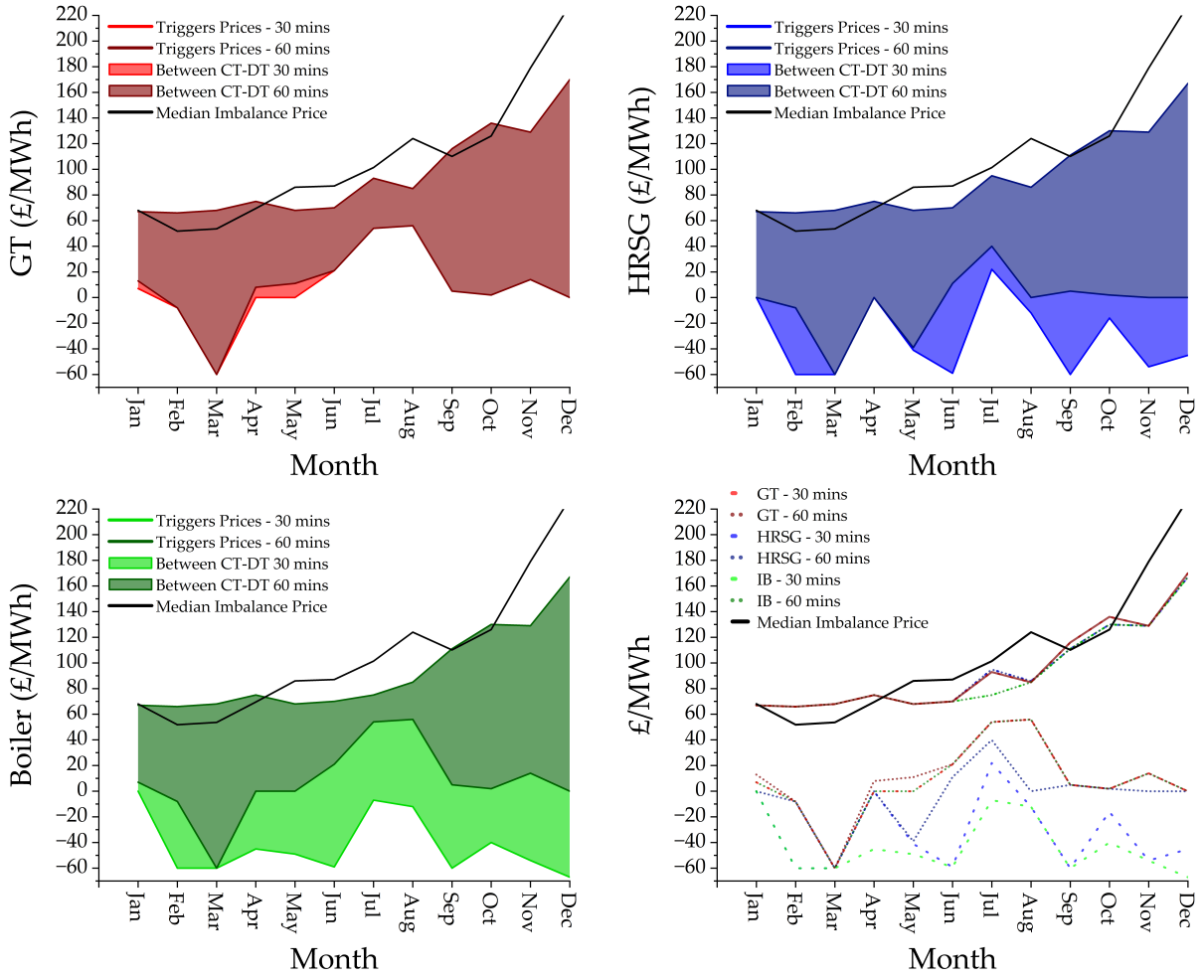


Figure 5.30: Operational boundaries per month in 2021 for GTs, HRSGs, and IBs optimised over 30 minute and 60 minute SPs, under the arbitrage model.

This increase in CT is a response to a decrease in the number of low-price SPs resulting in an increased cost associated with charging the UHTS when the time step is increased to 60 minutes. This is due to the higher allowable prices at which the model will buy electricity to charge the UHTS system.

Additionally, due to a reduction in price fluctuation opportunities, when the store does charge, a larger volume of energy is stored per cycle. This is because 60 minute SPs allow the stored energy to deplete to a greater extent when discharging, as the model does not allow the UHTS to stop discharging midway through a SP. While the 60 minute time step incurs a higher cost per charging session, this is offset by the enhanced profitability discussed previously. Figure 5.31 illustrates the difference in monthly charging costs when operating with a 30 minute versus a 60 minute time step. The bars for GT and HRSG represent costs on the primary y-axis, while the bars for IB refer to the secondary y-axis highlighting the differing scale of charging costs between the systems.

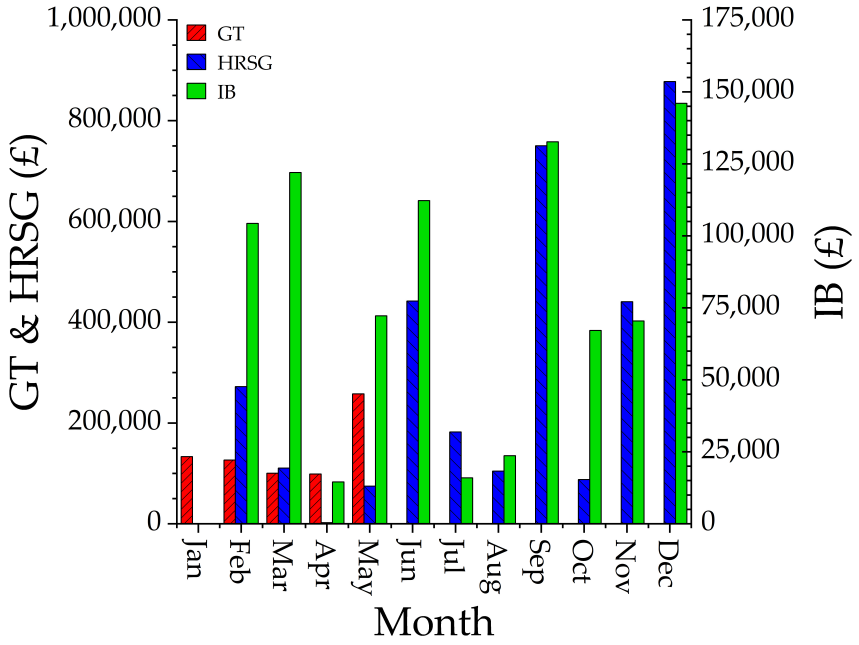


Figure 5.31: Charging cost differential per month in 2021 for GTs, HRSGs, and IBs optimised over 30 minute and 60 minute SPs, under the fuel displacement model.

Fuel Displacement - Time Step

The fuel displacement when integrating a UHTS system is also impacted by a change in SP length. The operational cost differences with and without the UHTS retrofit, when varying the SP time step from 30 to 60 minutes, reflect the degree of system optimisation. Lower cost differences indicate that a greater portion of the operational costs came from UHTS operations. This is consistent with the objective to maximise fuel displacement.

This is because the UHTS system was more flexible with a smaller time step, allowing a more economical operation due to its more active control. The results of this can be seen in Figure 5.32.

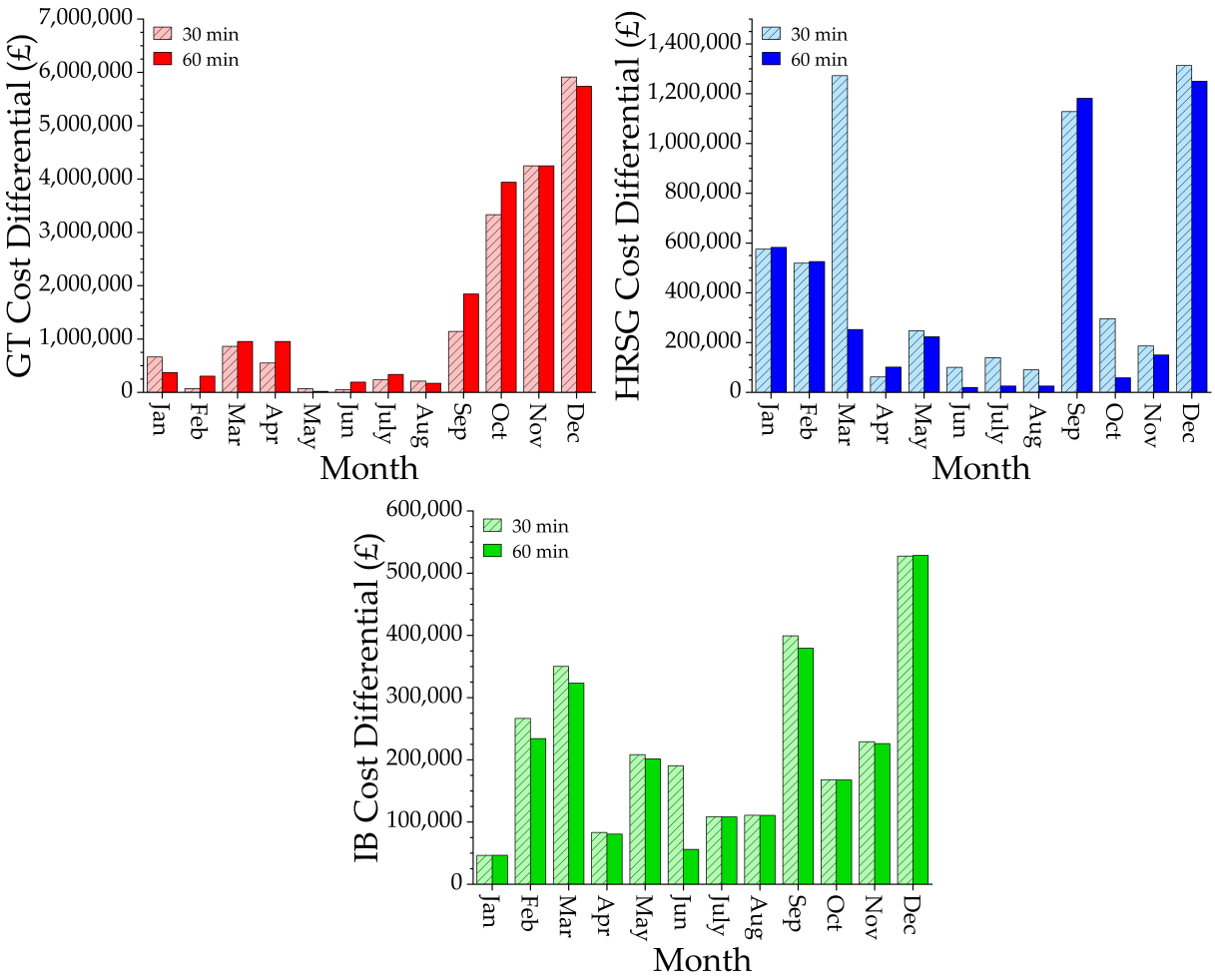


Figure 5.32: Operational cost differential per month in 2021 for GTs, HRSGs, and IBs optimised over 30 minute and 60 minute SPs, under the fuel displacement model.

For the GT and HRSG, a 30 minute SP yields a smaller operational cost difference, indicating the model is able to better optimise for fuel displacement. This is because the granularity provided by a shorter time step allows for more dynamic control over the charge cycles.

In contrast, the IB shows a negligible difference in operational costs between the two SP time steps. This is due to the IB having a lower energy requirement, reducing the likelihood of full discharge, as previously discussed. This highlights a lower sensitivity to the SP duration.

The economic improvement that allowed increased operation was due to the 30 minute time step providing lower CT points, making the charging of the system cheaper. A comparison of the CT at each time step is shown in Figure 5.33.

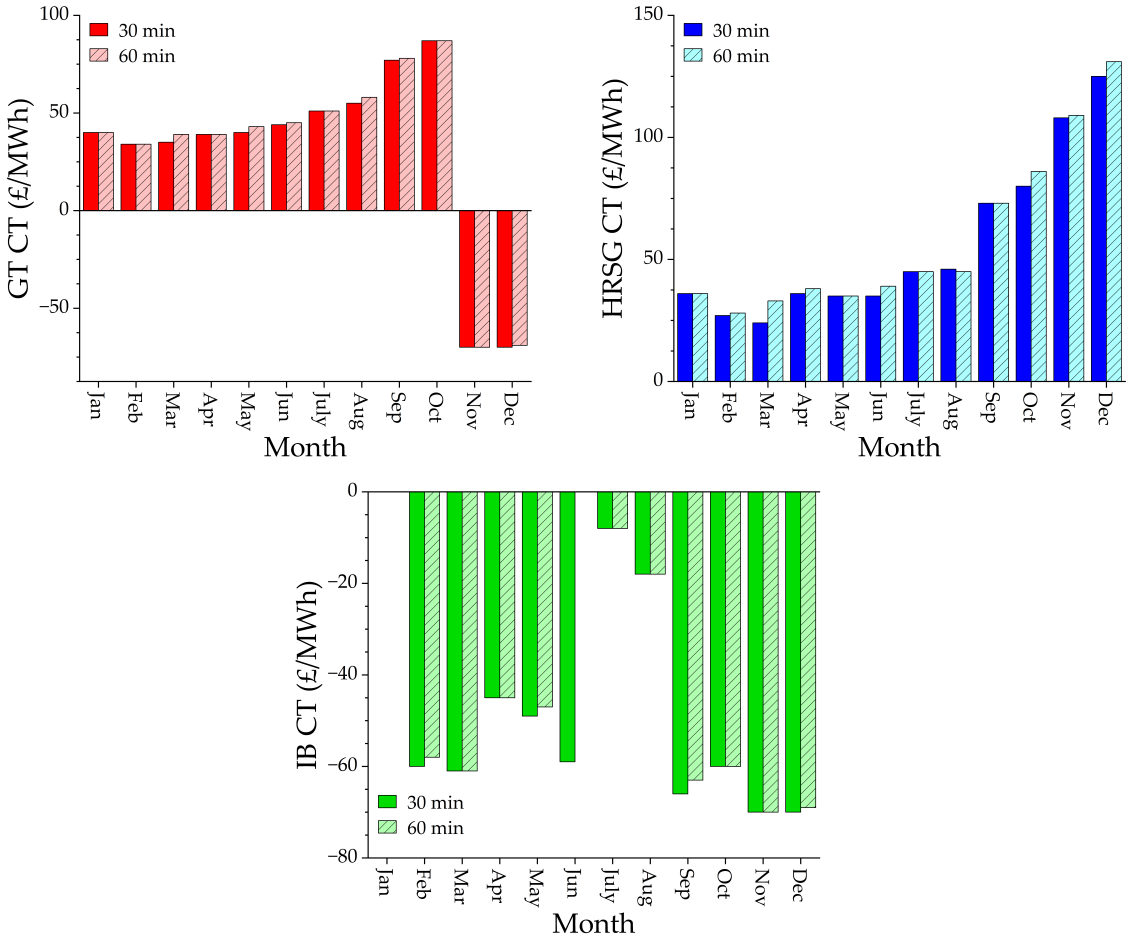


Figure 5.33: Charge Trigger variation per month in 2021 for GTs, HRSGs, and IBs optimised over 30 minute and 60 minute SPs, under the fuel displacement model.

When the goal is to optimise profits using arbitrage, the previously discussed months of November and December proved particularly profitable. Despite the increase in NG prices, the increased imbalance prices created an opportunity for arbitrage. By holding onto stored energy and only utilising it during periods of the highest SBPs, the UHTS system could maximise profits. Consequently, the utilisation of a UHTS system discharging was strategically low during this period, as the model optimised for the most profitable discharge times. This highlights the importance of timing in leveraging UHTS for arbitrage, ensuring that stored energy is used most economically.

5.5.7 Recommendations for Model Development

This section outlines proposed enhancements to the existing model based on the analysis results. These recommendations aim to address identified limitations and expand the model's capabilities.

Firstly, the interactions with external data can be enhanced. By allowing the model to read

the output data from previous optimisations, it may carry over the final store charge from one month to be used as initial conditions in the subsequent month. This modification will enable the model to maintain continuity over longer periods without losing the benefits of a detailed dataset. This would facilitate the development of a daily optimisation model currently prevented by the initialisation process.

Further analysis should also be conducted using a wider range of TES systems. Adjusting parameters such as store capacity, self-discharge rates, and temperature constraints, in addition to seasonally adapting operational hours, will provide insights into the adaptability of the model. This may be further developed to optimise TES system designs to align with specific discharge system requirements.

In conjunction with this, the current fuel displacement model does not simulate simultaneous charging and discharging. Although this scenario is impractical as it would likely be cheaper to directly heat the air with electricity, spatial constraints at deployment sites may only allow for one system to be installed. In these situations, the model could account for the use of the UHTS system as an alternative.

Incorporating the remaining future energy scenarios from the National Grid predictions will allow for a comprehensive assessment of the UHTS system across various potential energy networks. This approach will produce a broader dataset, likely containing accurate future UK energy system predictions up to 2050, enhancing confidence in the model's applicability and accuracy.

To improve the optimization process's effectiveness, a refinement of the precision of CT and DT values from £1 to £0.01 can be incorporated. This adjustment will enable the model to capture a wider array of charge and discharge scenarios, thus optimising the model to a greater extent. However, this change will necessitate a significant increase in computational resources due to the increase in the number of required iterations for data set optimisation. This would not be required in this case as the minimal change in accuracy would not justify the increased expense. However, if this model were to be used in industry, the potential increase in profitability may be justified.

These recommendations address specific areas for development within the model, enhancing its accuracy, applicability, and utility in the prediction of the economic viability of a UHTS system.

5.6 Summary of Economic Feasibility

This chapter provides insights into the economic viability and environmental impact of integrating UHTS systems into pre-existing thermal generators, operating within the UK energy market. Through techno-economic modelling, the potential of UHTS systems to both produce a profit and contribute to the decarbonisation of the energy sector has been quantified.

The development of the bottom-up techno-economic model allowed for the evaluation of UHTS deployment. This approach allowed for the technical parameters of both the UHTS system and three thermal generation systems to be accounted for. Due to the nature of the model, these parameters are easily adapted to apply to a range of global markets.

The results highlight the influence of market-driven mechanisms, such as carbon and NG

pricing, and electricity price volatility, on the operational strategies of UHTS systems. By leveraging periods of low electricity prices for charging and high prices for discharging, UHTS systems can achieve profitable arbitrage. Furthermore, the displacement of fossil fuels with UHTS systems not only produces operational cost savings but also significantly reduces CO_2 emissions, aligning with the UK's decarbonisation goals.

The outcomes highlight that UHTS systems could provide an average monthly arbitrage profitability of up to £2,225,000, underlining their financial viability within the current and projected energy market scenarios. Additionally, CO_2 emission reductions achieved through the deployment of UHTS systems are estimated to be up to an average of 33,900 tonnes monthly, contributing significantly to the UK's commitment to reduce GHG emissions by 2050.

The results from the simulation of UHTS operation reveal the system is able to flexibly adapt to changing market conditions, ensuring economic viability and environmental benefits over time. Moreover, the research highlights the necessity for policy support and market mechanisms that encourage the deployment of ES technologies.

The chapter emphasises the potential of UHTS systems as an economically viable solution for retrofitting into current infrastructure. By optimising operational strategies, UHTS systems can significantly contribute to the UK's energy resilience, economic competitiveness, and climate objectives. Future research should focus on expanding the applicability of the model, covering a wider range of energy systems, storage technologies and optimisation tools.

Chapter 6

Conclusion

This thesis explored the integration of Ultra-High Temperature Thermal Energy Storage (UHTS) systems into generation technologies that are currently part of the UK energy network. As the UK transitions towards a low-carbon system, integrating energy storage into the network can play a crucial role in balancing supply and demand, mitigating the variability of renewable energy sources (RES), and supporting decarbonisation.

A review of current energy storage technologies identified UHTS as a key technology in enabling a reliable energy supply, built around renewably generated energy. Novel approaches to integrating UHTS systems into the UK energy network are presented. The store enables an increase in the penetration of RES into the grid by storing excess energy at times of high demand, transitioning it from an intermittent to a dispatchable resource. This is achieved via discharge through existing thermal generation infrastructure, reducing reliance on fossil fuels, through integration into proven, pre-existing technologies.

Through computational models and quantitative analysis, the feasibility of retrofitting thermally driven systems such as gas turbines (GTs), heat recovery steam generators (HRSGs), and industrial boilers (IBs) with UHTS systems was assessed, highlighting significant improvements in environmental performance, operational efficiency and economic potential.

6.1 Key Findings

Key findings from the study include:

- Highlighted the advantages of integrating UHTS into existing infrastructure over establishing standalone storage systems. This strategy not only exploits the high energy density and low capital costs but also suits the geographical flexibility of the UHTS system. This allows for a reduction in the capital expenditure associated with storage deployment by approximately 50 %, compared to independent systems.
- Demonstrated the practicality of retrofitting HRSGs with UHTS is shown to be feasible, outlining the potential for additional heat to be incorporated via flow augmentation. This process enables the thermal augmentation of GT exhaust gases, increasing the flow temperature and, consequently, the overall system output, whilst maintaining the structural integrity of the HRSG by producing suitable flow characteristics.

- Identified significant improvements in fuel efficiency through the retrofitting of existing GTs with UHTS. This integration has been shown to facilitate up to 88.9 % fuel displacement while maintaining constant thermal output.
- Evaluated the environmental benefits of incorporating UHTS within GT combustion chambers, demonstrating a substantial reduction in emissions. The application of UHTS for fuel displacement has been found to decrease NOx emissions by 93.8 %, CO emissions by 98.6 %, and CO_2 emissions by 86.6 %.
- Quantified the benefits of UHTS integration using real market data. A thermal generator retrofitted with UHTS may achieve an average monthly arbitrage profitability of up to £2,225,000 when optimised for maximum profitability. Additionally, optimisation for fuel displacement can lead to a monthly carbon emission reduction of 33,900 tonnes.
- Outlined the future cost-effectiveness and economic incentives for adopting UHTS technology, considering its impact on reducing operational costs and enhancing system profitability. Projections based on future market trends indicate that UHTS integration will continue to yield arbitrage profits and carbon tax savings until at least 2050.
- Illustrated the adaptability of UHTS technology for the current energy infrastructure, demonstrating its financial viability for GTs, HRSGs, and IBs, each with their unique technical parameters.

These results display the capability of the UHTS to contribute significantly to the UK's energy sustainability goals, providing a reliable method for dispatching stored renewable energy and minimising industrial carbon emissions, whilst producing economic benefits.

6.2 Future Work

Based on the research conducted, several avenues for future research to further advance UHTS technology and its integration into the UK's energy system are highlighted. These are:

- Refining the HRSG CFD model, substituting porous zones with heat exchangers, allowing for the quantification of the potential boost in output from the integration of a UHTS system.
- Integrating flow control technologies into the HRSG geometry to optimise downstream flow conditions further, leading to more beneficial flow regimes for a full replacement system.
- Increasing the variability of inlet flow conditions to a GT combustion chamber to account for more complex integration scenarios and operational conditions, widening the relevance of the model outputs.
- Exploring the development of advanced materials and technologies to enhance pre-existing systems to improve their compatibility with UHTS discharge conditions by addressing the challenges of material resilience.

- Conducting pilot projects to validate the computational findings with empirical evidence, and assess the practical feasibility and operational benefits of UHTS in industrial settings.
- Enhancing the applicability of the techno-economic model by incorporating additional data, improving initialisation processes and including further optimisation methodologies.
- Conducting in-depth economic analyses to assess the long-term financial viability of UHTS integration across various future energy grid scenarios to provide a broader picture of UHTS potential.
- Investigating the integration of UHTS with a wider array of industrial processes, beyond the current focus on GTs, HRSGs and IBs such as Fluidised Bed combustion for power generation, or more specific industrial applications, such as cement production.

This further work would allow for increased confidence in the deployment of UHTS, further developing an understanding of both the technical and economic aspects of this emerging technology.

The findings from this thesis contribute valuable insights into the role of UHTS in transitioning towards a more sustainable energy system. As the UK increasingly relies on RES generation and process electrification, UHTS technologies stand out as a promising solution for enhancing grid resilience in a RES-led energy system.

It is demonstrated that UHTS integration is able to enhance the thermal efficiency and environmental sustainability of current power generation and industrial processes. As a result, it can prolong the life cycles of sunk assets, which may otherwise be phased out. Given the UK's commitment to achieving net-zero emissions by 2050, and the necessity to address climate change, UHTS systems are demonstrated to have the potential to be a critical technology in the transition towards a low-carbon energy system.

The author hopes this research lays the foundation for further advancements around the integration of UHTS technologies into sunk thermal assets, encouraging policy and economic changes that foster an energy system which aligns with international climate goals.

Bibliography

P. M. Forster, C. J. Smith, T. Walsh, W. F. Lamb, R. Lamboll, M. Hauser, A. Ribes, D. Rosen, N. Gillett, M. D. Palmer, J. Rogelj, K. Von Schuckmann, S. I. Seneviratne, B. Trewin, X. Zhang, M. Allen, R. Andrew, A. Birt, A. Borger, T. Boyer, J. A. Broersma, L. Cheng, F. Dentener, P. Friedlingstein, J. M. Gutiérrez, J. Gütschow, B. Hall, M. Ishii, S. Jenkins, X. Lan, J. Y. Lee, C. Morice, C. Kadow, J. Kennedy, R. Killick, J. C. Minx, V. Naik, G. P. Peters, A. Pirani, J. Pongratz, C. F. Schleussner, S. Szopa, P. Thorne, R. Rohde, M. Rojas Corradi, D. Schumacher, R. Vose, K. Zickfeld, V. Masson-Delmotte, P. Zhai, Indicators of Global Climate Change 2022: Annual update of large-scale indicators of the state of the climate system and human influence, Earth System Science Data 15 (2023) 2295–2327.

D. Lüthi, M. Le Floch, B. Bereiter, T. Blunier, J.-M. Barnola, U. Siegenthaler, D. Raynaud, J. Jouzel, H. Fischer, K. Kawamura, T. F. Stocker, High-resolution carbon dioxide concentration record 650,000–800,000years before present, Nature 453 (2008) 379–382.

The Royal Society, Climate change: A summary of the science, The Royal Society (2010) 16.

Y. Liu, S. Goodrick, M. Williams, A. Zhang, Climate change and variability overview, Future Forests: Mitigation and Adaptation to Climate Change (2024) 7–48.

K. Cobourn, Climate change adaptation policies to foster resilience in agriculture: Analysis and stocktake based on UNFCCC reporting documents, Technical Report, 2023. doi:10.1787/5fa2c770-en.

G. Durand, M. R. van den Broeke, G. Le Cozannet, T. L. Edwards, P. R. Holland, N. C. Jourdain, B. Marzeion, R. Mottram, R. J. Nicholls, F. Pattyn, F. Paul, A. B. Slangen, R. Winkelmann, C. Burgard, C. J. van Calcar, J. B. Barré, A. Bataille, A. Chapuis, Sea-Level Rise: From Global Perspectives to Local Services, Frontiers in Marine Science 8 (2022).

R. D. Semba, S. Askari, S. Gibson, M. W. Bloem, K. Kraemer, The Potential Impact of Climate Change on the Micronutrient-Rich Food Supply, Advances in Nutrition 13 (2022) 80–100.

DEFRA, Air Pollution in the UK 2016, Technical Report, 2017. URL: www.nationalarchives.gov.uk/doc/open-government-licence/version/3/.

Office for Health Improvement & Disparities, Air pollution: applying All Our Health, 2022. URL: https://www.gov.uk/government/publications/air-pollution-applying-all-our-health/air-pollution-applying-all-our-health.

F. Kelly, Associations of long-term term average concentrations of nitrogen dioxide with mortality, Technical Report, Committee on the Medical Effects of Air Pollutants, 2018. URL: https://assets.publishing.service.gov.uk/government/uploads/system/uploads/attachment_data/file/734799/COMEAP_NO2_Report.pdf.

E. Foster, M. Contestabile, J. Blazquez, B. Manzano, M. Workman, N. Shah, The unstudied barriers to widespread renewable energy deployment: Fossil fuel price responses, Energy Policy 103 (2017) 258–264.

EIA, Energy Prices by Sector and Source, 2018. URL: https://www.eia.gov/outlooks/aeo/data/browser/#/?id=3-AEO2018&region=1-0&cases=ref2018&start=2016&end=2050&f=A&linechart=ref2018-d121317a.36-3-AEO2018.1-0~ref2018-d121317a.37-3-AEO2018.1-0~ref2018-d121317a.38-3-AEO2018.1-0~ref2018-d121317a.39-3-AEO2018.1-.

A. Seely, Climate change levy, Technical Report, 2009. URL: http://www.hm-treasury.gov.uk/d/EconomicInstruments.pdf.

United Nations, Kyoto Protocol to the United Nations Framework, Technical Report, 1998. URL: https://unfccc.int/resource/docs/convkp/kpeng.pdf.

United Nations, Doha Amendment to the Kyoto Protocol, Technical Report, 2012. URL: https://treaties.un.org/doc/Publication/CN/2012/CN.718.2012-Eng.pdf.

UNFCCC, ADOPTION OF THE PARIS AGREEMENT, 2015.

UNFCCC, Glasgow Climate Pact, Technical Report, United Nations, Glasgow, 2021. URL: https://www.ipcc.ch/report/ar6/wg1/.

COP, The UAE Consensus, 2024.

S. Oberthur, H. Ott, The Kyoto Protocol : International climate policy for the 21st century, Springer, 1999. URL: https://books.google.co.uk/books?hl=en&lr=&id=-qp7Wt9GvccC&oi=fnd&pg=PA1&dq=kyoto+protocol&ots=ZHFNlzaFNH&sig=3k4Jag-QJqome80csQ4iXcoyXEI#v=onepage&q=common%20but&f=false.

M. J. Bortscheller, Equitable But Ineffective: How The Principle Of Common But Differentiated Responsibilities Hobbles The Global Fight Against Climate Change, Sustainable Development Law & Policy 10 (2010).

Department of Energy & Climate Change, 2010 UK Greenhouse Gas Emissions, Final Figures, Technical Report, 2012. URL: https://assets.publishing.service.gov.uk/government/uploads/system/uploads/attachment_data/file/408063/2012_Final_UK_greenhouse_gas_emissions_national_statistics_1990-2010.pdf.

UK Parliament, The Climate Change Act 2008, s.1, 2008.

M. Bell, O. Bellamy, A. Gault, M. Hemsley, S. Smith, M. Thompson, J. Barrett, N. Pawar, P. Seera, S. Taylor, S. Westlake, S. Wildeshaus, UK Climate action following the Paris Agreement - Committee on Climate Change - October 2016, Technical Report, Committee on Climate Change, 2016. URL: https://www.theccc.org.uk/wp-content/uploads/2016/10/UK-climate-action-following-the-Paris-Agreement-Committee-on-Climate-Change-October-2016.pdf.

E. . I. S. Department for Business, 2016 UK GREENHOUSE GAS EMISSIONS, FINAL FIGURES, Technical Report, 2018. URL: https://www.gov.uk/government/collections/final-.

V. Masson-Delmotte, P. Zhai, A. Pirani, S. Connors, C. Péan, S. Berger, N. Caud, Y. Chen, L. Goldfarb, M. Gomis, M. Huang, K. Leitzell, E. Lonnoy, J. Matthews, T. Maycock, T. Waterfield, O. Yelekçi, R. Yu, B. Zhou, Summary for Policymakers, in: Climate Change 2021 – The Physical Science Basis, Cambridge University Press, 2023, pp. 3–32. doi:10.1017/9781009157896.001.

V. Masson-Delmotte, P. Zhai, H. Pörtner, D. Roberts, J. Skea, P. Shukla, A. Pirani, W. Moufouma-Okia, C. Péan, R. Pidcock, S. Connors, J. Matthews, Y. Chen, X. Zhou, M. Gomis, E. Lonnoy, T. Maycock, M. Tignor, T. Waterfield, Summary for Policymakers. In: Global Warming of 1.5°C. An IPCC Special Report on the impacts of global warming of 1.5°C above pre-industrial levels and related global greenhouse gas emission pathways, in the context of strengthening the global response to the threat of climate change, sustainable development, and efforts to eradicate poverty, Technical Report, 2018. URL: www.environmentalgraphiti.orghttps://report.ipcc.ch/sr15/pdf/sr15_spm_final.pdf%0Ahttp://www.ipcc.ch/report/sr15/.

National Grid, Future Energy Scenarios 2023, Technical Report, National Grid, 2023. URL: www.nationalgrideso.com/future-energy/future-energy-scenarios.

BEIS, Electricity Networks Strategic Framework: Enabling a secure, net zero energy system, Technical Report, 2022.

Department for Energy Security and Net Zero, UK ENERGY IN BRIEF 2023, Technical Report, 2023. URL: https://www.gov.uk/government/organisations/department-for-energy-.

National Grid, Future Energy Scenarios, Energy (2019) 168.

L. Butcher, S. Hinson, D. Hirst, Electric vehicles and infrastructure, House of Commons Library (2018) 295–314.

E. . I. S. Department for Business, Updated energy and emissions projections 2021 to 2040, Technical Report, 2022. URL: https://www.gov.uk/government/collections/energy-and-emissions-projections.

C. Matson, J. Knighton, Renewable curtailment and the role of long duration storage, Technical Report, LCP, 2022.

L. Barelli, U. Desideri, A. Ottaviano, Challenges in load balance due to renewable energy sources penetration: The possible role of energy storage technologies relative to the Italian case, Energy 93 (2015) 393–405.

K. Wang, S. Chen, L. Liu, T. Zhu, Z. Gan, Enhancement of renewable energy penetration through energy storage technologies in a CHP-based energy system for Chongming, China, Energy 162 (2018) 988–1002.

M. C. Argyrou, P. Christodoulides, S. A. Kalogirou, Energy storage for electricity generation and related processes: Technologies appraisal and grid scale applications, Renewable and Sustainable Energy Reviews 94 (2018) 804–821.

J. Rouse, S. Garvey, B. Cárdenas, T. Davenne, A series hybrid "real inertia" energy storage system, Journal of Energy Storage 20 (2018) 1–15.

J. Fritzsch, P. Jacquod, A Novel Adaptive Inertia Strategy in Large-Scale Electric Power Grids, Electrical Engineering and Systems Science (2023).

P. Yang, A. Nehorai, Joint Optimization of Hybrid Energy Storage and Generation Capacity With Renewable Energy, IEEE Transactions on Smart Grid 5 (2014) 1566–1574.

M. Uddin, M. F. Romlie, M. F. Abdullah, S. Abd Halim, A. H. Abu Bakar, T. Chia Kwang, A review on peak load shaving strategies, Renewable and Sustainable Energy Reviews 82 (2018) 3323–3332.

M. N. DinAli, I. Dincer, Development and analysis of an integrated gas turbine system with compressed air energy storage for load leveling and energy management, Energy 163 (2018) 604–617.

Y. Hida, R. Yokoyama, J. Shimizukawa, K. Iba, K. Tanaka, T. Seki, Load following operation of NAS battery by setting statistic margins to avoid risks, in: IEEE PES General Meeting, IEEE, 2010, pp. 1–5. URL: `http://ieeexplore.ieee.org/document/5588170/`. doi:`10.1109/PES.2010.5588170`.

National Grid ESO, System Frequency, 2024. URL: `https://www.nationalgrideso.com/data-portal/system-frequency-data`.

X. Luo, J. Wang, M. Dooner, J. Clarke, Overview of current development in electrical energy storage technologies and the application potential in power system operation, Applied Energy 137 (2015) 511–536.

National Grid ESO, Historic GB Generation Mix, Technical Report, 2024.

L. Gao, J. Zhao, Z. Tang, A Review on Borehole Seasonal Solar Thermal Energy Storage, Energy Procedia 70 (2015) 209–218.

H. Blanco, A. Faaij, A review at the role of storage in energy systems with a focus on Power to Gas and long-term storage, 2018. doi:10.1016/j.rser.2017.07.062.

C. Rosenzweig, A. Iglesius, X. B. Yang, P. R. Epstein, E. Chivian, N. Lincoln Rosenzweig, Climate change and extreme weather events - Implications for food production, plant diseases, and pests Challenges to Food Production and Nutrition Current and future energy use from burning of fossil fuels and clearing of forests for cultivation can have, GLOBAL CHANGE & HUMAN HEALTH 2 (2001) 90–104.

K. Loukatou, Potential Electricity Storage Routes to 2050, Technical Report, National Grid, 2022. URL: https://www.nationalgrideso.com/document/273166/download.

BEIS, Evidence Gathering: Thermal Energy Storage (TES) Technologies, Renewable and Sustainable Energy Reviews 80 (2016) 1–85.

A. Robinson, Ultra-high temperature thermal energy storage. Part 1: Concepts, Journal of Energy Storage 13 (2017) 277–286.

A. Robinson, Ultra-high temperature thermal energy storage. Part 2: Engineering and operation, Journal of Energy Storage 18 (2018) 333–339.

E. Dlugokencky, P. Tans, ESRL Global Monitoring Division - Global Greenhouse Gas Reference Network, 2018. URL: https://www.esrl.noaa.gov/gmd/ccgg/trends.

K. T. Møller, T. R. Jensen, E. Akiba, H. w. Li, Hydrogen - A sustainable energy carrier, Progress in Natural Science: Materials International 27 (2017) 34–40.

G. F. Frate, L. Ferrari, U. Desideri, Energy storage for grid-scale applications: Technology review and economic feasibility analysis, Renewable Energy 163 (2021) 1754–1772.

K. R. Pullen, The Status and Future of Flywheel Energy Storage, Joule 3 (2019) 1394–1399.

A. G. Olabi, T. Wilberforce, M. A. Abdelkareem, M. Ramadan, Critical Review of Flywheel Energy Storage System, Energies 2021, Vol. 14, Page 2159 14 (2021) 2159.

A. Buchroithner, Bearings for Flywheel Energy Storage, Flywheel Energy Storage (2023) 227–282.

K. V. Rao, D. Rani, Natraj, Magnetic levitation for flywheel energy storage system, International Journal of Applied Engineering Research 10 (2015) 4110–4112.

K. Erhan, E. Özdemir, Prototype production and comparative analysis of high-speed flywheel energy storage systems during regenerative braking in hybrid and electric vehicles, Journal of Energy Storage 43 (2021) 103237.

N. S. Hasan, M. Y. Hassan, M. S. Majid, H. A. Rahman, Review of storage schemes for wind energy systems, Renewable and Sustainable Energy Reviews 21 (2013) 237–247.

O. P. Mahela, A. G. Shaik, Comprehensive overview of grid interfaced wind energy generation systems, Renewable and Sustainable Energy Reviews 57 (2016) 260–281.

R. Rounds, G. H. Peek, Design & Development of a 20-MW Flywheel-based Frequency Regulation Power Plant, Technical Report, Sandia, Albuquerque, 2009. URL: http://www.ntis.gov/help/ordermethods.asp?loc=7-4-0#online.

P. C. Nikolaos, F. Marios, K. Dimitris, A Review of Pumped Hydro Storage Systems, Energies 2023, Vol. 16, Page 4516 16 (2023) 4516.

N. Sivakumar, D. Das, N. P. Padhy, Variable speed operation of reversible pump-turbines at Kadamparai pumped storage plant – A case study, Energy Conversion and Management 78 (2014) 96–104.

G. Fuchs, B. Lunz, M. Leuthold, D. U. Sauer, Overview of Nonelectrochemical Storage Technologies, Electrochemical Energy Storage for Renewable Sources and Grid Balancing (2015) 89–102.

B. Lu, M. Stocks, A. Blakers, K. Anderson, Geographic information system algorithms to locate prospective sites for pumped hydro energy storage, Applied Energy 222 (2018) 300–312.

A. G. Olabi, T. Wilberforce, M. Ramadan, M. A. Abdelkareem, A. H. Alami, Compressed air energy storage systems: Components and operating parameters – A review, Journal of Energy Storage 34 (2021) 102000.

Energy Encylopedia, Compressed air energy storage, 2024. URL: https://www.energyencyclopedia.com/en/free-downloads/images/compressed-air-energy-storage-103.

N. Khan, S. Dilshad, R. Khalid, A. R. Kalair, N. Abas, Review of energy storage and transportation of energy, Energy Storage 1 (2019).

A. M. Rabi, J. Radulovic, J. M. Buick, Comprehensive Review of Compressed Air Energy Storage (CAES) Technologies, Thermo 2023, Vol. 3, Pages 104-126 3 (2023) 104–126.

M. Howitt, Gigawatt Scale Storage for Gigawatt Scale Renewables, Journal of Energy and Power Engineering 12 (2018).

C. Guo, C. Li, K. Zhang, Z. Cai, T. Ma, F. Maggi, Y. Gan, A. El-Zein, Z. Pan, L. Shen, The promise and challenges of utility-scale compressed air energy storage in aquifers, Applied Energy 286 (2021) 116513.

S. Kalaiselvam, R. Parameshwaran, Energy Storage, Thermal Energy Storage Technologies for Sustainability (2014) 21–56.

B. E. Conway, Electrochemical Supercapacitors, Electrochemical Supercapacitors (1999).

P. Simon, Y. Gogotsi, Materials for electrochemical capacitors, Nature Materials 2008 7:11 7 (2008) 845–854.

A. Schneuwly, R. Gallay, Properties and Applications of Supercapacitors From the State-of-the-art to Future Trends, 2000.

S. Kaenket, P. Suktha, K. Kongsawatvoragul, T. Sangsanit, P. Wuamprakhon, R. Songthan, W. Tejangkura, K. Santiyuk, K. Homlamai, M. Sawangphruk, Large-scale production of 18650 cylindrical supercapacitors: Effects of separators, electrode thickness, electrolyte additives, and testing protocols, Journal of Power Sources 581 (2023) 233512.

P. Skoglund, Grid connected large-scale energy storage, Ph.D. thesis, Umeå University, 2017.

P. Nikolaidis, A. Poullikkas, A comparative review of electrical energy storage systems for better sustainability, Journal of Power of Technologies (2017).

M. E. Amiryar, K. R. Pullen, A review of flywheel energy storage system technologies and their applications, 2017. doi:10.3390/app7030286.

A. A. Kebede, T. Kalogiannis, J. Van Mierlo, M. Berecibar, A comprehensive review of stationary energy storage devices for large scale renewable energy sources grid integration, Renewable and Sustainable Energy Reviews 159 (2022) 112213.

A. Evans, V. Strezov, T. J. Evans, Energy Storage Technologies, Encyclopedia of Sustainable Technologies (2024) 548–555.

Y. Iwasa, Case Studies in Superconducting Magnets, 2 ed., Springer US, 2009.

S. K. Hossain, M. E. Hoque, Polymer nanocomposite materials in energy storage: Properties and applications, Polymer-based Nanocomposites for Energy and Environmental Applications: A volume in Woodhead Publishing Series in Composites Science and Engineering (2018) 239–282.

N. Nitta, F. Wu, J. T. Lee, G. Yushin, Li-ion battery materials: present and future, Materials Today 18 (2015) 252–264.

J. Mitali, S. Dhinakaran, A. A. Mohamad, Energy storage systems: a review, Energy Storage and Saving 1 (2022) 166–216.

M. A. Rosen, A. Farsi, Battery system design, Battery Technology (2023) 161–198.

J. O. Park, M. Kim, J.-H. Kim, K. H. Choi, H. C. Lee, W. Choi, S. B. Ma, D. Im, A 1000 Wh kg-1 Li-Air battery: Cell design and performance, Journal of Power Sources 419 (2019) 112–118.

A. Ulvestad, A Brief Review of Current Lithium Ion Battery Technology and Potential Solid State Battery Technologies, Technical Report, 2019. URL: https://arxiv.org/ftp/arxiv/papers/1803/1803.04317.pdf.

A. Jaradat, C. Zhang, K. Singh, J. Ahmed, A. Ahmadiparidari, L. Majidi, S. Rastegar, Z. Hemmat, S. Wang, A. T. Ngo, L. A. Curtiss, M. Daly, A. Subramanian, A. Salehi-Khojin, A. Jaradat, C. Zhang, S. K. Singh, A. Ahmadiparidari, L. Majidi, S. Rastegar, Z. Hemmat, S. Wang, A. Subramanian, A. Salehi-Khojin, A. T. Ngo, L. A. Curtiss, J. Ahmed, M. Daly, High Performance Air Breathing Flexible Lithium–Air Battery, Small 17 (2021) 2102072.

Z. Liang, W. Wang, Y. C. Lu, The path toward practical Li-air batteries, Joule 6 (2022) 2458–2473.

S. T. Revankar, Chemical Energy Storage, Storage and Hybridization of Nuclear Energy: Techno-economic Integration of Renewable and Nuclear Energy (2019) 177–227.

A. Ashok, A. Kumar, A comprehensive review of metal-based redox flow batteries: progress and perspectives, Green Chemistry Letters and Reviews 17 (2024).

C. N. Sun, M. M. Mench, T. A. Zawodzinski, High Performance Redox Flow Batteries: An Analysis of the Upper Performance Limits of Flow Batteries Using Non-aqueous Solvents, Electrochimica Acta 237 (2017) 199–206.

G. Kear, A. A. Shah, F. C. Walsh, Development of the all-vanadium redox flow battery for energy storage: a review of technological, financial and policy aspects, International Journal of Energy Research 36 (2012) 1105–1120.

L. Li, S. Kim, W. Wang, M. Vijayakumar, Z. Nie, B. Chen, J. Zhang, G. Xia, J. Hu, G. Graff, J. Liu, Z. Yang, A stable vanadium redox-flow battery with high energy density for large-scale energy storage, Advanced Energy Materials 1 (2011) 394–400.

M. G. . A. . Allam, M. A. . Abdelkareem, T. D. . Deepa, A. H. . Alami, Q. . Abbas, A. . Alkhalidi, A. Ghani Olabi, M. A. Allam, M. A. Abdelkareem, T. D. Deepa, A. H. Alami, Q. Abbas, A. Alkhalidi, E. T. Sayed, Redox Flow Batteries: Recent Development in Main Components, Emerging Technologies, Diagnostic Techniques, Large-Scale Applications, and Challenges and Barriers, Batteries 2023, Vol. 9, Page 409 9 (2023) 409.

S. G. Nnabuife, C. K. Darko, P. C. Obiako, B. Kuang, X. Sun, K. Jenkins, A Comparative Analysis of Different Hydrogen Production Methods and Their Environmental Impact, Clean Technologies 2023, Vol. 5, Pages 1344-1380 5 (2023) 1344–1380.

M. Fallah Vostakola, H. Ozcan, R. S. El-Emam, B. Amini Horri, Recent Advances in High-Temperature Steam Electrolysis with Solid Oxide Electrolysers for Green Hydrogen Production, Energies 2023, Vol. 16, Page 3327 16 (2023) 3327.

P. Breeze, Hydrogen Energy Storage, Power System Energy Storage Technologies (2018) 69–77.

O. Posdziech, K. Schwarze, J. Brabandt, Efficient hydrogen production for industry and electricity storage via high-temperature electrolysis, International Journal of Hydrogen Energy (2018).

K. Schwarze, O. Posdziech, S. Kroop, N. Lapeña-Rey, J. Mermelstein, Green Industrial Hydrogen via Reversible High-Temperature Electrolysis, in: ECS Transactions, 2017. URL: `http://ecst.ecsdl.org/content/78/1/2943.full.pdf`. doi:`10.1149/07801.2943ecst`.

A. Amid, D. Mignard, M. Wilkinson, Seasonal storage of hydrogen in a depleted natural gas reservoir, International Journal of Hydrogen Energy 41 (2016) 5549–5558.

S. Z. Al Ghafri, S. Munro, U. Cardella, T. Funke, W. Notardonato, J. P. Trusler, J. Leachman, R. Span, S. Kamiya, G. Pearce, A. Swanger, E. D. Rodriguez, P. Bajada, F. Jiao, K. Peng, A. Siahvashi, M. L. Johns, E. F. May, Hydrogen liquefaction: a review of the fundamental physics, engineering practice and future opportunities, Energy & Environmental Science 15 (2022) 2690–2731.

T. Zhang, J. Uratani, Y. Huang, L. Xu, S. Griffiths, Y. Ding, Hydrogen liquefaction and storage: Recent progress and perspectives, Renewable and Sustainable Energy Reviews 176 (2023) 113204.

H. Shao, Heat modeling and material development of Mg-based nanomaterials combined with solid oxide fuel cell for stationary energy storage, Energies 10 (2017) 1–11.

Y. Wang, Y. Wang, Recent advances in additive-enhanced magnesium hydride for hydrogen storage, Progress in Natural Science: Materials International 27 (2017) 41–49.

Office of Energy Efficiency & Renewable Energy, Comparison of Fuel Cell Technologies | Department of Energy, 2018. URL: `https://www.energy.gov/eere/fuelcells/comparison-fuel-cell-technologies`.

E. Soleymani, S. Ghavami Gargari, H. Ghaebi, Thermodynamic and thermoeconomic analysis of a novel power and hydrogen cogeneration cycle based on solid SOFC, Renewable Energy 177 (2021) 495–518.

M. Alhuyi Nazari, M. Fahim Alavi, M. Salem, M. E. H. Assad, Utilization of hydrogen in gas turbines: a comprehensive review, International Journal of Low-Carbon Technologies 17 (2022) 513–519.

J. F. González Álvarez, S. Sahota, L. Lombardi, Study on fuel flexibility of a medium size gas turbine fueled by different hydrogen-based fuels from biowaste as possible alternatives to natural gas, Environmental Research 250 (2024) 118399.

P. Chiesa, G. Lozza, L. Mazzocchi, Using Hydrogen as Gas Turbine Fuel, Journal of Engineering for Gas Turbines and Power 127 (2005) 73–80.

D. Prakash, Hydrogen for Large-scale Electricity Generation in USA, Technical Report, 2011. URL: `www.geni.orgpeter@geni.org`. doi:`10.1016/j.chroma.2005.02.013`.

H. Sadeghi, R. Jalali, R. M. Singh, A review of borehole thermal energy storage and its integration into district heating systems, Renewable and Sustainable Energy Reviews 192 (2024).

Y. Zhao, C. Zhao, T. Wen, C. N. Markides, High Temperature Sensible Storage—Industrial Applications, Encyclopedia of Energy Storage: Volume 1-4 1-4 (2022) 424–432.

L. Seyitini, B. Belgasim, C. C. Enweremadu, Solid state sensible heat storage technology for industrial applications – A review, Journal of Energy Storage 62 (2023) 106919.

T. B. Umate, P. D. Sawarkar, A review on thermal energy storage using phase change materials for refrigerated trucks: Active and passive approaches, Journal of Energy Storage 75 (2024) 109704.

S. Riahi, M. Liu, R. Jacob, M. Belusko, F. Bruno, Assessment of exergy delivery of thermal energy storage systems for CSP plants: Cascade PCMs, graphite-PCMs and two-tank sensible heat storage systems, Sustainable Energy Technologies and Assessments 42 (2020) 100823.

R. Vijjapu, S. Tiwari, Thermodynamics of Sensible Thermal Energy Storage Systems, Encyclopedia of Energy Storage: Volume 1-4 1-4 (2022) 171–185.

M. S. Guney, Solar power and application methods, Renewable and Sustainable Energy Reviews 57 (2016) 776–785.

W. A. K. Al-Maliki, F. Alobaid, V. Kez, B. Epple, Modelling and dynamic simulation of a parabolic trough power plant, Journal of Process Control 39 (2016) 123–138.

T. Bauer, C. Odenthal, A. Bonk, Molten Salt Storage for Power Generation, Chemie Ingenieur Technik 93 (2021) 534–546.

M. Cascetta, M. Petrollese, J. Oyekale, G. Cau, Thermocline vs. two-tank direct thermal storage system for concentrating solar power plants: A comparative techno-economic assessment, International Journal of Energy Research 45 (2021) 17721–17737.

J. Parham, P. Vrettos, N. Levinson, Commercialisation of ultra-high temperature energy storage applications: the 1414 Degrees approach, Ultra-High Temperature Thermal Energy Storage, Transfer and Conversion (2021) 331–346.

C. Prieto, L. F. Cabeza, M. C. Pavón-Moreno, E. Palomo, Thermal energy storage for direct steam generation concentrating solar power plants: Concept and materials selection, Journal of Energy Storage 83 (2024) 110618.

D. S. Jayathunga, H. P. Karunathilake, M. Narayana, S. Witharana, Phase change material (PCM) candidates for latent heat thermal energy storage (LHTES) in concentrated solar power (CSP) based thermal applications - A review, Renewable and Sustainable Energy Reviews 189 (2024) 113904.

S. Kahwaji, M. B. Johnson, A. C. Kheirabadi, D. Groulx, M. A. White, A comprehensive study of properties of paraffin phase change materials for solar thermal energy storage and thermal management applications, Energy 162 (2018) 1169–1182.

S. S. Magendran, F. S. A. Khan, N. M. Mubarak, M. Vaka, R. Walvekar, M. Khalid, E. C. Abdullah, S. Nizamuddin, R. R. Karri, Synthesis of organic phase change materials (PCM) for energy storage applications: A review, Nano-Structures & Nano-Objects 20 (2019) 100399.

C. Li, Q. Li, X. Lu, R. Ge, Y. Du, Y. Xiong, Inorganic salt based shape-stabilized composite phase change materials for medium and high temperature thermal energy storage: Ingredients selection, fabrication, microstructural characteristics and development, and applications, Journal of Energy Storage 55 (2022) 105252.

O. M. Adesusi, O. R. Adetunji, S. I. Kuye, A. I. Musa, T. J. Erinle, O. B. Gbadamosi-Olatunde, S. O. Ipadeola, A comprehensive review of the materials degradation phenomena in solid-liquid phase change materials for thermal energy storage, International Journal of Thermofluids 18 (2023) 100360.

S. C. Costa, M. Kenisarin, A review of metallic materials for latent heat thermal energy storage: Thermophysical properties, applications, and challenges, Renewable and Sustainable Energy Reviews 154 (2022) 111812.

M. Sun, T. Liu, H. Sha, M. Li, T. Liu, X. Wang, G. Chen, J. Wang, D. Jiang, A review on thermal energy storage with eutectic phase change materials: Fundamentals and applications, Journal of Energy Storage 68 (2023) 107713.

Q. Peng, J. Ding, X. Wei, G. Jiang, The Release Properties of Nitrogen Oxides of Solar Salt Used for Thermal Energy Storage in Different Environment, Energy Procedia 105 (2017) 4420–4427.

A. Tafone, E. Borri, L. F. Cabeza, A. Romagnoli, Innovative cryogenic Phase Change Material (PCM) based cold thermal energy storage for Liquid Air Energy Storage (LAES) – Numerical dynamic modelling and experimental study of a packed bed unit, Applied Energy 301 (2021) 117417.

IRENA, Electricity storae and renewables : costs and markets to 2030, 2017.

L. I. Asri, W. N. Ariffin, A. S. Zain, J. Nordin, N. S. Saad, Comparative Study of Energy Storage Systems (ESSs), in: Journal of Physics: Conference Series, volume 1962, IOP Publishing Ltd, 2021. doi:10.1088/1742-6596/1962/1/012035.

N. Rogalev, A. Rogalev, V. Kindra, V. Naumov, I. Maksimov, Comparative Analysis of Energy Storage Methods for Energy Systems and Complexes, Energies 2022, Vol. 15, Page 9541 15 (2022) 9541.

S. . Saha, P. K. . Basu, J. B. . Ustun, L. Hernández-Callejo, A. Aguilar Jiménez, C. Meza Benavides, M. R. Chakraborty, S. Dawn, P. K. Saha, J. B. Basu, T. Selim Ustun, A Comparative Review on Energy Storage Systems and Their Application in Deregulated Systems, Batteries 2022, Vol. 8, Page 124 8 (2022) 124.

F. Söderström, Energy Storage Technology Comparison From a Swedish perspective, Technical Report, 2016.

A. Datas, A. Ramos, A. Martí, C. del Cañizo, A. Luque, Ultra high temperature latent heat energy storage and thermophotovoltaic energy conversion, Energy 107 (2016) 542–549.

J. Chiu, Thermal Energy Storage Latent Heat Storage Part 1, 2020.

IRENA, INNOVATION OUTLOOK THERMAL ENERGY STORAGE, Technical Report, 2020. URL: www.irena.org.

A. Sánchez, Q. Zhang, M. Martín, P. Vega, Towards a new renewable power system using energy storage: An economic and social analysis, Energy Conversion and Management 252 (2022) 115056.

M. S. Ziegler, J. M. Mueller, G. D. Pereira, J. Song, M. Ferrara, Y. M. Chiang, J. E. Trancik, Storage Requirements and Costs of Shaping Renewable Energy Toward Grid Decarbonization, Joule 3 (2019) 2134–2153.

Schumacher, Maximilian, ETES: Electric Thermal Energy Storage How thermal power plants can benefit from the energy transition, Technical Report, Siemens Gamesa, 2019.

US Energy Information Administration, Cost and Performance Characteristics of New Generating Technologies, Annual Energy Outlook 2022, Technical Report, 2022.

Rondo Energy, How It Works — Rondo Energy, 2024. URL: https://rondo.com/how-it-works.

I. Dincer, M. A. Rosen, Recent Advances in TES Methods, Technologies, and Applications, in: Thermal Energy Storage, John Wiley & Sons, Ltd, 2010, pp. 483–583. URL: https://onlinelibrary.wiley.com/doi/abs/10.1002/9780470970751.ch9. doi:https://doi.org/10.1002/9780470970751.ch9.

H. Zhang, J. Baeyens, G. Cáceres, J. Degrève, Y. Lv, Thermal energy storage: Recent developments and practical aspects, Progress in Energy and Combustion Science 53 (2016) 1–40.

B. C. Wyatt, S. K. Nemani, G. E. Hilmas, E. J. Opila, B. Anasori, Ultra-high temperature ceramics for extreme environments, Nature Reviews Materials (2023).

J. Run, J. Huang, Development of Ultra-High-Pressure, High- and Low-Temperature Seals for Cage Throttle Valves, Journal of Failure Analysis and Prevention 23 (2023) 2351–2361.

Antora Energy, Technology — Antora Energy, 2024. URL: https://antoraenergy.com/technology.

Exergy3, Technology, 2024. URL: https://www.exergy3.com/technology.

C. C. Kelsall, Design Challenges for Ultra-High-Temperature Energy Storage with Thermophotovoltaics, Ph.D. thesis, 2023.

I. Dincer, Exergy, Comprehensive Energy Systems: Volumes 1-5 (2018) 1–212.

J. Horlock, Advanced Gas Turbine Cycles, 2003. URL: http://www.sciencedirect.com:5070/book/9780080442730/advanced-gas-turbine-cycles.

G. Rogers, Y. Mayhew, Engineering Thermodynamics: Work and Heat Transfer, 4 ed., Longman Scientific & Technical, 1992. URL: https://research-information.bris.ac.uk/en/publications/engineering-thermodynamics-work-and-heat-transfer-4th-edition.

R. Kehlhofer, Combined-cycle gas and steam turbine power plants, 3 ed., Lilburn, GA (US); Fairmont Press, Inc., 1999.

M. J. Moran, H. N. Shapiro, D. D. Boettner, M. B. Bailey, Fundamentals of Engineering Thermodynamics, 9 ed., 2018. URL: https://www.wiley.com/en-us/Fundamentals+of+Engineering+Thermodynamics%2C+9th+Edition-p-9781119391388.

S. Quoilin, M. V. D. Broek, S. Declaye, P. Dewallef, V. Lemort, Techno-economic survey of organic rankine cycle (ORC) systems, 2013. doi:10.1016/j.rser.2013.01.028.

Siemens Gamesa, Energy storage recharges the transition I Siemens Gamesa, 2019. URL: https://www.siemensgamesa.com/explore/innovations/energy-storage-on-the-rise.

I. Dincer, Energy and Exergy Efficiencies, Comprehensive Energy Systems: Volumes 1-5 (2018) 1–265.

J. Inumaru, S. Hara, T. Hasegawa, Future perspective and remarks, Elsevier, 2021. URL: http://www.sciencedirect.com:5070/book/9780128203606/advances-in-power-boilers. doi:10.1016/B978-0-12-820360-6.00010-2.

R. Noroozian, P. Asgharian, Microturbine Generation Power Systems, in: Distributed Generation Systems, Elsevier, 2017, pp. 149–219. doi:10.1016/B978-0-12-804208-3.00004-2.

E. Kosieniak, K. Biesiada, J. Kaczorowski, M. Innocenti, Corrosion failures in gas turbine hot components, Journal of Failure Analysis and Prevention 12 (2012) 330–337.

M. P. Boyce, Gas Turbine Engineering Handbook, 4 ed., Elsevier, 2011. URL: http://www.sciencedirect.com:5070/book/9780123838421/gas-turbine-engineering-handbook. doi:10.1016/C2009-0-64242-2.

V. Dostal, M. J. Driscoll, P. Hejzlar, Advanced Nuclear Power Technology Program, Technical Report, 2004. URL: http://web.mit.edu/canes/.

T. Adefarati, R. C. Bansal, Energizing Renewable Energy Systems and Distribution Generation, Pathways to a Smarter Power System (2019) 29–65.

P. Deshmukh, S. Kasar, N. Sapkal, Experimental study of heat transfer in a helical coiled tube biomass fired rotary device, Journal of Thermal Engineering 8 (2022) 772–785.

M. J. S. Zuberi, A. Hasanbeigi, W. Morrow, Electrification of industrial boilers in the USA: potentials, challenges, and policy implications, Energy Efficiency 15 (2022) 1–28.

J. Saari, E. Sermyagina, J. Kaikko, M. Haider, M. Hamaguchi, E. Vakkilainen, Evaluation of the Energy Efficiency Improvement Potential through Back-End Heat Recovery in the Kraft Recovery Boiler, Energies 2021, Vol. 14, Page 1550 14 (2021) 1550.

N. K. M. N. A. Rahman, S. Saadon, M. H. C. Man, Waste Heat Recovery of Biomass Based Industrial Boilers by Using Stirling Engine, Journal of Advanced Research in Fluid Mechanics and Thermal Sciences 89 (2022) 1–12.

D. Nor Arifin, P. Riset Sumber Daya Geologi, B. Riset dan Inovasi Nasional, P. Riset Lingkungan dan Teknologi Bersih, Utilization of BCFS (Biomass Coal Fuel-Sludge) As Substitution of Energy Sources in Industrial Boilers, Procedia of Engineering and Life Science 4 (2023).

K. Piawanich, P. Aggarangsi, J. Moran, Modifications of SME Biomass Boiler for High Efficiency Multi-Fuel Input, Proceedings of the Conference on the Industrial and Commercial Use of Energy, ICUE 2018-October (2018).

J. Pan, X. Long, L. Zhang, A. Shoppert, D. Valeev, C. Zhou, X. Liu, The Discrepancy between Coal Ash from Muffle, Circulating Fluidized Bed (CFB), and Pulverized Coal (PC) Furnaces, with a Focus on the Recovery of Iron and Rare Earth Elements, Materials 2022, Vol. 15, Page 8494 15 (2022) 8494.

J. Moreda-Piñeiro, J. Sánchez-Piñero, M. Fernández-Amado, P. Costa-Tomé, N. Gallego-Fernández, M. Piñeiro-Iglesias, P. López-Mahía, S. Muniategui-Lorenzo, Evolution of gaseous and particulate pollutants in the air: What changed after five lockdown weeks at a southwest atlantic european region (northwest of spain) due to the sars-cov-2 pandemic?, Atmosphere 12 (2021) 562.

A. Datas, Ultra High Temperature Thermal Energy Storage for Dispatchable Power Generation, in: Encyclopedia of Energy Storage, Elsevier, 2022, pp. 141–150. doi:10.1016/B978-0-12-819723-3.00088-3.

Z. Huili, B. Jan, L. Shuo, D. Raf, D. Yimin, Power Generation upon Demand by Using Thermal Energy Storage in Concentrated Solar Power Plants: Recent Developments, in: 2021 5th International Conference on Power and Energy Engineering (ICPEE), IEEE, 2021, pp. 96–102. doi:10.1109/ICPEE54380.2021.9662531.

E. Crespi, D. Ragaglia, F. Panaccione, M. Testi, Control of a Solid Oxide Electrolysis system for hydrogen generation from solar power and thermal energy storage, in: 2023 International Conference on Clean Electrical Power (ICCEP), IEEE, 2023, pp. 765–774. doi:10.1109/ICCEP57914.2023.10247493.

P. F. Dobson, T. A. Atkinson, W. Jin, M. Acharya, D. Akindipe, B. Li, T. McLing, R. Kumar, Hybrid Uses of High-Temperature Reservoir Thermal Energy Storage: Lessons Learned from Previous Projects, in: Day 1 Tue, August 22, 2023, SPE, 2023. doi:10.2118/215750-MS.

J. Alzaili, A. I. Sayma, The Future of Gas Turbine Technology 8 th International Gas Turbine Conference 12-13, Technical Report, 2016. URL: http://openaccess.city.ac.uk/publications@city.ac.uk.

S. S. M. Shamsi, S. Maccarini, S. Trevisan, S. Barberis, R. E. Guedez Mata, sCO2 Based Pumped Heat Thermal Energy Storage Systems Valorizing Industrial Waste Heat Recovery: A Techno-Economic Analysis of the Role of High Temperature TES, in: Volume 6: Education; Electric Power; Energy Storage; Fans and Blowers, American Society of Mechanical Engineers, 2023. doi:10.1115/GT2023-103080.

C. Villada, W. Ding, A. Bonk, T. Bauer, Simulation-Assisted Determination of the Minimum Melting Temperature Composition of MgCl2–KCl–NaCl Salt Mixture for Next-Generation Molten Salt Thermal Energy Storage, Frontiers in Energy Research 10 (2022).

L. F. Cabeza, D. Vérez, G. Zsembinszki, E. Borri, C. Prieto, Key Challenges for High Temperature Thermal Energy Storage in Concrete—First Steps towards a Novel Storage Design, Energies 15 (2022) 4544.

R. Kunwer, S. Pandey, G. Pandey, Technical Challenges and Their Solutions for Integration of Sensible Thermal Energy Storage with Concentrated Solar Power Applications—a Review, Process Integration and Optimization for Sustainability 6 (2022) 559–585.

J. Mudi, C. K. Shiva, B. Vedik, V. Mukherjee, Frequency Stabilization of Solar Thermal-Photovoltaic Hybrid Renewable Power Generation Using Energy Storage Devices, Iranian Journal of Science and Technology, Transactions of Electrical Engineering 45 (2021) 597–617.

K. M. Al Naimi, J.-F. Hoffmann, K. Al Ali, N. Calvet, Influencing parameters on the sintering process of steel slag-based ceramics for high-temperature thermal energy storage, in: AIP Conference Proceedings, 2020, p. 020001. doi:10.1063/5.0028940.

S. Kuravi, J. Trahan, D. Y. Goswami, M. M. Rahman, E. K. Stefanakos, Thermal energy storage technologies and systems for concentrating solar power plants, 2013. doi:10.1016/j.pecs.2013.02.001.

A. Gil, M. Medrano, I. Martorell, A. Lázaro, P. Dolado, B. Zalba, L. F. Cabeza, State of the art on high temperature thermal energy storage for power generation. Part 1—Concepts, materials and modellization, Renewable and Sustainable Energy Reviews 14 (2010) 31–55.

M. Ameri, S. H. Hejazi, K. Montaser, Performance and economic of the thermal energy storage systems to enhance the peaking capacity of the gas turbines, Applied Thermal Engineering 25 (2005) 241–251.

J. Arteaga, H. Zareipour, A Price-Maker/Price-Taker Model for the Operation of Battery Storage Systems in Electricity Markets, IEEE Transactions on Smart Grid 10 (2019) 6912–6920.

M. Legrand, R. Labajo-Hurtado, L. M. Rodríguez-Antón, Y. Doce, Price arbitrage optimization of a photovoltaic power plant with liquid air energy storage. Implementation to the Spanish case, Energy 239 (2022) 121957.

W. T. Hamilton, T. W. Neises, Dispatch optimization of electric thermal energy storage within System Advisor Model, Journal of Energy Storage 61 (2023).

G. J. Soto, B. Lindley, T. Neises, C. Stansbury, M. J. Wagner, Dispatch Optimization, System Design and Cost Benefit Analysis of a Nuclear Reactor with Molten Salt Thermal Storage, Energies 2022, Vol. 15, Page 3599 15 (2022) 3599.

C. Budny, R. Madlener, C. Hilgers, Economic Feasibility of Pipeline and Underground Reservoir Storage Options for Power-to-Gas Load Balancing, Institute for Future Energy Consumer Needs and Behavior (2013).

M. Jonsson, Advanced Power Cycles with Mixtures as the Working Fluid, Ph.D. thesis, 2003.

A. L. Kalina, M. Asme, H. M. Leibowitz, Applying Kalina Technology to a Bottoming Cycle for Utility Combined Cycles, in: Proceedings of the ASME 1987 International Gas Turbine Conference and Exhibition, Anaheim, 1987. URL: https://asmedigitalcollection.asme.org/GT/proceedings-pdf/GT1987/79269/V004T10A012/2397343/v004t10a012-87-gt-35.pdf.

Nasruddin, R. Monasari, B. R. Dewantoro, M. I. Attharik, A. S. Wibowo, A. Surachman, Thermodynamic analysis and multi objective optimization of kalina and absorption cycle for power and cooling driven by lahendong geothermal source, IOP Conference Series: Earth and Environmental Science 105 (2018) 012099.

D. A. Dellasala, M. I. Goldstein, M. Whitmore, Development of Coal-Fired Steam Technology in Britain, Encyclopedia of the Anthropocene (2018) 285–305.

J. Paulides, E. Post, J. Post, L. Encica, E. Lomonova, Green turbine: A high speed double turbine solution for sustainable energy harvesting from waste heat, in: 2015 Tenth International Conference on Ecological Vehicles and Renewable Energies (EVER), IEEE, 2015, pp. 1–7. URL: http://ieeexplore.ieee.org/document/7112926/. doi:10.1109/EVER.2015.7112926.

Siemens, SGT5-8000H Heavy-duty gas turbine - Gas turbines - Siemens Global Website, 2018. URL: https://www.siemens.com/global/en/home/products/energy/power-generation/gas-turbines/sgt5-8000h.html#!/.

T. Tanuma, Introduction to steam turbines for power plants, Advances in Steam Turbines for Modern Power Plants (2017) 3–9.

D. Kumar, D. Kumar, Sustainable management of coal preparation, Sustainable Management of Coal Preparation (2018) 1–454.

J. M. Pringle, D. Al-Masri, F. Mahmoudi, A. Akbarzadeh, P. Phelan, Other technologies, Elsevier, 2023. URL: http://www.sciencedirect.com:5070/book/9780128180228/power-generation-technologies-for-low-temperature-and-distributed-heat. doi:10.1016/B978-0-12-818022-8.00007-7.

A. D. Gianfrancesco, Materials for Ultra-Supercritical and Advanced Ultra-Supercritical Power Plants. Technologies for chemical analyses, microstructural and inspection investigations, 2017. URL: http://www.sciencedirect.com:5070/book/9780081005521/materials-for-ultra-supercritical-and-advanced-ultra-supercritical-power-plants.

K. Nakamura, T. Tabei, T. Takano, Recent Technologies for Steam Turbines, Fuji Electric Review 56 (2010).

F. Starr, High temperature materials issues in the design and operation of coal-fired steam turbines and plant, Structural Alloys for Power Plants (2014) 36–68.

A. Ohji, M. Haraguchi, Steam turbine cycles and cycle design optimization: The Rankine cycle, thermal power cycles, and IGCC power plants, Advances in Steam Turbines for Modern Power Plants (2017) 11–40.

B. Kościelniak, B. Chmiela, M. Sozańska, R. Swadźba, M. Drajewicz, Oxidation behavior of inconel 740h nickel superalloy in steam atmosphere at 750 ▫ c, Materials 14 (2021).

M. Johnson, M. Fiss, Superheated steam production from a large-scale latent heat storage system within a cogeneration plant, Communications Engineering 2 (2023).

D. Y. Cui, Y. Dai, X. Z. Cai, Y. Fu, X. X. Li, Y. Zou, J. G. Chen, Preconceptual nuclear design of a 50 kWth heat pipe cooled micro molten salt reactor (micro-MSR), Progress in Nuclear Energy 134 (2021) 103670.

X.-H. An, J.-H. Cheng, T. Su, P. Zhang, Determination of thermal physical properties of alkali fluoride/carbonate eutectic molten salt, in: AIP Conference Proceedings, volume 1850, AIP Publishing LLC, 2017, p. 070001. URL: http://aip.scitation.org/doi/abs/10.1063/1.4984415. doi:10.1063/1.4984415.

R. R. Romatoski, L. W. Hu, Fluoride-Salt-Cooled High-Temperature Test Reactor Thermal-Hydraulic Licensing and Uncertainty Propagation Analysis, Nuclear Technology (2019) 1–18.

M. S. Manohar S. Sohal, M. A. Matthias A. Ebner, P. Piyush Sabharwall, P. Phil Sharpe, Engineering Database of Liquid Salt Thermophysical and Thermochemical Properties, Technical Report, Idaho National Laboratory (United States), 2010. URL: http://www.osti.gov/servlets/purl/980801-mXK8gS/. doi:10.2172/980801.

A. M. Bonanos, M. C. Georgiou, K. G. Stokos, C. N. Papanicolas, Engineering aspects and thermal performance of molten salt transfer lines in solar power applications, Applied Thermal Engineering 154 (2019) 294–301.

R. Adinberg, D. Zvegilsky, M. Epstein, Heat transfer efficient thermal energy storage for steam generation, Energy Conversion and Management 51 (2010) 9–15.

M. Liu, W. Saman, F. Bruno, Review on storage materials and thermal performance enhancement techniques for high temperature phase change thermal storage systems, Renewable and Sustainable Energy Reviews 16 (2012) 2118–2132.

C. Chen, Z. Ge, Y. Zhang, Study of combined heat and power plant integration with thermal energy storage for operational flexibility, Applied Thermal Engineering 219 (2023) 119537.

S. Stultz, J. Kitto, Steam: Its generation and use, 1, 41 ed., The Babcock & Wilcox Company, 2005.

A. Ahmed, K. K. Esmaeil, M. A. Irfan, F. A. Al-Mufadi, Design methodology of heat recovery steam generator in electric utility for waste heat recovery, International Journal of Low-Carbon Technologies 13 (2018) 369–379.

S. P. Hennessey, Superheaters and reheaters, Heat Recovery Steam Generator Technology (2017) 95–113.

V. S. Polonsky, D. A. Tarasov, D. A. Gorr, Configuration of Evaporators for Once-Through Heat Recovery Steam Generators of Combined-Cycle Units, Thermal Engineering 66 (2019) 340–349.

S. A. Rackley, Power generation fundamentals, Carbon Capture and Storage (2017) 37–71.

A. González Díaz, E. Sánchez Fernández, J. Gibbins, M. Lucquiaud, Sequential supplementary firing in natural gas combined cycle with carbon capture: A technology option for Mexico for low-carbon electricity generation and CO2 enhanced oil recovery, International Journal of Greenhouse Gas Control 51 (2016) 330–345.

S. Shiozaki, T. Fujii, K. Takenaga, M. Ozawa, A. Yamada, Gas turbine combined cycle, Advances in Power Boilers (2021) 305–344.

A. G. Díaz, E. S. Fernandez, J. Gibbins, M. Lucquiaud, Sequential Supplementary Firing in Combined Cycle Power Plant with Carbon Capture: Part-load Operation Scenarios in the Context of EOR, in: Energy Procedia, volume 114, Elsevier Ltd, 2017, pp. 1453–1468. doi:10.1016/j.egypro.2017.03.1901.

I. E. Cáceres, R. M. Montañés, L. O. Nord, Flexible operation of combined cycle gas turbine power plants with supplementary firing, Technical Report, 2018.

J. Morales-Hernández, A. Mandujano-Ruiz, F. Castañeda-Zaldivar, R. Antaño-López, J. T. González, High Temperature Corrosion Resistance of Coatings Deposited by Hvof for Application in Steam Turbines, Procedia Chemistry 12 (2014) 80–91.

Siemens Gamesa, Thermal energy storage with ETES, 2020. URL: https://www.siemensgamesa.com/en-int/products-and-services/hybrid-and-storage/thermal-energy-storage-with-etes.

D. C. Stack, D. Curtis, C. Forsberg, Performance of firebrick resistance-heated energy storage for industrial heat applications and round-trip electricity storage, Applied Energy 242 (2019) 782–796.

Siemens Gamesa, Same forces. New rules. Introducing Electric Thermal Energy Storage (ETES)-putting gigawatt hours of energy at your command, 2019. URL: https://www.siemensgamesa.com/-/media/siemensgamesa/downloads/en/products-and-services/hybrid-power-and-storage/etes/siemens-gamesa-storage-etes-storage-brochure-en.pdf.

Z. Huda, T. Zaharinie, H. A. Al-Ansary, Enhancing power output and profitability through energy-efficiency techniques and advanced materials in today's industrial gas turbines, 2014. doi:10.1186/s40712-014-0002-y.

F. J. Collado, J. Guallar, A review of optimized design layouts for solar power tower plants with campo code, 2013. doi:10.1016/j.rser.2012.11.076.

S. Arpit, P. K. Das, A state-of-the-art review of heat recovery steam generators and waste heat boilers, Energy Efficiency 16 (2023).

H. Shin, D. Kim, H. Ahn, S. Choi, G. Myoung, Thermal Stress Analysis in Structural Elements of HRSG Casing, International Journal of Energy Engineering 2 (2012) 202–209.

S. Sanaye, M. Rezazadeh, Transient thermal modelling of heat recovery steam generators in combined cycle power plants, International Journal of Energy Research 31 (2007) 1047–1063.

M. Nadir, A. Ghenaiet, Thermodynamic optimization of several (heat recovery steam generator) HRSG configurations for a range of exhaust gas temperatures, Energy 86 (2015) 685–695.

S. W. Kim, J. Y. Ahn, S. D. Kim, D. Hyun Lee, Heat transfer and bubble characteristics in a fluidized bed with immersed horizontal tube bundle, International Journal of Heat and Mass Transfer 46 (2003) 399–409.

S. Z. Tang, Y. L. He, F. L. Wang, Y. B. Tao, Parametric study on fouling mechanism and heat transfer characteristics of tube bundle heat exchangers for reducing fouling considering the deposition and removal mechanisms, Fuel 211 (2018) 301–311.

K. A. Pleshanov, R. S. Maslov, V. S. Pankov, K. V. Sterkhov, D. A. Khokhlov, Investigation into Factors Causing Damage to Low-Pressure Loop Evaporating Tubes of Large-Capacity Heat-Recovery Steam Generators, Thermal Engineering 67 (2020) 543–553.

A. Fabricius, J. Malloy, M. Taylor, D. Moelling, Predicting and Preventing Risk of Vibration Induced Failures in Boilers and Heat Recovery Steam Generators (HRSG), in: ASME 2022 Power Conference, 2022. URL: http://asmedigitalcollection.asme.org/POWER/proceedings-pdf/POWER2022/85826/V001T03A001/6920279/v001t03a001-power2022-82445.pdf.

I. F. Galindo-García, A. K. Vázquez-Barragán, M. Rossano-Román, CFD Simulations of Heat Recovery Steam Generators Including Tube Banks, American Society of Mechanical Engineers, Power Division (Publication) POWER 2 (2014).

A. Boonloi, W. Jedsadaratanachai, EFFECTS OF BLOCKAGE LOCATIONS FOR ENHANCED HEAT TRANSFER AND FLOW VISUALIZATION IN A TESTED DUCT WITH DUAL-INCLINED BAFFLES (DIB): A CFD ANALYSIS, Frontiers in Heat and Mass Transfer 18 (2022).

G. J. Yoo, H. K. Choi, K. L. Choi, Numerical study on heat transfer characteristics of turbulent flow in transition duct, Transactions of the Korean Society of Mechanical Engineers, B 35 (2011) 923–932.

A. F. Tenbusch, CFD Modeling of Cogeneration Burner Applications and the Significance of Thermal Radiative Heat Transfer Effects, Proceedings of the 2003 International Joint Power Generation Conference (2008) 731–742.

D. Li, Y. Hu, D. Li, J. Wang, Combined-cycle gas turbine power plant integration with cascaded latent heat thermal storage for fast dynamic responses, Energy Conversion and Management 183 (2019) 1–13.

V. V. S. K. Vytla, CFD Modeling of Heat Recovery Steam Generator and its Components Using Fluent, Ph.D. thesis, University of Kentucky, 2005.

M. Torresi, A. Saponaro, S. M. Camporeale, B. Fortunato, CFD Analysis of the Flow Through Tube Banks of HRSG, Proceedings of the ASME Turbo Expo 7 (2009) 327–337.

P. Hanafizadeh, S. Falahatkar, P. Ahmadi, M. Mirzakhani Siahkalroudi, A novel method for inlet duct geometry improvement of heat recovery steam generators, Applied Thermal Engineering 89 (2015) 125–133.

V. V. Katti, S. N. Yasaswy, S. V. Prabhu, Local heat transfer distribution between smooth flat surface and impinging air jet from a circular nozzle at low Reynolds numbers, Heat and Mass Transfer/Waerme- und Stoffuebertragung 47 (2011) 237–244.

R. N. Gopalakrishnan, P. J. Disimile, CFD analysis of twin turbulent impinging round jets at different impingement angles, Fluids 3 (2018).

P. Singh, N. K. Grover, V. Agarwal, S. Sharma, J. Singh, M. Sadeghzadeh, A. Issakhov, Computational Fluid Dynamics Analysis of Impingement Heat Transfer in an Inline Array of Multiple Jets, Mathematical Problems In Engineering (2021).

D. Lytle, B. W. Webb, Air jet impingement heat transfer at low nozzle-plate spacings, International Journal of Heat and Mass Transfer 37 (1994) 1687–1697.

Y. Ahmimache, M. Fénot, F. Plourde, L. Descamps, Heat transfer and flow velocity study of a row of jets emerging from a perforated pipe at a low Reynolds number, International Journal of Heat and Mass Transfer 183 (2022) 122067.

G. Lindner, S. Schmelter, R. Model, A. Nowak, V. Ebert, M. Bar, A Computational Fluid Dynamics Study on the Gas Mixing Capabilities of a Multiple Inlet System, Journal of Fluids Engineering 138 (2016).

Ansys Inc, ANSYS FLUENT 12.0 Theory Guide - 8.5 The Steady Laminar Flamelet Model Theory, 2009. URL: `https://www.afs.enea.it/project/neptunius/docs/fluent/html/th/node159.htm`.

J. Smagorinsky, GENERAL CIRCULATION EXPERIMENTS WITH THE PRIMITIVE EQUATIONS: I. THE BASIC EXPERIMENT, Monthly Weather Review 91 (1963) 99–164.

S. Wuryanti, R. D. Jadmiko, Design of Heat-Recovery Steam Generator Components in Gas Turbine (70 MW) Combined Cycle Power Plants (105 MW), International Journal of Mechanical Engineering and Robotics Research 10 (2021) 612–619.

P. R. Silva, A. J. Leiroz, M. E. Cruz, Evaluation of the efficiency of a heat recovery steam generator via computational simulations of off-design operation, Journal of the Brazilian Society of Mechanical Sciences and Engineering 42 (2020).

A. Sharif Ahmadian, Numerical Methods and Procedures, Numerical Models for Submerged Breakwaters (2016) 93–108.

J. Chu, D. Zhu, W. Wang, B. Li, J. Du, G. Yang, Analysis and Optimization of Mixing Performance of the High-Temperature Gas Flow in a Mixing Chamber, Journal of Applied Fluid Mechanics 16 (2023) 603–617.

O. N. Kashinskii, P. D. Lobanov, A. S. Kurdyumov, N. A. Pribaturin, Experimental simulation of a liquid-metal heat-transfer fluid flow in a T-shaped mixer, Technical Physics 61 (2016) 783–785.

S. Chantasiriwan, Determination of optimal total area of heat recovery steam generator, Case Studies in Thermal Engineering 53 (2024) 103909.

M. Nawaz, M. Hamzaoui, M. D. Bukhari, G. Mustafa, S. U. Khan, A. Aydi, L. Kolsi, A numerical study on the superheater tubes bundle of a 660 MW coal-fired supercritical boiler, https://doi.org/10.1142/S0217979224502266 (2023).

V. B. Zametaev, I. I. Lipatov, Energy exchange in a compressible turbulent mixing layer, Journal of Turbulence 22 (2021) 48–77.

L. Zhang, X. Dong, K. Liu, X. Zhang, F. Hou, Z. Hu, Effect of Flue Gas Recirculation on Nitrogen Oxide Emission of Coal-Fired Unit Boiler, IOP Conference Series: Earth and Environmental Science 440 (2020) 042106.

R. A. Antonia, T. Zhou, G. Xu, Second-order temperature and velocity structure functions: Reynolds number dependence, Physics of Fluids 12 (2000) 1509–1517.

J. C. López-López, M. Salinas-Vázquez, M. P. Verma, W. Vicente, I. F. Galindo-García, Computational Fluid Dynamic Modeling to Determine the Resistance Coefficient of a Saturated Steam Flow in 90 Degree Elbows for High Reynolds Number, Journal of Fluids Engineering, Transactions of the ASME 141 (2019).

L. Prakash, T. Ramesh, Sustainability analysis of HRSG modules against high velocity exhaust of advance class Fr9FB gas turbines, Materials Today: Proceedings 27 (2020) 2870–2879.

H. Liang, C. Tang, C. Xie, R. Hu, H. Yuan, A numerical simulation of high-Reynolds-number opposed impinging wall water jets in a limited field, AIP Advances 13 (2023) 115301.

S. P. Venkateshan, Heat transfer / S. P. Venkateshan., 3rd ed. 2021. ed., Springer, Cham, Switzerland, 2021.

Z. Wang, Q. Zhang, Y. Yan, K. Liu, P. M. Ligrani, Secondary Flows and Extra Heat Transfer Enhancement of Ribbed Surfaces With Jet Impingement, Technical Report, 2017. URL: http://openaccess.city.ac.uk/publications@city.ac.uk.

K. Harris, C. Michaels, Z. Clark, A. Mettrick, V. Martin, W. Spry, B. Cupples, I. Andrewes, L. Waters, Energy Trends September 2022, Technical Report, Department for Business, Energy & Industrial Strategy, 2022.

DECC, Planning our electric future: a white paper for secure, affordable and low-carbon electricity, Technical Report, Department of Energy and Climate Change, London, 2011. URL: https://books.google.co.uk/books?id=pG6ZCiAg9UEC.

ESSEA, Carbon Monoxide: Its Environmental Impact, 2015. URL: https://esseacourses.strategies.org/module.php?module_id=170http://essea.strategies.org/module.php?module_id=170.

A. T. Evulet, A. M. ELKady, A. R. Branda, D. Chinn, On the Performance and Operability of GE's Dry Low NOx Combustors utilizing Exhaust Gas Recirculation for PostCombustion Carbon Capture, Energy Procedia 1 (2009) 3809–3816.

J. Spelling, B. Laumert, T. Fransson, Advanced hybrid solar tower combined-cycle power plants, in: Energy Procedia, volume 49, Elsevier Ltd, 2014, pp. 1207–1217. doi:10.1016/j.egypro.2014.03.130.

S. D. Garvey, Integrating Energy Storage with Renewable Energy Generation, Wind Engineering 39 (2015) 129–140.

F. Holy, M. Textor, S. Lechner, Gas turbine cogeneration concepts for the pressureless discharge of high temperature thermal energy storage units, Journal of Energy Storage 44 (2021).

S. Hada, K. Takata, Y. Iwasaki, M. Yuri, J. Masada, High-efficiency Gas Turbine Development applying 1600°C class "J" Technology, Technical Report 2, Mitsubishi Heavy Industries, 2015.

B. Grange, C. Dalet, Q. Falcoz, F. Siros, A. Ferrière, Simulation of a hybrid solar gas-turbine cycle with storage integration, in: Energy Procedia, volume 49, 2013, pp. 1147–1156. URL: www.sciencedirect.com. doi:10.1016/j.egypro.2014.03.124.

Z. Long, Z. Zhou, Z. Qin, J. Luo, M. Bai, J. Liu, D. Yu, Research on active modulation of gas turbine cooling air flow, Applied Thermal Engineering 230 (2023) 120874.

S. Can Gülen, Gas Turbines for Electric Power Generation, in: Gas Turbines for Electric Power Generation, Cambridge University Press, 2019, pp. 308–361. URL: https://www.cambridge.org/core/product/identifier/9781108241625%23CN-bp-12/type/book_part. doi:10.1017/9781108241625.013.

R. G. Bhuvana, S. A. Srinivasan, D. Thanikaivel Murugan, CFD analysis on swirl angle effect in gas turbine combustion chamber, in: IOP Conference Series: Materials Science and Engineering, volume 402, Institute of Physics Publishing, 2018. doi:10.1088/1757-899X/402/1/012206.

M. Huth, A. Heilos, Fuel flexibility in gas turbine systems: impact on burner design and performance, Modern Gas Turbine Systems: High Efficiency, Low Emission, Fuel Flexible Power Generation (2013) 635–684.

N. Shelil, Flashback Studies with Premixed Swirl Combustion, Ph.D. thesis, Cardiff University, Cardiff, 2009.

A. R. Kutlumukhamedov, D. V. Skiba, F. G. Bakirov, Combined Method for Prediction of Carbon Monoxide Emission from Gas Turbine Combustion Chambers, 2021 International Scientific and Technical Engine Conference, EC 2021 (2021).

M. K. Lila, Numerical and Experimental Analysis of Combustion Characteristics of Gas Turbine Engines, Mathematical Statistician and Engineering Applications 70 (2021) 509–518.

S. Hermeth, G. Staffelbach, L. Y. M. Gicquel, V. Anisimov, C. Cirigliano, T. Poinsot, Bistable swirled flames and influence on flame transfer functions, Combustion and Flame (2013).

B. S. Brewster, S. M. Cannon, J. R. Farmer, F. Meng, Modeling of lean premixed combustion in stationary gas turbines, Progress in Energy and Combustion Science (1999).

Y. Zheng, M. Zhu, D. Mira Martinez, X. Jiang, Large-eddy simulation of mixing and combustion in a premixed swirling combustor with synthesis gases, Computers & Fluids (2013).

R. De Robbio, Innovative combustion analysis of a micro-gas turbine burner supplied with hydrogen-natural gas mixtures, in: Energy Procedia, volume 126, Elsevier Ltd, 2017, pp. 858–866. doi:10.1016/j.egypro.2017.08.291.

P. Laranci, E. Bursi, F. Fantozzi, Numerical analysis of a microturbine combustion chamber modified for biomass derived syngas, in: ASME Turbo Expo 2011, 2011. URL: http://asmedigitalcollection.asme.org/GT/proceedings-pdf/GT2011/54624/541/2757727/541_1.pdf.

H.-Y. Shih, C.-R. Liu, COMBUSTION CHARACTERISTICS AND HYDROGEN ADDITION EFFECTS ON THE PERFORMANCE OF A CAN COMBUSTOR FOR A MICRO GAS TURBINE, in: ASME Turbo Expo 2010: Power for Land, Sea and Air, Power for Land, 2010. URL: http://asmedigitalcollection.asme.org/GT/proceedings-pdf/GT2010/44007/271/2687215/271_1.pdf.

Y. N. Dabwan, G. Pei, T. Hu, H. Zhang, B. Zhao, Development and assessment of a low-emissions gas turbine system for power utilities incorporating intercooling and solar preheating, Applied Thermal Engineering (2022).

O. Behar, A novel hybrid solar preheating gas turbine, Energy Conversion and Management (2017).

Ansys Inc, Ansys Fluent 19.1, 2018.

A. H. Lefebvre, D. R. Ballal, D. W. Bahr, GAS TURBINE COMBUSTION-Alternative Fuels and Emissions, Journal of engineering for gas turbines and power 132 (2010) 116501 (1)–116501 (1).

T. Poinsot, D. Veynante, Theoretical and Numerical Combustion, Prog. Energy Combust. Sci. 28 (2005).

V. Zimont, W. Polifke, M. Bettelini, W. Weisenstein, An Efficient Computational Model for Premixed Turbulent Combustion at High Reynolds Numbers Based on a Turbulent Flame Speed Closure, in: ASME 1997 International Gas Turbine and Aeroengine Congress and Exhibition, volume 2, American Society of Mechanical Engineers Digital Collection, 1997. URL: https://dx.doi.org/10.1115/97-GT-395. doi:10.1115/97-GT-395.

C. D. Pierce, P. Moin, Progress-variable approach for large-eddy simulation of non-premixed turbulent combustion, Journal of Fluid Mechanics 504 (2004) 73–97.

Y. Hu, H. Olguin, E. Gutheil, Transported Joint Probability Density Function Simulation of Turbulent Spray Flames Combined with a Spray Flamelet Model Using a Transported Scalar Dissipation Rate, Combustion Science and Technology 189 (2017) 322–339.

S. K. Kim, S. M. Kang, Y. M. Kim, FLAMELET MODELING FOR COMBUSTION PROCESSES AND NOx FORMATION IN THE TURBULENT NONPREMIXED CO/H2/N2 JET FLAMES, Combustion Science and Technology 168 (2001) 47–83.

Z. Li, E. R. Hawkes, A. Wehrfritz, B. Savard, A DNS evaluation of three MMC-like mixing models for transported PDF modelling of turbulent nonpremixed flames, Combustion and Flame 258 (2023) 113039.

P. Kundu, J. Scroggins, M. M. Ameen, A Novel In Situ Flamelet Tabulation Methodology for the Representative Interactive Flamelet Model, Combustion Science and Technology 192 (2020) 1–25.

S. M. J. Razeghi, M. Safarzadeh, H. Pasdarshahri, Comparison of combustion models based on fast chemistry assumption in large eddy simulation of pool fire, Journal of the Brazilian Society of Mechanical Sciences and Engineering 42 (2020) 1–15.

J. Göttgens, F. Mauss, N. Peters, Analytic approximations of burning velocities and flame thicknesses of lean hydrogen, methane, ethylene, ethane, acetylene, and propane flames, Symposium (International) on Combustion 24 (1992) 129–135.

Y. Hu, R. Kurose, Nonpremixed and premixed flamelets LES of partially premixed spray flames using a two-phase transport equation of progress variable, Combustion and Flame 188 (2018) 227–242.

R. J. Kee, F. M. Rupley, J. A. Miller, M. E. Coltrin, J. F. Grcar, E. Meeks, H. K. Moffat, A. E. Lutz, G. Dixon-Lewis, M. D. Smooke, J. Warnatz, G. H. Evans, R. S. Larson, R. E. Mitchell, L. R. Petzold, W. C. Reynolds, M. Caracotsios, W. E. Stewart, P. Glarborg, C. Wang, O. Adigun, The Chemkin Thermodynamic Database, Technical Report, Reaction Design, San Diego, 2000. URL: `www.ReactionDesign.com`.

G. P. Smith, D. M. Golden, M. Frenklach, N. W. Moriarty, B. Eiteneer, M. Goldenberg, C. T. Bowman, R. K. Hanson, S. Song, W. C. Gardiner Jr, V. V. Lissianski, Z. Qin, GRI-Mech 3.0, 1999. URL: `http://combustion.berkeley.edu/gri-mech/version30/text30.html#cite`.

V. Raman, H. Pitsch, R. O. Fox, Hybrid large-eddy simulation/Lagrangian filtered-density-function approach for simulating turbulent combustion, Combustion and Flame 143 (2005) 56–78.

L.-Y. Jiang, I. Campbell, A Critical Evaluation of NOx Modeling in a Model Combustor, Journal of Engineering for Gas Turbines and Power 127 (2005) 483–491.

C. Russo, G. Mori, V. V. Anisimov, J. Parente, Micro gas turbine combustor emissions evaluation using the chemical reactor modelling approach, Proceedings of the ASME Turbo Expo 2 (2007) 531–542.

B. Stiehl, T. Genova, M. Otero, J. Reyes, K. Ahmed, S. Martin, NOx emission of an axial-staged combustor at high-pressure, in: AIAA Propulsion and Energy 2020 Forum, American Institute of Aeronautics and Astronautics Inc, AIAA, 2020, pp. 1–10. doi:`10.2514/6.2020-3693`.

S. Karyeyen, Combustion characteristics of a non-premixed methane flame in a generated burner under distributed combustion conditions: A numerical study, Fuel 230 (2018) 163–171.

A. K. Sharma, S. Sen, C. Bhattacharya, A. Mukhopadhyay, A. Datta, ANALYSIS OF DIFFERENT RADIATION MODELS IN A SWIRL STABILIZED COMBUSTOR, in: ASME 2014 Gas Turbine India Conference, 2014. URL: `http://asmedigitalcollection.asme.org/GTINDIA/proceedings-pdf/GTINDIA2014/49644/V001T03A015/4240939/v001t03a015-gtindia2014-8318.pdf`.

S. Sen, I. K. Puri, Thermal radiation modeling in flames and fires, Transport Phenonema in Fires (2008).

S. S. Sazhin, E. M. Sazhina, O. Faltsi-Saravelou, P. Wild, The p-1 model for thermal radiation transfer: Advantages and limitations, Fuel 75 (1996) 289–294.

A. A. Hosseini, M. Ghodrat, M. Moghiman, S. H. Pourhoseini, Numerical study of inlet air swirl intensity effect of a Methane-Air Diffusion Flame on its combustion characteristics, Case Studies in Thermal Engineering 18 (2020).

Z. Xi, Z. Liu, X. Shi, T. Lian, Y. Li, Numerical investigation on flow characteristics and emissions under varying swirler vane angle in a lean premixed combustor, Case Studies in Thermal Engineering 31 (2022) 101800.

I. Andrić, A. Pina, P. Ferrão, J. Fournier, B. Lacarrière, O. Le Corre, M. Raghib Shakeel, Y. S. Sanusi, M. A. Mokheimer, Numerical Modeling of Oxy-Fuel Combustion in a Model Gas Turbine Combustor: Effect of Combustion Chemistry and Radiation Model, Energy Procedia 142 (2017) 0–000.

A. J. Aspden, J. B. Bell, S. E. Woosley, C. Leung, K. . Ichi Nomoto, T. Suzuki, S. P. Muppala, S. Paleli, M. Vasudevan, RANS studies of hydrogen-enrichment premixed turbulent flames, IOP Conference Series: Materials Science and Engineering (2021).

A. C. Benim, S. Iqbal, F. Joos, A. Wiedermann, Numerical Analysis of Turbulent Combustion in a Model Swirl Gas Turbine Combustor, Journal of Combustion (2016).

J. R. Nanduri, I. B. Celik, P. A. Strakey, D. R. Parsons, Assessment of RANS-based turbulent combustion models for prediction of gas turbine emissions: Turbulence model and reaction mechanism effects, Fall Technical Meeting of the Eastern States Section of the Combustion Institute 2007 "Chemical and Physical Processes in Combustion" (2007) 321–331.

R. Prieler, M. Demuth, D. Spoljaric, C. Hochenauer, Numerical investigation of the steady flamelet approach under different combustion environments, Fuel 140 (2015) 731–743.

N. J. Wilson, Developing the Rolls-Royce Tay, in: ASME 1988 International Gas Turbine and Aeroengine Congress and Exposition, The American Society of Mechanical Engineers, Amsterdam, 1988. URL: https://asmedigitalcollection.asme.org/GT/proceedings-pdf/GT1988/79191/V002T02A017/2397656/v002t02a017-88-gt-302.pdf.

K. Zhang, Turbulent Combustion Simulation in Realistic Gas-Turbine Combustors, Technical Report, 2017.

A. F. Bicen, D. G. Tse, J. H. Whitelaw, Combustion characteristics of a model can-type combustor, Combustion and Flame 80 (1990) 111–125.

V. Vilag, J. Vilag, R. Carlanescu, A. Mangra, F. Florean, CFD Application for Gas Turbine Combustion Simulations, in: Computational Fluid Dynamics Simulations, 2019, pp. 215–234. URL: https://books.google.co.uk/books?hl=en&lr=&id=SJYtEAAAQBAJ&oi=fnd&pg=PA215&dq=gas+turbine+combustion+chamber+cfd+model+ansys+n2+21%25&ots=DpKZNGB7cI&sig=CbLl2grgBiqR223pi83PKOxeuCs#v=onepage&q=gas%20turbine%20combustion%20chamber%20cfd%20model%20ansys%20n2%2021%25&f=false.

A. A. Gamil, T. Nikolaidis, I. Lelaj, P. Laskaridis, Assessment of numerical radiation models on the heat transfer of an aero-engine combustion chamber, Case Studies in Thermal Engineering 22 (2020) 100772.

G. C. Krieger, A. P. Campos, M. D. Takehara, F. Alfaia Da Cunha, C. A. Gurgel Veras, Numerical simulation of oxy-fuel combustion for gas turbine applications, Applied Thermal Engineering 78 (2015) 471–481.

M. P. Boyce, Combustors, Gas Turbine Engineering Handbook (2012) 427–490.

H. Hasini, S. S. Fadhil, N. Mat Zian, N. Om, CFD Investigation of Pollutant Emission in Can-Type Combustor Firing Natural Gas, LNG and Syngas, in: IOP Conference Series: Earth and Environmental Science, Institute of Physics Publishing, 2016. doi:10.1088/1755-1315/32/1/012073.

M. Yuri, J. Masada, K. Tsukagoshi, E. Ito, S. Hada, Development of 1600°C-Class High-efficiency Gas Turbine for Power Generation Applying J-Type Technology, Technical Report 3, Mitsubishi Heavy Industries, 2013.

A. De Santis, CFD analysis of CO 2-and H 2 O-diluted combustion in gas turbines, Ph.D. thesis, The University of Sheffield, Sheffield, 2016.

V. V. Anisimov, A. Chiarioni, L. Rofi, C. Ozzano, S. Hermeth, G. Hannebique, G. Staffelbach, T. Poinsot, Bi-stable flame behaviour of heavy duty gas turbine burner. Rans, LES and experiment comparison, in: Proceedings of the ASME Turbo Expo, volume 4A, American Society of Mechanical Engineers (ASME), 2015. doi:10.1115/GT2015-42536.

T. E. Lippert, D. M. Bachovchin, P. G. A. Cizmas, GAS TURBINE REHEAT USING IN-SITU COMBUSTION, Technical Report, 2004.

H. Tsuji, A. K. Gupta, T. Hasegawa, M. Katsuki, K. Kishimoto, M. Morita, High Temperature Air Combustion, CRC Press, 2002. doi:10.1201/9781420041033.

Y. Su, C. Chen, A. Su, Simulation of High Temperature Air Combustion with modified Eddy-Break-Up combustion model, Energy Procedia 14 (2012) 127–132.

L. Ye, Y. Pan, J. Jiang, W. Zhang, A numerical study of the auto-ignition temperatures of CH4-Air, C3H8-Air, CH4-C3H8-Air and CH4-CO2-Air mixtures, Journal of Loss Prevention in the Process Industries 29 (2014) 85–91.

M. A. Nemitallah, M. D. Azazul Haque, M. Hussain, A. Abdelhafez, M. A. Habib, Stratified and Hydrogen Combustion Techniques for Higher Turndown and Lower Emissions in Gas Turbines, Journal of Energy Resources Technology, Transactions of the ASME 144 (2022).

H. Hasini, N. H. Shuaib, W. A. F. Wan Abdullah, CFD analysis of temperature distribution in can-type combustor firing synthetic gas, in: Applied Mechanics and Materials, volume 393, 2013, pp. 741–746. doi:10.4028/www.scientific.net/AMM.393.741.

P. Egil Røkke, J. E. Hustad, N. A. Røkke, O. Birger Svendsgaard, Technology Update on Gas Turbine Dual Fuel, Dry Low Emission Combustion Systems, in: ASME Turbo Expo 2003, collocated with the 2003 International Joint Power Generation Conference, ASME, Atlanta, Georgia, 2003, pp. 97–107. URL: http://asmedigitalcollection.asme.org/GT/proceedings-pdf/GT2003/36851/97/4547693/97_1.pdf.

W. S. Y. Hung, Carbon Monoxide Emissions From Gas Turbines as Influenced by Ambient Temperature and Turbine Load, Journal of Engineering for Gas Turbines and Power 115 (1993) 588–593.

H. M. Rouzbahani, H. Karimipour, L. Lei, A review on virtual power plant for energy management, Sustainable Energy Technologies and Assessments 47 (2021) 101370.

Elexon, Virtual Lead Party - Elexon Digital BSC, 2021. URL: https://bscdocs.elexon.co.uk/guidance-notes/virtual-lead-party/v-3-0/id-62e244fcd3ac240007b673a0.

Y. Wang, G. Li, B. Zhou, H. Ma, Z. Li, Optimal Dispatch Strategy for Virtual Power Plants with Adjustable Capacity Assessment of High-Energy-Consuming Industrial Loads Participating in Ancillary Service Markets, Sustainability 2023, Vol. 15, Page 10479 15 (2023) 10479.

P. Denholm, W. Cole, A. W. Frazier, K. Podkaminer, N. Blair, Storage Futures Study: The Four Phases of Storage Deployment: A Framework for the Expanding Role of Storage in the U.S. Power System, National Renewable Energy Laboratory (2021).

A. Datas, A. B. Cristobal, C. Del Cañizo, E. Antolín, M. Beaughon, N. Nikolopoulos, A. Nikolopoulos, M. Zeneli, N. Sobczak, W. Polkowski, M. Tangstad, J. Safarian, D. M. Trucchi, A. Bellucci, M. Girolami, R. Marx, D. Bestenlehner, S. Lang, A. Vitulano, G. Sabbatella, A. Martí, AMADEUS: Next generation materials and solid state devices for ultra high temperature energy storage and conversion, in: AIP Conference Proceedings, volume 2033, American Institute of Physics Inc., 2018. doi:10.1063/1.5067168.

M. Ryland, W. He, Domestic thermal energy storage applications: What parameters should they focus on?, Journal of Energy Storage 60 (2023) 106685.

M. C. Soini, D. Parra, M. K. Patel, Disaggregation of energy storage operation by timescales, Journal of Energy Storage 23 (2019) 480–494.

T.-T. Nguyen, V. Martin, A. Malmquist, C. A. Silva, A review on technology maturity of small scale energy storage technologies, Renewable Energy and Environmental Sustainability 2 (2017) 36.

C. Rathgeber, E. Lävemann, A. Hauer, Economic top–down evaluation of the costs of energy storages—A simple economic truth in two equations, Journal of Energy Storage 2 (2015) 43–46.

S. Puschnigg, J. Lindorfer, S. Moser, T. Kienberger, Techno-economic aspects of increasing primary energy efficiency in industrial branches using thermal energy storage, Journal of Energy Storage 36 (2021) 102344.

C. Rathgeber, S. Hiebler, E. Lavemann, P. Dolado, A. Lazaro, J. Gasia, A. de Gracia, L. Miro, L. F. Cabeza, A. Konig-Haagen, D. Bruggemann, A. Campos-Celador, E. Franquet, B. Fumey, M. Dannemand, T. Badenhop, J. Diriken, J. E. Nielsen, A. Hauer, IEA SHC Task 42 / ECES Annex 29 – A Simple Tool for the Economic Evaluation of Thermal Energy Storages, Energy Procedia 91 (2016) 197–206.

K. Bradbury, L. Pratson, D. Patiño-Echeverri, Economic viability of energy storage systems based on price arbitrage potential in real-time U.S. electricity markets, Applied Energy 114 (2014) 512–519.

L. Kriechbaum, G. Scheiber, T. Kienberger, Grid-based multi-energy systems—modelling, assessment, open source modelling frameworks and challenges, Energy, Sustainability and Society 2018 8:1 8 (2018) 1–19.

M. G. Prina, D. Groppi, B. Nastasi, D. A. Garcia, Bottom-up energy system models applied to sustainable islands, Renewable and Sustainable Energy Reviews 152 (2021) 111625.

S. M. Schoenung, J. Eyer, Benefit/Cost Framework for Evaluating Modular Energy Storage, Technical Report, Sandia National Laboratories, 2008. URL: `http://www.ntis.gov/help/ordermethods.asp?loc=7-4-0#online`.

S. Schoenung, SANDIA REPORT Energy Storage Systems Cost Update A Study for the DOE Energy Storage Systems Program, Technical Report, 2011. URL: `http://www.ntis.gov/help/ordermethods.asp?loc=7-4-`.

A. Abrams, R. Fioravanti, J. Harrison, W. Katzenstein, M. Kleinberg, S. Lahiri, C. Vartanian, Energy Storage Cost-effectiveness Methodology and Preliminary Results Prepared, Technical Report, Public Interest Energy Research (PIER) Program, 2013. URL: `www.dnvkema.com`.

O. O. Ademulegun, P. Keatley, N. J. Hewitt, Techno-economic analysis of energy storage within network constraint groups for increasing the share of variable renewable energy, The Electricity Journal 34 (2021) 106974.

J. Martinek, J. Jorgenson, M. Mehos, P. Denholm, A comparison of price-taker and production cost models for determining system value, revenue, and scheduling of concentrating solar power plants, Applied Energy 231 (2018) 854–865.

J. Lin, F. H. Magnago, Electricity Markets: Theories and Applications, IEEE Press Series on Power Engineering, John Wiley & Sons, Incorporated, Somerset, 2017.

G. Moore, D. Long, G. Wenban-Smith, GTM : Gas Trading Manual, Woodhead Pub., Cambridge, England, 2003.

National Grid, End-to-end balancing guide, Technical Report, 2017.

UK Parliament, Gas Act 1986 c. 44, 1986.

P. Maneejuk, N. Kaewtathip, W. Yamaka, The influence of the Ukraine-Russia conflict on renewable and fossil energy price cycles, Energy Economics 129 (2024) 107218.

J. Liu, J. Wang, J. Cardinal, Evolution and reform of UK electricity market, Renewable and Sustainable Energy Reviews 161 (2022) 112317.

S. Halbrügge, P. Heess, P. Schott, M. Weibelzahl, Negative electricity prices as a signal for lacking flexibility? On the effects of demand flexibility on electricity prices, International Journal of Energy Sector Management 18 (2024) 596–616.

N. Watson, P. Bolton, Contracts for Difference Summary, Technical Report, 2023.

Elexon, Imbalance Pricing Guidance, Technical Report, 2020. URL: www.elexon.co.uk.

A. Fairbairn, Imbalance Prices Intro Seminar, 2020.

UK ETS Authority, Report on the Functioning of the UK Carbon Market for 2021 and 2022, Technical Report, London, 2023.

Department for Energy Security & Net Zero, UK Emissions Trading Scheme markets, 2024a. URL: https://www.gov.uk/government/publications/uk-emissions-trading-scheme-markets/uk-emissions-trading-scheme-markets.

Department for Energy Security & Net Zero, Participating in the UK ETS, 2024b. URL: https://www.gov.uk/government/publications/participating-in-the-uk-ets/participating-in-the-uk-ets.

Department for Energy Security & Net Zero, UK Emissions Trading Scheme (UK ETS) - Maintaining Market Stability, Technical Report, 2023.

A. Lyden, PyPSA-GB: An open source model of the GB power system for simulating future energy scenarios — PyPSA-GB documentation, 2022. URL: https://pypsa-gb.readthedocs.io/en/latest/index.html.

J. Hörsch, F. Hofmann, D. Schlachtberger, T. Brown, PyPSA-Eur: An open optimisation model of the European transmission system, Energy Strategy Reviews 22 (2018) 207–215.

M. Parzen, H. Abdel-Khalek, E. Fedotova, M. Mahmood, M. M. Frysztacki, J. Hampp, L. Franken, L. Schumm, F. Neumann, D. Poli, A. Kiprakis, D. Fioriti, PyPSA-Earth. A new global open energy system optimization model demonstrated in Africa, Applied Energy 341 (2023) 121096.

Elexon, System Sell & System Buy Prices, 2024. URL: https://www.bmreports.com/bmrs/?q=balancing/systemsellbuyprices.

Montel, Gas - UK Overview, 2024. URL: https://app.montelnews.com/en/exchanges/gas/ukoverview?126.

Ofgem, Gas Prices: Day Ahead Contracts - Monthly Average (GB), 2024. URL: https://www.ofgem.gov.uk/energy-data-and-research/data-portal/wholesale-market-indicators.

Nord Pool, N2EX Day-Ahead, 2024. URL: https://data.nordpoolgroup.com/auction/n2ex/capacities?market=N2EX%20Day-ahead.

EPEX, Market Data, 2024. URL: https://www.epexspot.com/en/market-data.

Department for Energy Security & Net Zero, Fuel mix disclosure data table, 2023. URL: https://www.gov.uk/government/publications/fuel-mix-disclosure-data-table/fuel-mix-disclosure-data-table.

Intercontinental Exchange, UK NBP Natural Gas Futures Pricing, 2024. URL: https://www.ice.com/products/910/UK-NBP-Natural-Gas-Futures/data?marketId=5600724.

European Commission, Development of EU ETS (2005-2020), 2022. URL: https://climate.ec.europa.eu/eu-action/eu-emissions-trading-system-eu-ets/development-eu-ets-2005-2020_en.

Department for Energy Security & Net Zero, UK Emissions Trading Scheme markets, 2024. URL: https://www.gov.uk/government/publications/uk-emissions-trading-scheme-markets/uk-emissions-trading-scheme-markets.

D. Hirst, Carbon Price Floor (CPF) and the price support mechanism, Technical Report, 2018. URL: www.parliament.uk/commons-library|intranet.parliament.uk/commons-library|papers@parliament.uk|@commonslibrary.

Montel, Green Market - Carbon Overview, 2024. URL: https://app.montelnews.com/en/exchanges/carbonoverview?21.

Investing.com, EUR/GBP - Euro British Pound Sterling, 2023. URL: https://uk.investing.com/currencies/eur-gbp-chart.

HM Revenue & Customs, Environmental Taxes Bulletin historical rates, 2024. URL: https://www.gov.uk/government/statistics/environmental-taxes-bulletin/environmental-taxes-bulletin-historical-rates.

Investing.com, Carbon Emissions Futures Historical Prices UK, 2024. URL: https://uk.investing.com/commodities/carbon-emissions-historical-data.

UK Government, Government conversion factors for company reporting of greenhouse gas emissions, https://www.gov.uk/government/collections/government-conversion-factors-for-company-reporting, 2023. URL: https://www.gov.uk/government/collections/government-conversion-factors-for-company-reporting.

A. Lyden, Future Years, 2022. URL: https://pypsa-gb.readthedocs.io/en/latest/notebooks/5b%20-%20Future%20Years.html.

Ofgem, Spark and dark spreads (GB), 2024. URL: https://www.ofgem.gov.uk/energy-data-and-research/data-portal/wholesale-market-indicators.

M. A. Alarcón, R. G. Alarcón, A. H. González, A. Ferramosca, A scenario-based economic-stochastic model predictive control for the management of microgrids, Sustainable Energy, Grids and Networks 36 (2023).

Python Core Developers, Python 3.12, 2023.

T. pandas development team, pandas-dev/pandas: Pandas, 2024. URL: https://doi.org/10.5281/zenodo.10697587. doi:10.5281/zenodo.10697587.

National Grid, TNUoS in 10 Minutes, Technical Report, 2024.

Scottish & Southern Electricity Networks, What are DUoS Charges?, Technical Report, 2023. URL: https://www.dcusa.co.uk/SitePages/Home.aspx.

National Grid, Introduction to Balancing Services Use of System Charges (BSUoS), Technical Report, 2019.

National Grid, Demand Flexibility Service, Technical Report, 2023.

P. Virtanen, R. Gommers, T. E. Oliphant, M. Haberland, T. Reddy, D. Cournapeau, E. Burovski, P. Peterson, W. Weckesser, J. Bright, S. J. van der Walt, M. Brett, J. Wilson, K. J. Millman, N. Mayorov, A. R. J. Nelson, E. Jones, R. Kern, E. Larson, C. J. Carey, I. Polat, Y. Feng, E. W. Moore, J. VanderPlas, D. Laxalde, J. Perktold, R. Cimrman, I. Henriksen, E. A. Quintero, C. R. Harris, A. M. Archibald, A. H. Ribeiro, F. Pedregosa, P. van Mulbregt, SciPy 1.0: Fundamental Algorithms for Scientific Computing in Python, Nature Methods 17 (2020) 261–272.

H. E. Thornton, Atmospheric circulation, seasonal predictability and Britain's energy system, 2020. doi:10.48683/1926.00095832.

B. Singh, A. H. Strømman, E. Hertwich, Life cycle assessment of natural gas combined cycle power plant with post-combustion carbon capture, transport and storage, International Journal of Greenhouse Gas Control 5 (2011) 457–466.